RCA Review

March 1969 Volume 30 No. 1

PRINTED IN U.S.A.

RCA REVIEW, published quarterly in March, June, September, and December by RCA Research and Engineering, Radio Corporation of America, Princeton, New Jersey 08540. Entered as second class matter July 3, 1950 under the Act of March 3, 1879. Second-class postage paid at Princeton, New Jersey, and at additional mailing offices. Subscription price in the United States and Canada: one year $4.00, two years $7.00, three years $9.00; in other countries, one year $4.40, two years $7.80, three years $10.20. Single copies up to five years old $2.00. For copies more than five years old, contact Walter J. Johnson, Inc., 111 Fifth Ave., New York, N. Y. 10003.

RCA REVIEW

a technical journal

Published quarterly by
RCA RESEARCH AND ENGINEERING
in cooperation with all subsidiaries and divisions of
RADIO CORPORATION OF AMERICA

VOLUME 30 MARCH 1969 NUMBER 1

CONTENTS

RCA REVIEW is regularly abstracted and indexed by *Abstracts of Photographic Science and Engineering Literature, Applied Science and Technology Index, Bulletin Signalétique des Télecommunications, Chemical Abstracts, Electronic and Radio Engineer, Mathematical Reviews, and Science Abstracts* (I.E.E.-Brit.).

RCA REVIEW

BOARD OF EDITORS

AVALANCHE DIODES AS UHF AND L-BAND SOURCES*

BY

K. K. N. CHANG

RCA Laboratories
Princeton, N. J.

Summary A summary of recent experimental results with UHF and L-band avalanche diodes is given. These diodes, which have yielded peak output powers between 200-400 watts at efficiencies between 20-60%, have excellent potential as high-power pulsed microwave sources.

INTRODUCTION

IN THE PAST decade, three solid-state devices—the tunnel diode, the varactor, and the transistor—have found application in rf power generation systems because of their small size, modest voltage requirements, and long life. The powers involved, however, are limited to a few watts. Furthermore, they are mainly cw devices. For pulsed applications, electron tubes have remained supreme because of their huge power-handling capability.

During the last few years, two new solid-state devices—the Gunn diode and the avalanche diode—have been developed. Both of these new devices are capable of generating about 100 times the pulsed power possible with the earlier devices, and are beginning to challenge the electron tube in several applications. The avalanche diode is particularly interesting because it is usually constructed of silicon, a material for which the technology is very well developed.

The silicon avalanche diode has become even more interesting with the discovery of an "anomalous" mode diode that is capable of generating pulse power of hundreds of watts at over 25% efficiency. While the work on this diode is still in what might be considered an explor-

* The research reported in this paper was jointly sponsored by the Air Force Avionics Laboratory, Wright-Patterson Air Force Base, Ohio under Contracts F33615-67-C-1981 and F33615-68-C-1688; and RCA Laboratories, Princeton, New Jersey.

atory phase, hundreds of diodes have already been built and tested in a variety of circuits. Among these diodes, many have achieved efficiences exceeding 40% and three have accumulated thousands of hours of life test. Both the efficiency and the long life are vitally important for applications requiring high peak power.

This paper describes these high-power, high-efficiency avalanche diodes and the experimental results obtained with them, and discusses briefly the anomalous mode in the context of IMPATT (IMpact Avalanche Transit-Time) diodes in general.

Microwave Oscillations in Silicon Avalanche Diodes

Semiconductors exhibit a breakdown phenomenon in the presence of a high electrical field. Such fields may be reached in a reverse-biased p-n junction diode. The work of McKay[1] has experimentally established an ionization rate (α) for silicon diodes at breakdown as a function of the electrical field (E). This experimental curve has been approximated by three different generating functions;[2-4]

$$(1) \quad \alpha_1 = a_1(E)^6,$$

$$(2) \quad \alpha_2 = a_2 \exp(b_2 E),$$

$$(3) \quad \alpha_3 = a_3 \exp\left(-\frac{b_3}{E}\right),$$

where the a's and b's are constants. The first and second functions agree with the experimental data only in a certain range, and the second is apparently not valid at low fields because the generation rate does not vanish at zero field. In addition, the functions are divergent. The third function, being convergent, is the best approximation.

Based on the experimental data on electron–hole pair generation, Read[2] proposed an n+-p-i-p+ structure and predicted microwave oscillation in such a diode. The model is straightforward. A $\pi/2$-radian phase shift occurs between the electrical field and the carrier

[1] K. G. McKay, "Avalanche Breakdown in Silicon," *Phys. Rev.*, Vol. 94, p. 877, May 15, 1954.

[2] W. T. Read, Jr., "A Proposed High-Frequency, Negative-Resistance Diode," *Bell Syst. Tech. Jour.*, Vol. 37, p. 401, March 1958.

[3] H. Egawa, "Avalanche Characteristics and Failure Mechanism of High Voltage Diodes," *IEEE Trans. on Electron Devices*, Vol. ED-13, p. 754, Nov. 1966.

[4] S. M. Sze and G. Gibbons, "Avalanche Breakdown Voltages of Abrupt and Linearly Graded p-n Junctions in Ge, Si, GaAs, and GaP," *Appl. Phys. Letters*, Vol. 8, p. 111, March 1966.

current during ionization, and another $\pi/2$-radian shift results from the transit-time effect of the moving carriers through a properly designed intrinsic region of the diode. The total shift by π radians leads to a negative resistance that is responsible for the microwave oscillation. In spite of the analytically derived prediction, such an oscillation did not materialize until Johnston, DeLoach, and Cohen[5] disclosed a similar transit-time oscillation in an avalanching p-n diode. Since then, many impact avalanche transit-time (IMPATT) diodes have been developed for X-band or higher frequencies. These diodes give, typically, cw power outputs of less than a watt at efficiencies of a few percent. Virtually no diodes were available for the lower-frequency range of UHF and L-band.

A New Mode of Operation of Avalanche Diodes

In 1967, Prager, Chang, and Weisbrod of RCA Laboratories discovered a new mode of operation[6] that dramatically deviated from the IMPATT mode and opened up the possibility of high power at high efficiencies in the lower-frequency range. To obtain such lower-frequency operation, the conventional avalanche diode was modified in its doping profiles and physical junction dimensions. In the course of this work we procured from the RCA Electronic Components division at Somerville, New Jersey, some experimental varactor diodes* that were similar to our avalanche-diode design. One of these diodes gave 280 watts peak power at 1.07 GHz with an efficiency of 43%. Other diodes from the batch gave frequencies ranging from 425 to 1400 MHz, peak powers from 150 to 435 watts, and efficiencies from 25% to 40%. Since that time, several hundred of these diodes have been made at RCA Laboratories. A summary of selected data on such diodes is given in Table I.

Subsequent to our observation of this new mode of operation, it was substantiated by other workers in germanium[7] and in silicon[8,9] avalanche diodes.

---

[5] R. L. Johnston, B. C. De Loach, Jr., and B. G. Cohen, "A Silicon Diode Microwave Oscillator," *Bell Syst. Tech. Jour.*, Vol. 44, p. 369, Feb. 1965

[6] H. J. Prager, K. K. N. Chang, and S. Weisbrod, "High-Power, High-Efficiency Silicon Avalanche Diodes at Ultra High Frequencies," *Proc. IEEE*, Vol. 55, p. 586, April 1967.

* H. Kressel designed the varactor diode and A. Pikor developed the process specifications.

[7] R. L. Johnston, D. L. Scharfetter, and D. J. Bartelink, "High-Efficiency Oscillations in Germanium Avalanche Diodes Below the Transit-Time Frequency," *Proc. IEEE*, Vol. 56, p. 1611, Sept. 1968.

[8] C. P. Snapp and B. Hoefflinger, "An Efficient Multiresonant Avalanche Diode Oscillator in the 1.5 to 11 GHz Range," *Proc. IEEE* (Letters), Vol. 56, p. 2054, Nov. 1968.

[9] M. I. Grace and G. Gibbons, *Electronic Letters*, Vol. 4, No. 25, p. 564, Dec. 1968.

Diode Fabrication

The anomalous diode is a p+-n-n+ structure wherein the n region has a resistivity of about 5 ohm-cm. The depletion layer sweeps across the n region and the diode "punches through" before reaching the point of avalanche breakdown. Typically the n region is 8 to 10

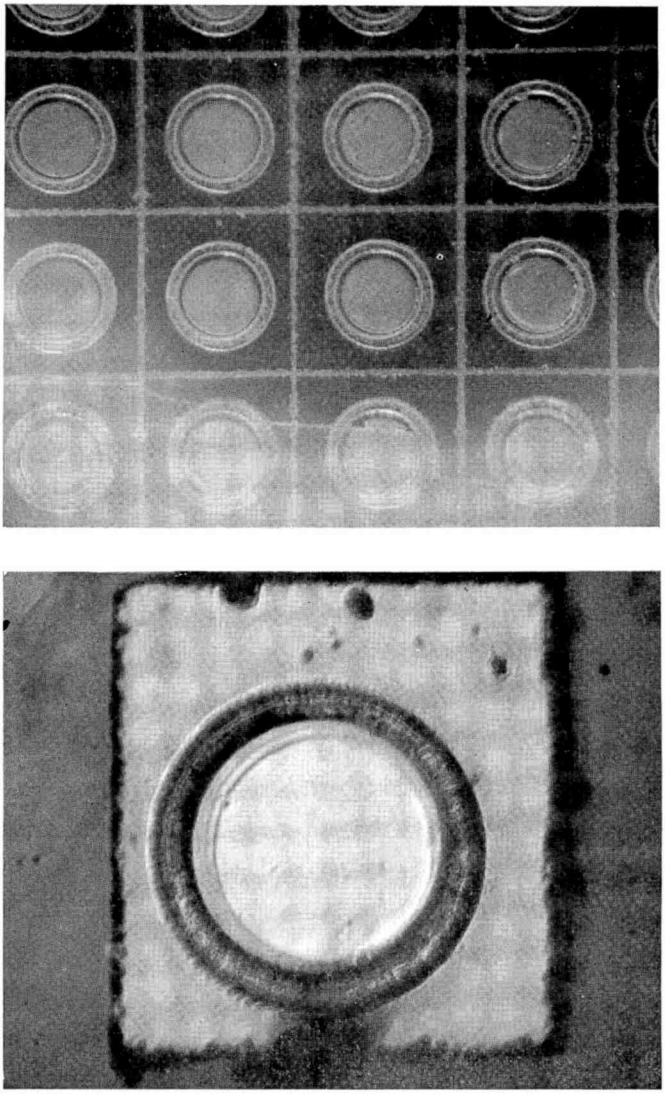

Fig. 1—(Top) Array of mesa diodes (× 16); (bottom) single mesa diodes (× 50).

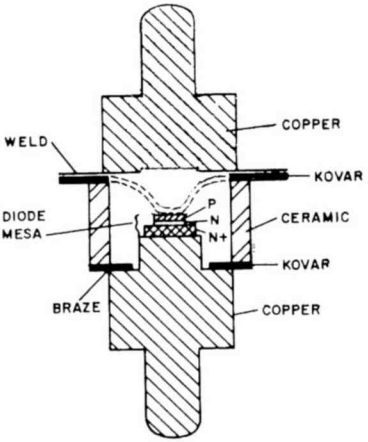

Fig. 2—Avalanche diode package.

microns wide, with a breakdown voltage of 160 volts at a punch-through of 75 volts. The p+ region of the mesa diode is obtained through a boron deposition and diffusion on the n-layer. The diffused p+-n junction is of a nearly abrupt type.

An important step in diode processing is formation of the mesas* by photoresist masking and chemical etching. An array of mesa diodes before dicing is shown in Figure 1. The mesa diameters are typically 20 to 25 mils. Diced diodes are mounted in standard varactor packages as shown in Figure 2.

Circuit Design

A tunable coaxial cavity (Figure 3) was chosen as one of the first circuits used for our tests. This circuit has the advantage of a wide

Table I—Selected Data on Anomalous Avalanche Diodes

Diode	P_o (Watts)	Efficiency (%)	Frequency (MHz)
1	435	22	425
23	280	22.5	425
70	200	25	420
X-10	420	32.5	1050
60-24	280	43	1050
X-10/16	177	59	820
X-12/3	180	60	775
S-4 (stacked)	500	25	1140

* More recently, we have had the help of J. Assour who processed several of the wafers.

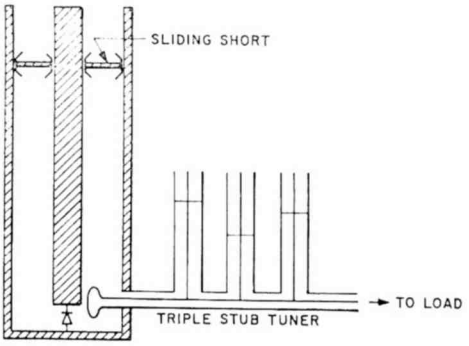

Fig. 3—Coaxial cavity with loop coupling.

tuning range. Diodes operated in this circuit were usually found to exhibit AM noise for the duration of the rf pulse. The noise could sometimes be minimized by proper adjustment of a stub tuner.

In addition to the coaxial cavity, *G-R* coaxial lines, striplines, and lumped circuits have also been attempted and, with proper adjustment, they all function. The most successful circuit is the combined coaxial-lumped circuit (Figure 4), which produces a pulse power output of 180 watts at 1.3 GHz with an efficiency of 40%. The circuit has a movable short circuit and a tunable capacitor for impedance matching. Continuous frequency tuning from 1.0 GHz to 1.7 GHz with a variation in power output of less than 1 dB has been obtained by adjusting the settings of the short circuit and capacitor.

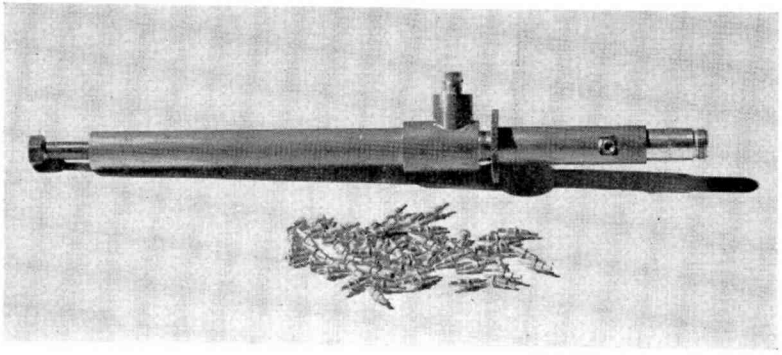

Fig. 4—Coaxial lumped circuit.

PERFORMANCE EVALUATION

1. Rise Time

Figure 5 shows oscilloscope tracings of pulse voltage, pulse current, and rf power output when the diode is in an oscillating condition.

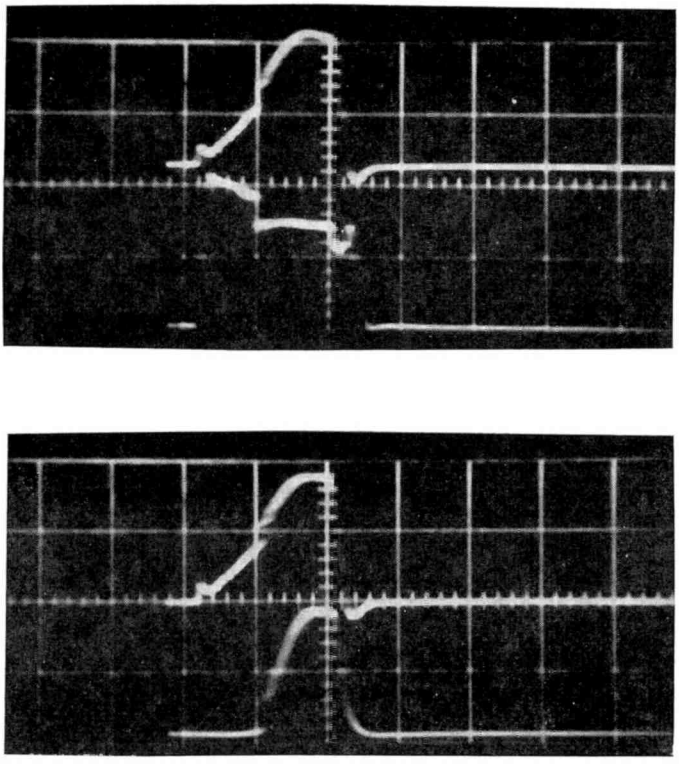

Fig. 5—Pulse voltage, pulse current, and rf power output.

Trace B shows a typical pulse voltage. One observes first a very steep rise in the reverse breakdown voltage of the diode and then, after a few hundred nanoseconds, an abrupt decrease to a lower level. Trace A shows the pulse current, which rises gradually to a certain level at which a sharp increase occurs simultaneously with a sharp decrease in the pulse voltage. When the pulse current has reached the level at which the sharp increase occurs, an rf power output can be observed, as shown in trace D (trace C is a repetition of A.)

The rf pulse rise time is dependent to a large extent on the circuit and to a lesser extent on the particular diode. Good rise times were

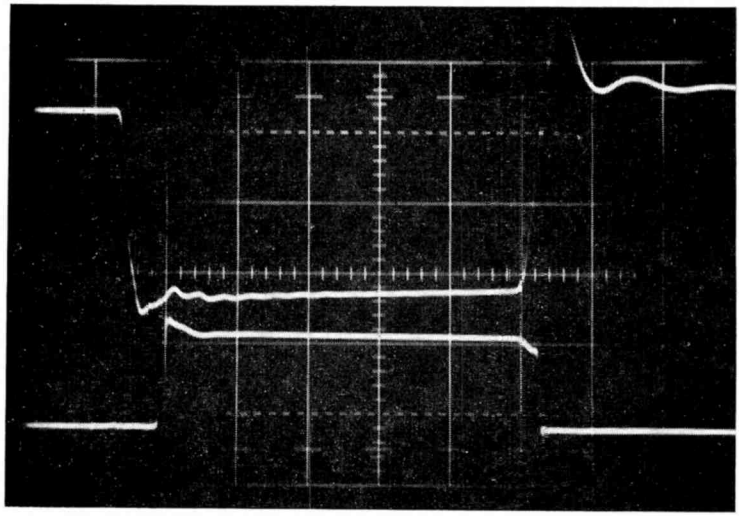

Fig. 6—Upper trace: dc current pulse (bias current 2 A/cm); lower trace: detected rf pulse. Horizontal scale is 0.2 μsec/cm.

obtained with both cavity and lumped circuits. Well-fabricated diodes that are operated in a properly tuned circuit exhibit a typical rise time of between 30 and 100 nsec. Figure 6 shows the rf pulse shape and the dc current pulse. The corresponding output spectrum is shown in Figure 7.

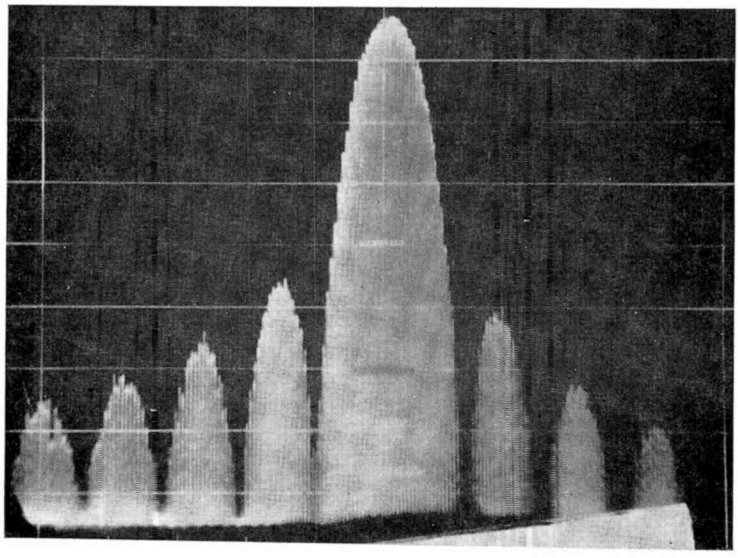

Fig. 7—Output spectrum (center frequency: 850 MHz).

2. *Delay Time*

The delay time appears to be almost entirely a function of the pulser and the bias network used to drive the device. With the pulsers and biasing schemes used, the measured delay times ranged from 100 to 200 nsec.

3. *Variations with Temperature*

A check of the variation of diode performance with temperature showed that only the diode breakdown voltage was significantly affected. The tests covered the temperature range from −61°C to 150°C. The change in the breakdown voltage followed the expected theoretical variation given by,

$$E_B(T) = E_B(T_o)\,[1 + \beta(T - T_o]\,; \quad \beta = 4.4 \times 10^{-4}/°\mathrm{C}\,.$$

When the pulse voltage was changed to allow for the change in the breakdown voltage, the power was found to vary less than 1 dB over this temperature range. The frequency change over this range was approximately 2 MHz (the operating frequency was 760 MHz.) Presumably, for a practical application involving these temperature extremes, a compensating network would have to be incorporated in the pulser to allow it to adjust to the change in breakdown voltage.

4. *Thermal Considerations*

Calculations show that a power output of 1 kW (+30 dBw) is possible at a 1% duty cycle with pulses of the order of 1 microsecond. An efficiency of 33% is assumed, which is somewhat lower than we expect these diodes to achieve.

The average power dissipation for such a case with an infinite heat sink is 20 watts. For a diode mesa of 0.040-inch diameter mounted p+ side down on a copper heat sink, this is a rise of 17°C at the junction. The maximum permissible junction temperature for silicon is of the order of 200°C. Therefore, a 17°C rise could be tolerated by a diode operating at an ambient temperature of well over 100°C.

Recently, cw diodes operating in the anomalous mode have been reported by Iglesias and Evans.[10]

[10] D. E. Iglesias and W. J. Evans, "High-Efficiency CW IMPATT operation," *Proc. IEEE*, Vol. 56, p. 1610, September, 1968.

5. *Power-Supply Variations*

Once the bias current and the circuit are adjusted for an optimum output at a particular frequency, small variations in bias current will not cause a severe shift in frequency. However, the power output will be more seriously affected. Tests on a typical diode operating at 1.055 GHz, showed that a change in the bias current from 8.5 to 10.2 amperes caused a shift in frequency of 2.2 MHz. However, the power increased from 78 to 115 watts. Expressed as a percentage, this means that a 20% change in the bias current caused only a 0.2% change in frequency, whereas the power changed by 47%. Although there are variations from diode to diode, these numbers are typical of diodes examined to date, and represent the type of variations usually encountered.

6. *Power and Efficiency*

We have observed two distinct regimes with respect to power and efficiency. Diodes with abrupt junctions tend to give the largest output powers and highest efficiencies. Graded junctions, on the other hand, yield lower power and efficiency but are much less susceptible to burn out. It is extremely difficult to strike the delicate balance between a junction that is sufficiently abrupt to yield high powers but not so abrupt as to cause it to burn out at low current levels. Typical output power for successful abrupt-junction devices was in the range of 100 to 400 watts. Efficiencies for these diodes ranged from 22 to 60%. For the graded junctions, typical power levels were 20 to 150 watts at efficiencies ranging from 15 to 45%.

To realize high powers, both series- and parallel-operated multiple diodes have been attempted.* A unit consisting of four stacked diodes in a series has produced 500 watts at 1.05 GHz with an efficiency of 25%, while a single diode gives about 100 watts with approximately the same efficiency. A parallel unit has yielded similar results.

7. *Life Tests*

Two diodes were placed on life test in September, 1967. One diode yielded an output of 172 watts with 50% efficiency at a frequency of 740 MHz. The other diode yielded 90 watts with 15% efficiency at 1020 MHz. As of Feb. 14, 1969, these diodes had accumulated 11,427 and 12,068 hours, respectively, without degradation in power output or

* Private communication with S. G. Liu.

change in frequency. The duty cycles are 0.04% and 0.02%, respectively.

Recently another life test was added to evaluate the diodes at a higher duty factor. The diode is operated at an output power of 90 watts, an efficiency of 21% at 1040 MHz, and with a duty factor of 0.5%. So far, 2,498 hours have elapsed without failure.

8. *Amplifier*

Preliminary experiments have also been performed on the possible applications of the high-efficiency diodes in amplifiers. During the course of these experiments, we have already observed phase locking, a phenomenon that in itself has several possible applications.

One of the observations was made with a diode yielding 25 watts of peak pulse power at a frequency of 1090 MHz. A locking signal that was pulsed on in synchronization with the diode oscillator was injected through a circulator, and the resultant signal observed on a spectrum analyzer. Results thus far obtained show a locking range of 10 MHz at a center frequency of 1090 MHz, with a locking gain of 10 dB.

Model Discussion

This paper would not be complete without at least a sketchy discussion of a physical model. We have called the behavior of these diodes anomalous because our experimental results differed from those of other IMPATT diodes, primarily in two aspects:

1) we have observed oscillations with transit-time angles as low as 3/10 radian, instead of the normal value of π;

2) we have observed efficiencies nearly twice as great as predicted by the most optimistic model, namely that of Read.[2]

The first step in constructing a model was to examine a one-dimensional model under static conditions. Such a model has been investigated independently by several authors.[11-14] The calculation yields the

[11] S. G. Liu and J. J. Risko, "High-Power Punch-Through Avalanche Diode Microwave Oscillators," *Int. Solid-State Circuits Conf.*, Vol. 11, p. 146, 1968.

[12] H. C. Bowers, "Static Negative Resistance in Avalanche Diodes," *Proc. IEEE*, Vol. 56, p. 222, Feb. 1968.

[13] B. Hoefflinger, "High-Frequency Oscillations of p^{++}-n^{+}-n-n^{++} Avalanche Diodes Below the Transit-Time Cutoff," *IEEE Trans. on Electron Devices*, Vol. ED-13, p. 151, Jan. 1966.

[13] R. A. Giblin, *Electronics Letters*, Vol. 4, No. 3, 1968.

field profile for the depletion region, the generated carrier distribution, and the *I-V* characteristic. At high current densities, the *I-V* characteristic shows a negative resistance. However, the negative resistance is too small to account for the observed efficiencies. We conclude that the static case is inadequate to explain the active mchanism, and that the dynamic case must be considered. Analysis of the dynamic case poses severe mathematical problems and requires resort to a computer, an approach that sometimes obscures the physics. Nevertheless, Johnson, Scharfetter, and Bartelink[7] have recently arrived at remarkable numerical solutions using a sophisticated computer program. We are endeavoring to minimize programming complexities by constructing as simple a model as possible.

Conclusions

All experimental results already achieved show that the anomalous avalanche diode has excellent potential as a high-power pulsed microwave source for operation from 400 to 1500 MHz. A considerable amount of information has been obtained about the circuit requirements for those diode oscillators. Among them, a highly successful coaxial circuit has been developed that is capable of tuning over nearly an octave in frequency, with less than 1 dB variation in output power. However, further research is needed to reach full understanding of the mode of operation and to achieve the full potential of the diode.

Acknowledgment

A. S. Clorfeine, R. J. Ikola, P. Levine, S. G. Liu, and H. J. Prager have participated in all experimental work reported here.

LARGE-SIGNAL TRANSIT-TIME EFFECTS IN THE MOS TRANSISTOR

By
J. R. Burns

RCA Laboratories
Princeton, N.J.

Summary The characterization of the MOS transistor as a nonlinear distributed system leads to the prediction of a time delay in the drain-current response to a gate-voltage step. This delay is inversely proportional to a characteristic frequency of the MOS device, a frequency that also determines its performance as a small-signal, high-frequency amplifier. Experiments conducted on specially designed test devices are in good agreement with theoretical predictions.

Introduction

THE WORK reported here is an extension of the results presented in previous work,[1,2] wherein a small-signal high-frequency model for the MOS transistor was obtained. Further study of the theoretical model used in the analysis predicted that, in addition to the high-frequency fall-off in small-signal transconductance, there should be a corresponding time dependence of the drain-current response of the MOS device when operated as a large-signal switch. This time dependence is a previously unreported phenomenon and has been ignored in all analyses of the switching behavior of MOS digital circuits.

The primary purpose of this investigation is, therefore, to present theoretical and experimental results that verify the existence of this large-signal phenomenon. In addition, small-signal experimental results are presented for identical devices in order to demonstrate the validity of the theoretical model for both large- and small-signal operation.

High-Frequency Model of the MOS Transistor

For the purposes of this analysis, we will consider an n-channel MOS transistor having a channel width W, channel length L, insulator

[1] J. R. Burns, "High Frequency Characteristics of the Insulated Gate Field Effect Transistor," *RCA Review*, Vol. 28, p. 385, Sept. 1967.
[2] J. R. Burns, "Switching Response of Complementary Symmetry MOS Transistor Logic Circuits," *RCA Review*, Vol. 25, p. 627, Dec. 1964.

thickness T_{ox}, permittivity ϵ_{ox}, and the physical construction shown in Figure 1.

The high-frequency performance of the MOS transistor is best analyzed for both small- and large-signal applications as a nonlinear *RC* transmission line. This model is shown schematically in Figure 2, where the capacitance per unit length is constant and the resistance

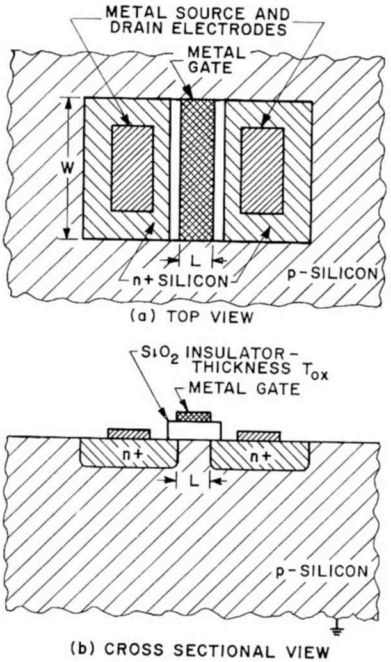

Fig. 1—Physical construction of MOS transistor.

per unit length is a function of the induced charge and, thus, of the voltage at a particular point. The voltage, in turn, is a function of both time and distance from the electrode. This model is identical to that used previously[1] for the small-signal analysis, where the solution was an exact analytic expression in terms of the Laplace transform variable.

Accordingly, we set down the well-known transmission-line equations,

$$\frac{\partial I(X,t)}{\partial X} = -\overline{C}\frac{\partial}{\partial t}\left(V(X,t) - V_G(t)\right), \qquad (1(a))$$

$$\frac{\partial V(X,t)}{\partial X} = -I(X,t)\overline{R}, \tag{1(b)}$$

where $\overline{R}$ and $\overline{C}$ are the resistance and capacitance per unit length. The capacitance is given by[1]

$$\overline{C} = \frac{\epsilon_{ox} W}{T_{ox}} = \text{constant},$$

and for $\overline{G} = \overline{R}^{-1}$,

$$\overline{G} = \bar{\mu}_n \overline{C}(V_G - V_T - V(X,t)),$$

where $\bar{\mu}$ is the effective mobility of charge carriers in the active region.

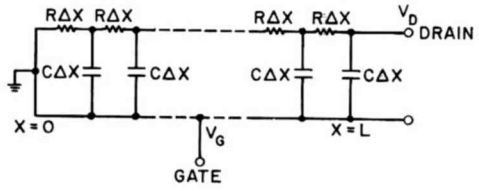

Fig. 2—Transmission-line model of MOS channel.

Substitution of these relations in Equations (1) gives

$$\frac{\partial I(X,t)}{\partial X} = -\overline{C}\frac{\partial}{\partial t}(V(X,t) - V_G(t)), \tag{2(a)}$$

$$I(X,t) = -\bar{\mu}_n \overline{C}(V_G - V_T - V(X,t)\frac{\partial V(X,t)}{\partial X}. \tag{2(b)}$$

This set of equations can be simplified by a change in variable given by

$$\overline{V}(X,t) = V_G(t) - V_T - V(X,t). \tag{3}$$

On substitution, Equations (2) become

$$\frac{\partial I(X,t)}{\partial X} = C\frac{\partial \overline{V}(X,t)}{\partial t} \tag{4(a)}$$

$$I(X,t) = \bar{\mu}_n \overline{CV}(X,t) \frac{\partial \overline{V}(X,t)}{\partial X}, \qquad (4(b))$$

which represents a pair of nonlinear partial differential equations in the dependent variables $I(X,t)$ and $\overline{V}(X,t)$. The equations cannot be solved explicity for I because of this nonlinearity in $\overline{V}(X,t)$, but an equation for $\overline{V}$ can be readily obtained by differentiation of Equation (4(b)) with respect to X and substitution in Equation (4(a)):

$$\overline{V} \frac{\partial^2 \overline{V}}{\partial X^2} + \left(\frac{\partial \overline{V}}{\partial X}\right)^2 = \frac{1}{\bar{\mu}_n} \frac{\partial \overline{V}}{\partial t},$$

or

$$\frac{\partial^2}{\partial X^2} (\overline{V}^2(X,t)) = \frac{2}{\bar{\mu}_n} \frac{\partial \overline{V}(X,t)}{\partial t}. \qquad (5)$$

These equations must be solved for $\overline{V}$ subject to various boundary conditions, and the current (which is usually the variable of interest) is then derived from the defining relationship Equation (4(b)).

The object of this paper, then is to obtain the solution of Equation (5) subject to appropriate boundary conditions and to obtain the transient response of the device when operated under large-signal switching conditions.

Large-Signal Drain-Current Response

An area of major commercial importance is the use of the insulated-gate field-effect transistor (IGFET) in digital switching circuits. The advantages of the device in these applications are manyfold, particularly in large integrated-circuit arrays, and have been described extensively in the literature.[3-6]

The switching speed of MOS logic gates has been analyzed in some detail elsewhere.[2] In the analysis in Reference (5), it was assumed that

[3] P. K. Weimer, U.S. Patent No. 3,191,061, June 22, 1965.

[4] J. R. Burns, J. J. Gibson, A. Harel, K. C. Hu, and R. A. Powlus, "Integrated Memory Using Complementary Field Effect Transistors," *Int. Solid State Circuits Conference*, 1966.

[5] J. R. Burns and J. J. Gibson, "High Speed Complementary MOS Memories," *National Aerospace Electronics Conference*, May 1966.

[6] J. F. Allison, J. R. Burns, and F. P. Heiman, "Silicon-On-Sapphire Complementary MOS Memory Systems," *Int. Solid State Circuits Conference*, 1967.

because the MOS transistor is a majority-carrier device, the drain current follows the gate voltage with no time lag and that, as a consequence, the switching time is determined only by the charging time of the load capacitance through the MOS transistor. Although experimental results seemed to confirm this theory, the initial assumption on which it is based is invalid. As shown in the small-signal analysis,[1] the output current is a decreasing function of frequency because of the distributed nature of the active region of the device. It should be expected, therefore, that in the large-signal case, there will be a corresponding time dependence of the drain current under short-circuit conditions. This is, in fact, the case as will now be shown.

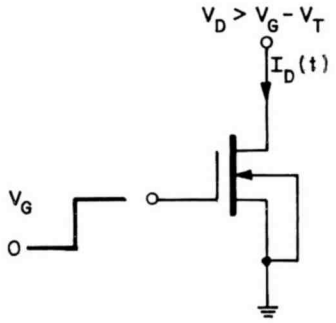

Fig. 3—Large-signal step response.

The following analysis is based on the response of an n—channel enhancement transistor ($V_T > 0$) to a gate-voltage step of value $+ V_G$. The drain voltage is assumed to be V_D, which is greater than $V_G - V_T$ as indicated in Figure 3. The governing equations for this case have been derived in the previous section. Making the simplifying substitutions

$$v = 1 - \frac{V}{V_G - V_T} \tag{6}$$

$$Z = 1 - \frac{X}{L}$$

$$t' = \frac{\bar{\mu}_n (V_G - V_T)}{L^2} t = \omega_o t ,$$

the partial differential equation for the normalized voltage distribution $v(Z,t')$ becomes

$$\frac{\partial}{\partial Z}\left(v\frac{\partial v}{\partial Z}\right)=\frac{\partial v}{\partial t'}. \tag{7}$$

The above represents the case of nonstationary one-dimensional diffusion where the diffusion coefficient* is directly proportional to the concentration. The boundary conditions appropriate for the problem are

$$\begin{aligned} &v(1,\ t')=1,\ \text{(gate to source voltage constant} = V_G)\\ &v(0,\ t')=0,\ \text{(gate to drain voltage constant} = 0)\\ &v(Z,\ 0)=0,\ \text{(channel oxide initially uncharged)} \end{aligned} \tag{8}$$

From the form of Equation (7), it is apparent that the rate of change of voltage is extremely low at low voltages and is identically zero when $v=0$. This behavior is entirely different from that exhibited in a linear RC line, where the voltage is never identically zero at any finite distance or time. The solution will, therefore, be in the form of a traveling wave front where, for any given time, the voltage will be identically zero for distances greater than a certain value.

Problems of this type have been studied[3] in the past for diffusion into a semi-infinite medium where there was no boundary condition at a finite distance as is the case here with the constant drain voltage. However, this presents no difficulty, because the wave-propagation nature of the solution will enable the treatment to be divided into two sections:

1. An initial portion based on the solution for a semi-infinite medium that is valid for times less than t_d, the time required for the voltage wave front to reach the drain. During this period, the boundary condition at the drain, i.e., $v=0$, will always be satisfied because of the wave propagation behavior.
2. A portion valid for $t'>t_d'$, where the voltage distribution is changing to its steady-state value, $v=\sqrt{Z}$.

Following the treatment of Wagner,[7] the partial differential Equation (7) can be transformed into an ordinary differential equation by

* The corresponding variables in the case of the MOS transistor are, of course, the electrical conductivity and the voltages.

[7] C. Wagner, "Diffusion of Lead Chloride Dissolved in Solid Silver Chloride," *Jour. Chem. Phys.*, Vol. 18, No. 9, p. 1227, Sept. 1950.

introducing a new independent variable Y, defined as

$$Y = \frac{(1 - Z)}{2\sqrt{t'}} . \tag{9}$$

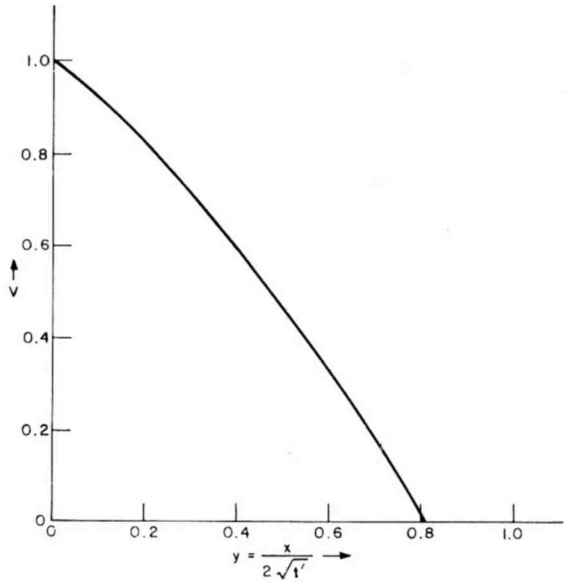

Fig. 4—Numerical solution of nonlinear diffusion equation.

Substituting into Equation (7), we obtain

$$v \frac{d^2v}{dY^2} + \frac{dv}{dY} + 2Y \frac{dv}{dY} = 0 , \tag{10}$$

with boundary conditions

$$v = 1 \text{ at } Y = 0,$$
$$v = 0 \text{ at } Y = \infty, \ (t' = 0). \tag{11}$$

Equation (10) has been integrated numerically and the results are shown in Figure 4, where v is plotted as a function of the variable Y. Note that for all values of Y greater than 0.81, v is identically zero (as expected), so that the advancing wave front is characterized by a dimension Z_o, which is a function of time;

$$Z_o = 1 - 1.62\sqrt{t'}. \tag{12}$$

Solving the above for $Z_o = 0$ gives

$$t_d' = 0.38\,, \tag{13}$$

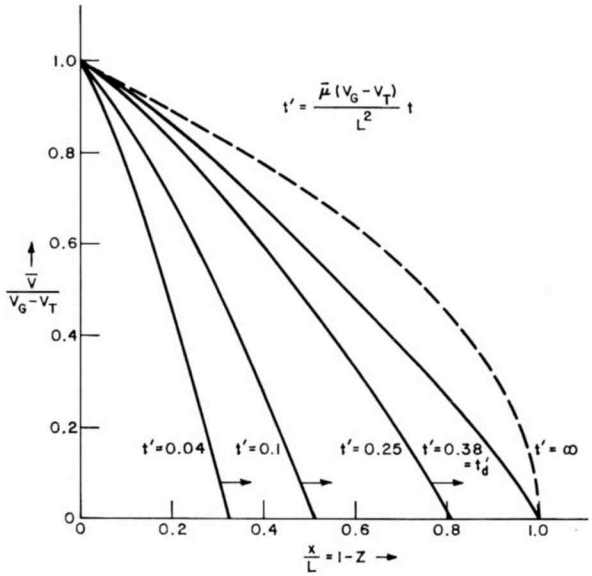

Fig. 5—Voltage distribution in channel as function of time.

or

$$t_d = 0.38 \frac{L^2}{\bar{\mu}_n (V_G - V_T)}.$$

The complete voltage distribution for increasing values of t' is plotted in Figure 5 along with the steady-state distribution

$$v = \sqrt{1 - \frac{x}{L}} = \sqrt{Z}.$$

The remainder of the solution can be carried out by making an approximation wherein the diffusion coefficient is considered a function of distance rather than voltage, thereby linearizing the partial

differential Equation (7). From Figure 5, it can be seen that the voltage distribution at $t' = t_d'$ is reasonably close to that existing at $t' = \infty$ in the steady state. A good approximation, therefore, is to assume that the distribution corresponds to the steady-state voltage distribution and that, as a consequence, a small-signal analysis can be employed. Accordingly, a solution of the form

$$v(Z,t') = \sqrt{Z} + \frac{1}{2}\epsilon(Zt') \tag{14}$$

will be assumed for $t' > t_d'$. Substituting into Equation (7), the following linear partial differential equation is obtained in ϵ:

$$Z^2 \frac{\partial^2 \epsilon}{\partial Z^2} + Z \frac{\partial \epsilon}{\partial Z} - \frac{\epsilon}{4(Z)^{3/2}} = \frac{\partial \epsilon}{\partial t'}. \tag{15}$$

The above equation can be handled by standard separation-of-variables techniques, yielding a general solution of the form*

$$\epsilon(Z,t' - t_d') = \sum_{n=1}^{\infty} C_n J_{2/3}\left(\frac{4}{3} k_n [Z]^{3/4}\right) \exp\{-k_n^2 (t' - t_d')\} \tag{16}$$

where k_n is the separation constant and $t' > t_d'$. The boundary condition $\epsilon(0, t') = 0$ is ensured since $J_{2/3}(0) = 0$. The condition $\epsilon(1, t') = 0$ can be met by choosing k_n so that $J_{2/3}\,[(4/3)k_n] = 0$, or

$$\frac{4}{3} k_n = \alpha_n, \tag{17}$$

where the α_n are the zeros of the Bessel function of order $\frac{2}{3}$. Denoting the distribution at $t' = t_d'$ by $v_o(Z)$, the remaining condition becomes

$$\epsilon(Z, 0) = 2[v_o(Z) - \sqrt{Z}], \tag{18}$$

which is plotted in Figure 6.

Also plotted in Figure 6 is the first term of the general solution*

* This is the same form as that for the small-signal transient response derived in Appendix II of Reference(1).

* The Bessel function was evaluated with a computer program.

weighted by a constant factor, 0.53, chosen to fit the desired function in Equation (18) as closely as possible. The agreement is seen to be quite good so that the first term in the series adequately represents $\epsilon(Z, t' - t_d')$. The complete solution is, therefore,

$$\epsilon(Z, t' - t_d') = 0.53 J_{2/3}(3.3746[Z]^{3/4}) \exp\{-6.406(t' - t_d')\} \quad (19)$$

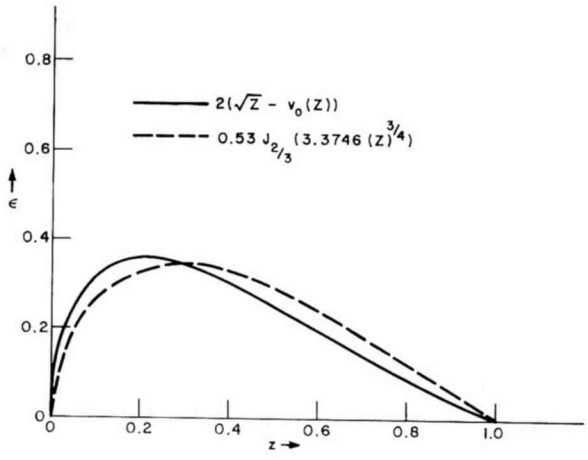

Fig. 6—Initial voltage deviation.

Substituting Equation (19) into Equation (14) and using the defining current relation of Equation (4(b)) gives

$$I_D(t' - t_d') = \frac{\bar{\mu}_n \epsilon_{ox} W}{L T_{ox}} (V_G - V_T)^2$$

$$\left(1 - 0.83 \exp\{-6.406\,(t' - t_d')\} - 0.17 \exp\{-12.812\,(t' - t_d')\}\right), \quad (20)$$

which is shown plotted in Figure 7. It is seen that, for the drain current to reach its final value, there is, in addition to the delay time, a finite rise time equal to

$$0.3 \frac{L^2}{\bar{\mu}_n (V_G - V_T)}.$$

In summary, as a consequence of the distributed nature of the MOS transistor channel, the drain current does *not* follow an applied voltage step, but rather exhibits a time delay as well as a finite rise time, both of which are proportional to the quantity

$$\frac{L^2}{\bar{\mu}_n(V_G - V_T)}.$$

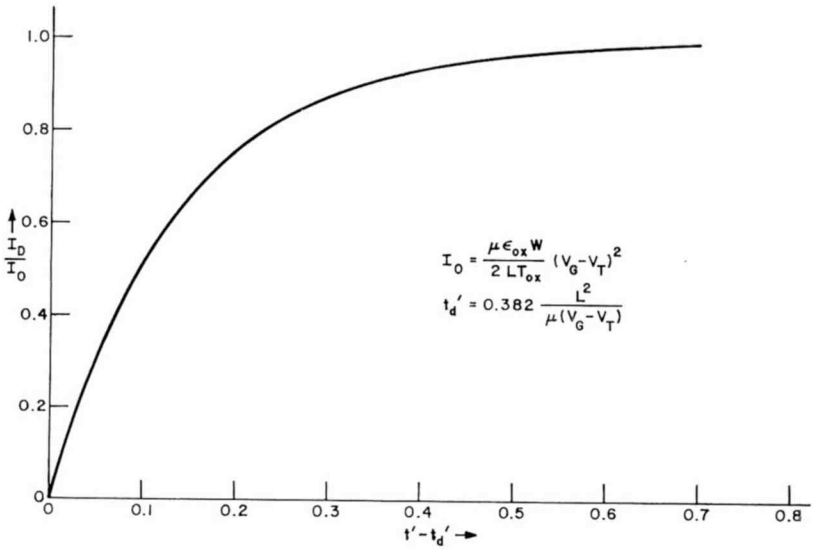

Fig. 7—Large-signal drain-current response.

It is important to note at this point that this quantity is equal to $1/\omega_0$ where ω_0 is the characteristic frequency of the MOS transistor operating as a small-signal rf amplifier. Determination of this parameter will, therefore, completely specify both the small-signal frequency response and large-signal transient response of the device.

Experimental Results

General Experimental Approach

Inasmuch as the object of this paper is the characterization of the MOS transistor at high frequencies, both as a small-signal amplifier and as a large-signal switch, any experimental technique should be capable of determining the small-signal y parameters and the large-signal transient response of the same device. Commercial devices pres-

sent considerable difficulties when used for both these types of measurement, as the channel lengths of these devices are of the order of 5 microns (5×10^{-6} meter), necessitating large-signal measurements of fractions of nanoseconds and small-signal measurements in the 100 to 1000 MHz range. It therefore becomes quite difficult to determine actual device performance, because parasitic elements such as lead inductance, transistor-case capacitance, and stray reactances associated with the physical configuration of the device on the silicon substrate dominate the measured response. Accordingly, devices were designed that would facilitate the measurement and yet provide a test of the theoretical device models.

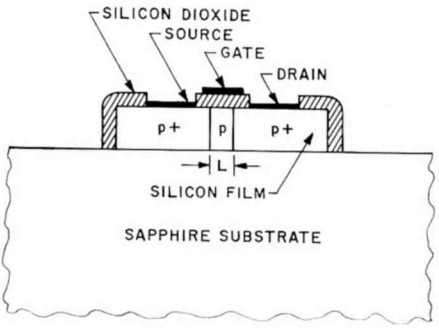

Fig. 8—Silicon-on-sapphire transistor.

The two special test devices designed have relatively long channel lengths, one of 0.001 inch and the other of 0.002 inch (25 and 50 microns, respectively), these channel lengths scale the frequency response down by a factor of about 100 relative to commercial devices.* Channel widths of 0.010 inch and 0.020 inch were chosen so that both devices would have the same width to length ratio and, thus, the same nominal dc characteristics. The devices were fabricated in silicon-on-sapphire[8-10] (to eliminate parasitic substrate effects present in the bulk silicon MOS transistor) and were of the p-channel deep-depletion type,[8] i.e., holes are the carriers of channel current and at zero gate-to-source voltage, negligible current flows from source to drain. A cross-

* The characteristic device frequency is inversely proportional to the square of the channel length.

[8] C. W. Mueller and P. Robinson, "Grown Film Silicon Transistors on Sapphire," *PROC. IEEE*, p. 1487-1490, Dec. 1964.

[9] E. C. Ross and C. W. Mueller, "Extremely Low Capacitance Silicon Film MOS Transistors," *Trans. IEEE on Electronic Devices*, March 1966.

[10] F. P. Heiman, "Thin Film Silicon-On-Sapphire Deep Depletion MOS Transistors," *IEEE Trans. Electron Devices*, Dec. 1966.

sectional diagram of the transistor construction is shown in Figure 8, while a top view of the two test devices on the sapphire substrate is shown in the photomicrograph of Figure 9.

Starting with a 1.5-micron-thick film of 50 ohm-centimeter resistivity p-type silicon on a sapphire substrate, the following procedure was used in the fabrication of these devices:

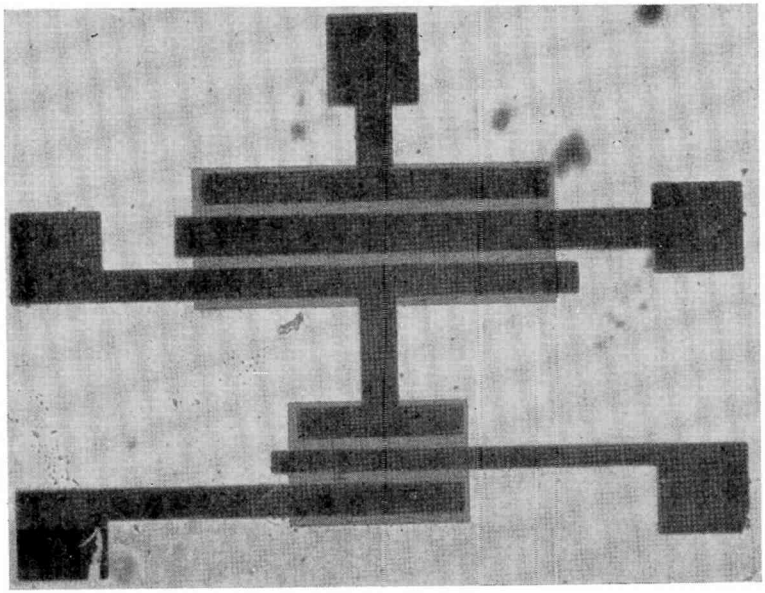

Fig. 9—Photomicrograph of test transistor (100 × magnification).

1. diffuse boron to define heavily doped source and drain contact areas and the channel region,
2. remove unused silicon areas,
3. thermally grow channel oxides (~ 1000 Å),
4. define contact areas by exposing source and drain regions,
5. evaporate aluminum metallization and define source, gate, and drain electrodes,
6. dice sapphire substrate and mount individual chips containing the two test devices in a 10-pin TO-5 header.

Large- and Small-Signal Measurements

The test devices were first measured for their dc behavior and yielded the typical drain characteristics shown in Figure 10. Note that

the characteristics of the respective devices are nearly the same, which should be expected, since the width-to-length ratios were made equal. Also, all other factors, such as oxide thickness and permittivity and carrier mobility are nearly identical,* because the devices were fabri-

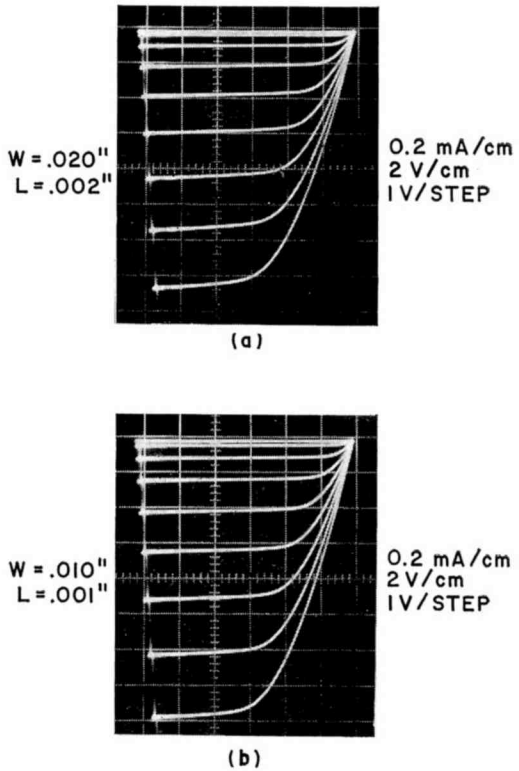

Fig. 10—Drain characteristics of test devices.

cated simultaneously and in close proximity on the substrate. Variations of these parameters, however slight, do occur and make absolute determination of transconductance, oxide capacitance, and mobility relatively difficult for a given device. In addition, there are also variations in channel width and length due to tolerances in the photographic masks and lateral diffusion of the p+ source and drain regions during high-temperature processing. For these reasons, an experimental approach was used to obtain low-frequency values of those critical device parameters that influence the high-frequency behavior.

* Variations in these parameters did cause slight variations in transconductance and oxide capacitance for devices that had the same nominal dimensions but were spatially separated on the substrate.

The most important parameter is the ratio $\bar{\mu}_p/L^2$, a quantity that, together with the gate voltage, determines the characteristic frequency f_o. A special experimental procedure was developed to accurately obtain this frequency for each device. The procedure is as follows:

1. Measure the device threshold voltage V_T by observing the gate voltage at which the dc drain current ceases to decrease.
2. Measure the dc drain current for a known gate voltage V_G when the device is biased into the current saturation region $(V_D > V_G - V_T)$. This permits the determination of the device constant

$$K_P = \frac{I_{DS}}{(V_G - V_T)^2} = \frac{\bar{\mu}_p C_{ox}}{2L^2}. \tag{21}$$

3. Measure the low-frequency oxide capacitance, C_{ox}, and combine with Equation (21) to obtain the desired quantity

$$\frac{\bar{\mu}_p}{L^2} = \frac{2K_p}{C_{ox}}.$$

In practice, the measurement of C_{ox} is quite difficult because of the existence of stray capacitance in the test set-up, the transistor package, and in the transistor itself due to gate overlap of the source and drain electrodes. These effects can be eliminated by making two such capacitance measurements, one with drain and source tied together $(V_{DS} = 0)$ and the other with a drain-to-source voltage sufficient to bias the transistor in the current saturation region. In the first case, the gate capacitance (exclusive of strays) will be just C_{ox}, because of the uniform charge distribution in the channel, while in the second case, the gate capacitance will be $\frac{2}{3}C_{ox}$.* Therefore,

$$C_1 = C_{ox} + C_{\text{stray}}, \qquad (V_{DS} = 0)$$

$$C_1 = \frac{2}{3} C_{ox} + C_{\text{stray}}, \qquad (V_{DS} > V_{gs} - V_T)$$

so that $C_{ox} = 3(C_1 - C_2)$ can be measured quite accurately, independent of stray capacitance. The value of stray capacitance, which is quite helpful in the small-signal measurements, can also be obtained from these measurements.

* This is the effective small-signal input capacitance for an MOS biased in current saturation and is derived in Reference (1), pp. 402-403.

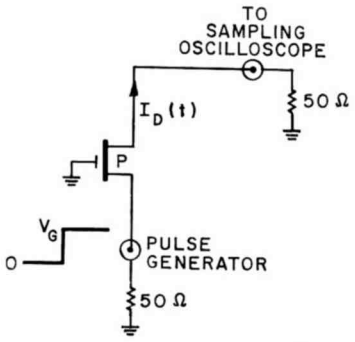

Fig. 11—Experimental set-up for determination of large-signal response.

Using this procedure, a 20×2 mil (nominal dimensions) and a 10×1 mil device were characterized as having $\bar{\mu}_p/L^2$ equal to 6.67×10^6 volt^{-1}second^{-1} and 28.6×10^6 volt^{-1}second^{-1}, respectively. Both devices had threshold voltages of zero volts and were measured for large-signal transient response using the experimental set-up shown in Figure 11. Figure 12 shows the drain-current waveforms of the 2-mil channel length transistor for applied gate voltages of 5 and 10 volts, respectively. The finite delay and rise times are clearly indicated in this photograph. A comparative plot of the experimental and theoretical curves of delay time versus voltage (see Figure 13) for both the 1- and 2-mil channel length devices shows the excellent agreement obtained in both cases. Similar agreement is noted for the drain current rise time versus voltage (Figure 14), indicating that the approximations made in this derivation are reasonably well justified.

Small-signal measurements were carried out on the 2-mil devices

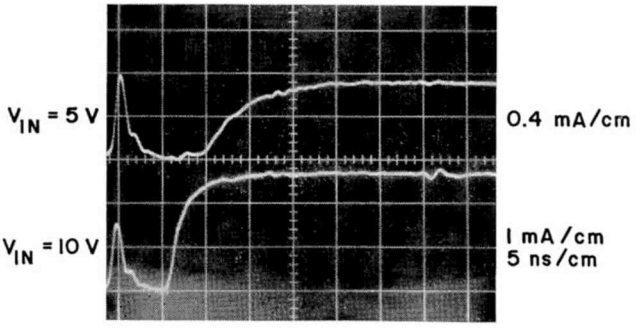

Fig. 12—Drain-current waveforms.

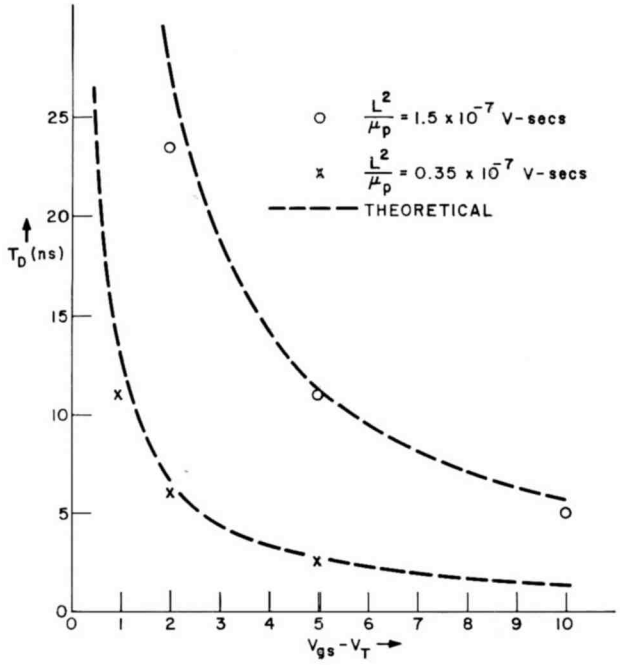

Fig. 13—Drain-current delay time versus voltage.

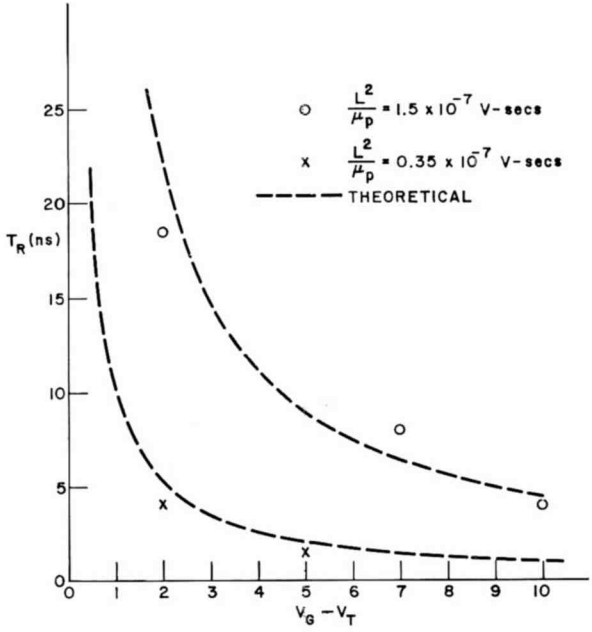

Fig. 14—Drain-current rise time versus voltage.

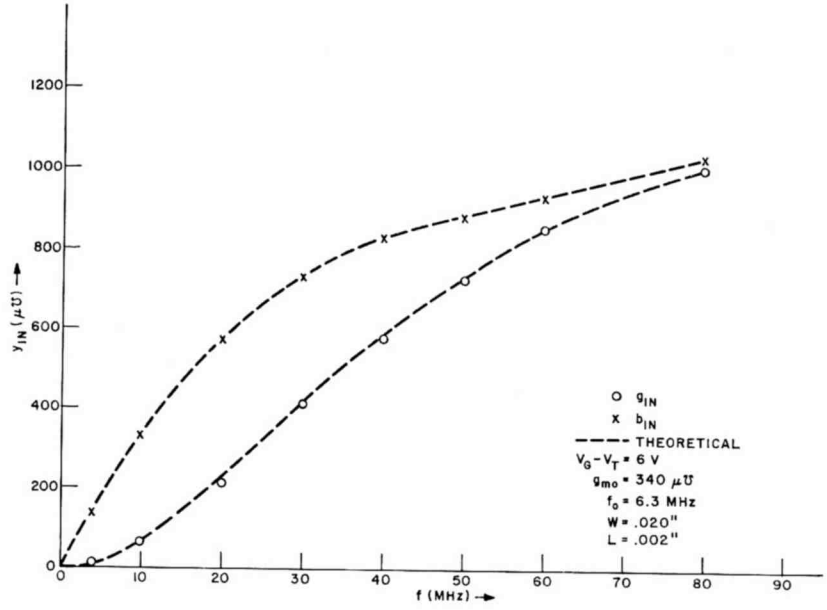

Fig. 15—Input admittance versus frequency.

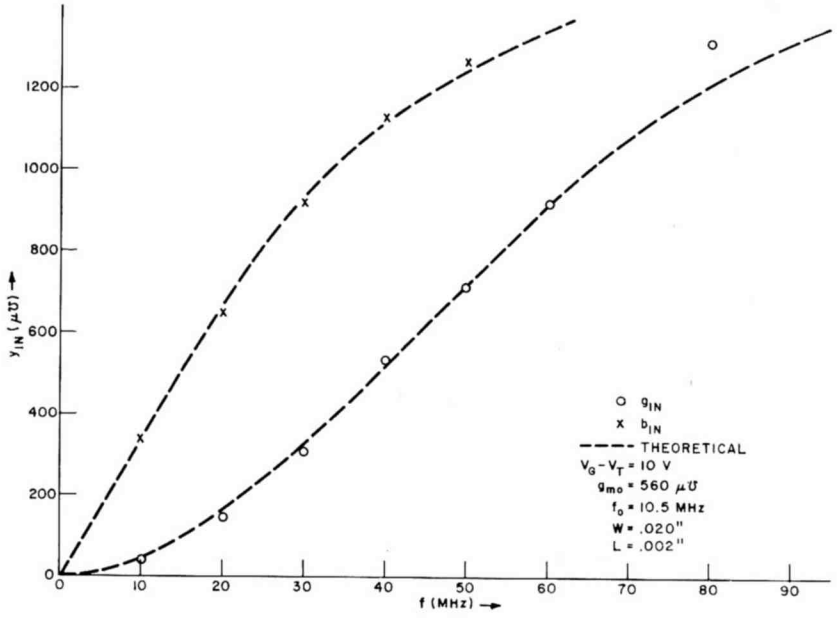

Fig. 16—Input admittance versus frequency.

using an R-X meter; the real and imaginary parts of the input admittance and transconductance were obtained as functions of frequency and dc bias conditions. Care was taken to accurately obtain the value of stray capacitance associated with the device terminal being measured in order to properly account for the reactive part associated only with the active region of the transistor. Figures 15 and 16 show the input admittance plotted as a function of frequency, along with the theoretical curves for $V_G - V_T$ equal to 6 and 10 volts, respectively. (The appropriate stray reactance was substracted for all experimental points.) The agreement is seen to be extremely good. Measurement of

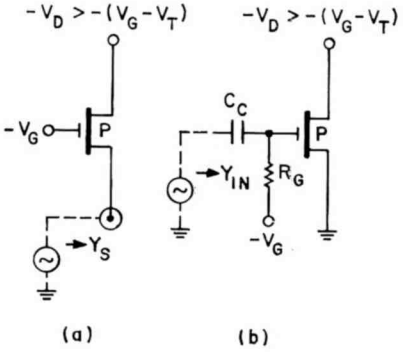

Fig. 17—Measurement of transconductance.

the transconductance involved two separate impedance measurements, one at the source terminal and one at the gate terminal as shown in Figure 17. Using the relationship*

$$g_m = Y_S - Y_{IN},$$

the transconductance is then obtained as a function of frequency. The experimental results are presented in Figure 18, where it is again seen that the theoretical predictions are well confirmed.

CONCLUSIONS

The major conclusion to be drawn from this work, a conclusion that has been experimentally and theoretically verified, is that all of the essential high-frequency parameters associated with the insulated-gate

* This follows immediately from Kirchoff's Law.

field-effect transistor are determined by a characteristic angular frequency

$$\omega_o = \frac{\bar{\mu}(V_G - V_T)}{L^2},$$

where $\bar{\mu}$ is the effective mobility of charge carriers in the active region, $V_G - V_T$ is the operating voltage, and L is the length of the active channel region. Knowledge of ω_o and the dc, or low-frequency char-

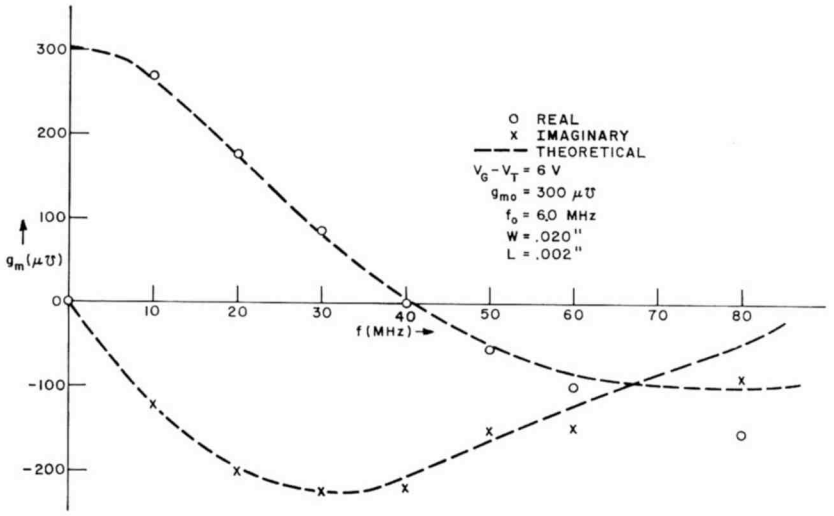

Fig. 18—Transconductance versus frequency.

acteristics of a given transistor will completely specify its small-signal high-frequency response and large-signal transient response. Exact closed-form expressions give the behavior of small-signal transconductance and input admittance as a function of these device characteristics and the frequency of operation.

It is interesting to note that, in contrast to the small-signal case where the theory was developed after experimental data was available (in the form of Y-parameter measurements as a function of frequency), the existence of a finite time delay and rise time in the large-signal drain-current response was first determined theoretically (by an examination of the partial differential equation governing this effect) and then confirmed experimentally with the special test transistors. Such a situation exists because of the relative practical sig-

nificance of transit-time effects in tuned rf amplifiers and digital switching circuits. State of the art IGFET switching circuits operate in the 50-nanosecond stage-delay range and are limited in speed by capacitive charging at the output through the transistor. Transit times of the order of 1 nanosecond are negligible in comparison and, therefore, need not be considered. In an rf amplifier, however, all output capacitance is tuned out and transit-time limitations are all-important in the realization of substantial power gain at high frequencies. However, when the fabrication technology of IGFET digital circuits enables the elimination of all parasitic capacitance associated with present devices, these effects will become significant and will, in fact, represent the ultimate limit in switching speed.

If one were to examine the expression for the characteristic frequency, ω_o, it would seem that further improvements in high-frequency performance can be readily made by an increase in operating voltage and a reduction in channel length. This conclusion follows directly if the assumption made in the derivation of these relations holds true, i.e., that the carrier mobility is independent of the electric field in the channel. For small values of the field, this is a good assumption, but as operating voltages are increased and lengths are decreased to improve frequency response, the field becomes quite large, and the mobility tends to decrease. In fact, as the field tends to infinity, the mobility tends to zero in such a way that the carriers move at a constant limiting velocity. An investigation of this effect may well show that further increase in voltage and/or decrease in channel length will yield no further improvement in gain–bandwidth product.

Acknowledgment

I am indebted to Professor S. Fich of the Electrical Engineering Department, Rutgers University, New Brunswick, N.J., for his many valuable suggestions, particularly on the use of the Laplace Transform in distributed parameter systems, to Professor J. L. Potter for his discussions and suggestions on equivalent circuit synthesis, and to G. B. Herzog and M. H. Lewin of RCA Laboratories for providing the opportunity to carry out this work.

I greatly appreciate the efforts of A. O'Toole for the fabrication of the test transistors and Mrs. B. Denton for mounting and packaging the test devices.

RESOLUTION LIMITATIONS OF ELECTROMAGNETICALLY FOCUSED IMAGE-INTENSIFIER TUBES

By
I. P. Csorba

RCA Electronic Components
Lancaster, Pa.

Summary The four major factors that limit resolution in electromagnetically focused cascaded image-intensifier tubes are electron-optical aberrations, the thickness of the interstage separator sheet, the phosphor screens, and (at low illumination levels) electron-fluctuation noise. For an image tube that has homogeneous axial magnetic and electric fields, the resolution of the electron image varies directly as the voltage and inversely as the distance between the phosphor screen and the photocathode. The thin phosphor-photocathode separator sheet, usually mica, and the phosphor screen also have resolution limits inversely proportional to their thicknesses. The image structure introduced by electron scintillations has a resolution limit proportional to the square root of the product of the cathode illumination, photocathode sensitivity, and integration time.

In this paper, the electron optical resolution of an image intensifier is derived as a function of the voltage between photocathode and phosphor screen. The resolution characteristics of the phosphor-mica-photocathode "sandwich" are analyzed as a function of phosphor thickness and mica thickness. Experimental data are presented to support the analytical data.

Introduction

THIS PAPER discusses the factors affecting image resolution in multistage electromagnetic image-intensifier tubes. The basic components of a two-stage magnetic image intensifier[1] are shown in Figure 1. The photocathodes convert light images to electron images; the accelerating electrodes produce uniform electric fields for accelerating the electrons to high velocities; the phosphor screens convert the high-velocity electron images to light images; the focus coil (or in some cases a permanent magnet) produces a uniform magnetic field to focus the electrons; mica spacers support the phosphor screens and the photocathodes in close proximity.

[1] I. P. Csorba, J. C. Moor, and R. G. Stoudenheimer, "Development of a Three-Stage Cascaded Image Tube," Final Report, Contract No. DA44-009-ENG-3914, NVL, Fort Belvoir, Virginia, Nov. 1962.

The major components affecting resolution capability are the electron-optical system, the mica spacer, and the phosphor screen. At low levels of illumination, resolution is also limited by the fluctuation (noise) produced by a finite number of electrons released at the first photocathode.

The resolution limitations caused by space charge and the resistivity of the photocathode are important at high input-light levels, but are not considered here because these limitations do not exist in normal operation, where the output current density is less than 10^{-6} ampere per square centimeter.

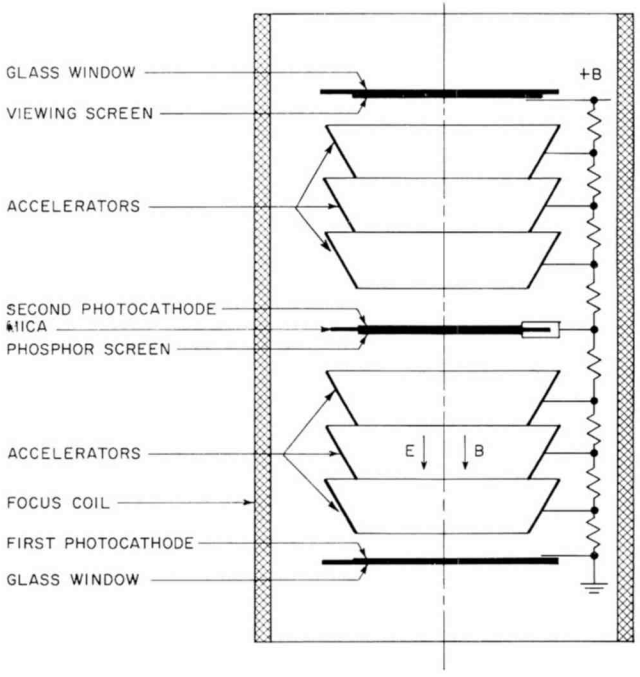

Fig. 1—Cross section of a two-stage magnetic image intensifier.

Resolution of the Electromagnetic Lens

Under ideal conditions, the electric and magnetic fields in an electromagnetic image intensifier are uniform over the useful beam diameter. The electron lens gives an erect image, unity magnification, flat object and image planes, freedom from distortion, and uniform resolution over the entire useful beam diameter. The only aberration present is caused by the variation of axial emission energy of the photoelectrons. Because of this variation, the image of a point at the photo-

cathode is a small disk at the plane of the phosphor screen. An analysis of the point image shows that the image diameter is proportional to the photocathode-to-screen distance and inversely proportional to the screen-to-photocathode voltage[2-4] (see Appendix). Because of the reciprocal relationship between the resolution and the diameter of the point image, the resolution R is

$$R = K(V_s/L_o) , \tag{1}$$

where V_s is the screen-to-photocathode voltage, L_o is the screen-to-photocathode distance, and K is a numerical constant. The value of K may be obtained by calculating the image current density distribution of a resolution test pattern[5,6] and defining the limiting resolution as a line frequency at which the image contrast is about 3%. For a practical photoemitter, these calculations, although conclusive, are laborious.

Experimentally, the value of K may be obtained by measuring the limiting resolution of an image intensifier that has a sufficiently uniform electric and magnetic field along the axis of the electron lens. For the measurements described here, a single stage of a developmental image-intensifier tube was used.* The tube was made with a monolayer willemite phosphor screen of the smallest particle size available in order to obtain a high screen resolution. The resolution of the phosphor screen was in excess of 400 line pairs per millimeter.

In the course of evaluation, the type of lens used for projecting the image on the image tube was found to be very critical. A microscope lens having an 8-millimeter focal length was used to project a highly demagnified resolution pattern on the photocathode of the image tube; a similar microscope objective was used in the microscope for viewing the image on the phosphor screen. The combined resolution of glass optics was in excess of 600 line pairs per millimeter.

The limiting resolution of the image tube as a function of screen

---

[2] A. Rose, "Electron Optics of Cylindrical Electric and Magnetic Fields," *Proc. IRE*, Vol. 28, p. 30, Jan. 1940.

[3] G. Papp, "Limits of Resolution in Magnetically-Focused Image Converter Tubes," *IRE Trans. on Nuclear Science*, Vol. NS-9, p. 91, April 1962.

[4] R. L. Beurle and W. M. Wreathall, "Aberration in Magnetic Focus Systems," *Advances in Electronics and Electron Devices*, Vol. XVI, p. 333, Academic Press Inc., New York, 1962.

[5] G. Wendt, "Sur Le Pouvoir Separateur Du Convertisseur D'Images A Champs Homogenes Electrostatique Et Magnetique," (Resolution of an Image Converter with Homogeneous Electric and Magnetic Fields) *Annales de Radioelectricite*, Vol. 10, p. 74, Jan. 1955.

[6] I.P. Csorba, "Theoretical Studies of Factors Limiting the Resolution of Magnetically-Focused Cascaded Image Intensifier Tubes," presented at the IEEE Winter General Meetings on Imaging and Counter Tubes, New York City, Jan. 30, 1963, unpublished.

* This developmental tube had a three-alkali photocathode [(Cs)Na_2 KSb].

voltage was measured by projecting the resolution pattern on the photocathode and observing the image at the phosphor screen with the microscope. The circled points in Figure 2 indicate observed measurements of resolution. At high screen voltages, the system resolution asymptotically approaches the 343 line pairs per millimeter value, which

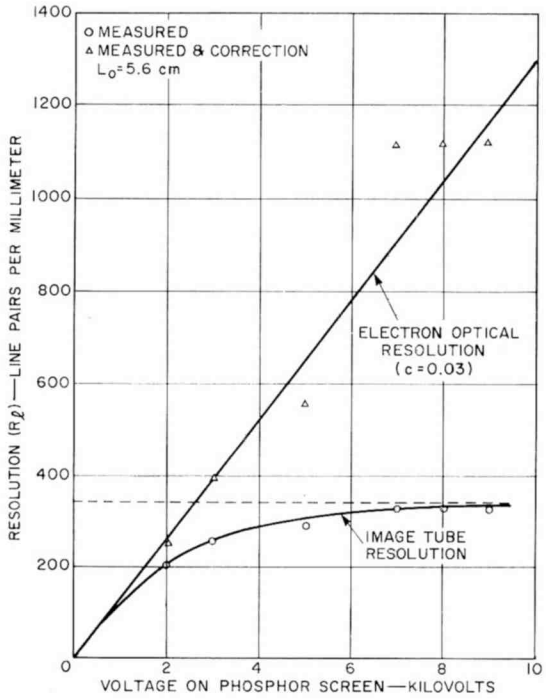

Fig. 2—Resolution of a magnetic lens as a function of applied voltage.

is the resolution of the combined glass optics and phosphor screen. This value was obtained by application of the following equation* to the observed resolution values:

$$\left(\frac{1}{R_o}\right)^2 = \left(\frac{1}{R_{lo}}\right)^2 - \left(\frac{1}{R_{l\Delta}}\right)^2,$$

where $R_{l\Delta}$ is the electron optical resolution, R_{lo} is the observed resolu-

* This equation gives an approximate relationship between the combined resolution of two cascaded optical elements and the resolution of the individual optical elements.[7]

tion, and R_o is the resolution of combined glass optics and phosphor screen. In the above equation, $R_{l\Delta}$ is proportional to the screen voltage. The electron-optical resolution was obtained by subtracting the limitations of screen and glass optics using the following equation:[7]

$$\left(\frac{1}{R_{l\Delta}}\right)^2 = \left(\frac{1}{R_{lo}}\right)^2 - \left(\frac{1}{343}\right)^2$$

The experimental electron-optical resolution calculated from the last equation is indicated in Figure 2 by the delta (Δ) points. At a screen voltage of 2000 volts, the observed system resolution differs by only about 20% from the electron optical resolution, because the observed resolution is primarily limited by the electron optics.

As shown in Figure 2, the experimental electron-optical resolution at a screen voltage of 1000 volts is 130 line pairs per millimeter. When values of 130 line pairs per millimeter, 1000 volts, and 5.6 centimeters are substituted in Equation (1) for R_l, V_s, and L_o, respectively, K is found to have a value of 0.73. Therefore, from Equation (1)

$$R_l = 0.73 \frac{V_s}{L_o}, \tag{1a}$$

where V_s is in volts, L_o is in centimeters, and R_l is in line pairs per millimeter.

In the preceding discussion, the electromagnetic lens was assumed to consist of homogeneous electric and magnetic fields. However, this ideal condition is not realized in practical image intensifiers over the entire useful diameter. The nonuniformity is discernible at points away from the axis and causes a change in the transit time and the loop period. In some cases, nonuniform fields give rise to a curved image field. More frequently, regional nonuniformities cause aberrations that impair resolution even when the transit time and loop period are adjusted for best focus in the area under observation.

To demonstrate the effect of the off-axial field nonuniformities, the resolution of the previously described tube was measured as a function of the radial distance from the center of the phosphor screen; the results are shown in Figure 3. In curve A, the measured resolution is shown with the loop period adjusted for the best focus at each radius. The measurements were repeated in curve B by adjusting for best

[7] O. H. Schade, Sr., "Electro-Optical Characteristics of Television Systems," *RCA Review*, p. 5, March 1948.

focus at the center of the screen. It is concluded that, although the electron-optical resolution at the center of the screen is very high, a small nonuniformity in the electric or magnetic fields may seriously degrade resolution in areas away from the center. Experience indicates that, for electron-optical resolutions greater than 100 line pairs per millimeter over the diameter of the tube, it is necessary to maintain the cross-sectional variation of the magnetic flux density at less than 1% over this diameter. Although the cross-sectional variation of the electric field E may not be critical, it is important to have good uniformity in the vicinity of the photocathode.

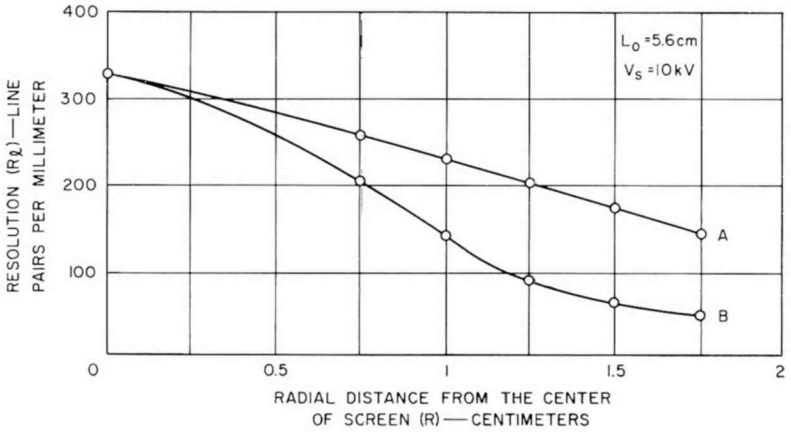

Fig. 3—Experimental resolution as a function of radial distance from the center of the viewing screen. Curve A gives the resolution when the loop time is adjusted for best focus at each point. Curve B was obtained by focusing the tube at the center.

Resolution of the Mica-Coupled Image

At moderate input illumination levels, a serious limitation to the resolution of a cascaded image tube exists as a result of the thickness (5 to 10 microns) of the mica spacer. The spacer serves as a support for the interstage phosphor screen and photocathode and also couples the light image from the phosphor screen to the photocathode. The resolution of the mica-coupled image may be obtained by tracing light paths through the mica, as shown in Figure 4. The illumination dI of the screen side of the mica spacer produced by a small excited area (ΔA) of the screen is given by*

* A lambertain light emission of phosphor screens is assumed.

$$dI = \frac{i_o}{\pi} \frac{\Delta A}{(d')^2} \cos^4 \alpha_2 , \tag{2}$$

where i_o is the luminous emittance of the phosphor screen, d' is the distance of ΔA from the mica, and α_2 is the angle of incidence of light. The light flux within the incremental angle $\Delta\alpha_2$ illuminates the screen side of the mica over an annular element $dA = 2\pi r_1 dr_1$. The same light

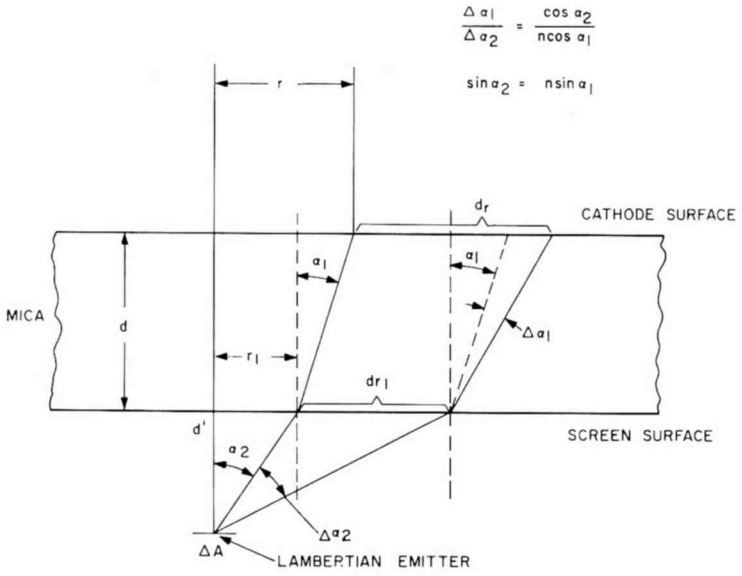

Fig. 4—A mica spacer illuminated by a Lambertain emitter. The light flux within $\Delta\alpha_2$ angle after the refraction on the screen surface illuminates an annular element of width dr on the cathode surface.

flux illuminates an annular element $dA' = 2\pi r dr$ on the cathode side of the mica. Consequently, the illumination of the cathode side with respect to the screen side is reduced by a factor ρ, as follows,

$$\rho = \frac{dA}{dA'} = \frac{r_1 dr_1}{r dr} .$$

From Figure 4,

$$\rho = \frac{(d')^2 n^2 \cos^4 \alpha_1}{(d \cos^3 \alpha_2 + d' n \cos^3 \alpha_1)\ (nd' \cos\alpha_1 + d \cos\alpha_2)} . \tag{3}$$

The illumination on the cathode side of the mica spacer is calculated as the product of Equations (2) and (3). For $d' \ll d$, the illumination on this surface becomes*

$$dI' = \frac{i_o \Delta A n^2}{\pi d^2} \cos^4 \alpha_1 = \frac{i_o \Delta A n^2}{\pi d^2} \left(1 + \frac{r^2}{d^2}\right)^{-2} . \qquad (4)$$

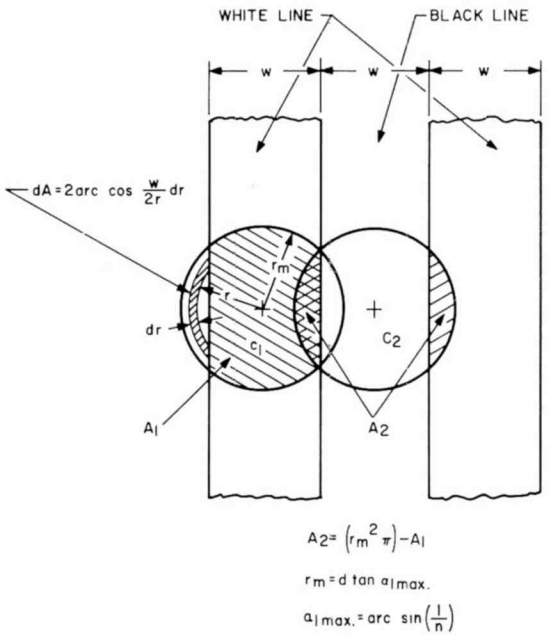

Fig. 5—Two white lines and a black line of a resolution pattern in contact with the screen side of the mica spacer. C_1 and C_2 are points on the cathode side of the mica.

Upon illumination of the mica spacer through a resolution pattern that is in contact with the screen side of the mica ($d' \ll d$), the illumination of the cathode side in the center of a black or white line may be obtained as shown in Figure 5. Because of the refraction at the screen side of the mica, a point on the cathode side may receive illumination only from those points on the screen side that are within a circular area having a radius $r_m = d \tan \alpha_{1max}$ where $\alpha_{1max} = \text{arc sin}\ (1/n)$, d is the thickness of the mica, and n is the index of refraction.

* This simplified analysis does not consider light from the phosphor in optical contact with the mica and light reflected back to the phosphor screen by the photocathode.

Therefore, the illumination in the mica-coupled image of the white line (I_W) at the point C_1 of Figure 5 may be obtained by integrating dI' over the area A_1:

$$I_W = \frac{i_o n^2}{\pi d^2} \int_{A_1} \left(1 + \frac{r^2}{d^2}\right)^{-2} dA$$

$$= i_o - \frac{4 i_o n^2}{\pi d^2} \int_{w/2}^{r_m} r \left(1 + \frac{r^2}{d^2}\right)^{-2} \arccos \frac{w}{2r}\, dr\,. \tag{5}$$

The illumination in the image of the black line (I_B) at C_2 is given by

$$I_B = \frac{i_o n^2}{\pi d^2} \int_{A_2} \left(1 + \frac{r^2}{d^2}\right)^{-2} dA = 4 \frac{i_o n^2}{\pi d^2} \int_{w/2}^{r_m} r \left(1 + \frac{r^2}{d^2}\right)^{-2} \arccos \frac{w}{2r}\, dr\,. \tag{6}$$

The contrast between these two images may be expressed as

$$C' = \frac{I_W - I_B}{I_W + I_B} = 1 - \frac{8 n^2}{\pi d^2} \int_{w/2}^{r_m} r \left(1 + \frac{r^2}{d^2}\right)^{-2} \arccos \frac{w}{2r}\, dr\,. \tag{7}$$

The range is limited in Equation (7), where

$$\frac{\tan \alpha_{1(\max)}}{1.5} < \frac{w}{d} < 2 \tan \alpha_{1(\max)}\,.$$

Figure 6 shows the contrast C' as a function of the ratio of mica thickness to line width. If, at the line frequency corresponding to the limiting resolution, a sinusoidal variation of the luminance across a white and a black line is assumed, then at 3% average luminance difference, C' is $0.03/0.637 = 0.047$. Because the value of d/w is 1.60

at $C' = 0.047$, the limiting resolution R_l is

$$R_l = \frac{1}{2w} = \frac{1}{2(0.625d)} = \frac{0.80}{d} \text{ line pairs per millimeter,} \tag{8}$$

where d is the thickness of the mica spacer in millimeters.

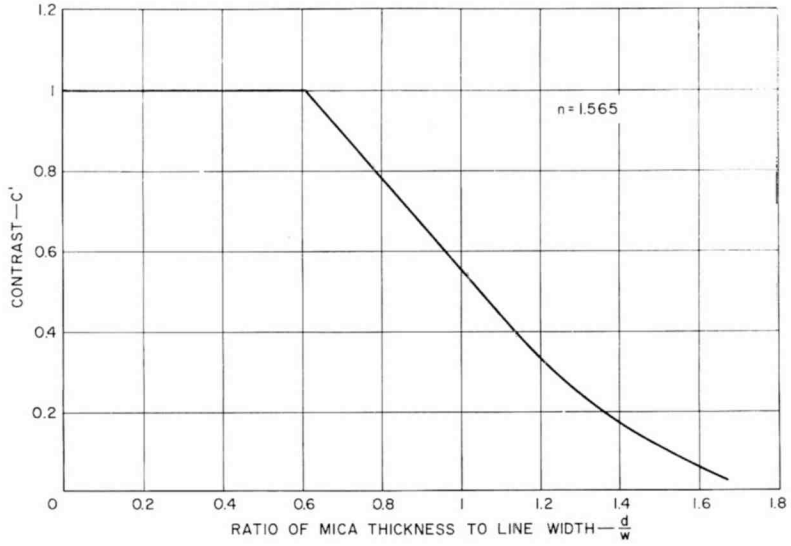

Fig. 6—Contrast as a function of the ratio of mica thickness to line width.

Equation (8) was experimentally verified by sandwiching mica wafers of various thicknesses between a strip of photographic film and a resolution pattern. During the exposure, the resolution pattern was illuminated by a diffuse light source. The results, plotted in Figure 7, show that the measured data and Equation (8) agree very closely.

Resolution of Phosphor Screens

Another serious limitation to the resolution of a cascaded image tube results from light scattering in the phosphor screen. The width of the white lines appears to increase as the thickness of the phosphor screen increases. To determine the relationship between screen thicknes and resolution, a number of phosphor screens were made with various thicknesses, and their resolutions were measured by projecting an optical resolution pattern on each screen. Figure 8 shows the measured resolution as a function of screen thickness.

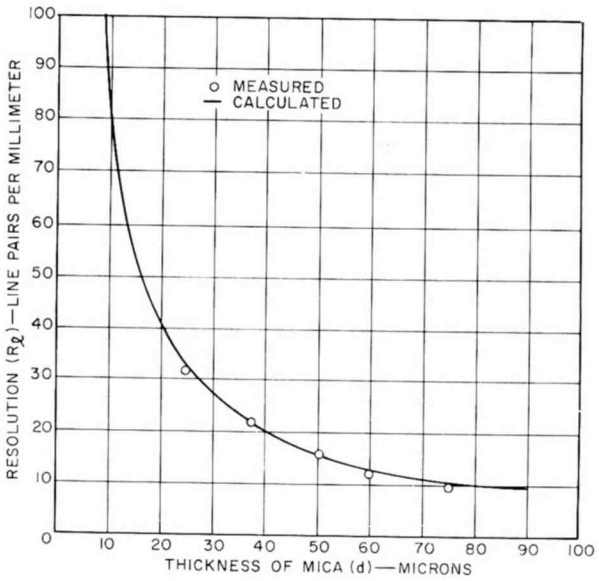

Fig. 7—Resolution of the mica spacer as a function of thickness.

It is interesting to note that resolution depends only on thickness and not on screen particle size, except for very thin screens, where the thickness of the particle is greater than the average screen thickness. In these cases, the use of larger-particle phosphors resulted in very

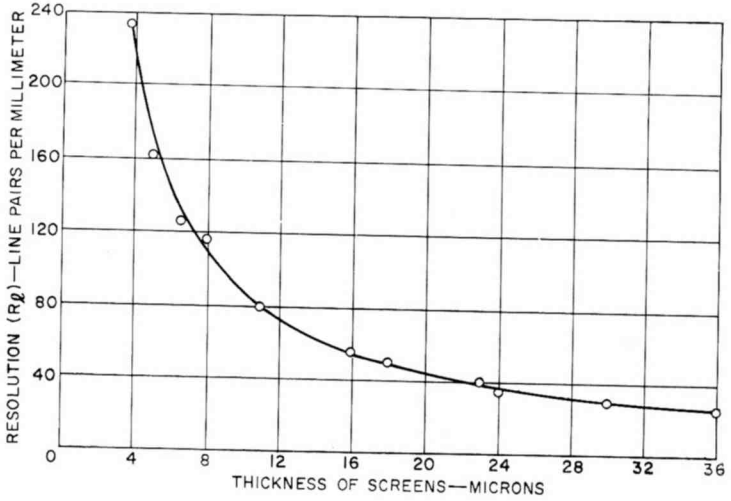

Fig. 8—Measured values of limiting resolution as a function of screen thickness.

grainy images and poor resolution. The data in Figure 8 were taken using phosphors having particle diameters up to 3 microns. For a screen thickness of 4 microns, the resolution is shown to be approximately 235 line pairs per millimeter. When larger-diameter particles (up to 8 microns) are used, for the same screen thickness, the resolution is reduced considerably. The reason is that the thickness of the particle becomes the limiting factor. For particle sizes up to 8 microns, therefore, the best resolution is obtained at a screen thickness of 8 microns.

Because the function of the phosphor screen is to convert electron kinetic energy into light energy, the conversion efficiency of the phosphor screen must also be considered in designing for the optimum thickness of the phosphor screen. In general, the larger the particle size of the phosphor, the greater the conversion efficiency. However, because the use of a large-particle phosphor with a thin screen results in a loss of resolution, an optimum balance of conversion efficiency and resolution requires a trade-off between the size of the phosphor particle and the thickness of the screen. A suitable compromise is to make the diameter of the phosphor particle equal to the thickness of the screen (essentially a monolayer screen). In such screens, however, the microscopic irregularities in the effective thickness reduce the performance of the screen somewhat. In usual practice, therefore, smaller particles are also included to provide a smooth screen layer. An important characteristic of high-resolution screens is that their screen density is considerably higher than that of regular screens (such as, for example, those used in television picture tubes) in which the phosphor particles are loosely packed. Because of the higher screen density, it is possible to reduce the screen thickness for a given screen weight, and thus to improve the resolution.

High-resolution screens presently used in image-tube applications are processed from material having a particle size of up to 5 microns in diameter. These screens have a resolution of about 120 line pairs per millimeter and a conversion efficiency of 8 to 10% at an operating voltage of 12 to 15 kilovolts. By processing the screen from finer particles the above resolution can be improved, but with a loss of conversion efficiency.

Electron-Fluctuation-Limited Resolution of a Photocathode at Low Illumination Levels

At very low levels of photocathode illumination, the resolution of a high-gain image intensifier is primarily limited by the finite number

of photoelectrons released at the photocathode during the storage time of the eye. Because of the small amount of light, the intensified image is no longer continuous, but is broken up into discrete scintillations, one for each electron released at the input photocathode. Inspection of the intensified image of a resolution pattern at very low illumination levels reveals that the resolution of the smaller white bars is reduced as the photocathode illumination (and, consequently, the number of scintillations in the white bars) is gradually decreased. Therefore, a certain minimum number of perceivable flashes per bar per storage time of the eye are required to resolve a bar. The theory for resolution of electronic image devices at low light levels has been developed by Morton and others.[8-10]

Consider two adjacent elements, a white and a black bar, with an average number of photoelectrons per storage time $\overline{N}_w$ and $\overline{N}_b$ respectively. In this case, the average luminance difference between the images of the bars is proportional to $\overline{N}_w - \overline{N}_b$, and the root-mean-square fluctuation of the luminance is proportional to $\sqrt{\overline{N}_w + \overline{N}_b}$. For the bars to be resolved, the average luminance difference must exceed the fluctuation by a factor of k,

$$\overline{N}_w - \overline{N}_b = k\sqrt{\overline{N}_w + \overline{N}_b}\,. \tag{9}$$

The larger the value of k in Equation (9), the greater the certainty for resolving the bars. Therefore, k is frequently designated as a "certainty coefficient." By substitution $\overline{N}_b = \rho\overline{N}_w$ in Equation (9) and rearranging the average number of electrons in a white bar becomes

$$\overline{N}_w = k^2\frac{(1+\rho)}{(1-\rho)^2}, \tag{10}$$

where ρ is the ratio of the average luminances of a black and a white line.

Because the average number of emitted electrons is proportional to the illumination, the emitting area, and the storage time, it may also be expressed as

[8] G. A. Morton and J. E. Ruedy, "The Low-Light-Level Performance of the Image Intensifier Orthicon," *Advances in Electronics and Electron Physics*, Vol. XII, 1960.

[9] R. Clark Jones, "Quantum Efficiency of Detectors for Visible and Infrared Radiation," *Advances in Electronics and Electron Physics*, Vol. XI, p. 88, Academic Press Inc., New York, 1959.

[10] A. Rose, "Television Pickup Tubes and Problem of Vision," *Advances in Electronics and Electron Physics*, Vol. I, 1948.

$$\overline{N}_w = \frac{E'stlw}{e}, \tag{11}$$

where l and w are the length and width of a line, e is the electron charge in coulombs, E' is the illumination in lumens per square centimeter, s is the photocathode sensitivity in amperes per lumen, and t is the storage time.

If a resolution pattern in which $l = 5w$ (U.S. Air Force resolution pattern) is used, and if $w = 1/2R_l$, Equation (11) becomes

$$\overline{N}_w = \frac{5E'stw^2}{e} = \frac{5E'st}{4R_l^2(1.6 \times 10^{-19})} = k^2 \frac{(1+\rho)}{(1-\rho)^2}.$$

Upon rearrangement, the resolution R_l is

$$R_l = \frac{2.79 \times 10^8}{k} \frac{(1-\rho)}{\sqrt{1+\rho}} \sqrt{E'st} \text{ line pairs/mm} \tag{12}$$

In Equation (12), the resolution is proportional to the square root of the product of the photocathode illumination, photocathode sensitivity, and storage time. Figure 9 shows the log of the limiting resolution as a function of the log of the illumination of the photocathode for $k = 5$, $\rho = 0$, and several values of storage time. Three measured points of the limiting resolution for visual observation of a high-contrast resolution pattern are also shown.* If 0.2 second is accepted as a storage time of the human eye,[10] the certainty coefficient, k, can be calculated from Equation (12) and the observed resolution. (The ρ-values indicated in Figure 9 were estimated from the equivalent background illumination of the photocathode, 10^{-11} lumen per cm^2, and the contrast transfer of the image tube.) k was found to be 4.5 and 4.6 for the two lower resolution points, while the upper point k was 3.1.

CONCLUSION

Of the various limitations to the resolution of magnetically focused image-intensifier tubes, the finite thicknesses of the mica separators

* This experiment was limited to a small number of observers. The data represent the average reading of the resolution.

and of the phosphor screens are the most severe for light levels above 10^{-3} foot-candle on the photocathode. The loss of resolution resulting from the electromagnetic lens capability is inconsequential unless there are substantial nonuniformities in the electric or magnetic fields. At very low light levels (less than 10^{-4} footcandle on the photocathode), statistical variations of photoelectron current limit resolution. From a comparison of measurements and theory, in the case of a parallel black-and-white resolution pattern, a value of 3.1 to 4.6 has been determined for the coefficient k.

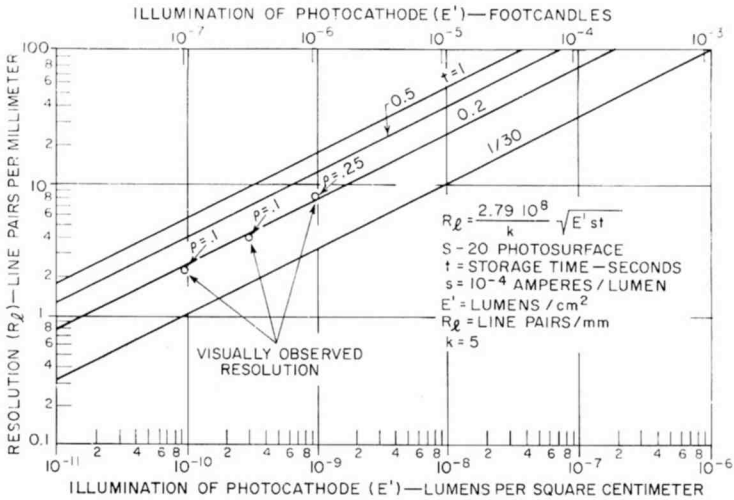

Fig. 9—Electron-fluctuation-limited resolution of a multialkali photocathode as a function of illumination. Circled points indicate the limiting resolution for visual observation.

Acknowledgment

The author thanks G. Stoudenheimer and R. W. Engstrom for their valuable assistance in the preparation of this paper, and A. E. Bishop for the processing of phosphor screens used for evaluating resolution.

Appendix—Focusing Error of an Electron Lens Consisting of Homogeneous Axial Electric and Magnetic Fields

In general, a photoelectron emitted from the photocathode enters the electron lens with small initial transverse and axial components of velocity. The transverse velocity component causes the electron to move on a circle in a plane perpendicular to the electric and magnetic

fields. The period of the circular motion is

$$T = \frac{2\pi m}{Be}, \tag{1}$$

where m is the electron mass, B the magnetic flux density, and e the electron charge. The axial distance from the photocathode at which the electron completes its period of rotation is:

$$L = T\left(v_a - \pi\frac{E}{B}\right) \tag{2}$$

where v_a is the axial emission velocity and E is the electric field.

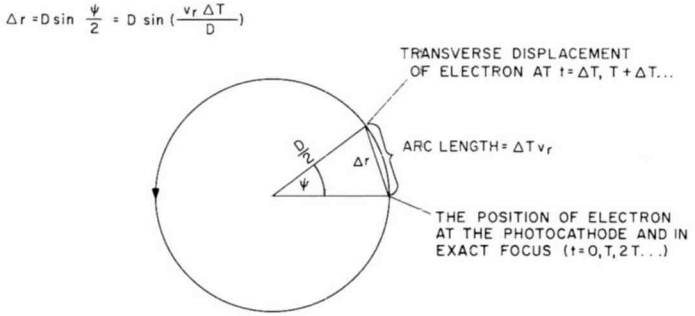

Fig. 10—Transverse orbit of an electron in a plane perpendicular to the electric and magnetic fields and moving with the electron in the axial direction.

In the case of a monoenergetic Lambertain electron emitter, if the phosphor screen is placed in the image plane of the electrons emitted at an angle θ_f, the axial focusing error may be obtained from Equation (2) by calculating the electron image distance difference of the electrons emitted at angles θ and θ_f:

$$\Delta L = \pm\, T v_i(\cos\theta_f - \cos\theta) \tag{3}$$

where v_i is the emission velocity of photoelectrons.

The electrons that complete a period of rotation a distance ΔL in front of the screen continue their transverse motion on a circular path for an additional time, ΔT. These electrons strike the screen at an arc length $\Delta T v_r$ from the image center, where v_r is the transverse emission motion velocity, as shown in Figure 10. The situation is simi-

lar for the electrons completing a period of rotation behind the screen except in this case ΔT has a negative value. The transverse focusing error of the electrons associated with particular values of v_i, θ_f, and θ from the geometry of Figure 10 is given by

$$\Delta r = D\sin\left(\frac{v_r \Delta T}{D}\right) \tag{4}$$

where D is the diameter of circular motion.

From the equation of electron motion in a uniform electric field,

$$v_s^2 t^2 + 4L_o v_a t - 4L_o^2 = 0\,,$$

the transit time difference ΔT may be obtained as

$$\Delta T = \frac{2L_o}{v_s^2}\left[v_i(\cos\theta_f - \cos\theta) - \sqrt{v_i^2\cos^2\theta_f + v_s^2} + \sqrt{v_i^2\cos^2\theta + v_s^2}\right], \tag{5}$$

where t is the transit time and v_s is the electron velocity corresponding to an accelerating voltage (screen-to-photocathode) V_s. For $v_s \gg v_i$, Equation (5) reduces to

$$\Delta T = L_o \frac{\sqrt{V_i}}{V_s}\sqrt{\frac{2m}{e}}\,(\cos\theta_f - \cos\theta)\,, \tag{5a}$$

Approximating the value of Δr by the arc length $\Delta T v_r$, and using Equation (5a), Equation (4) reduces to

$$\Delta r = 2L_o \frac{V_i}{V_s}(\cos\theta_f - \cos\theta)\sin\theta\,, \tag{6}$$

where L_o is the screen-to-photocathode distance and V_i is the accelerating voltage required for a photoelectron at rest to acquire its emission energy.

The electron transit time is identical for magnetic fields that produce single or multiloop paths. Therefore in a first-order approximation, Δr is also identical in both modes of operation.

A POTENTIAL SOLID-STATE FLYING-SPOT SCANNER

By
J. I. Pankove and A. R. Moore

RCA Laboratories
Princeton, N. J.

Summary An acoustoelectric domain propagating past an array of GaAs floating p-n junctions causes sequential light emission. Experiments were conducted on a GaAs strip consisting of an undoped n-type layer on which a thin p-type layer had been grown. Discrete junctions were formed by cutting grooves in the p-type layer. Light is emitted most strongly at the floating junction nearest the anode and its relationship to the domain is confirmed by the time dependence of the emissions at adjacent junctions as measured with a photomultiplier. The emission spectrum is also discussed. Beside its application as a solid-state flying-spot scanner, the device might also be useful in a flat panel display.

Introduction

When a field of 200 to 300 V/cm is applied along the [110] direction in GaAs, an acoustoelectric domain forms at the cathode and propagates toward the anode with the velocity of sound in this material (3.5×10^5 cm/sec).[1] The formation and propagation of acoustoelectric domains is manifested as a periodic time-dependent fluctuation in current or voltage (or in both). The period is determined by the transit time of the domain between the electrodes, and therefore does not depend on the applied voltage.

A floating p-n junction[2] is a structure such as that shown in Figure 1, where the net current through the p-n junction is zero. In the pres-

[1] P. O. Silva and R. Bray, "Oscillatory Current Behavior in GaSb and Its Relation to Spontaneous Generation and Amplification of Ultrasonic Flux," *Phys. Rev. Letters*, Vol. 14, p. 372, 8 March 1965; C. Hervouet, J. Lebailly, P. Leroux Hugon, and R. Veilex, "Current Oscillations in GaAs Under Acoustic Amplification Conditions," *Solid State Com.*, Vol. 3, No. 12 p. 413, 1965; H. Hayakawa, M. Kikuchi, and Y. Abe, "Continuous Current Oscillation in GaAs Caused by Acoustoelectric Effect," *Japan Jour. Appl. Phys.*, Vol. 5, p. 734, Aug. 1966.

[2] A. R. Moore and W. M. Webster, "The Effective Surface Recombination of a Germanium Surface with a Floating Barrier," *Proc. IRE*, Vol. 43, p. 427, April 1955.

ence of a potential distribution such that the equipotential planes intersect the p-n junction, part of the junction is reverse biased and the rest of the junction is forward biased. The ratio of forward- to reverse-bias areas adjusts itself in such a manner that the forward current is equal to the reverse current. Since the average reverse-current density is much lower than the average forward-current

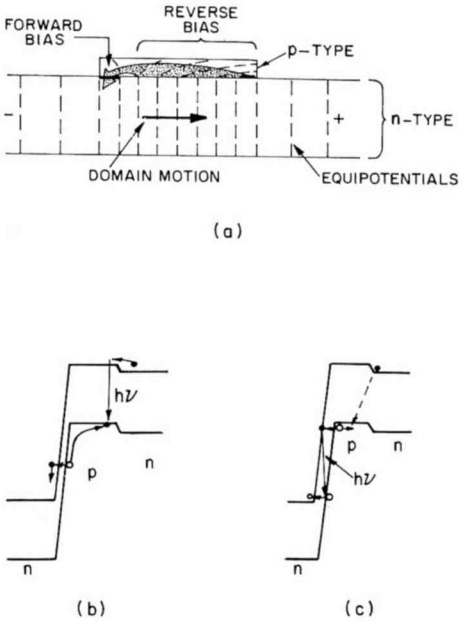

Fig. 1—Current flow in a floating p-n junction.

density, the reverse-biased area is much larger than the forward-biased area. In GaAs, and hopefully in $GaAs_{1-x}P_x$, it is possible to get efficient radiative recombination in the forward-biased portion of the floating p-n junction. This mode of operation contrasts to the case of floating p-n junctions of Cu_2S on CdS, where inefficient luminescence is caused by the breakdown of the reverse-biased portion of the p-n junction.[3]

A floating junction is equivalent to an n-p-n "hook" (Figure 1b); one side is reverse biased and the other is forward biased. To maintain charge neutrality in the p-region, the electrons injected in the p-region by the forward-biased junction are compensated by holes collected at the reverse-biased junction (these holes may result from

[3] B. W. Hakki, "Solid-State Acoustoelectric Light Scanner," *Appl. Phys. Letters*, Vol. 11, p. 153, 1 Sept. 1967.

electrons tunneling to the conduction band in the high-field region). The radiative recombination is very efficient in the case of two-carrier flow to the p-type region. In the case of breakdown luminescence, (Figure 1(c)), the two carriers are formed in the high-field region when their encounter time is very short. The holes flow to the p-type region where they are majority carriers. In the forward-biased Cu_2S-CdS junction, charge neutrality must be obtained by nonradiative recombination (or tunneling), since injection luminescence is not found in the Cu_2S-CdS system.

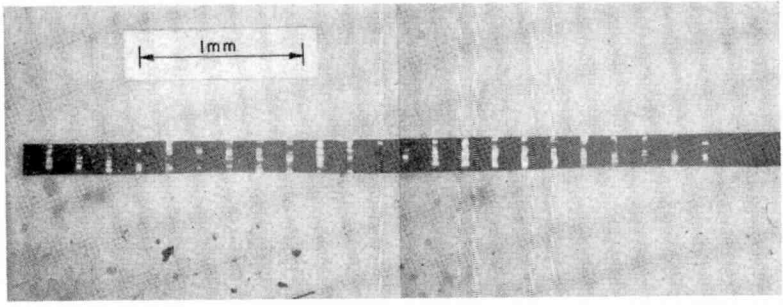

Fig. 2—GaAs acoustoelectric scanner.

Experiment with GaAs

The series of floating p-n junctions was arrayed along a thin bar of GaAs. Thematerial consisted of an undoped n-type layer on which a thin p-type layer had been grown. Both layers had been fabricated by vapor transport.[4] The doping of the n-type layer corresponded to 10^{16} electrons/cm^3, the p-type layer was doped to a hole concentration of about 10^{19}/cm^3 and was about 5 microns thick. The wafer was cleaved into bars about 300 microns wide and about 5 mm long. Then, the p-layer was grooved with a fine grinding wheel to divide the continuous p-type layer into discrete p-type regions. P-type strips 50 microns wide were obtained on 0.6-mm centers in some bars and on 175-micron centers in other bars (Figure 2). Ohmic connections were made at the ends of the n-type bar by evaporating tin through a suitable mask.

The resistance of the bar was about 150 ohms when immersed in liquid nitrogen. A pulse generator with 400 ohms internal impedance

[4] J. J. Tietjen and J. A. Amick, *Jour. Electrochem. Soc.*, Vol. 113, p. 724, 1966.

was used to apply fields of 200-300 V/cm for a duration of several microseconds at a low repetition rate. Because of the comparable magnitudes of generator and load impedances, neither constant voltage nor constant current bias could be obtained. Hence, both voltage and current show the characteristic instabilities due to acoustoelectric domains, wherein electrons traveling in the [110] direction faster than sound velocity interact with the lattice, emitting phonons and losing kinetic energy in the process. This interaction, in effect, increases the local longitudinal resistance. Consequently a greater voltage drop appears across the domain region. The formation of the high-resist-

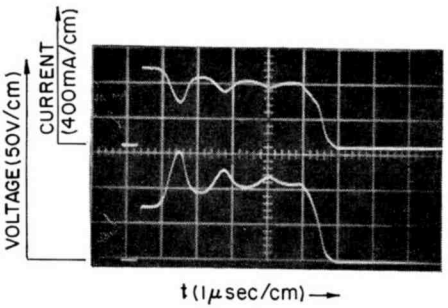

Fig. 3—Current and voltage waveforms above threshold for acoustoelectric domain formation.

ance domain causes a drop in the current and a rise in the voltage until the domain is swept out of the specimen. As soon as the domain is swept out at the anode, a new domain forms at the cathode. This behavior is shown in Figure 3 where the propagation of the acoustoelectric domain is observed through three cycles. The gradual attenuation of the domains is believed due to heating during the 5-microsecond pulse.

Light is emitted most strongly at the floating junction nearest the anode (where the domain has reached its greatest intensity). The position of greatest luminescence is determined visually with an image converter, and its relationship to the domain is confirmed by the time dependence of the emission as measured with a 7102 photomultiplier (Figure 4). Note that the maximum emission occurs when the domain is about to disappear at the anode.

A more definitive verification was made with the arrangement of Figure 5. The specimen is imaged on the plane of the slit (visible on

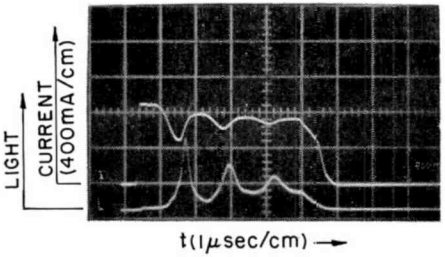

Fig. 4—Current and light emission waveforms.

the lab jack) in front of the 7102 detector. The slits are adjusted to select one portion of the imaged vertical bar and can be moved a measurable amount to scan the image. The time dependent output of the photomultiplier is shown in Figure 6. This figure demonstrates that light emission along the domain propagation path occurs at successively later times. If one plots the delay of emission with respect to the beginning of the pulse as a function of position along the bar, one obtains Figure 7, which shows the linear dependence expected from a domain propagating at a constant velocity. The value obtained for the sound velocity is 3.5×10^5 cm/sec, which is in accord with published values for GaAs.

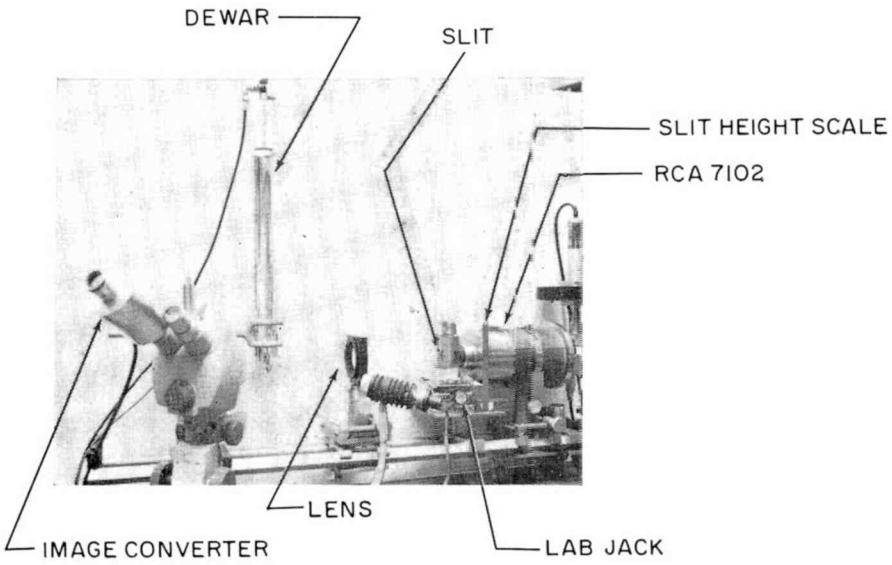

Fig. 5—Experimental set up for measuring the propagation of electroluminescent acoustoelectric domain.

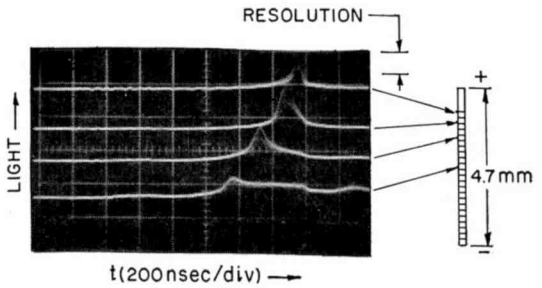

Fig. 6—Time dependence of electroluminescence along the scanner.

The emission spectrum was examined in a specimen already emitting in the absence of acoustoelectric domains, i.e., sufficient current in the steady state is shunted by the floating junction to cause electroluminescence. When the applied field is increased slightly to form a domain (shown by the wave shape on an oscilloscope), a different spectrum is obtained (Figure 8). In the presence of the acoustoelectric domain, a larger current flows through the p-n junction and the emission intensity increases. But the spectrum shifts to lower photon energy by 13 meV and the line width increases by 15-20 meV. The lower photon energy would be expected from the high local dilational stress induced by the acoustoelectric domain. Measurements were made with both polarities of applied voltage, i.e., with domains propagating in either direction along the bar, and similar results are obtained in both cases.

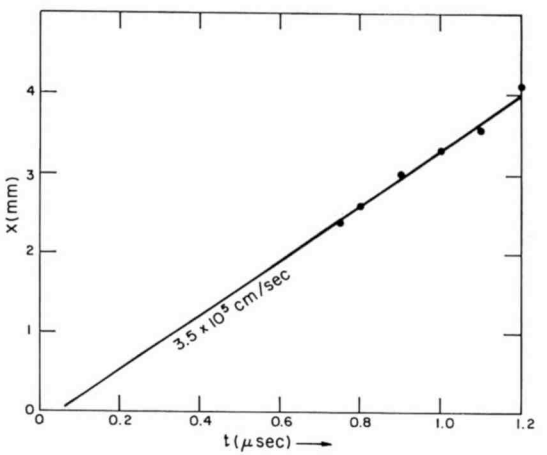

Fig. 7—Position–time correlation diagram.

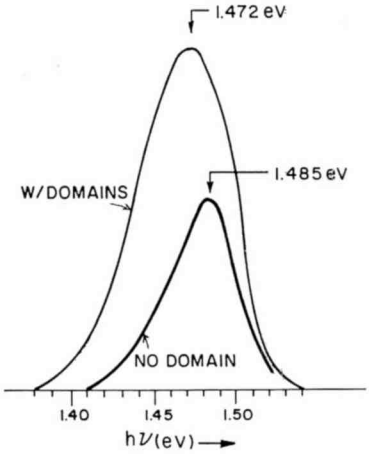

Fig. 8—Emission spectra from a floating p-n junction.

A transverse magnetic field is known to reduce the electron drift velocity at which domains are formed.[5] This was verified in our specimen (Figure 9). However, the effect is too small to be of practical value.

Potential Applications

In modern technology, a solid-state flying-spot scanner should be a welcome new device. It opens new possibilities for compactness and

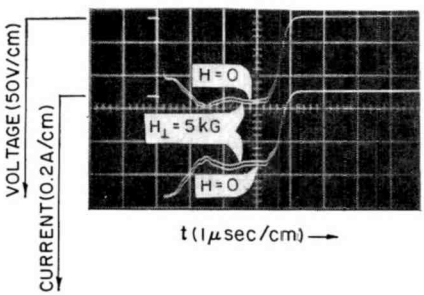

Fig. 9—Effect of transverse magnetic field on current and voltage waveforms during acoustoelectric fluctuations.

[5] M. C. Steele, "Magnetic Field Effect on Acoustoelectric Gain in Semiconductors," *RCA Review*, Vol. 28, p. 58, March 1967; C. Hervouet, *Phys. Stat. Sol.*, Vol. 21, p. 117, 1967; R. Bray, C. S. Kumar, J. B. Ross, P. O. Sliva, *Proc. Int. Conf. Phys. of Semiconductors*, Kyoto, 1966; *Jour. Phys. Soc. Japan*, Vol. 21, Supp. p. 483, 1966.

integration. It should find application in reading photographic data and in interrogating or controlling photosensitive or photoemissive arrays, and might also be useful for image reproduction with a flat-panel display. In the last application, a compatible thin flat television screen is conceivable. The constant propagation velocity of the domain dictates a screen width of 3.5×10^5 cm/sec $\times$ 62 μsec = 22 cm (8-½ inches). The modulation of the intensity could be controlled by an electro-optic modulator such as a Kerr cell.

Other Structures and Further Problems

To improve system sensitivity, the emission spectrum should be shifted into the visible. This shift should be obtainable by using $GaAs_{1-x}P_x$ as the active medium.* Even GaP should be a good prospect. In all these materials, the light intensity at floating p-n junctions would be enhanced by the presence of the high field domain due to increased local current. However, in slightly indirect-bandgap materials, still another effect should occur—deformation potential enhancement of radiative efficiency. The mechanism responsible for this effect is as follows. The piezoelectric stress associated with the moving domain deforms the conduction and valence bands so that the energy gap shrinks in regions of dilation (negative compression). Since the stress dependence of the direct valley is greater than that of the indirect valleys[6] of the conduction band, the material acquires a direct gap in a region that moves with the domain. The electrons redistribute themselves to occupy preferentially the lower-energy direct valley, where their radiative lifetime is greatly decreased. Hence, the local luminance is greatly increased.

Another desirable feature is the possibility of getting coherent emission. To evaluate this possibility, one needs to know what current density can be achieved in the forward-biased portion of the floating junction.

Of course, the ability to operate at room temperature is extremely

* Since this manuscript was written, the acoustoelectric domain has been obtained in several samples of $GaAs_{1-x}P_x$ with floating p-n junctions. In one of these materials, red luminescence at 6700 Å was obtained at the forward biased edge of each p-n junction (the p-type layer being very conducting). The luminescence was greatly enhanced by the passage of the acoustoelectric domain, especially at the junction nearest the anode.

[6] H. Ehrenreich, "Band Structure and Electron Transport of GaAs," *Phys. Rev.*, Vol. 120, p. 1951, Dec. 15, 1960; T. A. Fulton, D. B. Fitchen, and G. E. Fenner, "Pressure Effects in $Ga(As_{1-x}P_x)$ Electroluminescent Diodes." *Appl. Phys. Letters*, Vol. 4, p. 9, 1 Jan. 1964; G. E. Fenner, "Pressure Effect on Resistivity of $Ga(As_{1-x}P_x)$, *Phys. Rev.*, Vol. 134A, p. 1113, 18 May 1964.

important. Acoustoelectric domains have been propagated at room temperature and efficient electroluminescence can be obtained at room temperature. Hence, the potential usefulness of such a flying spot scanner is not seriously temperature limited.

Other problems still need further scrutiny: (1) determination of the size of the domain, since resolution depends on this quantity; (2) device design such that the energy gained by the domain from the applied field is equal to the energy dissipated in luminescence; and (3) system design such that the domain is fully formed at the cathode. This last problem can be solved by using (a) an acoustoelectric launching section in which a high field forms a domain that then travels through the cathode, beyond which the domain is sustained by a lower field, (b) a Gunn-effect domain-launching section,* (c) a piezoelectric transducer mechanically attached to the cathode, and/or (d) an applied voltage consisting of a spike of high voltage (to generate a large domain) followed by a lower voltage to sustain the drifting domain.

ACKNOWLEDGMENTS

We wish to thank R. E. Enstrom, J. J. Tietjen, and H. Gozemberg for supplying the special materials; F. Z. Hawrylo for processing them; R. E. Harwood for the delicate grinding operation; M. Falk for mounting the device; and J. E. Berkeyheiser for assistance with measurements.

* Suggested by M. C. Steele, RCA Laboratories, Princeton, N. J.

THE STATUS OF THRESHOLD LOGIC*

By
R. O. Winder

RCA Laboratories
Princeton, N. J.

Summary The theoretical work done in threshold logic since 1959 is surveyed, and the present state of its application in computers reviewed, including existing logic and circuit designs.

I. Introduction

A THRESHOLD GATE is an electronic-circuit building block for realizing logic (or switching) functions such as appear in the control, register, and processing portions of a digital computer. Inputs and outputs take on values we call "0" and "1". At present "Boolean" gates (AND, OR, NOT, and their complements) are used almost exclusively. Boolean gates perform an identification function only. The output of an AND gate, for example, specifies whether a certain pattern of inputs, e.g., all 1's, is present or not. The OR gate then identifies a pattern of all 0's. Boolean switching theory is well developed, providing a theoretical basis for logic design using Boolean gates.

In the late 1950's several variations of a new type of circuit were developed. This type of circuit performs the more sophisticated function of determining the *majority* signal among its inputs. A 5-input parametron, for example, has an output of 1 only when three or more (a majority) of its inputs are 1's. The obvious generalization of such a "majority gate" is the threshold gate, where, in effect, inputs are allowed different (possibly even negative) "weights" in the voting process; instead of a simple majority being determined, an arbitrary "threshold" is specified for the gate. The output then indicates whether or not the weighted sum of inputs attains the given threshold.

Since its decision process is much more sophisticated than that of the Boolean gate, the threshold gate is logically more powerful, and

* The preparation of this survey, and most of the theoretical RCA research reported, was sponsored by the Electronics Research Directorate, Air Force Cambridge Research Laboatories, Office of Aerospace Research, under contract AF19(628)-4789. The present paper is a revision of Winder-14.

fewer are needed to realize a given switching function. This affords savings both in the total cost of the circuits and, equally important, in the cost of interconnecting them.

A second important distinguishing feature of threshold gates is their ability to be modified conveniently (by variations of the weights), which makes them particularly suitable for use in adjustable networks. In these applications, there are typically many tens or even hundreds of inputs to each gate, and circuit errors can be tolerated because of the intrinsically statistical environment. However, the emphasis in this survey is on "switching theory", stressing 100% reliable circuits of few inputs in completely pre-designed computer-like applications.

This new type of building block, which provides what is called a "threshold function", has generated many interesting switching-theory problems. Three books, about 200 papers, and at least 15 PhD theses dealing with the subject of threshold logic have been published since 1959. Actual applications to computer problems have been much fewer, and a commercially competitive threshold-gate circuit has only recently been developed. This survey is divided into three parts: theory, threshold-gate circuits, and logic design. References, which are given by the author's name, are arranged alphabetically in the bibliography. Where more than one reference is listed under an individuals name, these are designated **1**,**2**,**3**, etc.

II. Theory

This discussion of threshold-logic theory is divided into four parts: (A) a basic system of properties possessed by all threshold functions, (B) test synthesis, i.e., the determination of whether or not a given switching function is a threshold function and, if it is, what weights and threshold realize it, (C) synthesis of networks of interconnected threshold gates to calculate specified switching functions, and (D) classification and enumeration of threshold functions, with statistics and estimates of various factors such as the number of threshold functions, the size of weights, and the number of threshold gates likely to be needed in a network. It should also be noted that several variations of this basic threshold logic are being developed, notably nonlinear threshold logic (see Ataka), a 3-valued threshold logic (for example, Varshavsky-Ovsievich-**3**), a multiple-threshold threshold logic (Haring-**1**), and a theory of partially separable functions (Slivinsky).

A. Properties of Threshold Functions

There are many simple but important properties of threshold functions that follow directly from the definitions; these can be found dis-

cussed in several of the early papers (Elgot, Gabelman-**1**, Muroga-**1,3**, and Winder-**1,3**)—and in books by Hu-**2** and by Lewis and Coates-**3**. These two general books are not referred to below, but they cover much of the material discussed. (Reviews of the first book can be found in Winder-**12** and Muroga-**13**; and a review of the second can be found in Haring-**2**.) Winder-**17** has also written a tutorial exposition of basic ideas, including a discussion of some practical tools.

The relationships between threshold functions as given by their algebraic expressions, with a view towards constructing interesting classes of functions, and as generated by variations in threshold are studied in Elgot, Muroga-**1,3,4,7,8**, Gabelman-**1,4**, and Meisel-**1,2**. Characterizations of optimal weight–threshold realizations are given in Willis. Other subjects are treated in Muroga-**6**, Mays, Gabelman-**5**, Kaszerman-**3**, and Coates-Supornpaibal.

A fundamental family of properties of threshold functions—k-monotonicities—were discussed in Paull-McCluskey and in McNaughton, and are treated more completely in Muroga-Toda-Takasu-**3** and Winder-**1,3**. A parallel series of properties—dual k-monotonicites—were defined in Muroga-Toda-Takasu-**3** and generalized in Liu-**1,2**. These ideas are unified into one theory by the idea of hyper-monotonicities (Winder-**7**). The recent paper by Yajima-Ibaraki-**2** is a further extension of this subject. Also relevant are Fischler-**1**, Varshavsky-**1**, Liss, and Quine.

E. F. Moore (unpublished) has shown that the monotonicity properties do not characterize threshold functions, and for this reason generalizations to stronger conditions have been explored by many authors (e.g., Elgot, Gabelman-**1**, and Winder-**3**). The adequacy of the monotonicities for limited value of n (the number of arguments) has been determined as $n \leq 8$ by Muroga-**12**; Gabelman-**1** showed the inadequacy for $n = 9$ (see also Cobham, Bargainer-Ccates-**1**, and Roy-**3**).

A necessary and sufficient condition that a switching function be a threshold function was published in Elgot, Chow-**1**, Gabelman-**1,2**, and Highleyman, but it is computationally equivalent to the original definition. In Chow-**2**, a set of $n + 1$ easily calculated numerical parameters were defined; among other important uses, they provide a theoretical characterization of threshold functions. In Dertouzos-**2,3,5**, these parameters are in fact used to give an analytic characterization. A closely related characterization is obtained by the use of the Tschebycheff approximation (Kaplan-Winder-**1**) of the given switching function, instead of the more customary least-sum-of-squares approximation.

Probably the most fertile area for further work on basic properties of threshold functions is the "Chow" parameters; a computationally simple characterization has not yet been found. Recent papers dealing with this subject are Levine and Winder-**20**,**23**.

B. Test-Synthesis

The problem of identifying and realizing threshold functions (finding weights and threshold when they exist) has unfortunately produced a large number of shallow papers. For small n, no more than 6, say, the problem is trival—most functions are not threshold functions and can be so recognized immediately, especially in any reasonable geometric representation, by the 1-monotonicity test (Winder-**1**,**3**,**6**). For those near-threshold functions passing this test, a calculation of Chow parameters and a table-look-up in tables that exist for $n \leq 7$ (Dertouzos-**2**,**3**, Winder-**9**) immediately provide the "best" realization, if one exists, or an indication that it doesn't.

For partially specified functions, or for large n, there is no practical method known other than the solution of a system of linear inequalities generated by the definition of a threshold function. This system must first be reduced to reasonable size by elimination of redundant inequalities, which amounts to determining the signs and relative magnitudes of the weights (Muroga-Toda-Takasu-**3**, Winder-**1**,**3**). Then it can be solved in a variety of fashions—by linear programming or game theory (Muroga-Toda-Takasu-**3**, Minnick, Akers-**1**, Einhorn), by algebraic determination of all solutions (McNaughton, Elgot, Winder-**1**,**3**, Opferman), and by various specialized iterative methods (Gabelman-**1**,**3**, Coates-Lewis-**1**,**2**, Dertouzos-**2**,**3**, Sheng-**1**,**4**,**5**, Roy-Choudhury, Wong-Eisenberg and others). The dual–simplex method of Muroga-Toda-Takasu-**3** is easily carried out by hand for n up to 12 and higher, is easily programmed for a computer, and gives (by definition) the best possible realization (see elaborations in Winder-**7** and evaluations in Winder-**21**).

For functions only sparsely specified, as in character recognition problems, methods have been developed in Singleton and in Gaston.

Other, fairly limited methods are discussed in the papers by Stram-**1**,**2**, Dadda-**1**,**2**, Kaszerman-**1**,**2**, Liu-**1**, Ho-Kashyap, Torng, Blomgrem-Torng, and Gonzalez-**1**.

In my opinion no further work in test synthesis is appropriate.

C. Networks

Methods to synthesize networks of threshold gates divide into four classes: (1) synthesis with majority gates of three or five inputs, (2)

synthesis of symmetric functions, (3) general combinational synthesis, and (4) sequential-machine synthesis.

When the basic gate is constrained to be a three-input majority gate, it is possible easily to realize arbitrary functions for small n (up to 5 or 6) by using geometric representations (Miiller-Winder, Horna-**2**). For larger n, truth-table representations can be used in computer programs to produce heuristically good networks (Akers-**3**, Negrin, Riseman). But there is much theoretical interest in using an algebraic approach, analogous to the Boolean algebra used for Boolean gates. This theory has been developed in a variety of papers, principally those by Cohn-Lindaman-**1**, Miyata-**1,2**, Hanson, Raship, Tohma and by Meo (see also Lindaman, Sutherland, Akers-**2**, Winder-**3**, and Horna-**1**). Typically these papers offer rules for manipulating the algebraic expressions, often suggesting a particular form that always gives realizations, but not necessarily the best ones. These ideas, and especially the algebra itself, should be organized into a coherent theory.

Methods for synthesis of symmetric functions have been developed in Muroga-**1**, Minnick, Kautz, Sheng-**2**, and Roy-**1**, and this problem is now much better solved than the technological problems of increasing the number of gate inputs, upon which the theory depends (see also Fishler-Tannenbaum-**3**).

Methods for realizing arbitrary functions have come more slowly. In Winder-**2,3**, an algorithm is given that, for a given function, provides a two-threshold-gate realization or proves that such a realization is impossible. These ideas have been extended in Hopcroft-**1,2** and Stabler; the problem of solving 3-gate realizability is now feasible (see also Winder-**10**). Heuristic extensions of these ideas (minimum number of gates not guaranteed) seem reasonable (Yajima-Ibaraki-**3**), but no useful guide lines are now known. Although other approaches have been developed that theoretically give optimal networks (Cameron-**2**, Breuer, Hu-**1,2**), they don't seem to offer practicable heuristic generalizations. In Lewis-Coates-**2** and in Breeding, network synthesis is approached with specific constraints on gate complexity.

When the network is restricted to two levels—e.g., several threshold gates driving a single OR gate—several approaches are possible (Minnick, Dertouzos-**2,3**, Sheng-**3**, Gonzalez-**1,2**, Butakov, Breeding). Other heuristic approaches are discussed in Lewis-Coates-**1,2**, Coates-Lewis-**3**, Hughes-**1,2**, Dearholt, and in Kashyap. Perhaps of more practical interest is the "slicing" idea (Varshavsky-**2**, Fischler-**1**), which, in effect, realizes, with separate threshold gates, a system of roughly parallel hyperplanes in n-space. These hyperplanes define alternating regions of 0's and 1's in the function; the corresponding gates drive a

final majority gate with alternating weights of plus and minus unity. This idea works well with geometric function representations and deserves more exploration.

One interesting approach to the synthesis of networks is the idea of "multiple-threshold" threshold gates; the gate output is determined by the pair of its several thresholds between which the weighted input sum lies. (Ercoli-Mercurio, Haring-**1**,**3**, Yen, Mow-Fu-**1**,**2**,**3**, Necula). Such a realization can be used to generate a network consisting of one gate per threshold, where the set of original input weights to each gate is identical. Another method of generating networks from a nonstandard kind of threshold gate, in this case a "threshold-product" gate, is given in Yau-Ostapko.

Sequential machine realization has been studied generally in Hadlock-Coates; more work in this area can be expected (see Erikkson-Danielsson). Logic hazards in networks have been treated in Howe-Coates.

Specific optimal realizations of each type of four-argument function have been enumerated in Minnick (known minimal in number of gates by methods of Winder-**2**,**3**), Cyprus (claimed minimal also in gate complexity), and Tsuboi (optimal realizations using either three-input or five-input majority gates).

Methods for using time-shared computers in a man–machine interactive-design mode are being developed (Dertouzos-Santos-**4**, Kaplan-Winder-**2**); combining the man's intuition with the machine's clerical abilities is likely to prove the best approach to logic design using threshold gates.

D. Classification, Enumeration, and Bounds

In Muroga-**3**,**8** and Winder-**3** efficient methods for listing the different types of 6-argument threshold functions are developed and carried out. In Goto-Takasi an important new idea for classification is suggested, and this idea is used in the enumeration of 7-argument functions (Winder-**8**,**9**). Roughly this idea puts constant biasing signals, 0 and 1, on an equivalent basis with other signals. See Dertouzos-**1**,**2**, Liu-**1**, and Winder-**16** for further discussions. An enumeration of 8-argument functions has recently been carried out by Muroga-**12**. Enumeration methods are also discussed in Muroga-**7**,**9**, Dertouzos-**2**,**3**, and Dearholt.

The number R_n of threshold functions is now known to satisfy $1/2n^2 < \log_2 R_n < n^2$ (Yajima-Ibaraki, Smith, Winder-**1**,**3**, Cameron-**1**, Muroga-**11**). Earlier work will be found in Muroga-**1**,**3** and Perkins-

Willis-Whitmore. The number of threshold functions specified on only m points is less than m^n (Winder-**5**) (see also Cover-**1**,**2**). It is my guess that the present upper bound on R_n is an asymptotic limit, but this remains to be shown (Winder-**22**). A paper by Winder-**11** treats one theoretical approach to this problem.

It is known that the worst necessary size of weights increases at least exponentially with n (Goto-Takahasi, Muroga-**10**; see also Myhill-Kautz).

It has apparently been shown by Nechiporuk that the number of threshold gates required to realize an arbitrary function is likely to be about $2^n/n$, which is $1/n$ times the expected number of Boolean gates. However, I have not checked this proof, and it contradicts two other Russian authors (Varshavsky-**2** and Zakharova). On the other hand, these two authors are also contradicted by results of Winder-**5**, which agree with, but are improved upon, by Nechiporuk. In Muroga-**1**, an easier upper bound is given. Another general approach is described in Smith-**2**. All these results, of course, are academic, since they assume gates with an unlimited number of inputs.

In summary, the theory is well developed, but important new ideas are to be expected in the difficult area of network synthesis, and there will probably be continuing progress in the unification and completion of the basic theory of the nature of threshold functions.

III. Circuit Design

Threshold gate circuits can be broadly divided into two classes—(1) those that sum directly the input signal representations and (2) those that do not. In either case, there is eventually a summation, and two methods have been used widely—magnetic flux summation and resistor current or voltage summation.

The threshold gate responsible for much of the earliest interest in threshold logic was simple and elegant, consisting of several input windings on a ferrite core and an output winding (Karnaugh). Signals could be represented by the direction of a unit pulse of current in each input; algebraic summation of fluxes takes place in the core, except that the flux saturates in one direction or the other at the equivalent of one unit pulse of current in the output winding. Magnitude and sign of input weighting were determined by the number of turns and direction of each input winding. There were many variations of this basic theme; elaborations were necessary for speed, tolerance, and other engineering reasons. A typical magnetic threshold gate system operated in a multi-phase system—"waves" of power supply activation

washed through the system to impress a directionality on otherwise bilateral signal propogation. Furthermore, it was typically necessary to add a transistor or other such active device to provide (1) gain, and/or (2) a sharper threshold discrimination, and/or (3) better standardization and driving capability in the output signal. Several computers have been built using such "magnetic" threshold gates (Muroga-Takashima-**2**), e.g., Ferranti's ORION.

Once an active element was introduced, it was natural to use a simple Kirchoff resistor summation of the inputs, with the active device used to restore proper levels. Important such devices used were the phase-locked-oscillator (Wigington, Rajchman), and the tunnel-diode balanced pair (Lo, Lewin). These examples represented phased ac and phased dc power supplies, respectively. Although some success was obtained, tolerance, speed, and power-supply distribution problems remained severe.

Resistor summation and transistor discrimination/restandardization represented the most important threshold-gate circuit for several years (Chao, Akers-Rutter-**4**, Coates-Lewis-**4**). (Earlier, vacuum tube threshold-gate circuits were used in some computers.) These circuits had two related difficulties: (1) close tolerances were required on the summing resistors and the threshold supply and (2) noise appearing on the different input signals was combined additively at the critical summation point. These effects combined to limit the gates to reasonable fan-in (i.e., number of equivalent majority-gate inputs) with poor noise immunity, or reasonable noise immunity with poor fan-in. And this typically with 1% uniformity resistors. Tolerance analyses can be found in Muroga-**5**, Winder-**3**, Wood, and Sheng-**6** (see also Haring-**4**). Although theory flourished in these years, very few applications were made.

Integrated circuit technology has permitted a solution to this dual problem (Amodei-Hampel-Mayhew-Winder, Marette). First, the relative uniformity of a cluster of resistors manufactured at the same time is very high—2% uniformity is standard and better uniformity is possible by increasing geometric dimensions. Second, it is now possible to provide a separate current switch for each input, the outputs of which are used in the summation process. This isolates the decision process from the possibly noisy inputs—all that's required of the inputs is that they lie at least 100 mV from the reference level that separates 1's from 0's. To my knowledge, integrated gates of this sort are the first threshold gates that, compared with contemporary Boolean gates, are (1) competitive in cost (approximately 25% more costly in exactly the

same fabrication technology), (2) compatible in all voltage levels and so usable as subsystems in conventional systems, (3) compatible in speed (initial experimental gates operate with 12 nanoseconds state delays, fully loaded, as compared with about 8 nanoseconds for comparable OR/NOR gates), and (4) have better noise immunity. The gates actually fabricated (Amodei-Hampel-Mayhew-Winder) have five inputs weighted respectively 2,2,1,1, and 1, with threshold 4, and provide both true and complemented outputs. This gate was combined with a 3-input majority gate in a 14-pin package to provide a versatile building block. Higher fan-ins are possible, but then only one gate per package is feasible with present technology.

Threshold-gate circuits are also being developed for the new large scale integration (LSI) technologies (Winder-**18**, Beinart-Hampel). These circuits, compared to the high-speed high-power threshold gates discussed above, are simpler, somewhat slower, and on a local level often have less noise immunity. They are designed to behave virtually independently of temperature variations and those power supply drops that show up symmetrically on the two power-supply lines. These particular circuits allow incorporation of very simple OR functions at inputs and outputs; they are most tolerant to component variations when their thresholds are highest. These properties seem likely to generate a new generation of logic-design problems and corresponding switching theory.

In summary, threshold-gate circuit technology has taken a long step forward, and is roughly on a par with the theory of threshold gates. In both areas, threshold gates are now competitive with Boolean gates. It is now essential to consider the application of each to the real problems of logic design in computer-like systems.

IV. Logic Design

Practical logic design with threshold gates is found in the phased power supply systems (Muroga-Takashima-**2**) and in Ferranti's ORION data-processing computer. However, detailed information on these efforts is not available and, moreover, the requirement for multiple phases places special constraints on the logic design that do not apply in the integrated-circuit technology. The known logic designs are, for the most part, realizations of computer subsystems, such as adders, parity checkers, registers, and counters. Several of the designs mentioned below are discussed in Winder-**18**.

A complete full adder, accepting three inputs and delivering a sum and a carry as outputs, can be realized using two threshold gates

(Amodei-Hampel-Mayhew-Winder or Winder-**18**). This realization typifies the advantages of using threshold gates: (1) one-third as many gates are needed as in the most sophisticated Boolean-gate adder (in fact, one of the 14-pin packages mentioned above constitutes an entire adder stage), (2) interconnection complexity is very low, and (3) only the true input signal representations are needed (saving a factor of two in the number of input connections to the adder).

Many other adder designs are known. For examples, only three 3-input majority gates are required per stage. (Curry, Harel, Cohn-Lindaman-**2**). Binary/decimal adder/subtractors are easily realized (Fischler-Poe-**2**). Carry look-ahead is very natural in threshold logic (Coates-Lewis-**7**, Cohn-Lindaman-**3**); a 64-bit adder can be built that uses 189 of the (2,2,1,1,1) gates mentioned above and operates in just 6 stage delays (Winder-**15**).

A fast, two-level, approximately $n/2$-gate n-bit parity checker is discussed by Minnick. Kautz gives a slower, less-expensive design using $\log_2 n$ of gates (this network also gives a complete binary count of the number of 1's present among the inputs). Since both of these designs require tolerances equivalent to a $(2n+1)$-input majority gate, probably the best solution is a $\log_2 n$-level tree network of approximately n 2-gate, 3-input full-adders of the sort described above.

Sequential networks of threshold gates offer very interesting possibilities. In Gustafson-Haring-Susskind-Wills-Sandford and Masters-Mattson, the realization of counters is investigated, assuming a collection of identical delay lines as in the standard synchronous sequential machine model, but then doing the next-state logic with one threshold gate per output. Of more practical interest are the ring counters developed (for $m \geq 3$) in Price and in Misiurewicz, which require one majority gate per full count and no capacative interconnection. Counters of this type are very simple (either all or all but one of the gates, can be 5-input majority gates) and can operate at very high speeds—one lightly-loaded stage delay per transition of the clocking pulse. Binary counters can be constructed using three gates per stage (Winder-**19**).

The Boolean idea of realizing a flip-flop or register stage by cross-connected NOR gates becomes, in threshold logic, a pair of minority gates (Dinman, Coates-Lewis-**6**). However, the same effect can be realized with a single threshold gate (Amodei-Hampel-Mayhew-Winder). Furthermore, the need for an isolating AND gate between sampled input signal and register stage is eliminated; control signals ("reset" and "gate in data") can be applied directly to the gate (see also Winder-**13**).

Other logic designs have been published; among them are comparators (Miiller-**1**, Lindaman-**2**, Cohn-Lindaman-**3**); a decoding system using 3-input majority gates (Cohn-Lindaman-**2**), pattern-recognition systems (Aker-Rutter-**4**, Brousil-Smith), a multipurpose accumulator (Coates-Lewis-**8**) and a multipurpose "logic array" (Cohn-**4**), methods of realizing large-fan-in majority gates using low-fan-in gates (Amarel-Cooke-Winder, Winder-**6**), and methods of improving reliability by suitable redundancy, an application for which threshold gates are especially appropriate (see Muroga-**6**, Massey, Liu-Liu, Constantine, Bargainer-Coates-**2**).

Two important principles should be mentioned here. First, because of pin limitations, an asymmetric basic building block (such as the 2,2,1,1, 1 gate) is preferable to a majority gate (Cohen-Winder); the full generality of the 7-input majority gate is rarely needed, and the saving of two pins is quite important. As examples of this, consider the full adder stage and the register stage with an AND gate for output isolation, each of which can be realized using one package of the type described earlier (Amodei-Hampel-Mayhew-Winder). Second, the functions of storage and logic can be combined in one threshold gate by using suitable feedback of the output; this, of course, is not true with a Boolean gate. The simplest example is the register stage, but much more sophisticated applications are possible. In particular, realization of control logic by chains (or trees) of one-gate flip-flops (an asynchronous digital version of delay lines) is an attractive scheme for reasons of economy, simplicity of design, and ease of diagnosis.

In Coates-Lewis-**4** a careful comparison was made in equivalent designs of a complete small computer using threshold gates and NOR gates. A reduction in gate count from 2:1 to 4:1 was reported, depending on the fan-in of the threshold gate assumed. Our experience at RCA has been similar—on subsystems such as those discussed above, using the integrated threshold gate, an average reduction from 2:1 to 3:1 is obtained. Equally significant—since the cost of printed-circuit plug-ins, platters, and racks can exceed the cost of the integrated circuit packages themselves—an average reduction of about 2:1 in the number of interconnections was obtained. These statistics, taken together with the 25% per/package cost increase for threshold gates, result in a total main-frame cost reduction of 50%.

V. Conclusions

The switching function performed by a threshold gate is by now very well understood, and an impressive array of methods exist for solving problems using them. Although the author has had good

success in teaching product-oriented logic designers some of these new methods, there is a clear need for a unification of the theory and a presentation of it on a practical level, as opposed to the mathematically elegant switching theory that is normally published.

A competitive, compatible integrated threshold gate now exists, with noise immunity superior to, and tolerance requirement comparable with, conventional gates. Further rapid developments in large-scale integration is underway. Much logic design has been carried out using threshold gates, covering a wide range of computer subsystems and promising substantial savings—on the order of 50%—in hardware cost and complexity. Threshold logic has progressed well on all fronts, and now offers a most attractive alternative to the use of conventional Boolean gates.

VI. References

Note: Two principal sources are: (1) the *IRE* (later, *IEEE*) *Transactions on Electronic Computers* (later, *Transactions on Computers*) which is abbreviated *TEC* (and *TC*) below; and (2) a series of conference *Proceedings* (later *Record*) on *Switching Theory and Logical Design,* IEEE Special Publications S-134 (1960 and 1961), S-141 (1962), S-156 (1963), 16 C 13 (1965), and (it was changed to *1966 Seventh Annual Symposium on Switching and Automata Theory*) 16 C 40 (1966); the abbreviations *SCTLD* and *SAT* are used below. My thanks to Samuel Cohen of RCA Patent Operations for his help with patent references.

S. B. Akers **1**, "Threshold Logic and Two-Person, Zero-Sum Games", *SCTLD,* pp. 27-33, Sept. 1961.

S. B. Akers **2**, "On the Algebraic Manipulation of Majority Logic", *IRE TEC,* Vol. EC-10, p. 779, Dec. 1961.

S. B. Akers **3**, "Synthesis of Combinational Logic Using Three-Input Majority Gates", *SCTLD* (1962), pp. 149-157, Sept. 1962.

S. B. Akers and B. H. Rutter **4**, "The Use of Threshold Logic in Charactor Recognition", 1963 WESCON (Aug. 1963), publ. *Proc. IEEE,* Vol. 52, pp. 931-938, Aug. 1964.

S. Amarel, G. Cooke, and R. O. Winder, "Majority Gate Networks", *IEEE TEC,* Vol. EC-13, pp. 4-13, Feb. 1964.

J. J. Amodei, D. Hampel, T. R. Mayhew, and R. O. Winder, "An Integrated Threshold Gate", 1967 International Solid-State Circuits Conference, Digest of Technical Papers, pp. 114-115, Lewis Winner, N. Y., Feb. 1967.

Hikosaburo Ataka, "A Basic Theorem on Threshold Devices", *IEEE TEC,* Vol. EC-13, pp. 631, Oct. 1964.

J. D. Bargainer and C. L. Coates **1**, "Decimal Numbers for Checking Summability", *IEEE TEC*, Vol. EC-15, p. 372, June 1966.

J. D. Bargainer and C. L. Coates **2**, "Minimal Multiplexed Threshold Gate Realizations", *IEEE TC*, Vol. C-17, pp. 566-578, June 1968.

G. H. Blomgren and M. C. Torng, "Single Threshold Device Realization Subject to Sensitivity Requirements", *J. Franklin Inst.*, Vol. 281, pp. 143-153, Feb. 1966.

K. J. Breeding, *An Approach to the General Synthesis of a Threshold Element Network*, Doctoral Dissertation, Dept. of E.E., Univ. of Illinois, Sept. 1967.

M. A. Breuer, "Implementation of Threshold Nets by Integer Linear Programming", *IEEE TEC*, Vol. EC-14, pp. 950-952, Dec. 1965.

J. K. Brousil and D. R. Smith, "A Threshold Logic Network for Shape Invariance", *IEEE TEC*, Vol. EC-16, pp. 818-828, Dec. 1967.

E. A. Butakov, "The Synthesis of Optimal Single-Row Circuits of Threshold Elements", translated in *Automation and Remote Control*, No. 7, pp. 1088-1093, July 1967.

S. H. Cameron **1**, "An Estimate of the Complexity Requisite in a Universal Decision Network", Bionics Symposium, WADD Report 60-600, pp. 197-212, Dec. 1960.

S. H. Cameron **2**, "The Generation of Minimal Threshold Nets by an Integer Program", *IEEE TEC*, Vol. EC-13, pp. 299-302, June 1964.

S. C. Chao, "A Generalized Resistor-Transistor Logic Circuit and Some Applications", *IRE TEC*, Vol. EC-8, pp. 8-12, March 1959.

C. K. Chow **1**, "Boolean Functions Realizable with Single Threshold Devices", *Proc. IRE*, Vol. 39, pp. 370-371, Jan. 1961.

C. K. Chow **2**, "On the Characterization of Threshold Functions", *SCTLD*, pp. 34-38, Sept. 1961.

C. L. Coates and P. M. Lewis, II, **1**, "Linearly Separable Switching Functions", *J. Franklin Inst.*, Vol. 272, pp. 360-410, Nov. 1961.

C. L. Coates, R. B. Kirchner, and P. M. Lewis, II, **2**, "A Simplified Procedure for the Realization of Linearly-Separable Switching Functions", *IRE TEC*, Vol. EC-11, pp. 447-458, Aug. 1962.

C. L. Coates and P. M. Lewis, II, **3**, "Threshold Gate Realizations of Logical Functions with Don't Cares", *SCTLD*, pp. 41-52, Sept. 1963.

C. L. Coates and P. M. Lewis, II, **4**, "DONUT, a Threshold Gate Computer", *IEEE TEC*, Vol. EC-13, pp. 240-247, June 1964.

C. L. Coates and V. Suporpnpaibul **5**, "On Maximum Stability Realizations of Linearly Separable Boolean Functions", *SCTLD*, pp. 12-24, Oct. 1965.

C. L. Coates and P. M. Lewis, II, **6**, "Bistable Device Employing Threshold Gate Circuits", U.S. Patent No. 3,275,849, Sept. 1966.

C. L. Coates and P. M. Lewis, II, **7**, "Threshold Gate Adder for Minimizing Carry Propagation", U.S. Patent No. 3,275,812, Sept. 1966.

C. L. Coates and P. M. Lewis, II, **8**, "Accumulator", U.S. Patent No. 3,300,628, Jan. 1967.

Alan Cobham, "The Assumability Condition for Seven-Variable Functions", IBM Research Note, March 1965.

S. Cohen and R. O. Winder, "Threshold Gate Building Blocks", submitted to *IEEE*.

M. Cohn and R. Lindaman **1**, "Axiomatic Majority-Decision Logic", *IRE TEC*, Vol. EC-10, pp. 17-21, March 1961. (See also correspondence in *IRE TEC* of Sept. 1961, p. 530.)

M. Cohn and R. Lindaman **2**, "Data Processing System", U.S. Patent No. 3,197,760, July 1965.

M. Cohn and R. Lindaman **3**, "Data Processing System", U.S. Patent No. 3,372,377, March 1968.

M. Cohn **4**, "General Purpose Majority-Decision Logic Arrays", U.S. Patent No. 3,296,424, Jan. 1967.

G. Constantine, "Error Correcting Redundant Logic Circuitry", U.S. Patent No. 3,305,830, Feb. 1967.

T. M. Cover **1**, *Geometrical and Statistical Properties of Linear Threshold Devices*, PhD Dissertation, E. E. Dept, Stanford Univ., May 1964,

T. M. Cover **2**, "Geometrical and Statistical Properties of Systems of Linear Inequalities with Applications in Pattern Recognition", *IEEE TEC*, Vol. EC-14, pp. 326-334, June 1965.

W. S. Curry, "Transistor Majority Logic Adder", U. S. Patent No. 2,999,637, Sept. 1961.

J. H. Cyprus, *Optimal Synthesis of the Boolean Functions of Four Variables with Majority Logic*, PhD Dissertation, E.E. Dept., Rice University, May 1963.

L. Dadda **1**, "Synthesis of Threshold Logic Combinatorial Networks", *Alta Frequenza*, n. 3. Vol. XXX, pp. 224-28E-231, 1961.

L. Dadda **2**, "Synthesis of Threshold Switching Networks by Map Methods", (Abstract) *Information Processing* 62, pp. 758, 760, North Holland, Amsterdam, 1963.

D. W. Dearholt, *On Threshold Logic*, PhD Dissertation, E.E. Dept., University of Washington, July 1965.

M. L. Dertouzos **1**, "An Approach to Single-Threshold-Element Synthesis", *IEEE TEC*, Vol. EC-13, pp. 519-528, Oct. 1964. See Correction in Vol. EC-14, p. 247, April 1965.

M. L. Dertouzos **2**, *Threshold-Element Synthesis*, PhD Dissertation, E.E. Dept., MIT, June 1964.

M. L. Dertouzos **3**, *Threshold Logic: A Synthesis Approach*, MIT Press, 1965.

M. L. Dertouzos and P. J. Santos **4**, "CADD: On-Line Synthesis of Logic Circuits", Report ESL-R-253, Electr. Syst. Lab of Mass. Inst. of Technology, Dec. 1965.

M. L. Dertouzos and Z. C. Fluhr **5**, "Minimizational and Convexity in Threshold Logic", *SAT*, pp. 195-200, Oct. 1966.

S. B. Dinman, "Storage Circuits", U.S. Patent No. 3,234,401, Feb. 1966.

S. N. Einhorn, "The Use of the Simplex Algorithm in the Mechanization of Boolean Switching Functions by Means of Magnetic Cores", *IRE TEC*, Vol. EC-10, pp. 615-622, Dec. 1961. See also correspondence in *IRE TEC* of Aug. 1962, p. 573.

C. C. Elgot, "Truth Functions Realizable by Single Threshold Organs", *SCTLD*, pp. 225-245, Sept. 1961 and AIEE Conference paper 60-1311, Oct. 1960, revised Nov. 1960.

P. Ercoli and L. Mercurio, "Threshold Logic with One or More Than One Threshold", *Information Processing 62*, (Proceedings of the IFIP Congress 62) pp. 741-746, North Holland, Amsterdam, 1963.

H. Eriksson and P. E. Davidsson, "Two Problems on Boolean Memories", *IEEE TEC*, Vol. EC-16, pp. 364-365, June 1967.

M. A. Fischler **1**, *Investigations Concerning the Theory and Synthesis of Linearly Separable Switching Functions*, PhD Dissertations, E.E. Dept., Stanford University, Jan. 1962.

M. A. Fischler and E. A. Poe **2**, "Threshold Realization of Arithmetic Circuits", *IEEE TEC*, Vol. EC-11, pp. 287-288, April 1962.

M. A. Fischler and M. Tannenbaum **3**, "Assumptions in the Threshold Synthesis of Symmetric Switching Functions", *IEEE TC*, Vol. C-17, pp. 273-279, March 1968.

I. J. Gabelman **1**, *The Functional Behavior of Majority (Threshold) Elements*, PhD Dissertation, E.E. Dept., Syracuse University, June 1961.

I. J. Gabelman **2**, "A Note on the Realization of Boolean Functions Using a Single Threshold Element", *Proc. IRE*, Vol. 50, pp. 225-226, Feb. 1962.

I. J. Gabelman **3**, "The Synthesis of Boolean Functions Using a Single Threshold Element", *IRE TEC*, Vol. EC-11, pp. 629-642, Oct. 1962.

I. J. Gabelman **4**, "Properties and Transformations of Single Threshold Element Functions", *IEEE TEC*, Vol. EC-13, pp. 684, Dec. 1964.

I. J. Gabelman **5**, "An Algorithm for Threshold Element Analysis", *IEEE TEC*, Vol. EC-14, pp. 623-625, August 1965.

C. A. Gaston, "A Simple Test for Linear Separability", *IEEE TEC*, Vol. EC-12, pp. 134-135, April 1963.

R. Gonzalez **1**, *Synthesis Problems in Linear Threshold Logic,* PhD Dissertation, E.E. Dept., Univ. of Michigan, June 1966.

R. Gonzalez and E. L. Lawler **2**, "Two-Level Threshold Minimization", *SCTLD,* pp. 41-44, Oct. 1965.

E. Goto and H. Takahasi, "Some Theorems Useful in Threshold Logic for Enumerating Boolean Functions", *Information Processing 62,* pp. 747-752, North Holland, Amsterdam, 1963, or see "Threshold, Majority and Bilateral Switching Devices", *Switching Theory in Space Technology,* pp. 47-67, Stanford University Press, 1963.

C. H. Gustafson, D. R. Haring, A. K. Susskind, and T. G. Wills-Sandford, "Synthesis of Counters with Threshold Elements", *SCTLD,* pp. 25-35, Oct. 1965.

F. O. Hadlock and C. L. Coates, "Realization of Sequential Machines with Threshold Elements", *SAT,* pp. 172-183, Oct. 1966.

W. H. Hanson, "Threshold-Logic Synthesis by Algebraic Methods", *IEEE TEC,* Vol. EC-12, pp. 401-402, Aug. 1963.

A. Harel, "Binary Adder", U.S. Patent No. 3,113,206, Dec. 1963.

D. R. Haring **1**, "Multi-Threshold Elements", *IEEE TEC,* Vol. EC-15, pp. 45-65, Feb. 1966.

D. R. Haring **2**, "Review of *Threshold Logic* by Lewis and Coates", *Comp. Revs.* 13,694, Vol. 9, Feb. 1968.

D. R. Haring and R. J. Diephuis **3**, "A Realization Procedure for Multithreshold Threshold Elements", *IEEE TEC,* Vol. EC-16, pp. 828-835, Dec. 1967.

D. R. Haring **4**, "A Technique for Improving the Reliability of Certain Classes of Threshold Elements", *IEEE TC,* Vol. C-17, pp. 997-998, Oct. 1968.

W. H. Highleyman, "A Note on Linear Separation", *IRE TEC,* Vol. EC-10, pp. 777-778, Dec. 1961.

Y. C. Ho and R. L. Kashyap, "An Algorithm for Linear Inequalities and Its Applications", *IEEE TEC,* Vol. EC-14, pp. 683-688, Oct. 1965.
J. E. Hopcroft, *Synthesis of Threshold Logic Networks,* PhD Dissertation, E.E. Dept., Stanford U., April 1964.

J. E. Hopcroft and R. L. Mattson **2**, "Synthesis of Minimal Threshold Logic Networks", *IEEE TEC,* Vol. EC-14, pp. 552-560, Aug. 1965.

O. A. Horna **1**, "Majority-Logic Synthesis", *IEEE TEC,* Vol. EC-12, pp. 131-132, April 1963.

O. A. Horna **2**, "A Geometric Synthesis Method of Three-Input Majority Logic Networks", *IEEE TEC,* Vol. EC-14, pp. 475-471, June 1965.

A. B. Howe and C. L. Coates, "Logic Hazards in Threshold Networks", *IEEE TC,* Vol. C-17, pp. 238-251, March 1968.

Sze-Tsen Hu **1**, "Minimal Linear Decompositions of Switching Functions", *SCTLD,* pp. 36-40, Oct. 1965.

Sze-Tsen Hu **2**, *Threshold Logic,* Univ. of Calif. Press. Berkeley, 1965.

G. F. Hughes **1**, *A Threshold Gate Feed-Forward Switching Net Algorithm,* PhD Dissertation, E.E. Dept., Calif. Inst. of Technology; 1964.

G. F. Hughes **2**, "Feed-forward Threshold Logic Nets for Digital Switching and Pattern Recognition", *IEEE TEC,* pp. 463-472, Aug. 1976.

K. R. Kaplan and R. O. Winder **1**, "Chebyshev Approximation and Threshold Functions", *IEEE TEC,* Vol. EC-14, pp. 250-252, April 1965.

K. R. Kaplan and R. O. Winder **2**, "Software for Threshold Gate Network Research", Section 1 of Special Scientific Report No. 2, AFCRL 66-808, for AF19(628)-4789, Oct. 1966.

M. Karnaugh, "Pulse-Switching Circuits Using Magnetic Cores", *Proc. IRE,* Vol. 43, pp. 570-584, May 1955.

R. L. Kashyap, "Synthesis of Switching Functions by Threshold Elements", *IEEE TEC,* Vol. EC-15, pp. 619-628, Aug. 1966.

P. Kaszerman **1**, *On the Synthesis of Threshold Devices,* PhD Dissertation, E.E. Dept., NYU, Sept. 1963.

P. Kaszerman **2**, "A Geometric Test-Synthesis Procedure for a Threshold Device", *Inf. and Contr.,* Vol. 6, pp. 381-398, Dec. 1963.

P. Kaszerman **3**, "A 'Region' Concept and Its Application to Threshold Logic", *Infor. and Contr.,* Vol. 8, pp. 531-551, Oct. 1965.

W. H. Kautz, "The Realization of Symmetric Switching Functions with Linear-Input Logical Elements", *IRE TEC,* Vol. EC-10, pp. 371-378, Sept. 1961.

E. Levine, "On the Characterizing Parameters of a Threshold Function", *IEEE TC,* Vol. C-17, pp. 696-697, July 1968.

M. H. Lewin, "Negative-Resistance Elements as Digital Computer Components", *Proc. EJCC,* pp. 15-27, Dec. 1959.

P. M. Lewis, II, and C. L. Coates **1**, "A Realization Procedure for Threshold Gate Networks", *SCTLD,* pp. 159-168, Sept. 1962. See also, *IEEE TEC,* Vol. EC-12, No. 5, pp. 454-461, Oct. 1963.

P. M. Lewis, II, and C. L. Coates **2**, "Realization of Logical Functions by a Network of Threshold Components with Specified Sensitivity", *IEEE TEC,* Vol. EC-12, pp. 443-454, Oct. 1963.

P. M. Lewis, II, and C. L. Coates **3**, *Threshold Logic,* John Wiley and Sons, Inc., N.Y., 1967.

R. Lindaman **1**, "A Theorem for Deriving Majority-Logic Networks within an Augmented Boolean Algebra", *IRE TEC*, Vol. EC-9, pp. 338-342, Sept. 1960.

J. R. Lindaman **2**, "Hamming Magnitude Comparator Using Multi-Input Binary Threshold Logic Elements", U.S. Patent No. 3,350,685, Oct. 1967.

Donal Liss, "A Test for Unate Truth Functions", *IEEE TEC*, Vol. EC-12, pp. 405, Aug. 1963.

Ming-Tsau Liu **1**, *The Triquare Map Method for Realization of Threshold Functions*, PhD Dissertation, E.E. Dept., U. of Penn., June 1964.

Ming-Tsau Liu **2**, "On the Dual-Monotonicity of Threshold Functions", *IEEE TEC*, Vol. EC-14, pp. 625-627, Aug. 1965.

A. Lo, "Bistable Amplifying Circuit Employing Balanced Pair of Negative Resistance Elements with Anode-to-Cathode Interconnection", U.S. Patent No. 3,075,087, Jan. 1963.

G. F. Marette, "Integrated Majority Logic Circuit Utilizing Base-Connected Parallel-Transistor Pairs and Multiple-Emitter Transistor", U.S. Patent No. 3,378,695, April 1968.

J. L. Massey, *Threshold Decoding*, PhD Dissertation, E.E. Dept., MIT, Aug. 1962.

G. M. Masters and R. L. Mattson, "The Application of Threshold Logic to the Design of Sequential Machines", *SAT*, pp. 184-194, Oct. 1966.

C. H. Mays, "The Boundary Matrix of Threshold Functions", *IEEE TEC*, Vol. EC-14, pp. 65-66, Feb. 1965.

R. McNaughton, "Unate Truth Functions", *IRE TEC*, Vol. EC-10, pp. 1-6, March 1961.

W. S. Meisel **1**, *Variable-threshold Threshold Elements*, Doctoral Dissertation, E.E. Dept., U. of So. Calif., May 1967 and *IEEE TC*, Vol. C-17, pp. 656-667, July 1968.

W. S. Meisel **2**, "Nets of Variable-Threshold Threshold Elements", *IEEE TC*, Vol. C-17, pp. 667-676, July 1968.

A. R. Meo, "Majority Gate Networks", *IEEE TEC*, Vol. EC-15, pp. 606-618, Aug. 1966.

H. S. Miiller **1**, "Majority Gates Applied to Simultaneous Comparators", *IEEE TEC*, Vol. EC-10, pp. 94-95, March 1961.

H. S. Miiller and R. O. Winder **2**, "Majority Logic Synthesis by Geometric Methods", *IRE TEC*, Vol. EC-11, pp. 89-90, Feb. 1962.

R. C. Minnick, "Linear-Input Logic", *IRE TEC*, Vol. EC-10, pp. 6-16, March 1961.

Piotr Misiurewicz, "Comment on 'Counting with Majority-Logic Networks' ", *IEEE TEC*, Vol. EC-15, p. 262, April 1966.

F. Miyata **1**, "Realization of Arbitrary Logical Functions Using Majority Elements", *IEEE TEC*, Vol. EC-12, pp. 183-191, June 1963.
F. Miyata **2**, "An Extension of the Method of Cohn and Lindaman", *IEEE TEC*, Vol. EC-13, pp. 625-629, Oct. 1964.
C. W. Mow and K. S. Fu **1**, "An Approach for the Realization of Multithreshold Threshold Elements", *IEEE TC*, Vol. C-17, pp. 32-46, Jan. 1968.
C. W. Mow and K. S. Fu **2**, "Input Tolerance Considerations for Multithreshold Threshold Elements", *IEEE TC*, Vol. C-17, pp. 46-54, Jan. 1968.
C. W. Mow and K. S. Fu **3**, "Generation of Self-dual and Self-complementary Dual Functions", *IEEE TC*, Vol. C-17, pp. 57-66, Jan. 1968.
S. Muroga **1**, "Logical Elements on Majority Decision Principle and Complexity of Their Circuits", *Proceedings of the International Conference on Information Processing* (June 1959), Columbia Univ. Press 1960.
S. Muroga and K. Takashima **2**, "The Parametron Digital Computer MUSASINO-1", *IRE TEC*, Vol. EC-8, pp. 308-316, Sept. 1959.
S. Muroga, I. Toda, and S. Takasu **3**, "Theory of Majority Decision Elements", *Jour. Franklin Inst.*, Vol. 271, pp. 376-418, May 1961.
S. Muroga **4**, "Functional Forms of Majority Functions and a Necessary and Sufficient Condition for their Realizability", *SCTLD*, pp. 39-46, Sept. 1961.
S. Muroga **5**, "Restrictions in Synthesis of a Network with Majority Elements", *Proc. IRE*, Vol. 49, p. 1455, Sept. 1961.
S. Muroga **6**, "Majority Logic and Problems of Probabilistic Behavior", *Self Organizing Systems 1962*, pp. 243-81, Spartan Books, 1962, (Proceedings of Conference May 1962).
S. Muroga **7**, "Generation of Self-Dual Threshold Functions and Lower Bounds of the Number of Threshold Functions and a Maximum Weight", *SCTLD*, pp. 169-184, Sept. 1962.
S. Muroga, I. Toda, and M. Kondo **8**, "Majority Decision Functions of up to Six Variables", *Jour. Math. of Comp.*, Vol. XVI, No. 80, pp. 459-472, (Published in Japanese in 1959 and 1960).
S. Muroga **9**, "Generation and Asymmetry of Self-Dual Threshold Functions", *IEEE TEC*, Vol. EC-14, pp. 125-136, April 1965.
S. Muroga **10**, "Lower Bounds of the Number of Threshold Functions and a Maximum Weight", *IEEE TEC*, Vol. EC-14, pp. 136-148, April 1965.
S. Muroga and I. Toda **11**, "Lower Bound of the Number of Threshold Functions", *IEEE TEC*, Vol. EC-15, pp. 805-806, Oct. 1966.
S. Muroga, T. Tsuboi, and C. R. Baugh **12**, "Enumeration of Threshold

Functions of Eight Variables", Rept. No. 245, Dept. of Computer Science, U. Illinois, Aug. 1967.

S. Muroga **13**, "Review of S. T. Hu's *Threshold Logic*", *Comp. Rev.*, Vol. 8, pp. 484-485, Sept.-Oct. 1967.

J. Myhill and W. H. Kautz, "On the Size of Weights Required for Linear-Input Switching Functions", *IRE TEC*, Vol. EC-10, pp. 288-290, June 1961.

E. I. Nechiporuk, "The Synthesis of Networks form Threshold Elements", *Problemy Kibernetiki*, No. 11, pp. 49-62, April 1964. (Translation in *Automation Express* Vol. 7, No. 7, pp. 35-39, and No. 2, pp. 27-32.)

N. N. Necula, "An Algorithm for Multithreshold Threshold Element Synthesis", *IEEE TC*, Vol. C-17, pp. 978-985, Oct. 1968.

A. E. Negrin, "Synthesis of Practical Three-Input Majority Logic Networks", *IEEE TEC*, Vol. EC-13, pp. 296-299, June 1964.

D. C. Opferman, *A Synthesis Procedure and Optimal Solutions for Threshold Functions*, Doctoral Dissertation, Univ. Pittsburgh, 1967.

M. C. Paull and E. J. McCluskey, Jr., "Boolean Functions Realizable with Single Threshold Devices", *Proce. IRE*, Vol. 48, pp. 1335-1337, July 1960.

D. T. Perkins, D. G. Willis, and E. A. Whitmore, unpublished work at Lockheed Aircraft Corporation, Missiles and Space Division, Sunnyvale, California.

J. E. Price, "Counting with Majority-Logic Networks", *IEEE TEC*, Vol. EC-14, pp. 256-260, April 1965.

W. V. Quine, "Two Theorems About Truth Functions", *Boletin de la Sociedad Matematica Mexicana*, Vol. X, pp. 64-70, 1953.

J. A. Rajchman, "Solid-State Microwave High Speed Computers", *Proc. EJCC*, pp. 38-47, Dec. 1959.

M. Raship, *On the Analysis and Synthesis of Switching Networks Composed of m-out-of-n Decision Gates*, PhD Dissertation, E.E. Dept., NYU, June 1964.

E. M. Riseman, "A Realization Algorithm Using Three-Input Majority Elements", *IEEE TEC*, pp. 456-462, Aug. 1967.

K. K. Roy and A. K. Choudhury **1**, "A Note on Testing and Realization of Threshold Functions", *IEEE TEC*, Vol. EC-15, pp. 242-244, April 1966.

P. K. Sinha Roy **1**, "Synthesis of Symmetric Switching Functions Using Threshold Logic Elements", *IEEE TEC*, Vol. EC-16, pp. 359-364, June 1967.

P. K. S. Roy **2**, "A Slide Rule Device for Checking 2-Summability", *IEEE TC*, Vol. C-17, pp. 279-283, March 1968.

C. L. Sheng **1**, "A Method for Testing and Realization of Threshold Functions", *IEEE TEC,* Vol. EC-13, pp. 232-239, June 1964.

C. L. Sheng **2**, "A Graphical Interpretation of Realization of Symmetric Boolean Functions with Threshold Logic Elements", *IEEE TEC,* Vol. EC-14, pp. 8-18, Feb. 1965.

C. L. Sheng **3**, "Compound Synthesis of Threshold Logic Network for the Realization of General Boolean Functions", *IEEE TEC,* Vol. EC-14, pp. 798-814, Dec. 1965.

C. L. Sheng and H. R. Hwa **4**, "Testing and Realization of Threshold Functions by Successive Higher Ordering of Incremental Weights", *IEEE TEC,* Vol. EC-15, pp. 212, 220, April 1966.

C. L. Sheng and H. R. Hwa **5**, "Testing and Realization of Threshold Functions with *Don't Cares*", *IREE TEC,* Vol. EC-16, pp. 868-870, Dec. 1967.

C. L. Sheng **6**, "Satisfaction of Sensitivity Requirements by Threshold Logic Elements", *Journ. Franklin Inst.,* Vol. 286, pp. 1-15, July 1968.

R. C. Singleton, "A Test for Linear Separability as Applied to Self-Organizing Machines", *Self-Organizing Systems* 1962, pp. 503-524, Spartan Books, 1962.

T. A. Slivinski, *Partially Separable Functions,* Doctoral Dissertation in Computer Science, U. Illinois, June 1967.

D. R. Smith **1**, "Bounds on the Number of Threshold Functions", *IEEE TEC,* Vol. EC-15, pp. 368-369, June 1966.

D. R. Smith **2**, "A Partitioning Method for Combinational Synthesis", *IEEE TC,* Vol. C-17, pp. 72-75, Jan. 1968.

E. B. Stabler, "Threshold Gate Network Synthesis", *SCTLD,* pp. 5-11, Oct. 1965.

O. B. Stram **1**, "Arbitrary Boolean Functions of N Variables Realizable in Terms of Threshold Devices", *Proc. IRE,* Vol. 49, pp. 210-220, Jan. 1961.

O. B. Stram **2**, "The Profile Technique for the Design of Threshold Device Logic", *SCTLD,* pp. 47-54, Sept. 1961.

C. W. Sutherland, "Limitations of the AND-OR to Majority-Logic Conversation Technique", *Proc. IRE,* Vol. 49, p. 519, Feb. 1961.

Y. Tohma, "Decompositions of Logical Functions Using Majority Decision Elements", *IEEE TEC,* Vol. EC-13, pp. 696-705, Dec. 1964.

H. C. Torng, "An Approach for the Realization of Linearly-Separable Switching Functions", *IEEE TEC,* Vol. EC-15, pp. 14-20, Feb. 1966.

Teiichi Tsuboi, "A Logical Design of Circuits Representing Boolean Functions with Four or Less Variables by Means of Three-Input Parametrons and Five-Input Parametrons", *Inf. Proc. in Japan,* Vol. 4, pp. 20-40, 1964.

V. I. Varshavsky **1**, "Functional Possibilities and Synthesis of Threshold Elements", *Soviet Physics Doklady,* Vol. 6, No. 8, pp. 678-680, Feb. 1962.

V. I. Varshavsky **2**, "On the Complexity of Networks of Depth Two Formulated from Threshold Elements", *Soviet Physics Doklady,* Vol. 6, No. 8, pp. 683-685, Feb. 1962.

V. Varshavsky and B. Ovsievich **3**, "Networks Composed of Ternary Majority Elements", *IEEE TEC,* Vol. EC-14, pp. 730-733, Oct. 1965.

R. L. Wigington, "A New Concept in Computing", *Proc. IRE,* Vol. 47, pp. 516-523, April 1959.

D. A. Willis, "Minimum Weights for Threshold Switches", *Switching Theory in Space Technology,* pp. 91-108, Stanford Univ. Press, 1963.

R. O. Winder **1**, "Single-Stage Threshold Logic", *SCTLD,* Sept. 1961, and AIEE Conference Paper 60-1261, Oct. 1960.

R. O. Winder **2**, "More About Threshold Logic", *SCTLD,* pp. 55-64, Sept. 1961.

R. O. Winder **3**, *Threshold Logic,* Doctoral Dissertation, Math. Dept., Princeton University, May 1962.

R. O. Winder **4**, "Threshold Logic in Artificial Intelligence", *Artificial Intelligence,* IEEE Publication S-142, pp. 107-128, Jan. 1963.

R. O. Winder **5**, "Bounds on Threshold Gate Realizability", *IEEE TEC,* Vol. EC-12, pp. 561-564, Oct. 1963.

R. O. Winder **6**, "Network for Obtaining a Threshold Function Utilizing Majority Gates in an Array", U.S. Patent No. 2,162,774, Dec. 1964.

R. O. Winder **7**, "Properties of Threshold Functions", *IEEE TEC,* Vol. EC-14, pp. 252-254, April 1965.

R. O. Winder **8**, "Enumeration of Seven-Argument Threshold Functions", *IEEE TEC,* Vol. EC-14, pp. 315-325, June 1965.

R. O. Winder **9**, "Threshold Functions Through $n = 7$", Scientific Report No. 7 for AFCRL on Contract with RCA Laboratories, AF19(604)-8423, available through DDC, and the IEEE Computer Group Repository, Oct. 1964.

R. O. Winder **10**, Review of papers by J. E. Hopcroft and R. L. Mattson, and E. P. Stabler, *IEEE TEC,* Vol. EC-15, pp. 267-269, April 1966.

R. O. Winder **11**, "Partitions of n-Space by Hyperplanes", *SIAM Jour. Appl. Math.,* Vol. 14, No. 4, pp. 811-818, July 1966.

R. O. Winder **12**, "Review of T. S. Hu's book *Threshold Logic*", *IEEE TEC,* Vol. EC-15, R66-70, pp. 953-954, Dec. 1966.

R. O. Winder **13**, "Threshold Gate One-Out-of-N Register", RCA Technical Note 701, Jan. 1967.

R. O. Winder **14**, "The Status of Threshold Logic", 1st Annual Prince-

ton Conf. Information Sciences and Systems, pp. 59-67, Princ. Univ. N.J., March 1967.

R. O. Winder **15**, "Logic Network for Realizing Associative Logic Functions", U.S. Patent No. 3,308,285, March 1967.

R. O. Winder **16**, "Symmetry Types in Threshold Logic", *IEEE TC*, Vol. C-17, pp. 75-78, Jan. 1968.

R. O. Winder **17**, "Fundamentals of Threshold Logic", Scientific Rept. No. 1 for AFCRL(68-0066) on Contract No. F19628-68-0070, Jan. 1968. Also in *Applied Automata Theory*, Academic Press, 1969.

R. O. Winder **18**, "Threshold Logic will Cut Costs, Especially with Boost from LSI", *Electronics*, pp. 94-103, May 27, 1968.

R. O. Winder **19**, "Flip-Flop Employing Three Interconnected Majority-Minority Logic Gates", U.S. Patent No. 3,403,267, Sept. 1968.

R. O. Winder **20**, "Threshold Gate Approximations Based on Chow Parameters", to appear *IEEE TEC*.

R. O. Winder **21**, "An Evaluation of Heuristics for Threshold-Function Test-Synthesis", Sci. Rept. No. 4 for AFOSR under contract No. AF49(638)-1184, May 1968.

R. O. Winder **22**, "Threshold Logic Asymptotes", submitted to *IEEE TC*.

R. O. Winder **23**, "Chow Parameters in Threshold Logic", in preparation.

E. Wong and E. Eisenberg, "Iterative Synthesis of Threshold Functions", *J. Math Anal and Appl.* 11, pp. 226-235, 1965.

Paul E. Wood, "A Note on Threshold Device Error Analysis", *IEEE TEC*, Vol. EC-12, pp. 403-405, Aug. 1963.

S. Yajima and T. Ibaraki **1**, "A Lower Bound of the Number of Threshold Functions", *IEEE TEC*, Vol. EC-14, pp. 926-929, Dec. 1965.

S. Yajima and I. Ibaraki **2**, "A Theory of Completely Monotonic Functions and its Application to Threshold Logic", *IEEE TC*, Vol. C-17, pp. 214-229, March 1968.

S. Yajima and I. Ibaraki **3**, "Realization of Arbitrary Logic Functions by Completely Monotonic Functions and Its Applications to Threshold Logic", *IEEE TC*, Vol. C-17, pp. 338-351, April 1968.

S. S. Yau and D. L. Ostapko, "Realization of a Class of Switching Functions by Threshold Logic Networks", *IEEE TC*, Vol. C-17, pp. 391-399, April 1968.

Yao-Tung Yen, *Multi-Threshold Threshold Logic*, Doctoral Dissertation, E.E. Dept., U. Illinois, Aug. 1966.

E. Iu Zakharova, "The Synthesis of Networks Containing Threshold Elements", *Problemy Kibernetiki* No. 9, pp. 317-319, Jan. 1963 (abstract: *Automation Expr.*, Vol. 6, No. 3, pp. 39, 1963).

A BROAD-BAND, HIGH-GAIN, L-BAND POWER-AMPLIFIER MODULE

By
R. L. Bailey and J. R. Jasinski

RCA Electronic Components
Lancaster, Pa.

Introduction

Summary—Sophisticated radar systems, such as phased arrays have created a need for rf power amplifiers that have large bandwidths as well as excellent phase stability and uniformity of characteristics. This paper describes the unique design and fabrication of a developmental six-stage, L-band amplifier module that fulfills these requirements. It provides a peak power of 5 kilowatts at 1300 MHz with an instantaneous electronic bandwidth of 10% measured at 1-db points. Variations of this module for other applications requiring small size and high gain–bandwidth product are also discussed.

AMPLIFIERS utilizing grid-controlled tubes have been operated successfully in phased-array radars for a number of years; it is only recently, however, that their full capabilities in broad-band high-gain applications have been demonstrated. The development of the amplifier module discussed here* substantially advances the state-of-the-art in this area. This compact, wide-band, pulsed amplifier module uses gridded electron tubes and is designed for operation at a center frequency of 1300 MHz with an instantaneous electronic bandwidth of 10% measured at the 1-dB points. Performance objectives included achievement of a peak output power of 5 kilowatts and an overall gain of 45 dB with a minimum number of stages. The amplifier module was limited to 24 inches in length and 4.5×4.5 inches in cross section.

For this particular phased-array application, each amplifier module was required to drive an individual radiating element. For proper

* The development of the gridded-tube L-band power amplifier module was supported by U.S. Army Electronics Command, under Contract DA36-039-AMC-03203(E).

antenna spacing, this modular approach requires that the amplifier not exceed one half-wavelength in cross section. The degree of phase variation from input to output as a function of drive level, frequency, and supply-voltage variation was required to be small to minimize the cost of auxiliary operating equipment.

Conventional Amplifiers

Analysis of the above specifications indicated that conventional cascading techniques would not yield the desired results, particularly if the overall size and gain–bandwidth requirements were to be achieved. Conventional L-band (390 to 1550 MHz) gridded power-tube amplifiers consist of tuned input and output cavities or stripline resonators in conjunction with the appropriate bypass circuits. A typical 5-kilowatt unit may be up to 7 inches in diameter and 12 to 15 inches in length. These amplifiers are normally single-tuned and yield characteristic gains of 10 to 15 dB. Gain is increased when two or more independent stages are cascaded with interconnecting coaxial cables. An impedance-matching transformer at the load end of each interconnecting cable permits transmission of interstage power at the cable surge impedance (usually 50 ohms) and, thus, makes interstage performance independent of cable length. Interstage loading and tuning adjustments are made with an impedance-matching transformer at the generator end of each cable. The overall gain of the amplifier chain increases with the addition of each new single-tuned stage, while system bandwidth continually decreases; desired gain–bandwidth characteristics can be achieved by changing the degree of coupling between stages and/or by use of stagger tuning.

Figure 1 shows a single-tuned, single-stage amplifier, (Dev. No. Y1015). This amplifier uses a 7651 tube, delivers a minimum peak output power of 6 kilowatts, and can be mechanically tuned across the 950-to-1225-MHz band with an average instantaneous bandwidth of 3%. The 7651 is capable of 39 kilowatts of peak output power at 1200 MHz when it operates at maximum ratings in a narrow-band circuit (less than 1% instantaneous bandwidth). The threaded coaxial fittings shown in Figure 1 permit connection of standard 50-ohm rf drive and rf output cables to the cavity; however, because the cables join the coaxial resonators at right angles to the main cavity axis, they add considerably to the cross-sectional dimension. This cavity measures about 6 inches in diameter at its major cross section. When the cavity is tuned to its lowest operating frequency of 950 MHz, the input tuning

rods extend 2 inches below the cavity and produce an overall length of 14½ inches.

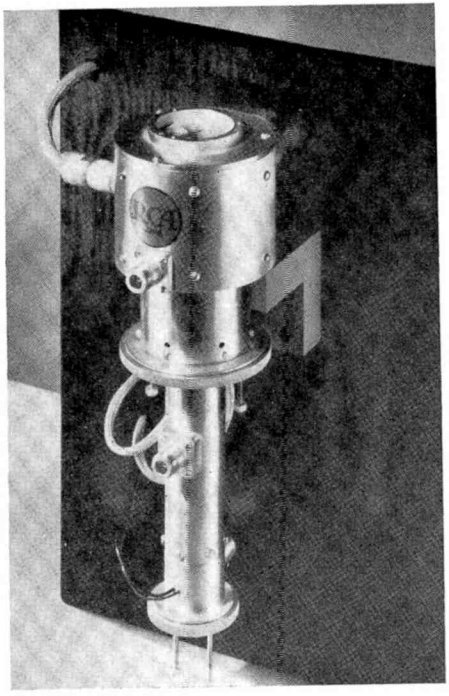

Fig. 1—Developmental type Y1015 single-tuned, single-stage amplifier.

This type of amplifier is generally not suitable for use in multistage, broad-band chains, because (1) the necessity for impedance transformations to the 50-ohm interconnecting-cable surge impedance severely limits gain–bandwidth product, (2) multituned circuits cannot be utilized to best advantage, and (3) the size of a cascaded amplifier chain exceeds the requirements of many applications.

New Cascading Technique

Figure 2 shows the developmental "totem-pole" amplifier (Dev. No. Y1043). This amplifier incorporates techniques to enhance the inherent gain–bandwidth capabilities of gridded tubes and, at the same time, achieves a considerable size reduction over classical cascaded amplifier

chains. The amplifier is shown with the external housing removed to illustrate the end-to-end configuration as viewed from the input end. In this system, six stages of gridded power tubes provide a peak output power of 5 kilowatts at 1300 MHz with a gain of 53 dB. The system uses two commercial 7768 planar triodes (small tubes) and four cermolox tetrodes (two 8226's and two 7651's), samples of which are shown

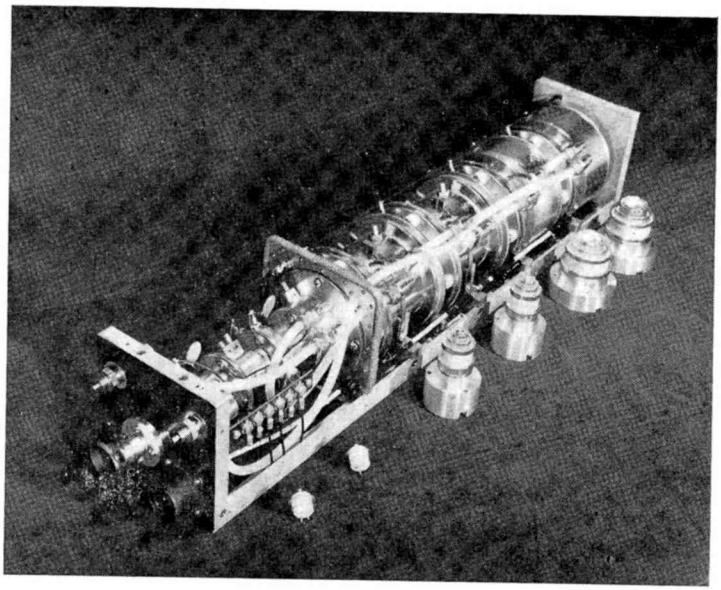

Fig. 2—Developmental type Y1043 amplifier module with cover removed to show the end-to-end configuration.

adjacent to the module. The cermolox tetrodes used in this amplifier differ from other tubes of the same generic type in that they use integral conduction-cooling aluminum jackets instead of air-cooled radiators. rf drive, liquid coolant (high purity at 0.5 gallon per minute), and all operating voltages are applied through the five connectors at the input bulkhead. Output power of the amplifier is extracted through a coaxial connector at the opposite end. A 3-kilovolt dc power supply, the highest voltage required for operation, provides plate voltage for the four tetrodes. The tetrodes are modulated by a 1-kilovolt pulse applied to the screen grids. The plate voltage for the 7768 planar triodes is provided by a 300-volt dc supply; the grids are modulated by a small 6-volt bias pulser. All voltages are applied through bus lines located in the corners of the module. A few of these bus lines are visible in Fig-

ure 2. The module is packaged in an aluminum container measuring 4⅜ by 4⅜ by 23 inches. This satisfies the required dimensions for use in a 1300-MHz phased-array radar.

Figure 3 shows the instantaneous bandwidth characteristic of the module for an applied peak drive power of 25 milliwatts. The module

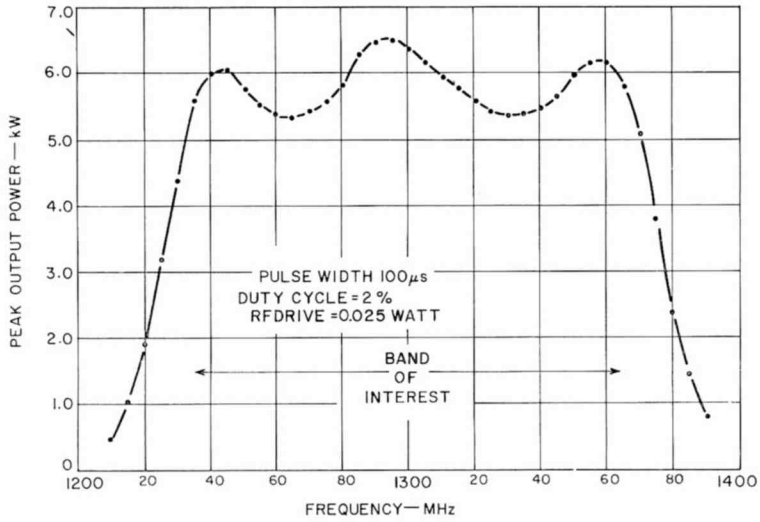

Fig. 3—Typical output response of developmental type Y1043.

measured produced a nominal peak output power of 5.75 kilowatts at 2% duty cycle, with a ripple factor of less than 1 dB and an instantaneous bandwidth of 10.5%. Figure 4 shows the final amplifier package. The absence of connectors on the large surfaces allows many such modules to be inserted side by side, honeycomb fashion, into an array panel to form a multimegawatt phase-steerable beam. Figure 5 shows a cross-sectional view of the amplifier. No conventional, lengthy interstage circuits are used in the amplifier chain; instead, the stages are stacked in totem-pole fashion, and each of the stages is directly connected to the following stage by a full-electrical-wavelength circuit. Minimum system dimensions are achieved with this coaxial, in-line configuration. A considerable portion of each interstage circuit, especially in the tetrode stages, is contained within the internal output and succeeding input sections of the tubes; as a result, the amplifier stages have an average length of only 4 inches. Two over-coupling elements are contained in the interstage circuit external to the tube (about one-half wavelength) to provide optimum gain–bandwidth in a minimum

amount of space. In each stage, these elements consist of shunt inductance and series capacitance. The inductor is composed of several ¼-inch-diameter spokes shunted across the cavity. In each tetrode stage, two of the spokes are hollow to allow anode coolant to flow into and through the anode seat, which is a portion of the coaxial center conductor. The series over-coupling capacitor is formed by a break

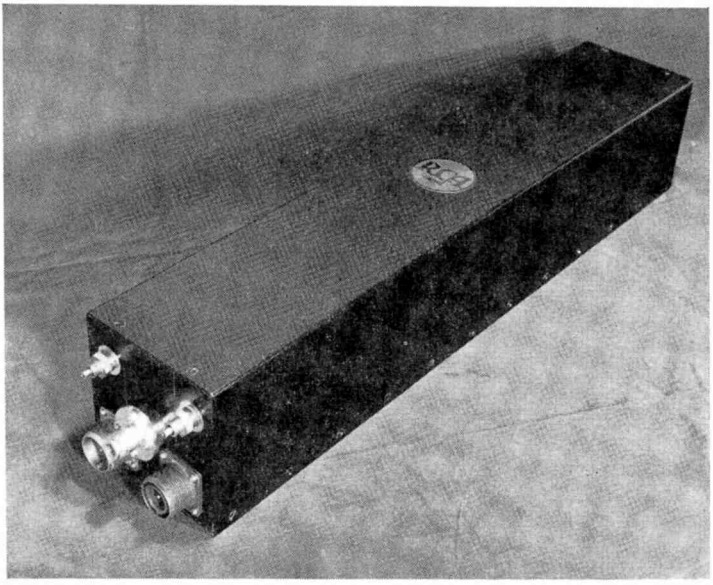

Fig. 4—Developmental type Y1043 shown fully housed to illustrate the modular concept.

in the center conductor of the interstage coaxial line. This capacitor also isolates the plate voltage of a particular stage from the cathode potential of the driven stage. The module contains mica rf radial bypass capacitors that provide dc isolation for the various tube elements.

Basic Design Techniques

Over-Coupled RF Circuits

The rf circuits used throughout the module are over-coupled resonant coaxial cavities that are aligned to produce triple-tuned, maximally flat responses. Each stage in the chain has the same response. This approach provided full freedom to change the number of stages at any time during the development of the module. The alternative

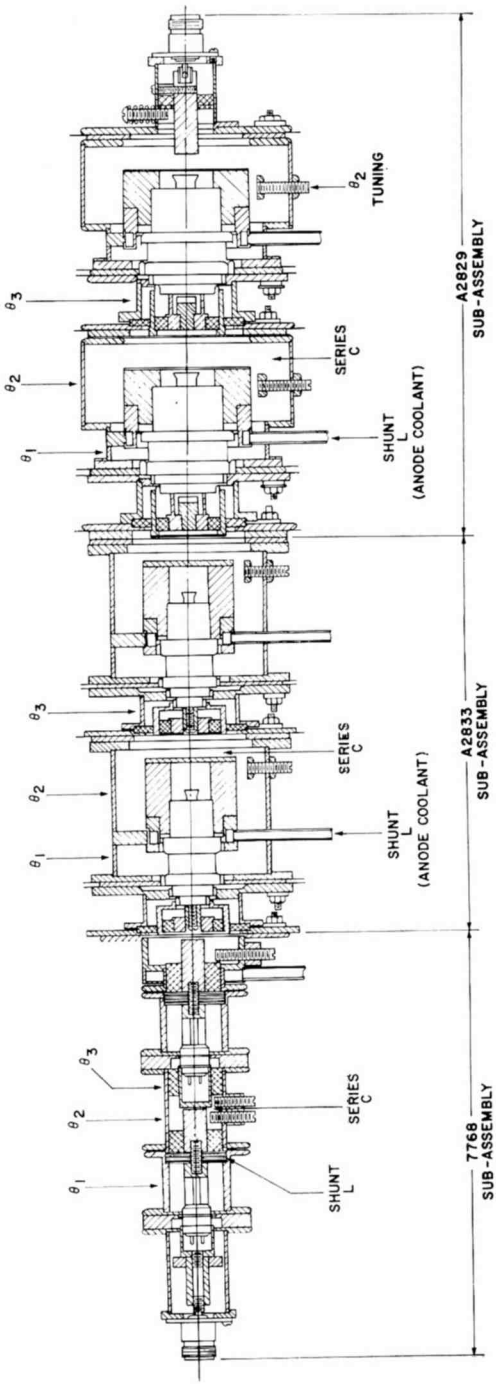

Fig. 5—Cross section of module.

approach, stagger tuning of individual stages, would restrict this freedom.

The over-coupled circuits have an inherently greater gain–bandwidth product than does the simple single-tuned circuit; the improvement is a function of the number of circuits coupled together. A useful figure of merit for broad-band circuits is the resistance-times-bandwidth ($R \times BW$) product the circuit presents to the fundamental component of the tube beam current. A circuit can be evaluated on the basis of the ratio of the actual ($R \times BW$) product to the maximum ($R \times BW$) product of a simple parallel resonant circuit having the same amplifier output capacitance. A valid comparison, however, must include a specification of the shape of the actual response. For this discussion, it is assumed that the response is maximally flat and, further, that the ($R \times BW$) value is the product of resistance and bandwidth referred to the points 1/6 dB down from the peak values of R. (Because the module has six stages, this reference provides the overall ($R \times BW$) product at the 1-dB points.) For the single-tuned circuit, the ($R \times BW$) product is the product of the half-power resistance and the half-power bandwidth.

On this basis, an optimized double-tuned circuit can provide an ($R \times BW$) product as great as 1.22 times that of a single-tuned circuit. A triple-tuned circuit can provide up to 1.66 times as much ($R \times BW$) product. The limit approaches π as the number of tuned circuits is increased. (These numbers were calculated from tabulated data for ladder networks by Weinberg;[1] the extension to high-frequency bandpass circuits was made by Green.[2]) Because the circuit complexity increases directly with the number of coupled circuits, a triple-tuned circuit provides a good compromise between ($R \times BW$) improvement and circuit complexity.

The triple-tuned coaxial circuits employed in the developmental L-band module are very similar conceptually to the double-tuned circuits employed in RCA superpower coaxitrons.[3-6]

---

[1] L. Weinberg, "Additional Tables for Design of Optimum Ladder Net-Works," *Jour. Frank. Inst.*, Vol. 264, p. 7, July 1957.

[2] E. Green, *Amplitude-Frequency Characteristics of Ladder Networks*, Marconi's Wireless Telegraph Co., Ltd., Chelmsford, England, 1954.

[3] W. N. Parker, "The Coaxitron Tube," *RCA Pioneer*, Feb. 1961.

[4] "The Development of an Experimental Model of a High-Power, Broadband Coaxitron Amplifier," RADC-TR-60-94, June 1960.

[5] "The Continuation of the Development of an Experimental Model of a High-Power Broadband Coaxitron Amplifier," RADC-TDR-61-315, Nov. 1961.

[6] K. F. Molz, "Selecting Tubes and Receivers for Large Phased-Arrays," *Microwaves*, p. 18, March 1964.

Simplified Overcoupled Circuit

Figure 6(a) shows a simplified, over-coupled, triple-tuned, two-wire transmission-line equivalent circuit consisting of three approximately resonant quarter-wave line lengths and two over-coupling elements, L and C. The frequency responses of this type of circuit is usually presented as a resistance plot on rectangular coordinates. In

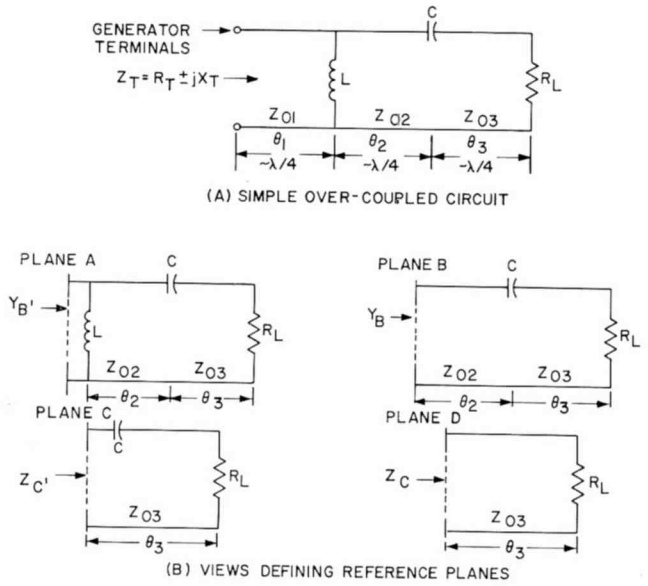

Fig. 6—(a) A simple over-coupled circuit and (b) views defining reference planes.

this case, the curve would be the result of nine interrelated parameters, and random adjustment of these parameters to find an acceptable response would be very tedious and time consuming. An extremely useful guide for converging on the correct response is the presentation of impedance information on a Smith chart. Smith plots of impedance (Z) as a function of frequency at key reference planes of an over-coupled circuit produce certain characteristic shapes. From observation of these curves, it is possible to obtain a set of parameters that establishes a starting point for the investigation, to determine which element is degrading the response, and to determine which element can be used to compensate for degrading elements that cannot be varied.

Figure 6(b) shows the key reference planes for the simple circuit in Figure 6(a), and Figures 7 and 8 show the Smith plots for these planes. A triple-peaked curve showing the variation in total resistance

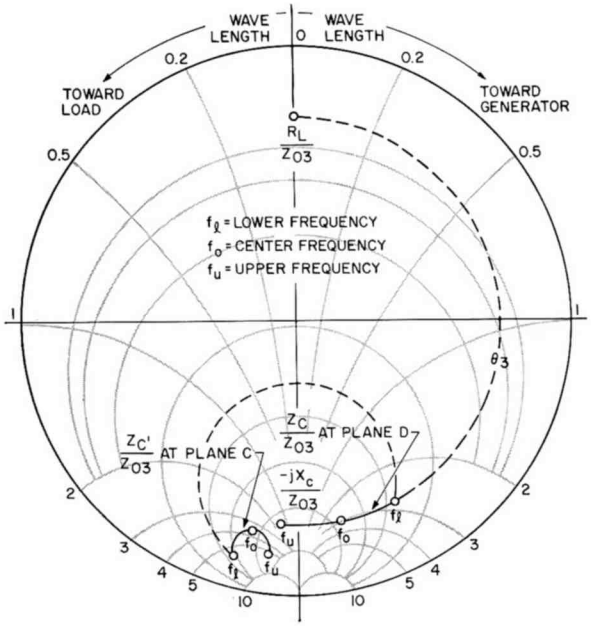

Fig. 7—Smith impedance plot.

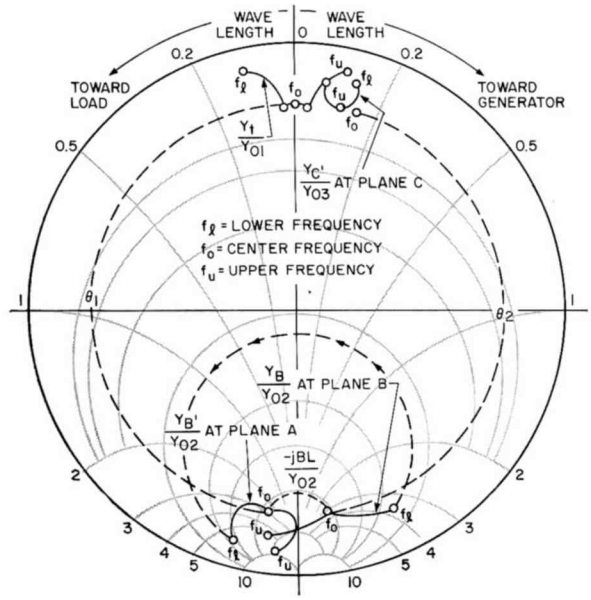

Fig. 8—Smith admittance plot.

R_T with frequency is needed. R_T, the real part of the total impedance Z_T, determines the power extracted from the beam current of the power tubes. For the series-resistance curve to be triple peaked, the Smith plot of admittance variation with frequency at the generator terminals must contain two cusps. If the resistance curve has a high enough ripple, the cusps are actually loops; if the resistance curve is maximally flat, the cusps are barely discernible. A typical two-cusp admittance response for the reference plane at the generator terminals (Y_T/Y_{01}) is shown in Figure 8. When this plot is transformed to impedance, it produces the desired triple-peaked series-resistance plot containing only a small amount of ripple.

Figure 7 shows that the reactive part of Z_T is zero at only one of the resistive peaks. Thus, the peaks do not coincide with resonances in the normal sense, where resonance is defined as the frequency at which the reactive component of the impedance vanishes. It is more meaningful to consider these resistance peaks as the result of interacting modes, or resonances, that the coupling elements have grouped together in the frequency spectrum. These coupled modes, pairs of which are represented by cusps on the Smith chart, are said to be resonant when the cusp lies on the resistive plane of the chart. If a resistance plot has m cusps, oriented symmetrically about the resistive plane, the response has $m + 1$ peaks and m valleys. If the cusps lie very far from a resistive plane, the resistance plot has only a single peak. The advantage of an impedance plot as compared to a resistance plot is that the Smith plot reveals potential coupled-mode resonances over an extremely wide range of circuit adjustment. The impedance plot also reveals the element responsible for mistuning, and furnishes a means for calculating the necessary amount of correction to be applied to that element. In the following paragraphs, the overall impedance transformation characteristic of the circuit in Figure 6(a) is analyzed as a function of frequency. The analysis starts with the load R_L and proceeds to the generator terminals. The effects of each of the line lengths and coupling elements at each of the key planes of Figure 6(b) are investigated. As shown in Figure 6(b), these key-plane plots are taken from the input terminals looking toward the load.

In Figure 7, the normalized load resistance R_L/Z_{03} is chosen as $0.12 + j0$ ohm, because this value closely approximates the drive-point impedance of the tetrode types used throughout the module. Other values, including those with a large imaginary component, may be used for this example; however, line length θ_3 must then be adjusted so that f_o occurs at the point of tangency.

In the Smith impedance plot of Figure 7, the normalized impedance

R_L/Z_{03} is purely resistive; therefore, it appears as a single point for each of the band-pass frequencies f_l, f_o, and f_u. Movement from R_L/Z_{03} through line length θ_3 produces the Z_C/Z_{03} plot of plane D, which shows an impedance-spreading effect that results from frequency with the addition of this line length. Frequency on this plot increases uniformily in a clockwise direction because line length θ_3 becomes increasingly longer with increasing frequency. The addition of the over-coupling capacitor C, represented by $-jX_C/Z_{03}$ produces the key plot Z_C/Z_{03} of plane C. Frequency inversion has occurred in this plot, i.e., frequency increases in a counter-clockwise direction with respect to the center of the Smith chart. For the impedance plot to be symmetrical about f_o at plane C, line length θ_3 must be adjusted so that the position of f_o is nearly tangent to a reactance circle at plane D.

The impedance plot of Figure 7 at plane C is shown shifted 180° as an admittance plot Y_C/Y_{03} in Figure 8. Increasing frequency is still counter-clockwise with respect to the center of the Smith chart. However, at the admittance plane B, (Y_B/Y_{02}) frequency again increases in a clockwise direction as a result of the addition of line length θ_2. The cusp at f_o is produced by the over-coupling capacitor C, which was previously added at plane C. Line length θ_2 is adjusted so that f_o is again nearly tangent to a reactance circle. The addition of the shunt coupling inductor L, represented by the normalized susceptance $-jB_L/Y_{02}$, produces the admittance plot (Y_B/Y_{02}) at plane A. The plot is symmetrical about f_o as a result of the proper adjustment of length θ_2. In this case, frequency inversion produces a kidney-bean-shaped response. The addition of line length θ_1 changes the kidney-bean response of plane A to the desired two-cusp admittance response at the generator terminals (Y_T/Y_{01}). Line length θ_1 is correctly adjusted when f_o occurs on the resistive plane with the cusps positioned symmetrically to either side.

This circuit analysis serves as a model for the slightly more complex triple-tuned circuits that were analyzed by computer and found satisfactory for use in the module, and shows generally how any number of peaks in the resistance plot can be produced at the generator terminals. The shape and location of the various Smith admittance–impedance plots are extremely helpful in obtaining convergence of parameter values for the desired multituned response. For a double-tuned circuit having two peaks, one over-coupling element and two approximately resonant lines are required. For a triple-tuned circuit having three peaks, two over-coupling elements and three resonant lines are needed. For an n-tuned circuit having n peaks, $n-1$ over-coupling elements and n resonant lines are necessary. The over-coupling

elements can be either series capacitors at high-rf-voltage planes, shunt inductors at low-rf-voltage planes, or any combination of the two. Shunt capacitance and series inductance, at the proper points, also achieve the same type of over-coupling, but are not nearly as practical from a mechanical standpoint. The length of the approximately resonant lines can be any multiple of a quarter wavelength, but should be kept as short as possible to minimize stored energy and thus optimize the $(R \times BW)$ product.

Practical Circuit Considerations

The simple, triple-tuned, over-coupled circuit shown in Figure 6 can be easily refined to serve either as a triple-tuned output circuit in which a tube is coupled to a resistive load, or as an interstage circuit in which one tube is coupled to or drives another. In the latter case, the load is not purely resistive, but can be considered as the dynamic impedance of the driven tube as measured at the input terminals. This impedance is not actually lumped at these terminals, but instead is the result of the lumped impedance at the grid–cathode active area transformed through an approximate quarter wavelength of line to the tube terminals. If this impedance is measured as a function of frequency, it can be considered, for calculation purposes, to be concentrated at the tube terminals.

The module described in this paper uses circuits that are basically the same as that shown in Figure 6. The lines θ_1, θ_2, and θ_3 are foreshortened quarter-wavelength resonators. Most of θ_1 is included within the vacuum envelope of the tube; thus, the shunt inductance L is positioned very close to the output terminals. This inductance is provided by spokes across the coaxial line, and the series capacitance C is easily obtained by a gap left in the center conductor.

Tube Selection and Computer Calculations

It was previously stated that the maximum $(R \times BW)$ product that can be achieved with a triple-tuned circuit having a given amplifier output capacitance is 1.66 times greater than one obtained with a simple parallel resonant circuit having the same amplifier output capacitance. Because the $(R \times BW)$ product for the simple parallel resonant circuit is easily calculated for a hypothetical lumped-constant circuit, it is possible to estimate the performance of any tube used with triple-tuned circuits. Tubes for use in the amplifier module were selected on this basis. For interstage analysis, the dynamic drive point impedance was measured at the input terminals of each tube at the

required drive power. A modified version of the 7651 Cermolox tetrode was chosen for the final stage; an equivalent circuit for this stage is shown in Figure 9(a). The impedance and admittance plots for such a circuit can be obtained from straightforward but tedious calculations. A program was written for the RCA-301 digital computer to reduce the calculation time. The program included provision for 15 different sections of transmission line and made allowances for lumped reactive elements at various line junctions. The output data provided the impedance as a function of frequency at key line junctions corresponding to the reference planes previously discussed. The computer program was sufficient for analysis of all interstage circuits and for the final output circuit.

The resistance and impedance plots in Figures 9(b) and (c) are comprehensive presentations of data obtained from computer analysis of the conceptual design of the final output stage. The particular values listed for the circuit parameters produced the Smith-plot variation in impedance (Z_T/Z_0) as a function of frequency, as shown in Figure 9(c). The impedance response shown contains no cusps within the pass band, but, instead, follows a constant R locus; this behavior indicates a maximally flat condition. The resistive component of Z_T is plotted in Figure 9(b). Obviously, the first set of parameters used in the computer calculation did not produce this optimized response since the values of the parameters were chosen primarily by educated guesses. However, with the Smith plots used as guides, successive computed sets of data converged rapidly on the correct values.

During the series of computer calculations made to determine the specific set of parameter values for optimum response, much valuable insight was gained on the quantitative effects of varying each parameter. This information was later found useful for circuit alignment. The computer results were used to calculate projected operating conditions for each stage. In practice, it is necessary to derate the computed value of R_T by approximately a factor of 30% to compensate for the practical limits on circuit efficiency and for the smearing of the rf current pulse because of transit-time effects.

Cold-Probe Verification of Amplifier Design

Cold-probe models were fabricated and analyzed to verify predictions based on computer calculations. These models consisted of cavities that included provisions for variation of every parameter external to the tube; they used dummy tubes consisting of only screen-grid and anode assemblies. The output gap of the dummy tube was energized with approximately 1 watt of frequency-swept power, and a crystal

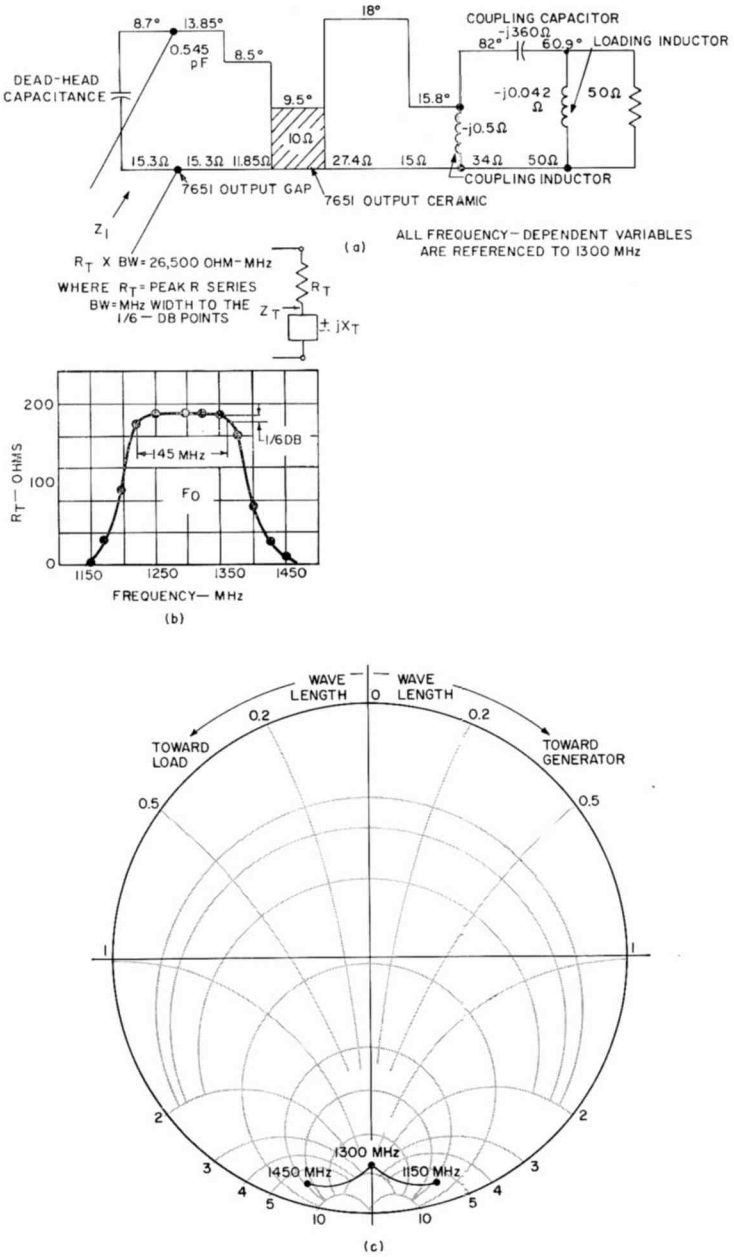

Fig. 9—(a) An equivalent circuit of triple-tuned final output; (b) resistance as a function of frequency for triple-tuned final output; and (c) Smith chart plot of impedance as a function of frequency for triple-tuned final output.

detector was used to monitor the transmission response of the cavity into a 50-ohm load. The output of the crystal detector was then displayed on an oscilloscope. While the instantaneous display was monitored, variation of parameters rapidly produced a flat response with the desired center frequency and bandwidth. Results obtained with models of the final output and the interstage circuits verified that the computer program accurately simulated the rf circuitry.

Amplifier Assembly and Alignment

The final design and fabrication of all the amplifier stages were based completely on computer and cold-probe results. As shown in Figure 5, the module consists of three basic subassemblies, each containing two stages of amplification. Each tube was extensively tested as a single-stage and then in a two-stage broad-band amplifier to confirm successful operation of each tube type at the required power level. The input to the first stage is not triple-tuned, but uses a shunt capacitive matching slug to produce a single-tuned transformation to 50 ohms. Because this transformation ratio is relatively low, the input VSWR is better than 1.5:1 (4% reflected power) across the 1200-to-1400-MHz band.

Final assembly and alignment of the module proceeded with one stage at a time, starting with the low-power stages. With this method, two stages were operated into a passive load, then three stages, and finally up to six stages, so that alignment of the most recently added stage could be accomplished at the correct drive level. The dc grid-current response of the driven stage served as an excellent indicator of interstage performance. The use of swept-frequency drive at all times provided comparative ease of circuit adjustment.

Figure 10 shows a series of response curves that illustrate the effect of the five basic tuning parameters, as discussed for the simple circuit of Figure 6. The parameters can be related to the actual circuit by reference to the cross section of the module shown in Figure 5. The parameters are shown for only one stage of each particular subassembly.

Figure 10(a) shows a typical optimized response. This curve represents a triple-peaked response in which the three peaks are not readily apparent because of the maximally flat condition. Ideally, all stages of the module should possess this characteristic.

If line θ_1 is changed (by change of the axial position of the shunt inductor L), the frequency spectrum of the response is shifted up or down correspondingly, as shown in Figure 9(b). Because of the mutual interaction between the various parameters, symmetrical response is

maintained with the change of more than one parameter at a time. In this case, parameters θ_2 and θ_3 were varied.

The effect of variation of θ_2 is shown in Figure 10(c). The change in θ_2 seems to "rock" the response about the center mode. No other parameter was varied for this particular figure. Coarse adjustment of θ_2 is obtained by changes in the number of caps or end plates on the

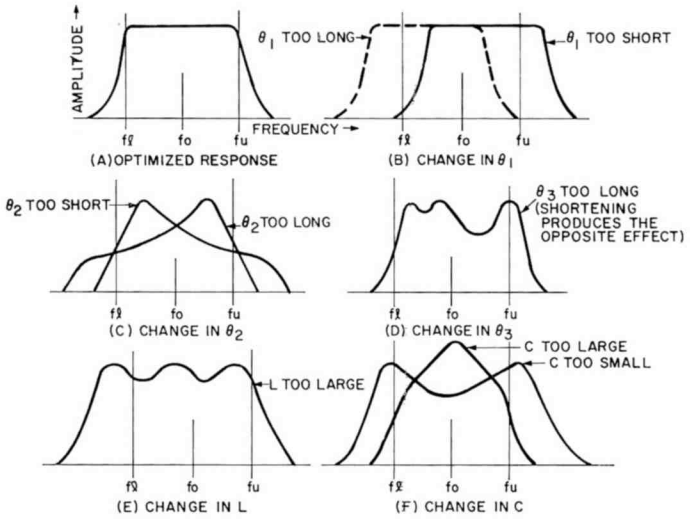

Fig. 10—Curves showing the effects of the five basic tuning parameters.

aluminum jacket of the tube. Fine adjustment of θ_2 is performed by means of a tuning screw that provides lumped capacitance for electric variation of this line length.

Figure 10(d) illustrates the effect of a change in θ_3. This parameter primarily varies the frequency of the center mode and has only secondary effects on the upper and lower modes. The tetrode stages contain a ceramic "window" at the high-voltage plane of θ_3 that provides conduction cooling of the tube heater terminals. Consequently, a considerable amount of electrical foreshortening occurs and there is insufficient space for the use of a fine-tuning screw adjustment. In this case, the electrical length of θ_3 is adjusted when the number of caps or end plates on the end of the cathode line is varied. In the triode stages, θ_3 is not foreshortened as much by the electrical structure of the tubes; therefore, a fine-tuning screw may be used for adjustment.

The effect of a change in value of the shunt inductor L is shown in

Figure 10(e). The value of L is determined by the total number and the angular position of the inductive posts shunted across the cavity at a given axial plane. Either θ_1 or θ_2 must be adjusted to maintain a symmetrical response. The magnitude of inductance controls the circuit bandwidth, i.e., the position of the low-frequency mode with respect to the high-frequency mode. The axial position of the inductor determines the position of the high-frequency mode.

Primary control over the valley in the response is maintained by the value of the coupling capacitor C, as shown in Figure 10(f). The series capacitor gap is physically varied when the spacers in the outer conductor of the coaxial line are changed, as indicated in Figure 5(a).

By the orderly adjustment of these five tuning parameters, the six stages of the module can be optimized progressively to produce the typical triple-tuned output response shown in Figure 3.

Phase Measurements

The phase characteristics of the module are of major interest for use in phased-array systems. Two independent measurements of these characteristics were made with nearly identical results: one at MIT Lincoln Laboratories and the other at RCA, Lancaster. These measurements were made with a differential phase bridge that had a resolution capability better than three degrees. The measured phase-sensitivity data are presented in Figure 11. As expected of any device that utilizes gridded power tubes, phase sensitivity of the module is extremely low. The most sensitive operating parameter, the tetrode screen-grid voltage, produced only an approximate one-degree shift per 1% change in voltage. Because of this high degree of phase stability, power-supply costs are reduced since voltage-regulation requirements are minimized. As a direct comparison, a velocity-modulated device, such as a traveling-wave tube, typically exhibits a twenty-degree phase change for 1% change in anode voltage,[6] so that a much better voltage regulation is required for the same degree of phase stability. Variations of dc voltages, the filament voltage, and the drive power produced negligible phase changes throughout the module.

Phase characteristics as a function of frequency, shown in Figure 11, indicate that extreme linearity (± 2 degrees) exists over 75% of the pass band with no significant irregularities in the curve.

Extended Applications

Since the successful development of the prototype Y1043 module described here, customer interest has warranted the establishment of

a manufacturing facility for fabrication of such modules on a continuing basis. Although the module was primarily designed for phased-array applications, present interest includes other areas where small size and high gain–bandwidth requirements are also important. The Y1043 module and variations of it have either been proposed for or are presently being used in rf-pulse-coded systems for command and guidance, phase-stable broad-band drivers for higher-power radar systems, and multichannel airborne nagivational beacons.

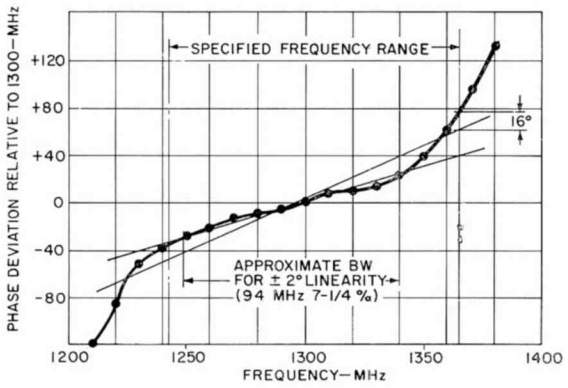

Fig. 11—Measured shift in phase with frequency of the module.

As an illustration, the Dev. No. Y1048C amplifier is shown in Figure 12. The module consists of 5 cascaded tetrode stages. It is designed to operate at a center frequency of 1375 MHz with an instantaneous 1-dB bandwidth of 5%. The peak output power is 10 kilowatts with a gain of 47 dB. Because this module is not intended for phased-array applications, the cross-sectional dimensions were increased to 5 by 6 inches; the length is 22 inches. The increased cross-sectional area was required to permit the module and its auxiliary components to meet shock and vibration specifications.

One- and two-kilowatt versions of the Y1043 have also been made. The one-kilowatt peak-power module (the Y1057) has a center frequency of 1270 MHz with an instantaneous 1-dB bandwidth of 70 MHz and a gain of 37 dB. The two-kilowatt peak power version (the Y1049) has a center frequency of 1088 MHz with an instantaneous 1-dB bandwidth of 125 MHz (11.5 per cent), and a gain of 27 dB. Both modules are capable of operating at 5% duty cycle and each contains a single tube type; the one-kilowatt module has four stages and the two-kilowatt module only three. Designs have been developed for 50-kilowatt and

100-kilowatt modules to cover the 750-to-850-MHz and the 405-to-450-MHz bands, respectively.

All of the above circuits use the same triple-tuned, coaxial, totem-pole circuit concepts described for the Y1043 module. For a particular tube type, the high-frequency limit is determined by the internal screen-grid–anode "strap resonance" of the tube, i.e., the frequency at which the shunt over-coupling inductor is positioned just at the tube terminals. Circuit attempts at frequencies above strap resonance

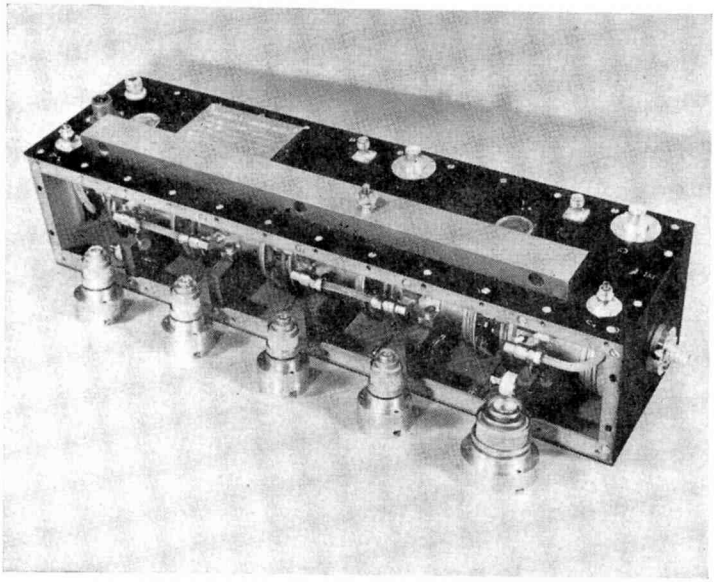

Fig. 12—Developmental type Y1048C five stage, ruggedized module shown with side cover removed.

would produce a loss of this shunt-inductor "tuning handle". A tube is ideally circuited, for a given frequency, when the shunt over-coupling inductor is very close to the output terminals of the tube. This condition produces interstage circuits of the shortest possible length. The upper frequency limits of the tetrodes used in the Y1043 are approximately 1410 MHz and 1600 MHz. Thus, the 1235-to-1365-MHz operating spectrum for the Y1043 permits use of the ideal circuit configuration. Because of their greater power capability, the larger tube types have inherently lower strap-resonant frequencies. The upper-frequency limit for the 100-kilowatt module is expected to be approximately 600 MHz, and for the 50-kilowatt module about 890 MHz.

Cross-sectional size and overall length of the module are the pri-

mary determinants of the lowest practical operating frequency. Lower frequencies require an increase in cross section for maintenance of effective rf radial bypassing of the mica dc blockers. A typical 800-MHz module would have to be increased to 8×8 inches in cross section to present blocker radiation. In addition, water-cooling requirements would have to be considered for lower-frequency operation. As the operational frequency is decreased, the shunt inductors move further from the tube and anode seat; therefore, a more complex mechanical configuration is required for the cooling.

Conclusions

High-gain, broad-band amplifiers using triple-tuned coaxial resonators in combination with gridded power tubes can be arranged in a very compact circuit. The design and analysis of these complex circuits are facilitated by the use of a digital computer. Several stages of power tubes with maximally flat responses can be cascaded or stacked totem-pole fashion to form a compact, high-gain amplifier module. Recent circuit refinements have produced overall gains of 60 dB, corresponding to 2.6 dB per linear inch of module.

Measurements on a six-stage module have proven that the excellent phase stability of gridded power tubes is preserved through as many as six stages of amplification. The phase-versus-frequency characteristics of the module are such that phase linearity compensation can be accomplished easily.

Acknowledgments

The authors thank W. P. Bennett, F. W. Peterson, M. V. Hoover, and L. F. Heckman for their important contributions to the design and testing of the modules described; H. Kaunzinger and G. Fincke of USAEL, the technical monitors of the contract work, for their many helpful suggestions; and L. Cartledge and others of MIT Lincoln Laboratories for measurements of the phase characteristics of the module.

CLOSE-CONFINEMENT GALLIUM ARSENIDE PN JUNCTION LASERS WITH REDUCED OPTICAL LOSS AT ROOM TEMPERATURE

By
H. Kressel and H. Nelson

RCA Laboratories
Princeton, N. J.

Summary The most efficient room-temperature GaAs injection lasers ever reported have been made with a new technique. Threshold current densities of 10,800 A/cm^2 have been obtained. These values are a factor of two lower then those previously reported for lasers of equal dimensions. Differential quantum efficiency values as high as 39% have been obtained with diodes 13 mils long. The improvements in laser performance is attributed to two factors: (1) improved optical confinement resulting from controlled variation of the bandgap energy in the vicinity of the p-n junction and (2) reduced absorption coefficient in the material adjoining the active region.

Introduction

THIS PAPER describes a modification of the conventional GaAs injection laser that gives greatly improved performance at room temperature. The improvement is due to close confinement of the optical flux by an internal optical structure produced by modifications of the standard liquid-phase epitaxy. Improvements in room-temperature injection lasers are indicated by the reduction in threshold current density J_{th} and by the increase in the differential external quantum efficiency η_{ext}. As a result, devices with much higher power efficiency are obtained.

The performance of the new lasers is illustrated by a threshold at 300°K of 10,800 A/cm^2 (30-mil cavity length)* with an external differential quantum efficiency of 25%. With a cavity 15 mils long, 13,000 A/cm^2 has been obtained. The lowest threshold reported to date in the open literature,[1] 26,000 A/cm^2 (15-mil length), is so much

[1] M. H. Pilkuhn and H. Rupprecht, "Optical and Electrical Properties of Epitaxial and Diffused GaAs Injection Lasers," *Jour. Appl. Phys.*, Vol. 38, p. 5, Jan. 1967.

* **Note added in proof:** A threshold current density of 8,000 A/cm^2 at room temperature has recently been obtained with a diode 12 mils long provided with a reflective film on one facet (R. Gill and A. Zouridies, RCA Electronic Components, Somerville, N. J., private communication).

higher than the present results that the new device must be considered as a significant step in the technology of injection lasers. In addition, the basic structure of the close-confinement laser diode can be adapted to other material systems and can be fabricated by epitaxial growth from either the liquid or vapor phases.

Fabrication and Results

A typical laser diode, shown in Figure 1(a), consists of three distinct regions. Region (1) is uncompensated p+ with bandgap energy E'_g. Region (2) is compensated p-type with bandgap energy E_g.

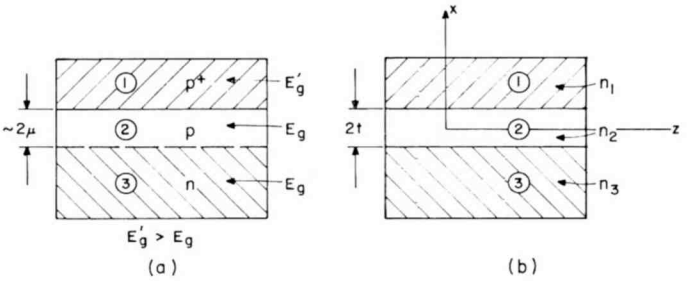

Fig. 1—(a) Injection laser structure and (b) schematic of the junction region showing index of refraction in the three regions in order to indicate the optical waveguide effect.

Region 3 is n-type, also with bandgap energy E_g. To clearly illustrate the significant improvement in device performance, we will compare data for two sets of lasers identical in all respects except for the composition of region (1). In the earlier devices, denoted "standard," all the regions are GaAs with $E_g' = 1.43$ eV; in the new devices, region (1) consists of $Al_xGa_{1-x}As$ with a higher energy bandgap.

The laser fabrication process previously described[2] is considered as the standard for comparison. It consists of the epitaxial deposition of region (1), a Zn-doped layer onto region (3), a (100) oriented substrate ($n \simeq 2 \times 10^{18}$ cm^{-3}). Deposition is followed by a heat treatment to diffuse the Zn and so displace the junction into the substrate a distance of about 2 μ, forming region (2). Lasing occurs in this region. In the present experiments, the standard and new lasers were

[2] H. Nelson, "High-Power Pulsed GaAs Laser Diodes Operating at Room Temperature," *Proc. IEEE*, Vol. 55, p. 1415, Aug. 1967.

grown on portions of the same substrate wafer in order to eliminate any possible variations between different substrates. They differed *only* in the addition of Al to the melt used to form the p+ region in the test lasers. All of the diodes were Fabry–Perot structures with uncoated cleaved ends and sawed sides.

Optical power measurements were made using an ITT F-4000 phototube and the calibration supplied by the manufacturer. The threshold current density was determined by extrapolation of the linear curve of power output versus diode current to the intersection with the current axis, which checked with the usual criterion of the onset of spectral narrowing. The current pulses were about 100 nanoseconds wide at a repetition rate of 500 Hz.

Table I—Comparative Data of Test Lasers (New Structure) and Standard Lasers. (Both groups were grown on adjoining sections of one wafer of a melt-grown ingot. The external efficiencies refer to the sum of the powers radiated from the cleaved ends of the diode.)

	Test Laser (4 × 12 mil)					Standard Laser (4 × 13.5 mil)				
T (°K)	J_{th} (A/cm²)	η_{ext} (%)	η_i (%)	δ	θ_m (%)	J_{th} (A/cm²)	η_{ext} (%)	η_i (%)	δ	θ_m
300	19,400	36	55	5.7	10	52,000	13	57	1.2	3
273	14,700	47				41,000	16			
195	7,300	47				13,500	31			
77	800	80				1,000	65			

$\delta \equiv$ electrical quality factor equal to $(\beta/\alpha)[E_g/(rA)]$, where r and A are the device resistance and area, respectively.

θ_m = maximum of power efficiency for optimum cavity.[3]

A comparison of the test and control lasers is given in Table I. The data shown are representative of the best lasers from the two groups, both of which were made on the one substrate; the variations within a batch are attributed to flaws in the substrate and are not important in this comparison. At room temperature, the threshold of a good laser from this test batch is 19,400 A/cm² as compared to 52,000 A/cm² for the standard ones. Even more startling is the contrast in the exterior differential quantum efficiency—36% versus 13%.

[3] H. S. Sommers, Jr., "Theoretical Maximum of the Power Efficiency of a Pulsed Injection Laser with a Fabry-Perot Cavity," *Solid-State Elect.*, Vol. 11, p. 909, Oct. 1968.

At lower temperature, the difference between the two sets of lasers narrows. Nevertheless, the test lasers are still more efficient at 77°K than the standard ones—80% versus 65%.

The lowest threshold current density observed for a longer diode (4 × 25 mils) in the material described in Table I was 13,000 A/cm² at room temperature and 450 A/cm² at 77°K. The differential quantum efficiency of this laser was 25% at room temperature, showing the expected reduction for a long diode. Figure 2 is the emission spec-

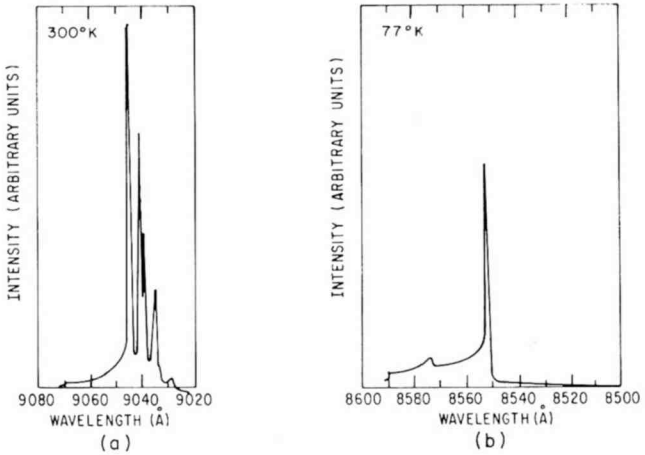

Fig. 2—Lasing peak of a laser 4 × 25 mils with junction current slightly above threshold: (a) 300°K, $J = 13{,}700$ A/cm²; (b) 77°K, $J = 430$ A/cm².

trum for this diode slightly above the room-temperature threshold (13,700 A/cm²). Threshold current densities as low as 10,800 A/cm² were obtained in other runs with 30-mil-long lasers (390 A/cm² at 77°K). With a cavity 15 mils long, 12,000 A/cm² has been obtained.

The above values are the best reported to date for GaAs injection lasers by a substantial margin. Best previously reported results[1] for room-temperature lasers was 26,000 A/cm² for a cavity length of 15 mils. The better comparison is the threshold for an infinitely long diode; we report 7000 A/cm² compared to their value of 24,000 A/cm².

The improved performance is due to a great reduction in the internal absorption, as shown from the following analysis. The experimental behavior of a double-ended laser is reasonably well described by the following equations:[4]

[4] M. H. Pilkuhn and H. Rupprecht, *Symposium of Radiative Recombination in Semiconductors*, p. 196, Dunod & Co., Paris, 1964.

$$J_{\text{th}} = \frac{1}{\beta}\left(\alpha + \frac{1}{L}\ln\frac{1}{R}\right) \tag{1}$$

$$\eta_{\text{ext}} = \eta_i \frac{\ln(1/R)}{\alpha L + \ln(1/R)} \tag{2}$$

Here R is the reflectivity coefficient, L the cavity length, α the internal loss coefficient, η_i the internal quantum efficiency, and β the gain coefficient.

From the dependence of the J_{th} on L, we find in the new units that $\beta \sim 3 \times 10^{-3}$ cm/A and $\alpha \cong 21$ cm^{-1}. For the standard units, β is also 3×10^{-3} but $\alpha \cong 100$ cm^{-1}. Thus, it is clear that the improvement in laser performance is due to a reduction of absorption by a factor of 5 rather than an increase in the gain.

In addition, it is the reduced value of α rather than an increase in η_i that explains the sharply improved external quantum efficiency of the new lasers. From Equation (2), we predict that for a cleaved diode 3×10^{-2} cm long and having $\alpha = 21$ cm^{-1}, $\eta_{\text{ext}} \cong 0.65\eta_i$; while for the standard units, $\eta_{\text{ext}} \cong 0.28\eta_i$. For the new diodes, we find a value at room temperature of $\eta_i \cong 55\%$; for the standard units, $\eta_i \cong 57\%$. These internal efficiency values are consistent with other estimates of the internal quantum efficiency at 300°K in GaAs—37 to 63%.[5]

The laser parameter of greater practical interest is the *power-conversion* efficiency. Sommers[3] has recently shown that the maximum power efficiency θ_m depends on the internal quantum efficiency η_i and an electrical quality factor δ, which is defined as the ratio of the photon equivalent voltage to the product (diode resistance × area × threshold current) for an infinitely long diode. For the devices described in Table I,

$$\delta = (4 \times 10^{-4})\frac{\beta}{\alpha}. \tag{3}$$

The factor δ is much larger for the improved lasers, as shown in Table I. As a result, at 300°K, the attainable power efficiency for the laser with the optimum design of Fabry–Perot cavity[3] is increased from 3% for the standard laser to 10% in the new structure.

[5] D. E. Hill, "Internal Quantum Efficiency of GaAs Electroluminescent Diodes," *Jour. Appl. Phys.*, Vol. 36, p. 3405, Nov. 1965.

INTERPRETATION

We attribute the drop in α to a combination of sharply improved optical waveguiding in the junction plane and to a lower absorption coefficient in the p^+ region at the lasing wavelength.

Mode confinement is of importance because it restricts the electric field to the active region of the junction, where the fundamental absorption across the bandgap has been inverted. Since the regions adjacent to the junction, which are not inverted, will absorb photons by creation of hole–electron pairs, a confinement to the region where the plasma density is high should reduce the optical losses toward the lower limit of free-carrier absorption.

Mode confinement in the p-n junction vicinity has been considered by a number of authors. The basic concept is that the active region has a higher index of refraction than the surrounding inactive region, thus forming a waveguide that concentrates the radiation in the junction vicinity.[6] The origin of the higher index in the junction region has been a subject of speculation. The factors considered have been: (1) the effects of absorption changes due to population inversion;[6] (2) differences in the free-carrier densities;[7] and (3) small differences in the absorption edge in the direction perpendicular to the junction plane such as those due to tails of states.[8]

Of these three factors, the first and second are essentially independent of the modification of our laser structure. However, there is a change in the third factor with a direct bearing on the present results. It is known that the index of refraction increases in the vicinity of the absorption edge in semiconductors.[9] The energy of the edge depends on the impurity level, the conductivity type, and of course on the bandgap energy of the material. Turning to Figure 1(b), the laser junction can be divided into three regions with different values of the index n evaluated at the frequency of the laser.

In the case of the standard GaAs solution-grown laser diode, region (1) is uncompensated, while region (2) is compensated because of Zn

---

[6] A. L. McWhorter, H. J. Zeiger, and B. Lax, "Theory of Semiconductor Maser of GaAs," *Jour. Appl. Phys.*, Vol. 34, p. 235, Jan. 1963.

[7] A. Yariv and R. C. C. Leite, "Dielectric-Waveguide Mode of Light Propagation in p-n Junctions," *Appl. Phys. Letters*, Vol. 2, p. 55, 1 Feb. 1963.

[8] F. Stern, "Dispersion of the Index of Refraction Near the Absorption Edge of GaAs," *Bull. Amer. Phys. Soc.*, Vol. 8, p. 201, 25 March, 1963.

[9] F. Stern, "Dispersion of the Index of Refraction Near the Absorption Edge of Semiconductors," *Phys. Rev.*, Vol. 133, p. A1653, 16 March 1964.

diffusion. Because of the differences in the absorption edge due to the difference in doping, n_1 is slightly smaller than n_2. Furthermore, because region (3) is n-type, n_3 is also smaller than n_2. Thus the basic conditions for a waveguide exist; its ability to confine radiation will be improved by enlarging the discontinuities between n_2 and the adjacent layers. In particular, because both the free carrier absorption and the band tailing are larger in p-type than n-type GaAs, the losses in region (1) will be large, and further decreases in n_1 should be especially important.

The analysis of mode confinement has treated a symmetrical waveguide, $n_1 = n_3 < n_2$, but the behavior of an unsymmetrical guide should be similar. It has been shown[7,10] that the optical electric field decreases exponentially in the x direction for $|x| > t$. The distance at which its intensity is reduced to $1/e$ of its value in region (2) is given approximately by

$$d \cong \left(k^2 t \, \mathrm{Re} \frac{\Delta\epsilon}{\epsilon} \right)^{-1} \approx \left(2k^2 t \frac{\Delta n}{n} \right)^{-1} . \tag{4}$$

Here t is defined in Figure 1(b), $k = 2\pi/\lambda$ and Δn is the discontinuity in the index of refraction. The free-space wavelength is λ and $\mathrm{Re}(\Delta\epsilon/\epsilon)$ is the fractional change in the real part of ϵ.

Since optical losses occur in the "inert" regions, particularly the p^+ side, d must be kept as small as possible. The increase in the bandgap energy by the addition of Al to the p^+ region accomplishes the desired goals of reducing both n_1 (and hence the flux's penetration into region (1)) and the absorption coefficient in that region.

Finally we note that the present structure may result in improved plasma confinement because electrons in region (2) must overcome a barrier $\Delta E \sim E_g' - E_g$ in order to enter region (1). Thus if $2t$ is less than the electron diffusion length (1 μ), the electron confinement will improve the gain coefficient β. However, the laser absorption losses will increase with decreasing t value because of the reduced optical confinement, Equation (4). Thus, there is an optimum $2t$ value which, in practice, is about 2 μ.

In conclusion, we have shown that great improvements in injection laser performance at room temperature are obtained with a construction that is basically simple. This structure has given a factor of 5 reduction in internal optical loss and an increase of a factor of 3 in

[10] R. E. Colin, *Field Theory of Guided Waves*, p. 470, McGraw-Hill Co., Inc., New York, 1960.

the limiting power efficiency at room temperature. The required technology is readily available in a number of alloy systems in addition to GaAs.

ACKNOWLEDGMENTS

The authors are grateful to H. S. Sommers, Jr., for discussions as well as a critical review of the manuscript, and to D. Marinelli for his skillful collaboration in the laser research effort. We are indebted to F. Hawrylo for collaboration in the device work, to V. Cannuli, J. Alexander, and M. Falk for assistance in the device fabrication, and to P. LeFur for assistance in the measurements.

STEPPED-SCANNED RING ARRAY*

By
J. Epstein† and O. M. Woodward‡

Summary A monopulse antenna configuration having a 360° azimuth scanning capability, on an operational bandwidth of over an octave, and a gain of 10 to 15 dB with respect to an isotropic antenna has been developed. An array with circular symmetry is particularly adaptive to the scanning requirement since any phasing arrangement that reinforces the radiation in a particular azimuth direction can be changed to a different azimuth direction by a simple rotary switching system.

The antenna array developed consists of eight vertical monopoles, equally spaced on a circle of radius α/λ and a ninth radiator located at the center of the array. The phases are nonoptimum, i.e., the array does not have complete vector addition of the element fields in the designated direction of maximum radiation. The excitation of the center radiator is adjusted to minimize the side-lobe level. A significant attribute of this configuration is that simple adjustments can be made in the feed networks to maintain the required excitation of the radiating elements as a function of frequency.

Introduction

MANY RADAR communication systems require an antenna system utilizing surface-wave propagation of vertically polarized fields. A study was made to develop a monopulse antenna configuration having 360° azimuth scanning capability, an operational bandwidth of over an octave, and a gain of 10 to 15 dB with respect to an isotropic antenna. An array with circular symmetry is particularly adaptive to the scanning requirement, since any phasing arrangement that reinforces the radiation in a particular azimuth direction can be changed to a different azimuth direction by a simple rotary switching system.

A considerable amount of attention has been directed to the study of a ring and concentric rings of radiators. This particular study has been restricted to a single ring of co-phased or quasi-phased radiators. This choice was basically influenced by the system requirement of an octave bandwidth operation. For the co-phased array, the phases of

* This work sponsored by Rome Air Development Center under Contract AF30(602)-4158.

‡ RCA Missile and Surface Radar Division, Moorestown, N. J.
† Formerly RCA Missile and Surface Radar Division, Moorestown, N. J.; now RCA Patent and Licensing, Princeton, N. J.

the excitation currents are chosen to give complete vector addition in the direction of maximum radiation; the phases of the quasi-phased radiators are nonoptimum and the array does not have complete vector addition in the direction of maximum radiation.

The quasi-phased array consists of eight vertical monopoles, equally spaced on a circle of radius a/λ, and a ninth radiator located at the center of the ring. The amplitude and phase of the currents in the center radiator are adjusted to minimize the side-lobe level. Despite these restrictions, the difference between the gain and beam width of this configuration and that of the co-phased array with the same number of radiators is negligible. Antenna performance—gain and patterns—are satisfactory for an octave bandwidth, $0.25 \leq a/\lambda \leq 0.50$. A significant advantage of the quasi-phased array is that a comparatively simple network can be used to ensure proper excitation of the radiating elements.

The initial step in the design of an antenna array is the determination of the amplitude and phase of the array feed coefficients and the array geometry required to obtain the desired radiation patterns and gain. We first discuss array pattern analysis and directivity. Both a co-phased and quasi-phased model are then discussed, and results of experimental work with a quasi-phased model are presented.

Pattern Analysis

The field strength of an array at any point P in space is proportional to the vector sum of the desired field component of each radiating element. The array of vertical monopoles is located in the XY plane. The coordinate system for an element of this array is shown in Figure 1. The relative field strength of the θ component of this element at P is

$$\overline{F}_n(\theta,\phi) = E(\theta) I_n \exp \{j(\delta_n + \psi_n)\} \tag{1}$$

where

$\overline{F}_n(\theta,\phi)$ = is the θ field component

θ,ϕ = spherical angle coordinates of point P

$$E(\theta) = \frac{\cos(k\,h\cos\theta) - \cos(k\,h)}{\sin(\theta)\,[1 - \cos(k\,h)]} = \text{(relative element pattern)}$$

$K = 2\pi/\lambda$

h = height of vertical monopole

a_n = radial distance to radiating element

ϕ_n = azimuth angle coordinate of element

I_n = amplitude of feeding coefficient

δ_n = phase of feed coefficient

$\psi_n = Ka_n \sin(\theta) \cos(\phi - \phi_n)$ = space phase referenced to origin of coordinate system.

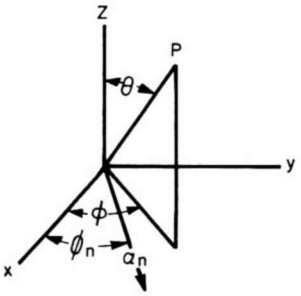

Fig. 1—Coordinate system for an array element.

The total field of an array of $(S+1)$ vertical monopoles is equal to

$$\overline{F}(\theta,\phi) = E(\theta) \sum_{n=1}^{(S+1)} I_n \exp\{j(\delta_n + \psi_n)\}. \tag{2}$$

The expression for $F(\theta,\phi)$ is general in that the values of I_n, δ_n, and ψ_n can be independently assigned for each radiator. In Equation (2), a radiator located at the origin is identified as the $(S+1)$ element. This is done to simplify the notation of a program written for use with the computer. We shall restrict our investigation to a study of a configuration of S radiators, equally spaced circumferentially on a circle of radius a_n and of an $(S+1)$ radiator centered at the origin. The azimuth location of the S radiators is given by

$$\phi_n = 360\, n/S \tag{3}$$

where n is an integer $1 \leq n \leq S$. The analysis of the ring array will be limited to two general cases. In one, we assign values to I_n and δ_n from physical considerations. For the other, we compute the value of δ_n on the basis of obtaining total vector addition of the fields in a designated coordinate direction. Each of these cases is discussed in detail.

Equation (2), with proper designation, can be used to compute both sum and difference patterns. The difference pattern is obtained by dividing the elements into two groups, symmetrically located with respect to the coordinates chosen for the direction of the maximum of the sum pattern. One group retains the same phases of the feeding coefficient as used for the sum pattern and the other group has π radians added to their sum values. These phases are designated δ_n for elements $1 \leq n \leq S/2$ and $(\delta_n + \pi)$ for elements $(S/2) + 1 \leq n \leq S$. The excitation of any elements that lie on the line of the maximum extended through the circle is zero. This ensures that the difference pattern will have a zero in the direction of the maximum of the sum pattern.

DIRECTIVITY

The directivity of an array is an expression for the ratio of the maximum power density to the average or isotropic power density. It tacitly assumes that there are no losses in the antenna system. Hence an integration of the power density $P(\theta,\phi)$ over the surface of a sphere totally enclosing the array will be equal to the input power W. Since the power density is proportional to the square of the field intensity, the average power intensity P_a is

$$P_a \propto \frac{1}{4\pi r^2} \int_s \int |F(\theta,\phi)|^2 ds ,$$

where s denotes integration over the surface of the sphere and r is the radius of the sphere.

The maximum power density P_m is proportional to $|F_m(\theta,\phi|^2$, the square of the absolute value of the maximum field intensity.

This study is restricted to arrays that radiate into a hemisphere and, in addition, have radiation patterns that are symmetrical with respect to a designated coordinate direction defined by $\theta = 90°$, $\phi = \phi_o$. Hence in the spherical coordinate system the directivity is equal to

$$D = \frac{2\pi |F_m(\theta,\phi)|^2}{\int_0^{\pi/2} \int_{\phi_o}^{\phi_o+\pi} |F(\theta,\phi)|^2 \sin\theta d\theta d\phi} \tag{4}$$

The expression for $F(\theta,\phi)$ is given by Equation (2). Equations (2) and (4) have been programmed for a computer.

Cophased Ring Array

For the cophased array, the phases of $(S+1)$ radiators are assigned to give vector addition of the radiated fields in the coordinate

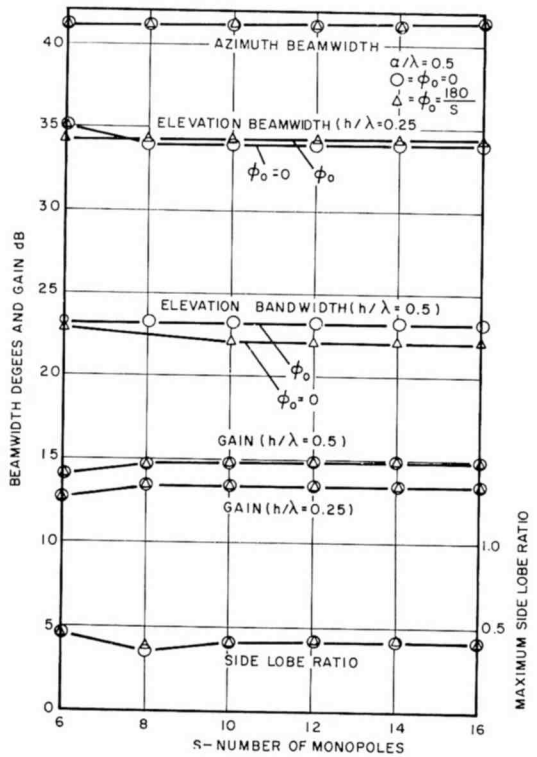

Fig. 2—Pattern characteristics of co-phased ring versus number of monopoles.

direction $\theta = 90°$, $\phi = \phi_o$. The required excitation phases of the S radiators located on a circle of radius a to achieve this vector addition are

$$\delta_n = -Ka \cos(\phi_o - \phi_n), \text{ for } 1 \leq n \leq S. \tag{5}$$

For the $(S+1)$ radiator, $\delta_{(S+1)} = 0$. The space phase of the S radiators is equal to

$$\psi_n = Ka \sin(\theta) \cos(\phi - \phi_n), \text{ for } 1 \leq n \leq S. \tag{6}$$

For the $(S+1)$ radiator, $\psi_{(S+1)} = 0$. Hence for $\theta = 90°$ and $\phi = \phi_o$, $(\delta_n + \psi_n)$ is zero for all values of n, which is the required condition for the vector addition of the radiated fields.

Pattern and gain calculations were made as a function of S to determine the minimum number of elements required to reasonably ap-

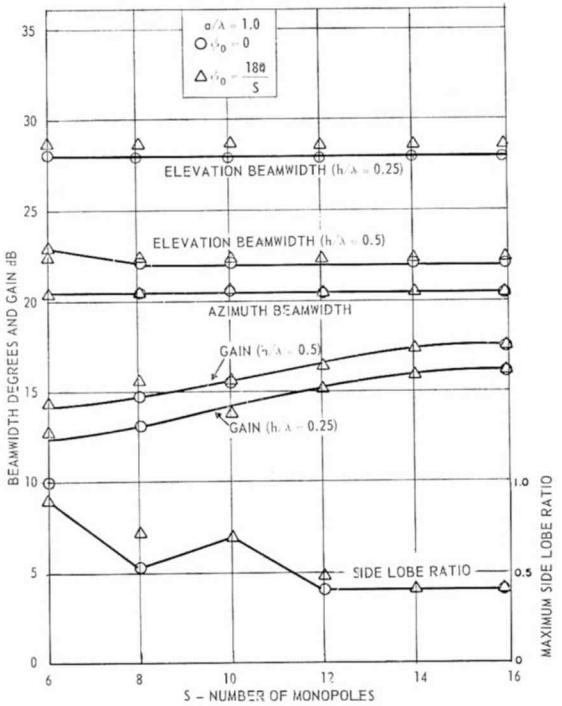

Fig. 3—Pattern characteristics of co-phased ring versus number of monopoles.

proximate the filled array, i.e., $S \to \infty$. Steering angles of zero and $180/S$ degrees were chosen. The maximum radiation for ϕ_o equal zero is always directed along a line through the Sth radiator, while for a steering angle of $180/S$ degrees, it lies between two radiators. Calculations were made for a/λ equal to 0.5 and 1.0 wavelength and monopole heights h/λ equal to 0.25 and 0.5 wavelength. The azimuth pattern is not affected by antenna height since the azimuth pattern of a vertical monopole is constant. However, the elevation patterns, and consequently gain, are a strong function of height. Examination of the data presented in Figures 2 and 3 indicates that the number of elements required to asymptotically approach the gain and patterns of the filled

array is obtained by letting $S = 16\,a/\lambda$. Consequently, the circumferential spacing between elements is $\pi/8$ wavelength. There is no significant difference in gain or patterns for the two different steering angles if $S \geq 16\,a/\lambda$.

A summary of gain, beam widths, and maximum side-lobe level of

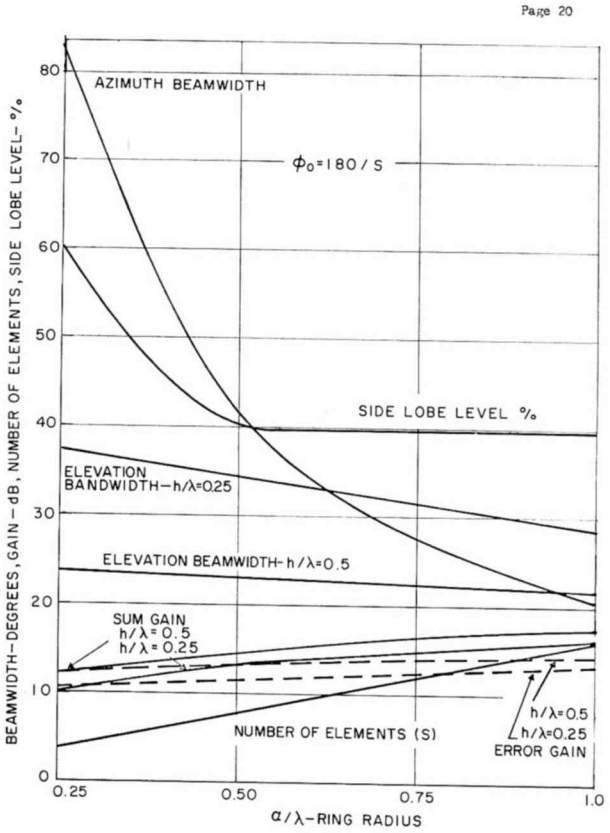

Fig. 4—Co-phased-array pattern characteristics versus a/λ.

the sum and error patterns as a function of a/λ are shown in Figure 4. The number of radiators used was 16 a/λ.

The sum and error patterns versus a/λ are shown in Figures 5 to 8. The curves shown in Figure 9 show the variation of gain, beam width, and maximum side-lobe level as a function of a/λ. In this analysis, the number of radiators and the amplitude of the feeding coefficient are held constant. The excitation phase, δ_n, is adjusted to give co-phased operations for each a/λ.

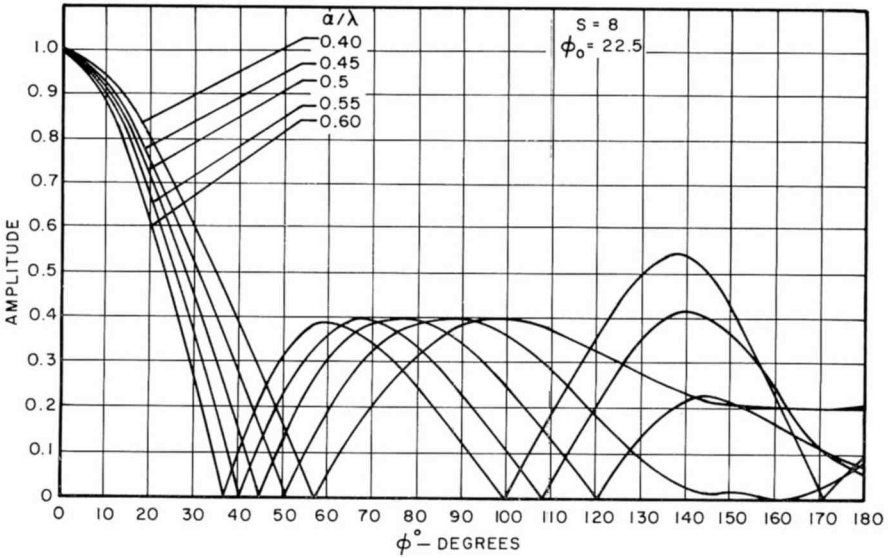

Fig. 5—Co-phased-array azimuth sum pattern versus ring radius.

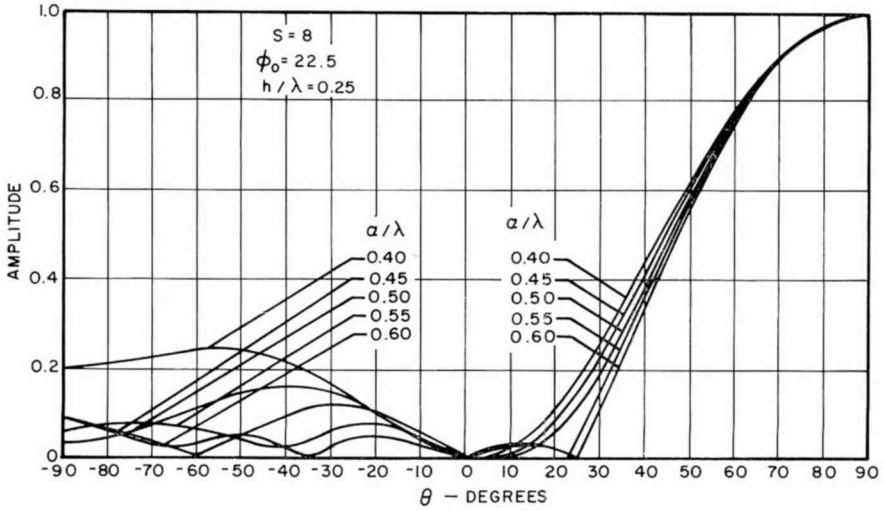

Fig. 6—Co-phased-array elevation sum pattern versus ring radius.

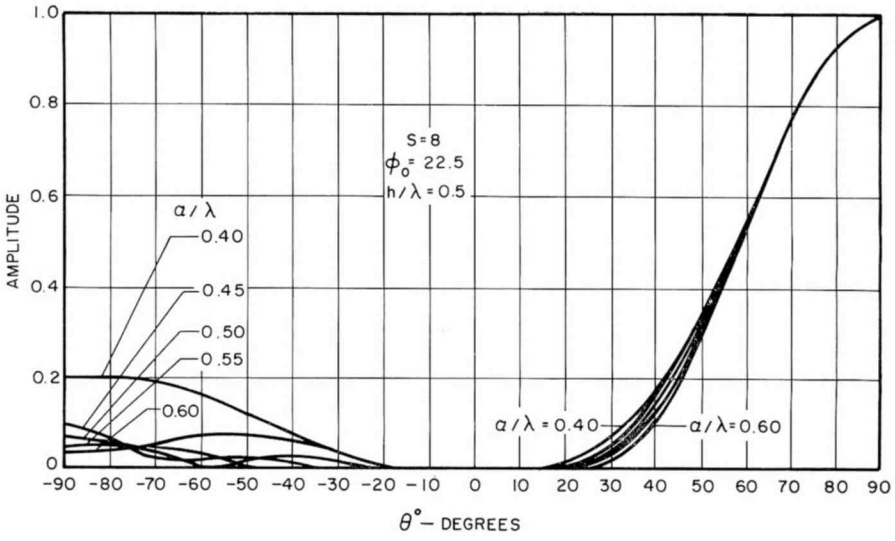

Fig. 7—Co-phased-array elevation sum pattern versus ring radius.

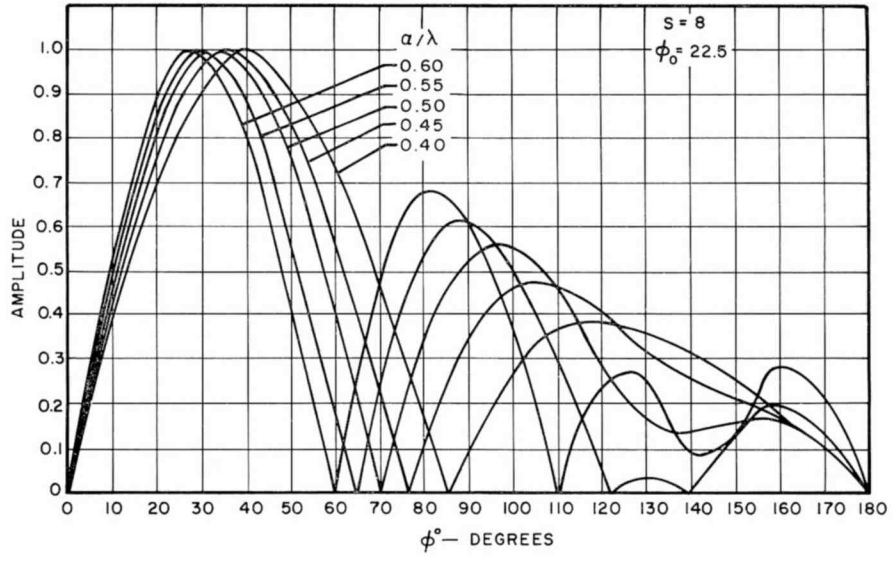

Fig. 8—Co-phased-array azimuth error pattern versus ring radius.

Quasi-Phased Ring Array

The quasi-phased ring is a simplified array that does not have complete vector addition of the radiated fields in the designated direction of maximum radiation. Despite this apparent limitation, the differences in gain and beam width between this configuration and the co-

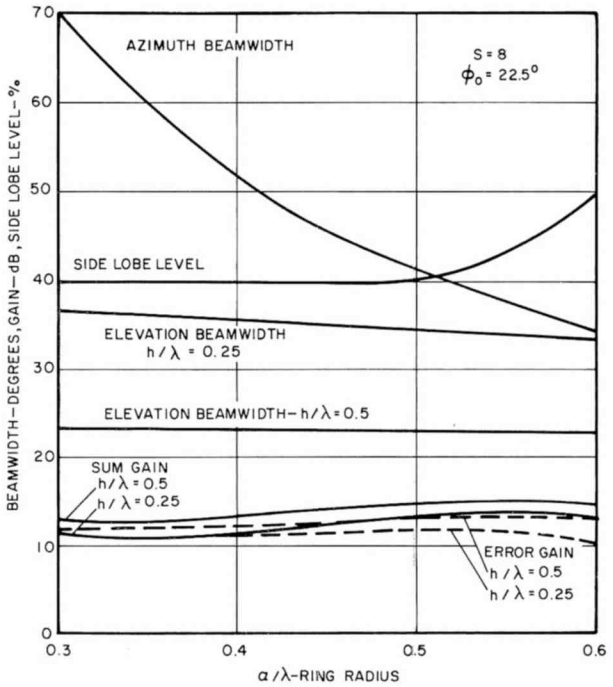

Fig. 9—Pattern characteristics of an 8-element co-phased array versus a/λ.

phased array with the same number of radiators are negligible. The significant advantage of this choice of excitation is that a comparatively simple network can be used to ensure proper excitation of the radiating elements. The details of this feed network are discussed later.

The feed coefficients of the four configurations that were analyzed are shown in Figure 10. Models A and B contain 8 elements on the ring, model C and D contain 10 elements. Both models A and B use eight equally spaced circumferential radiators and are analyzed with and without a radiator located at the center of the ring. The azimuth patterns of models A and B are shown in Figures 11 and 12. Both

exhibit high azimuth side lobes. These can be minimized by adding a center element. The amplitude and phase is chosen to equalize the first and second side lobes. Figures 13 and 14 show that reduction in side-lobe level is accompanied by an increase in azimuth beam width.

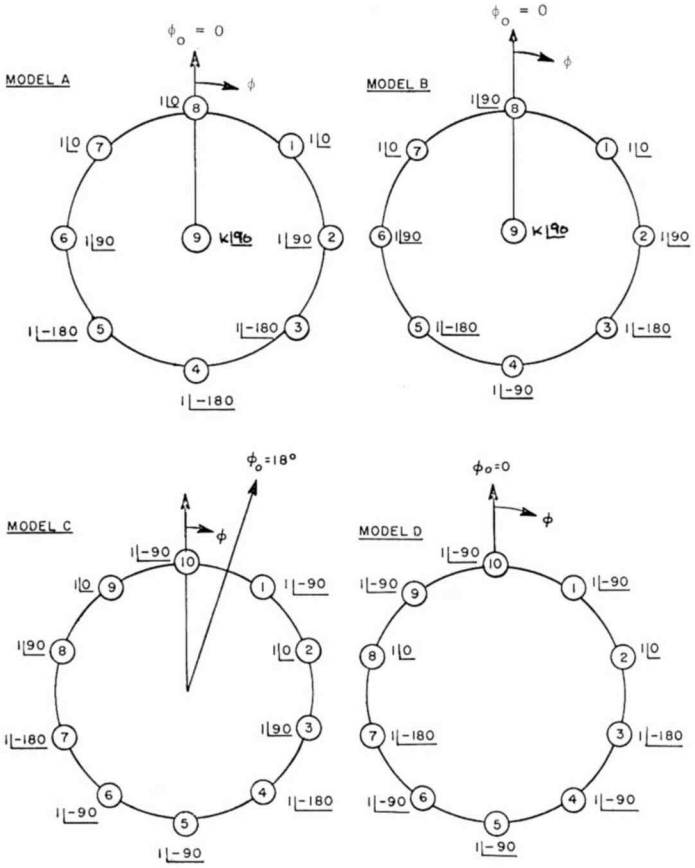

Fig. 10—Feeding coefficients of indicated array configuration.

The elevation patterns for 0.25-wavelength and 0.50-wavelength monopoles are shown in Figures 15 to 18. The elevation patterns of model A for $h/\lambda = 0.25$ wavelength indicate that the maximum radiation for a/λ greater than 0.50 wavelength is directed above the horizon. The difference patterns for both models are identical, and are shown in Figure 19. These are obtained by suppressing the excitation of elements 4, 8, and 9 and adding π radians to elements 5, 6, and 7. The

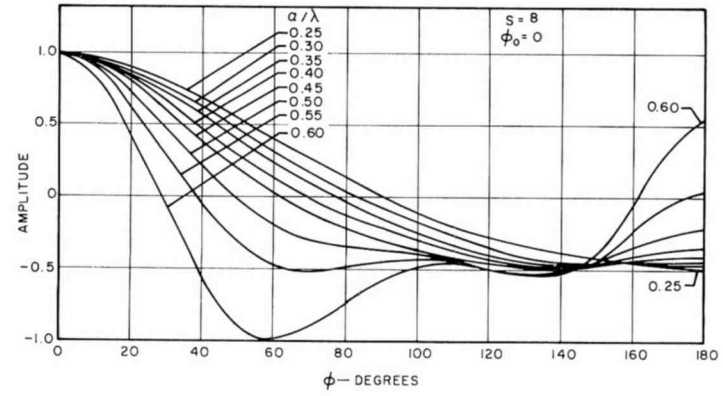

Fig. 11—Model A azimuth sum patterns versus ring radius.

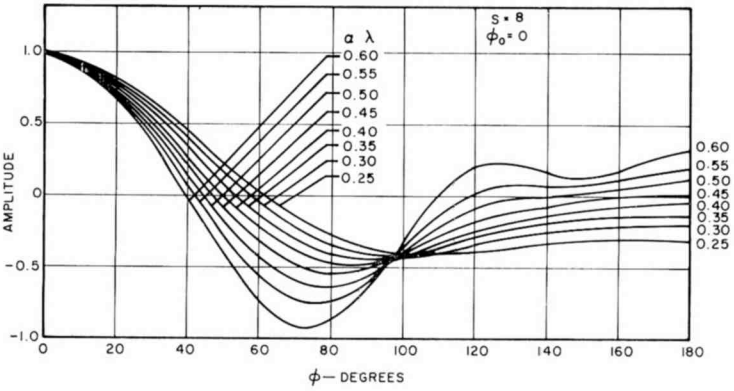

Fig. 12—Model B azimuth sum patterns versus ring radius.

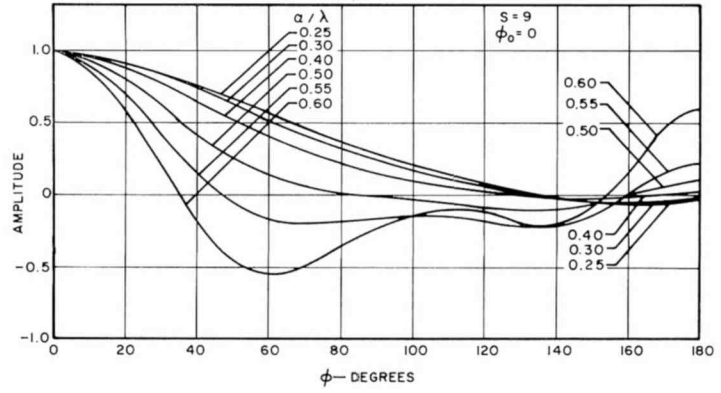

Fig. 13—Model A azimuth sum pattern with center antenna versus ring radius.

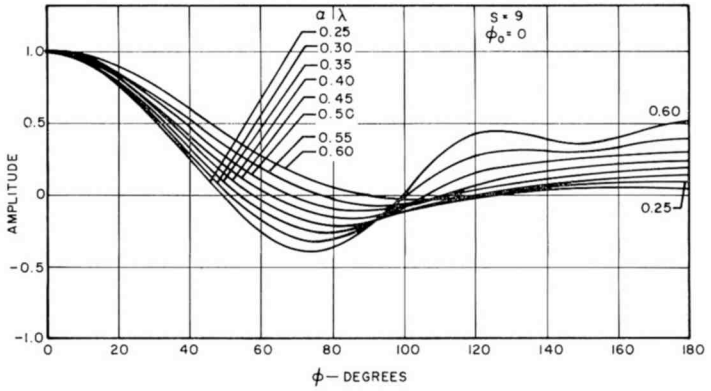

Fig. 14—Model B azimuth sum pattern versus ring radius.

side-lobe level can be controlled by amplitude grading. The effect of this procedure is shown in Figure 20 and indicates that minimum side-lobe level is obtained from $K = 0.45$ when a/λ is 0.5 wavelength. Different values of grading would be required for other ring radii.

A summary of the variations of beam widths, side-lobe level, and gain are shown in Figures 21 and 22. The error pattern characteristics are based on equal amplitude excitation of the elements. The gain and beam width characteristics of model B are better than those of model A, while model A has lower side-lobe levels over a consider-

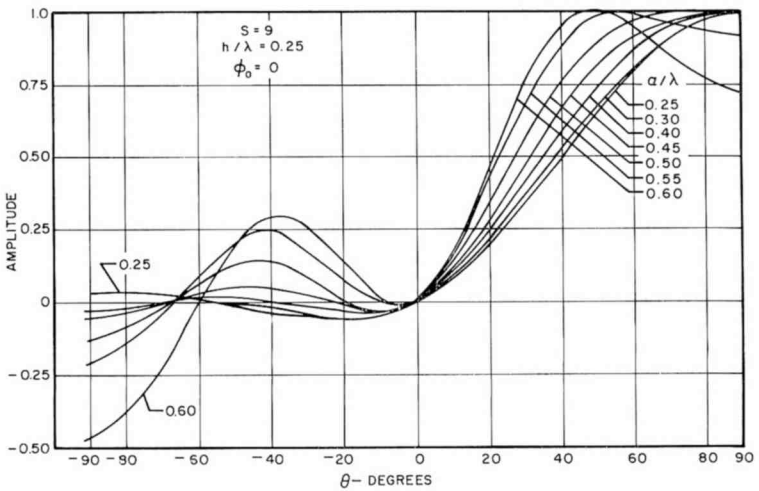

Fig. 15—Model A sum elevation pattern versus ring radius.

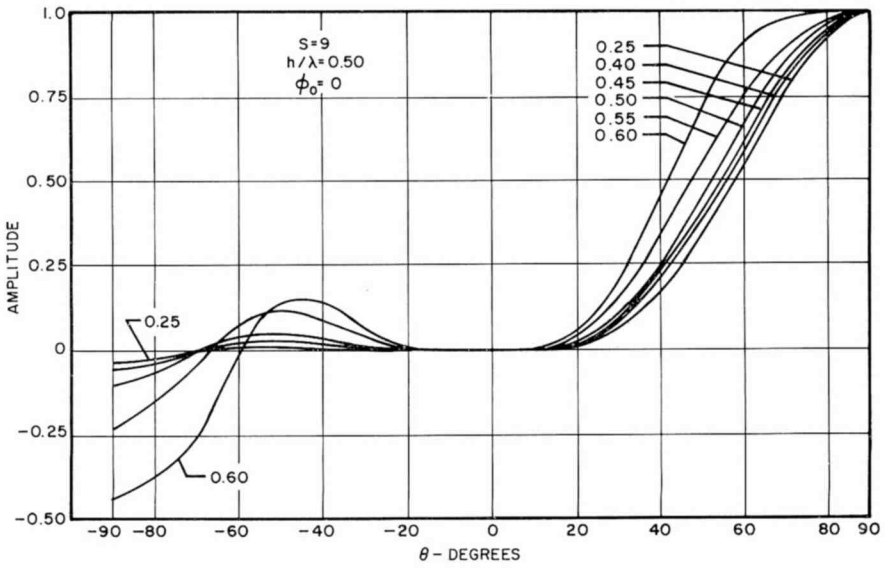

Fig. 16—Model A sum elevation pattern versus ring radius.

able range of a/λ. In addition, the excitation amplitude of the center element for model B remains constant, which is advantageous when circuit requirements are considered.

A similar analysis was made for the models C and D configurations. Each array contained ten radiating elements with simplified element phase coefficients similar to those used on models A and B. The feed coefficients of both arrays are shown in Figure 10. The patterns and gain of both were computed for a range of a/λ from 0.30 to 1.2 wavelengths and for a 0.25- and 0.50-wavelength-high monopole. Both arrays exhibited spotty pattern operation in the range of chosen a/λ.

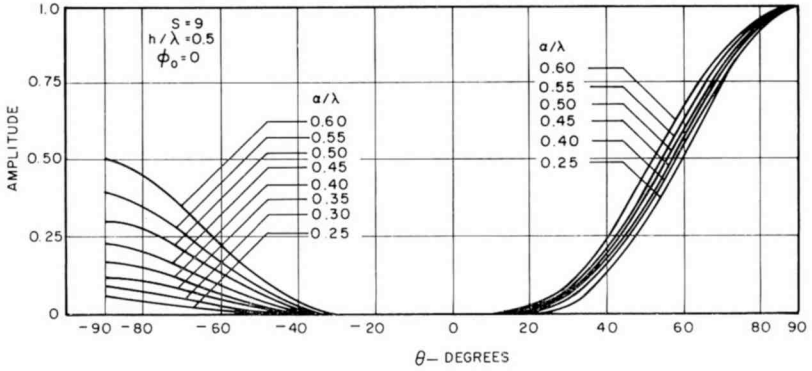

Fig. 17—Model B elevation sum pattern versus ring radius.

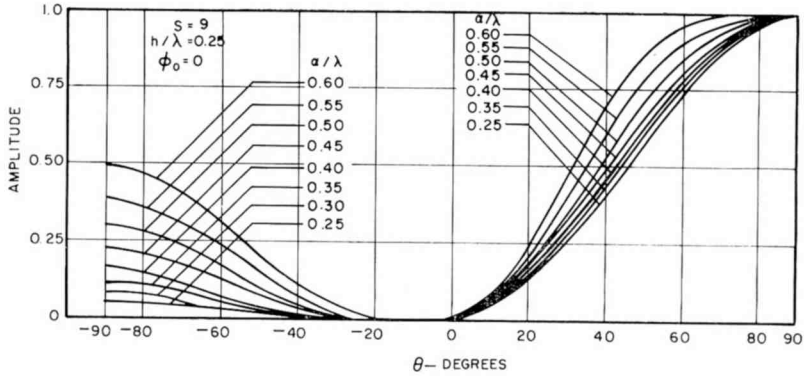

Fig. 18—Model B elevation sum pattern versus ring radius.

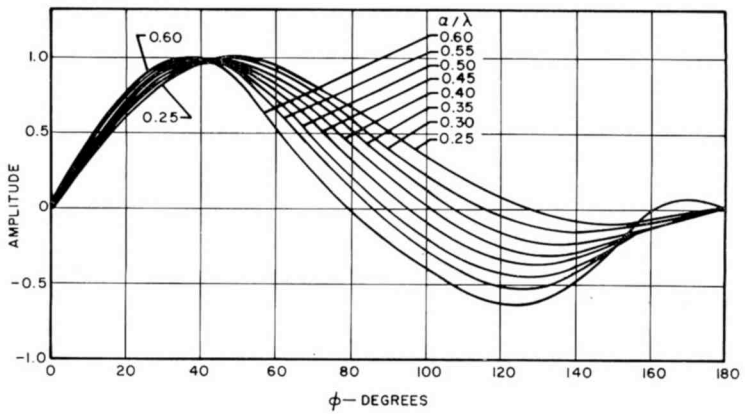

Fig. 19—Model A and B azimuth difference patterns versus ring radius.

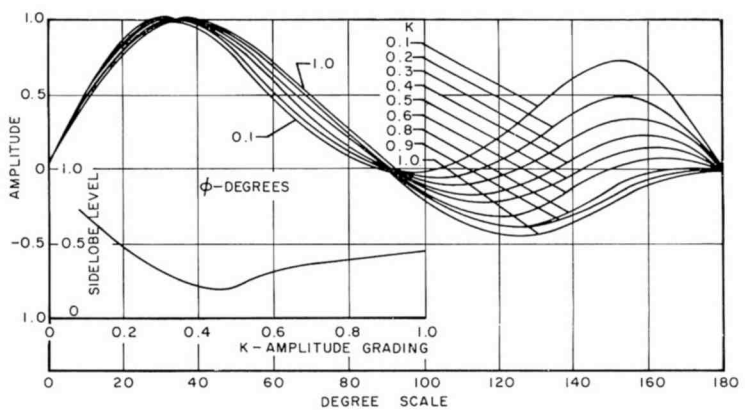

Fig. 20—Model A and B azimuth error pattern versus grading of element amplitude.

In the spotty regions the maximum of the patterns did not occur in the designated maximum coordinate directions. The maximum gain obtained for patterns that were properly formed were of the order of 15 dB. Gains of 14.5 dB were obtained for the model B array. On the

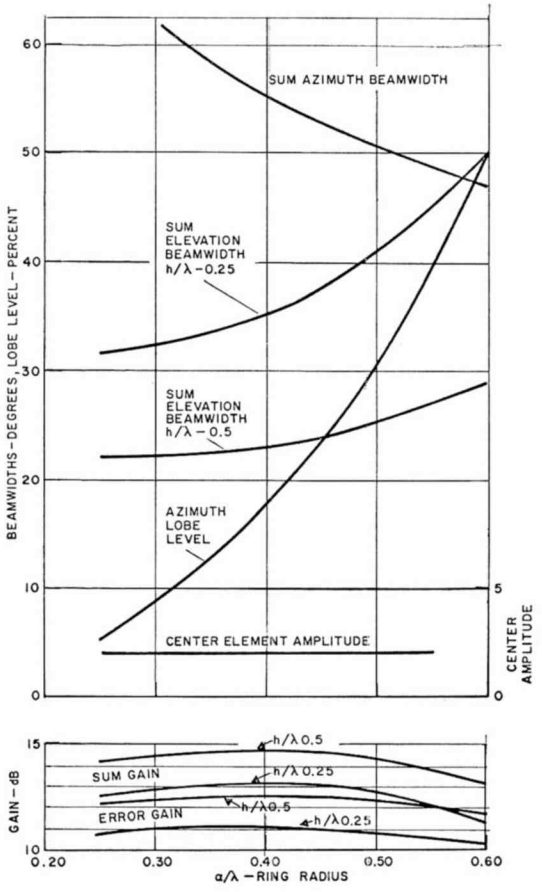

Fig. 21—Pattern characteristics of Model B array versus ring radius.

basis of pattern breakup and the marginal improvement of 0.5 dB in gain, both configurations are definitely inferior to models A and B.

The analysis of models A and B indicates that acceptable performance is obtainable over a considerable range of a/λ if the required element excitations can be realized. Excitation networks and components for models A and B that can achieve this objective will now be discussed.

Models A and B Excitation Networks

The networks for the excitation of the elements of the models A and B arrays should fulfill three fundamental requirements;

(1) ensure that the elements receive their required excitation.

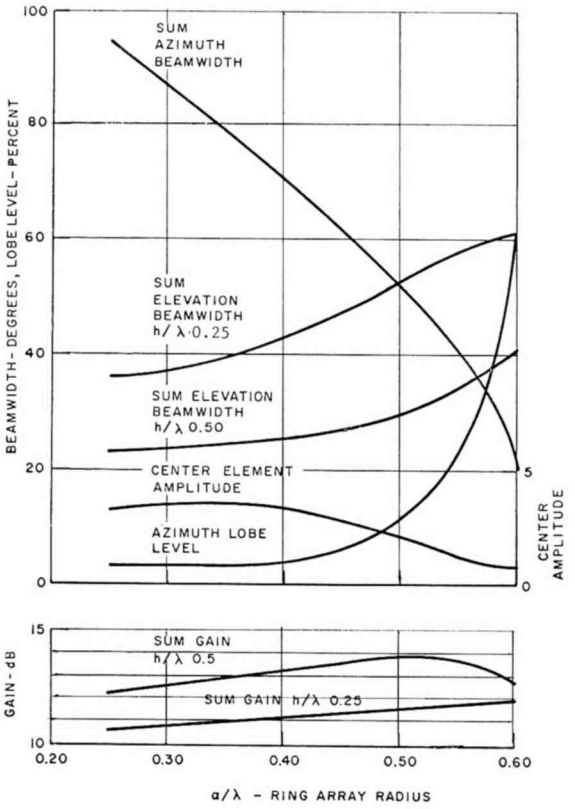

Fig. 22—Pattern characteristics of Model A array versus ring array radius.

(2) provide the required excitation over a ±8% band,

(3) contain simple adjustments, where required, to ensure proper control at any operating frequency in an octave bandwidth.

The feed networks developed are shown in Figures 23 and 24. Both circuits satisfy the three criteria listed above. An analysis of the model B circuit will be given, followed by details of operation of the power divider and hybrid circuits.

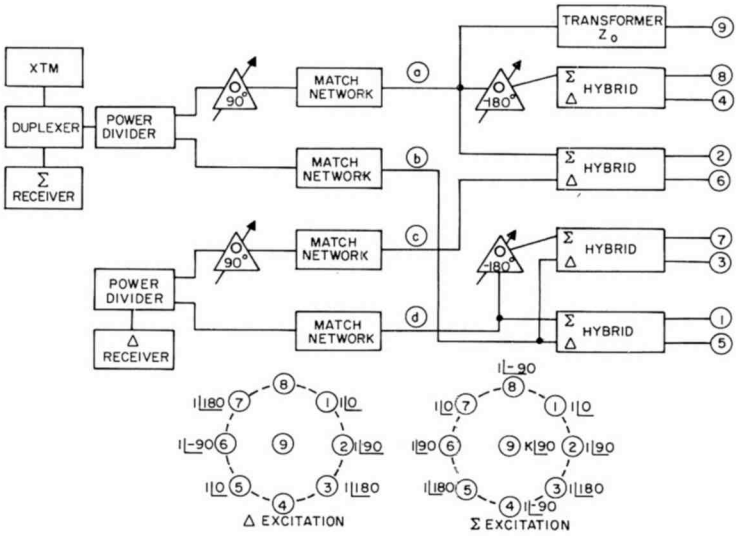

Fig. 23—Model B excitation net work schematic circuit.

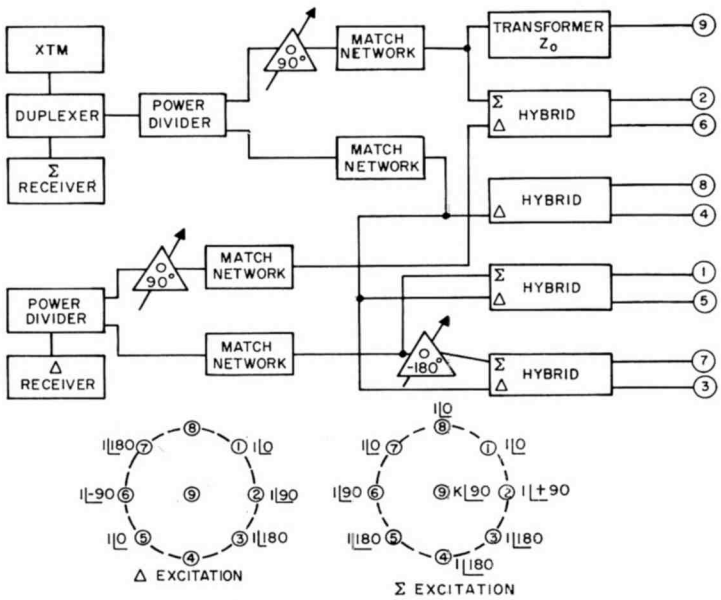

Fig. 24—Model A excitation network schematic circuit.

The sum transmitting and receiving patterns are generated by the elements interconnected to the transmitter and sum (Σ) receiver; the difference signal is generated via the circuitry between the elements and the difference (Δ) receiver. The hybrid is a coaxial line "rat-race" equivalent to that shown in Figure 26(a). For purposes of analysis, we will assume that the lengths of lines interconnecting junctions a, b, c, and d to the inputs of the hybrids and transformer are

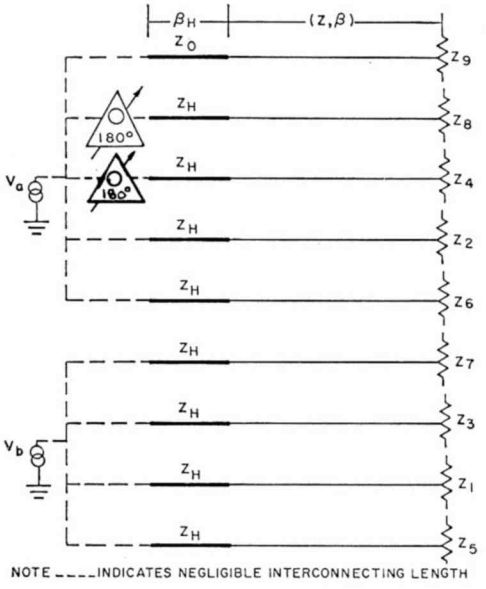

Fig. 25—Equivalent representations of interconnections between junctions a and b and respective radiators.

negligible, and that all the lines connecting the transformer and hybrids to their respective antennas are equal and have a characteristic impedance Z and an electrical length β degrees. Schematically, the interconnection between junctions a and b can be represented as shown in Figure 25. From the voltage equation for a transmission line, the relation between the input voltage, V_g, and the load current, I_L, for a 90° line of characteristic impedance Z is $V_g = jI_LZ$, i.e., the load current is determined by the ratio of input voltage to Z, and is independent of the load impedance. Hence, if β_H is equal to 90° and β equals $n180°$ (where n an integer), the relationships between the element currents and input voltages are

$$I_9 = V_a/(jZ_o)$$

$$-I_8 = -I_4 = I_2 = I_6 = V_a/(jZ_H)$$

$$I_7 = -I_3 = I_1 = -I_5 = V_b/(jZ_H)$$

To obtain the desired amplitude and phase excitation of the radiators requires that $V_a = jV_b$ and $Z_o = Z_H/2$. Assuming that this condition is satisfied, the drive impedance of each element can be computed

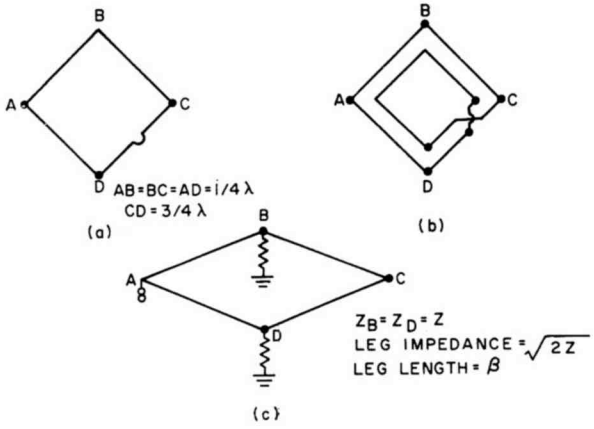

Fig. 26—Hybrid configuration.

by application of the general voltage equation

$$V_n = \sum_{m=1}^{S} \bar{I}_m Z_{nm}, \quad Z_n = V_n/I_n = \frac{1}{I_n} \sum_{m=1}^{S} \bar{I}_m Z_{nm}$$

where

Z_n = drive impedance of nth radiator,

Z_{nn} = self-impedance of nth radiator,

Z_{mn} = mutual impedance between nth and mth radiator,

$\bar{I}_n = I_n \exp\{j\delta_n\}$,

$\bar{I}_m = I_m \exp\{j\delta_m\}$,

S = number of radiators.

Hence the drive impedance, Z_n, is a function of the element current, phase, and interelement mutual impedance. Considerable simplification occurs for the ring because of symmetry. For example, by inspection we see that element 1 in the model B sum pattern is coupled only to elements 5 and 9, since the elements of pairs 2-8, 3-7, and 4-6 have equal negative current and hence the effect of induced fields on element 1 cancel. Verifying this by the expansion for Z_1 we obtain

$$Z_1 = Z_{11} - Z_{15} + j2Z_{19} ,$$

since

$$Z_{12} = Z_{18},\ Z_{13} = Z_{17},\ Z_{14} = Z_{16} ,$$

$$I_2 = -I_8,\ I_3 = -I_7,\ I_4 = -I_6 .$$

Let us designate the set of radiators (2, 4, 6, 8, 9) as the $\pm j$ subset and radiators (1, 3, 5, 7) as the ± 1 subset. The input admittance at junction a is

$$Y_a = (Z_2 + Z_4 + Z_6 + Z_8 + 4Z_9)/Z_H{}^2 ,$$

where

$$Z_2 = Z_6 = Z_{22} - 2Z_{24} + Z_{26} + 2Z_{29} ,$$

$$Z_4 = Z_{44} - j2Z_{43} - 2Z_{42} + j2Z_{41} + Z_{48} - 2Z_{49} ,$$

$$Z_8 = Z_{88} + j2Z_{81} - 2Z_{82} - j2Z_{83} + Z_{84} - 2Z_{89} ,$$

$$Z_9 = Z_{99} .$$

By symmetry, $Z_{43} = Z_{81}$, $Z_{41} = Z_{83}$ and hence will cancel when we sum $(Z_2 + Z_4 + Z_8 + Z_9)$. This is a useful and important property of both the models A and B circuits, since it indicates that though the drive impedance of an individual radiator is affected by coupling between the $\pm j$ and ± 1 elements, the input impedance of each subset is only determined by intercoupling between elements within the particular subset. Hence the inputs to each subset for both sum and difference configuration can be independently matched.

The power division between the two subsets required to effect proper excitation of the radiating elements is unequal. The division is obtained by independently matching the two subsets, introducing a 90° phase lead in the $\pm j$ subset leg and, finally, employing a power divider to obtain proper division between the two subsets.

Table I is a summary of the analysis for the model B configuration for the three values of a/λ and lists the drive impedance, voltage, current, and power of each element of the array. The element position is shown in Figure 10. Note that the resistance of some of the elements

Table I—Model B Circuit-Analysis Summary (Power Input to Array 1000 Watts)

a/λ	Element	Z	VSWR	P (watts)	V (volts)	I (amperes)
0.25	1	72.1+j78.5	2.8	168.8	165	1.53
	2	71.0−j21.3	1.5	166.2	113	
	3	16.1−j7.1	3.2	37.7	27	
	4	−11.5+j10.3	—	−26.9	26.8	
	5	16.1−j7.1	3.2	37.7	27	
	6	71.0−j21.3	1.5	166.2	113	
	7	72.1+j78.8	2.8	168.8	165	
	8	−26.3+j136.5	—	−61.5	213	
	9	36.6+j21.2	18	342.8	64.5	
0.375	1	86.6+j26.4	2.0	176.2	128	1.43
	2	35.6−j13.0	1.6	72.44	53.8	
	3	8.6+j6.4	6.0	17.5	20.6	
	4	−1.4+j31.0	—	−2.86	24.4	
	5	8.6+j6.4	6.0	17.5	20.6	
	6	35.6−j13.0	1.6	72.44	53.8	
	7	86.6+j26.4	2.0	176.2	128.0	
	8	84.8+j90.7	4.0	172.6	180.0	
	9	36.6+j21.2	1.8	297.9	61.0	
0.50	1	64+j15	1.4	131.2	94	1.43
	2	23.2+j1	2.1	47.54	32.5	
	3	6+j27.4	10	12.3	40	
	4	19+j42	4.6	38.93	66	
	5	6+j27.4	10.	12.3	40	
	6	23.2+j1	2.1	47.54	32.5	
	7	64+j15	1.4	131.2	94	
	8	136.2+j68	3.4	279.1	217	
	9	36.6+j21.2	1.8	300	60.5	

is negative. This indicates that power is being delivered back to the system. The total power delivered to the system is the algebraic sum of the element powers. The VSWR data are obtained by normalizing the drive impedances to a 50-ohm transmission line.

Balanced Hybrid Configurations

The hybrid used in the experimental work was a four-port stripline rat-race with three quarter-wavelength arms and one three-quarter wavelength arm as shown in Figure 26a. The input ports are A and C, and B and D are the output ports. The bandwidth of this configura-

tion is limited because of the use of the three-quarter wavelength line to effect a phase shift of 180°. Both the balance of the output ports and the coupling between input ports are frequency sensitive.

A balanced hybrid configuration that removes this limitation is shown in Figure 26(b). The 180° phase shift is obtained by a transposition of the transmission line, which is frequency independent. Hence, both the balance of the voltages across the output port and the decoupling between the input ports are frequency independent. The input impedance, however, is frequency sensitive. The equivalent circuit of this configuration can be represented by the circuit shown in Figure 26(c), where port C is shorted. When β is 90°, the input impedance at A is equal to Z. As β departs from 90°, the output loads are shunted with a reactance and, hence, the input impedance is affected.

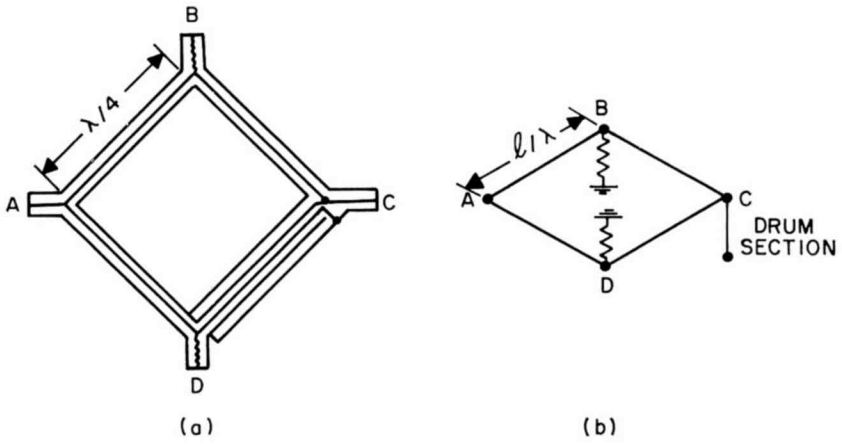

Fig. 27—Balanced coaxial-line hybrid.

A balance coaxial line configuration is shown in Figure 27(a). The transposition is achieved by using a quarter-wavelength drum around one coaxial leg and transposing the inner and outer conductors of the inner coaxial line. The equivalent circuit of this configuration is shown in Figure 27(b) where the drum appears as a shorted section of coaxial line across the input port C. The characteristic impedance of this line can be increased to about 500 ohms by coiling the inner coaxial line. The computed input VSWR for this mode of operation is shown in Figure 28.

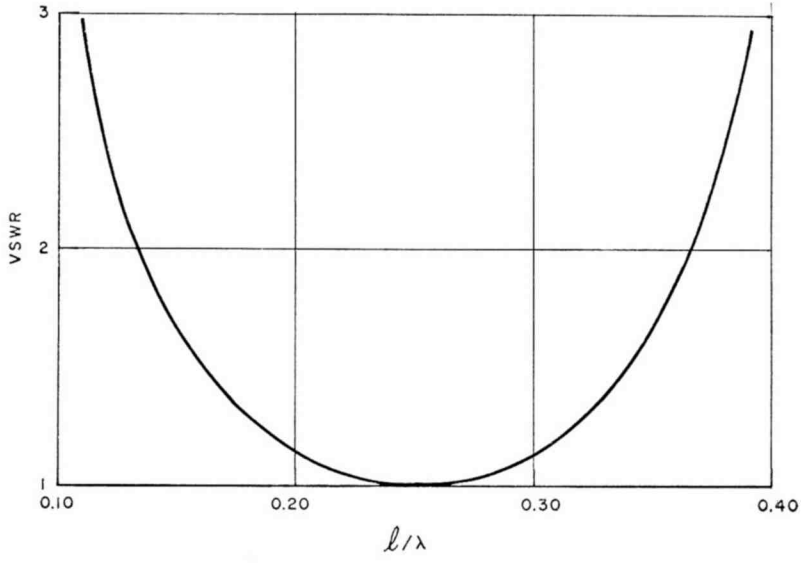

Fig. 28—Input VSWR of coaxial hybrid.

Control of Excitation Current

In the models A and B excitation networks described above, the property of a quarter-wavelength transmission line connecting the radiating and generator was utilized to control the excitation current. This control is lost as the frequency changes because of the change of electrical length of the quarter-wavelength section. An analysis indicates that the excitation current can still be made independent of the load impedance by a simple readjustment of length of the line between the hybrid and the radiating element.

For purposes of analysis, the circuit can be represented as shown in Figure 29. At the design frequency where $\beta_1 = 90°$, $\beta_2 = n180°$, I_3 is V_1/jZ_1. To analyze the operation as the frequency changes

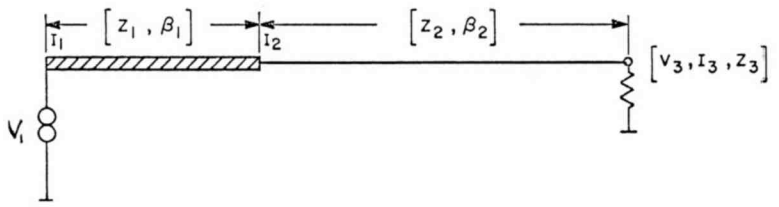

Fig. 29—Excitation current control equivalent circuit.

the following set of equations is used:

$$V_1 = V_2 \cos \beta_1 + jI_2 Z_1 \sin \beta_1 \qquad I_1 = I_2 \cos \beta_1 + \frac{jV_2 \sin \beta_1}{Z_1}$$

$$V_2 = V_3 \cos \beta_2 + jI_3 Z_2 \sin \beta_2 \qquad I_2 = I_3 \cos \beta_2 + \frac{jV_3 \sin \beta_2}{Z_2}$$

$$V_3 = I_3 Z_3$$

Solving for I_3, we find that

$$I_3 = \frac{V_1}{\left[\cos \beta_2 + \dfrac{jZ_3}{Z_2} \sin \beta_2\right][jZ_1 \sin \beta_1] + [Z_3 \cos \beta_2 + jZ_2 \sin \beta_2] \cos \beta_1}.$$

I_3 can be made independent of Z_3 by satisfying the condition that

$$\tan \beta_2 = \frac{Z_2}{Z_1 \tan \beta_1}.$$

This condition involves simply a change in the length of line L_2 connecting the hybrid to the radiating element as determined by the relationship between β_1 and β_2. The expression for I_3 for this condition becomes

$$I_3 = \frac{V_1}{j[Z_1 \cos \beta_2 \sin \beta_1 + Z_2 \sin \beta_2 \cos \beta_1]},$$

which reduces to the familiar relationship that $I_3 = V_1/jZ_1$ for $\beta_1 = 90°$ and $\beta_2 = n180°$.

Power Divider

The requirement of equal currents in the radiating elements requires unequal power division between the $\pm j$ and ± 1 subsets. The discussion of the models A and B excitation networks showed that this division is achieved by matching the input to both subsets (i.e., by introducing the required phase lead to the $\pm j$ input to establish the 90° lead between the two subsets) and by using a power divider to obtain the proper power division between the subsets.

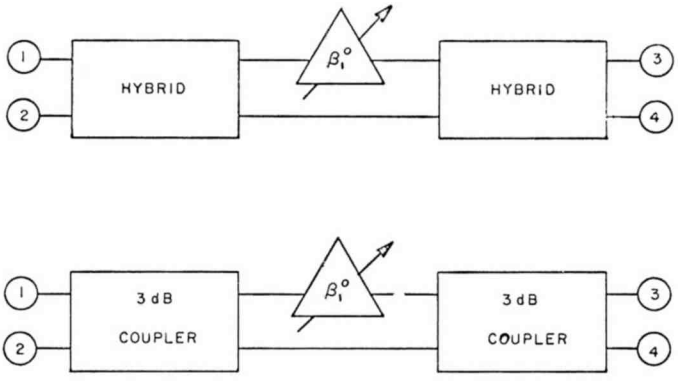

Fig. 30—Schematic of power divider.

Two configurations that perform the power division are shown in Figure 30. Ports 1 and 2 are the decoupled input ports. At midband the ratio of the output voltages, V_3/V_4, for the hybrid configuration is $\pm j \cos(\beta_1/2)/\sin(\beta_1/2)$. For the 3-dB directional coupler, the ratio of the output voltages is $\pm\cos(\beta_1/2)/\sin(\beta_1/2)$. Hence power division can be controlled by varying the magnitude of β_1. Note that the hybrid power divider introduces a quadrature lead or lag between V_3 and V_4, while the output voltages are out of phase for the coupler configuration. A plot of the power ratio (dB) as a function of β_1 is shown in Figure 31.

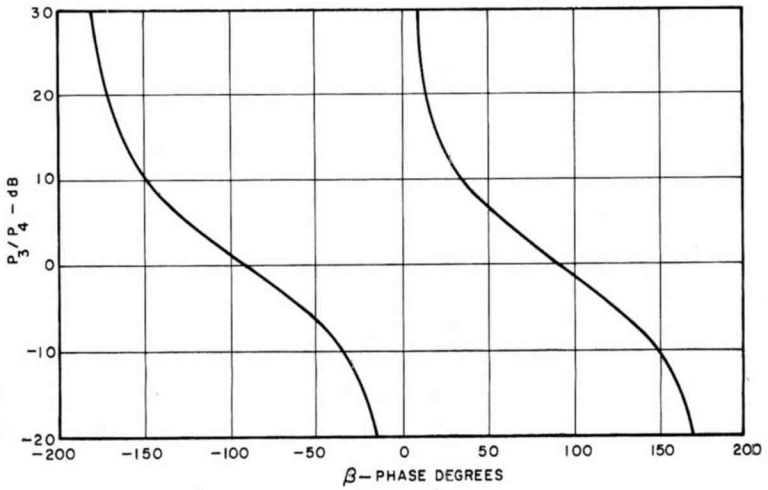

Fig. 31—Power ratio versus phase.

The general expression for the vector ratio of $\overline{V}_3/\overline{V}_4$ of the 3-dB coupler configuration is

$$\frac{\overline{V}_3}{\overline{V}_4} = \frac{j2 \sin \beta_2 \cos (\beta_1/2)}{1 - \sin^2 \beta_2 \exp \{j\beta_1\}}$$

and the ratio of the magnitudes is

$$\left|\frac{V_3}{V_4}\right| = \frac{2 \sin \beta_2 \cos (\beta_1/2)}{[1 + \sin^4 \beta_2 - 2 \sin^2 \beta_2 \cos \beta_1]^{1/2}}$$

where

$\beta_2 = 90°(f/f_o)$

f_o = midband frequency

f = operating frequency

β_1 = phase introduced by phase shifter

A study of this relationship indicates that $V_3/V_4 = 0$ for $\beta_1 = 180°$ for all values of β_2. As β_2 departs from 90°, β_1 can be readjusted to control the ratio of V_3/V_4. This provides a basis for a broad-band power divider that can readily be adjusted to control the ratio of the power outputs by varying the phase of the phase shifter.

Monopole Construction

The gain and elevation patterns of the ring array are functions of the electrical height, h/λ, of the monopole. The analysis indicates that an increase in gain of approximately 1.5 to 2.0 dB is obtained by increasing the height of the monopole from 0.25 to 0.50 wavelength. Normally the monopole is base fed. The self-impedance of a 0.25-wavelength monopole is $36 + j21.2$ ohms. The impedance of a base-fed 0.50-wavelength monopole is very high, because it is operating around its second resonance. This mode of operation is undesirable and can be avoided by center feeding a base-insulated 0.50-wavelength monopole. This mode of operation can be obtained by the configuration shown in Figure 32. The central pole is used as a structural support for two 0.25-wavelength cages. The top ends of both cages, sections T_1 and T_2, are tied to the central pole and their lower ends, sections L_1 and L_2, insulated from the pole as indicated. The cages are energized at the center gap, between sections L_1,T_2, by a coaxial transmission line attached to the center pole. This provides the required current distri-

bution (zero at sections T_1 and L_2 and maximum at sections L_1 and T_2) to obtain the 0.50-wavelength mode of operation. Alternative center-fed monopole configurations are shown in Figure 33.

Switching Matrix

The switching matrix for a ring array is relatively simple because of its circular geometry. Any phasing network that re-enforces the beam in a particular azimuth can be switched by a simple rotary mo-

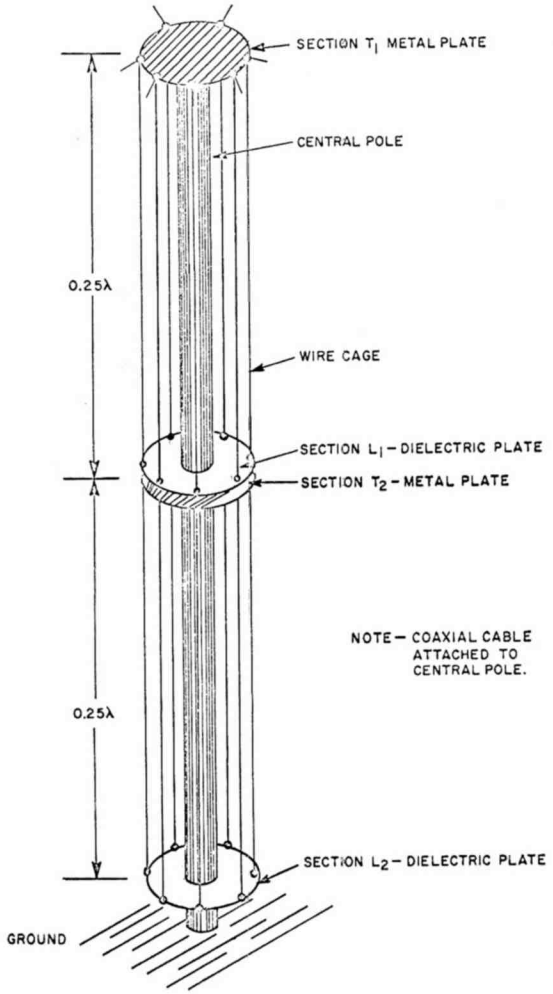

Fig. 32—Half-wavelength-monopole configuration.

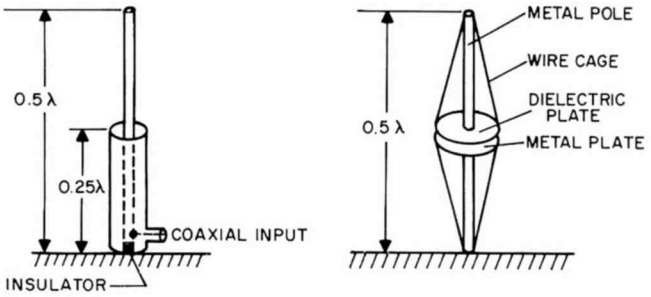

Fig. 33—Alternative center-fed monopole configurations.

tion to a different azimuth position. The number of pointing directions is equal to the number of radiators located on the circle of radius a. Hence, the number of pointing directions for models A and B is eight. A switching matrix that will point the beam in eight azimuth directions is shown in Figure 34. The switches designated S_1 through S_{16} are Jennings vacuum transfer relays with two-input, two-output contact configurations and a switching time of less than 30 milliseconds. In Figure 34 the terminal numbers without primes represent the input terminals of the switch, which are connected to the corresponding numbers shown on the schematic circuit of the models A and B networks illustrated in Figures 23 and 24. The primed numbers are the output switch terminals and are connected to the eight radiators located on the circumference of the circle. Table II gives the switching sequence that will rotate the beam through 180° in 45-degree steps. The switching sequence can easily be extended to obtain 360 degrees of azimuth scan.

Table II—Switching Sequence

Switch Number	Position				
S_1	P_1	P_1	P_2	P_2	P_1
S_2	P_2	P_1	P_2	P_1	P_1
S_3	P_2	P_2	P_1	P_2	P_2
S_4	P_1	P_2	P_1	P_1	P_1
S_5	P_2	P_1	P_2	P_1	P_2
S_6	P_2	P_2	P_2	P_1	P_2
S_7	P_1	P_1	P_2	P_1	P_1
S_8	P_1	P_1	P_1	P_2	P_2
S_9	P_2	P_2	P_1	P_2	P_2
S_{10}	P_2	P_2	P_2	P_1	P_2
S_{11}	P_2	P_2	P_1	P_1	P_1
S_{12}	P_1	P_2	P_1	P_2	P_1
S_{13}	P_2	P_1	P_2	P_1	P_2
S_{14}	P_2	P_2	P_2	P_1	P_2
S_{15}	P_1	P_1	P_2	P_1	P_2
S_{16}	P_2	P_1	P_2	P_1	P_2

Experimental Results (Model B)

The analysis of the co-phased and quasi-phased arrays indicates that the antenna system requirements were met by both configurations. The choice of quasi-phased arrays configuration was made on the basis of networks required to achieve proper excitation of the radiating elements. The models A and B networks meet three basic requirements: (1) They ensure that the elements are properly energized,

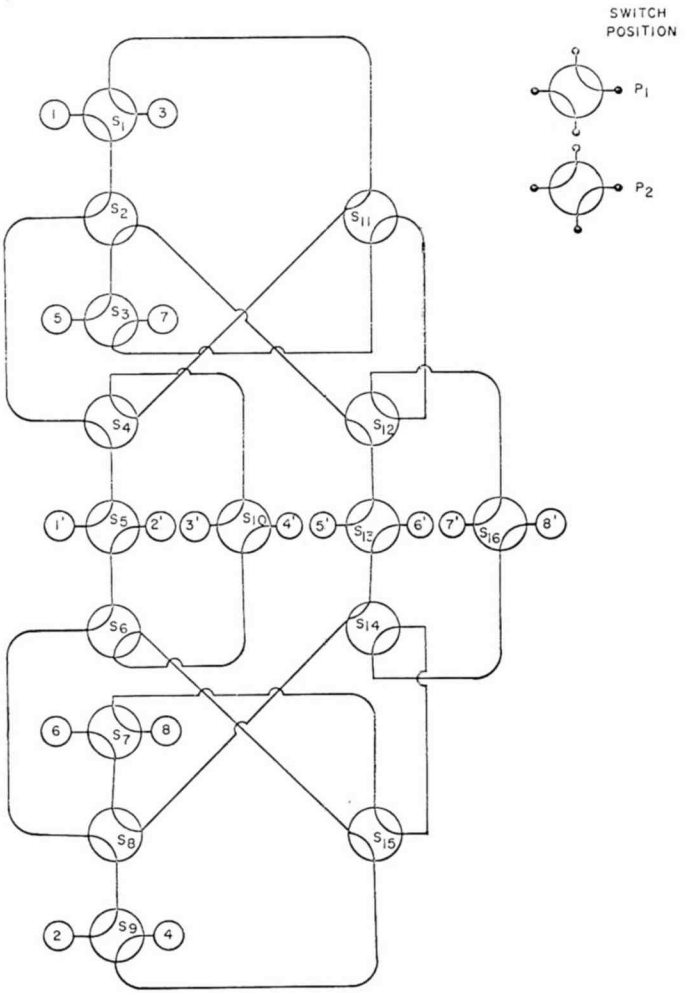

Fig. 34—Switching matrix.

(2) They provide the required excitation over a ±8% band.

(3) They contain simple circuit adjustments to obtain required element excitation at any frequency within an octave bandwidth. No comparable network could be devised for the co-phased configuration.

Experiments were performed at 630 MHz, and the work was limited to the model B configuration, since the analysis had indicated that,

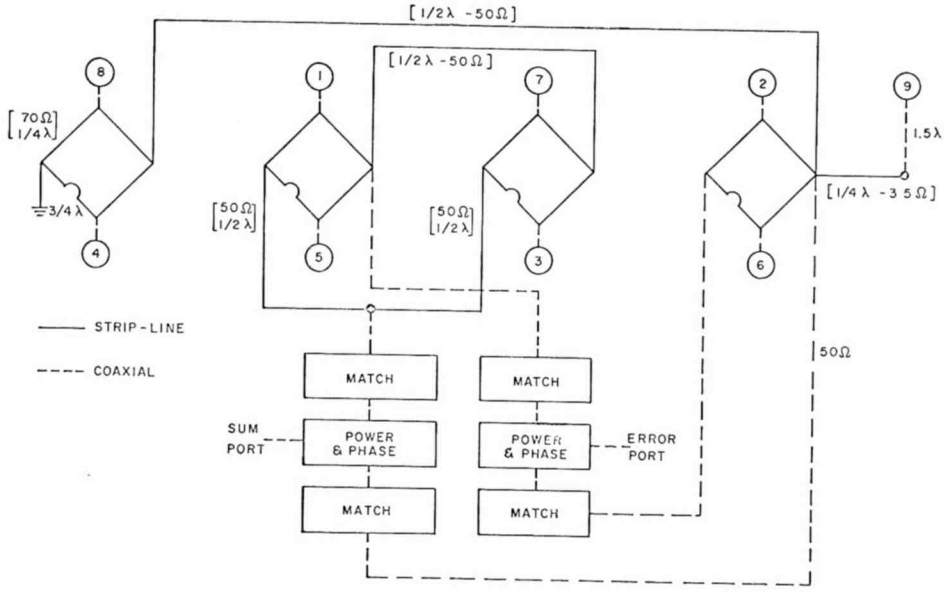

Fig. 35—Schematic wiring diagram of scaled model B ring array.

for wide-band operation, this model was preferable to model A. The schematic of the excitation network is shown in Figure 35. As indicated, this network is a combination of stripline and coaxial circuitry. The ring radius was physically changed so that a/λ's of 0.25, 0.375, and 0.5 could be measured with the same network at 630 MHz. This procedure ensures that the elements will receive the desired excitation, since the feed network is designed to fulfill the three requirements mentioned above.

Initial measurements were made of the subset patterns in an isolated configuration and in the presence of the other subset with terminations of the undriven subset. The intent was to determine that the elements of the subset were correctly excited by the feed network. Results

of these experimental checks of the subset patterns are shown in Figures 36 to 39. The curves indicate that the presence of the ± 1 subset has little effect on the $\pm j$ subset patterns. The $\pm j$ subset presence, however, does introduce sufficient coupling to slightly modify the $\pm j$ patterns in a limited range of radiation.

The following procedure was followed to obtain proper excitation of the array. For each a/λ, the inputs to the ± 1 and $\pm j$ subsets were

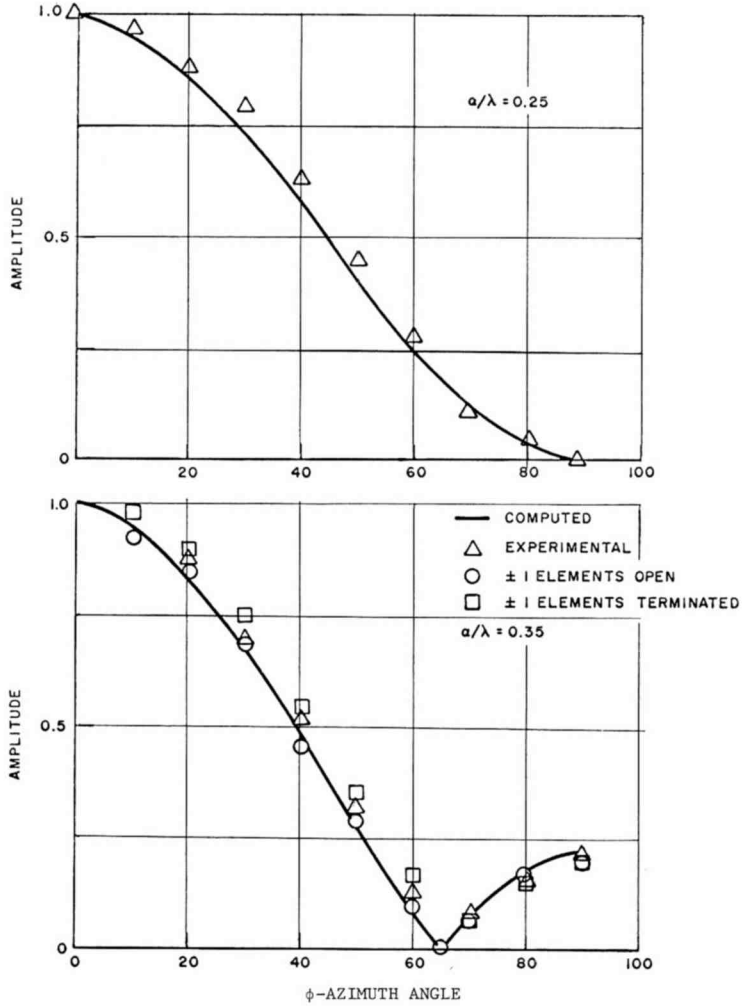

Fig. 36—Model B$\pm j$ subset azimuth sum pattern.

independently matched with a double stub configuration (Figure 35). The power divider and phase shifter were then adjusted to obtain the theoretical ratio of backward to forward radiation, $F(180°)/F(0°)$. A more direct procedure would be to provide means of monitoring the vector ratio of the excitation current of an element in each subset. The power divider and phase shifter would then be adjusted to obtain the required vector ratio of the element currents.

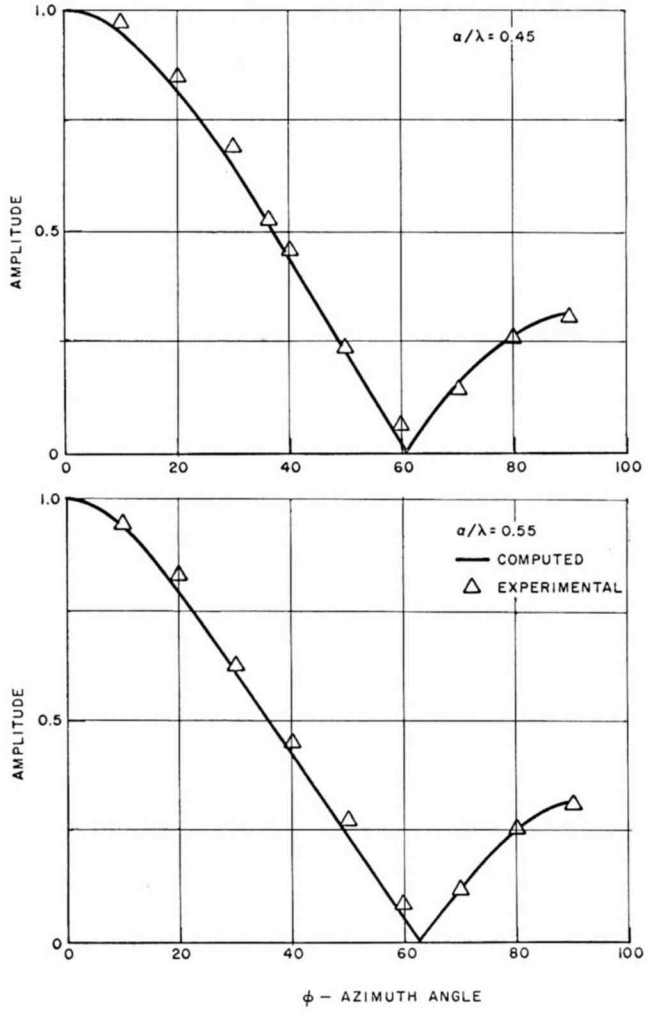

Fig. 37—Model B±j subset azimuth sum pattern.

The measured sum radiation patterns for $a/\lambda = 0.25$, 0.35, and 0.50 compared to the computed patterns are shown in Figure 40. The frequency sensitivity of the beam width and side-lobe level for a ring array of $a/\lambda = 0.50$ is shown in Figure 41 and indicates that the bandwidth is of the order $\pm 8\%$. The data indicates good correlation between the theoretical and experimental patterns. In addition the networks maintain the correct excitation over the designated bandwidth.

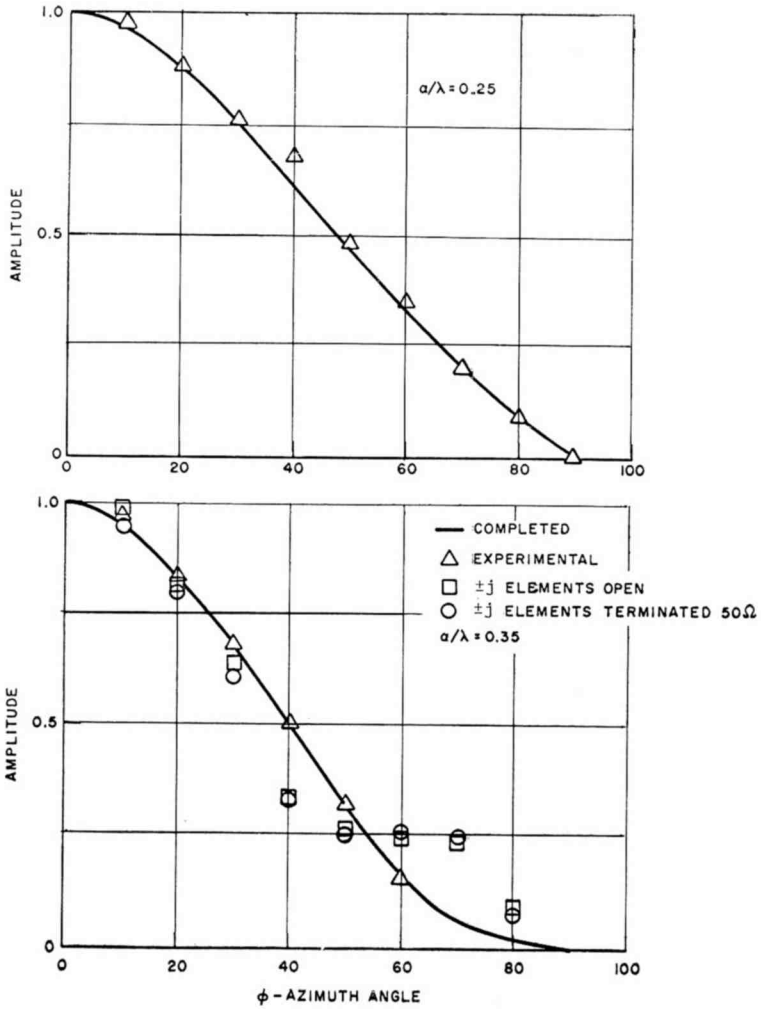

Fig. 38—Model B±1 subset azimuth sum pattern.

REFERENCES

1. H. L. Knudsen, "Radiation from Ring Quasi-Arrays," *IEEE Trans AP*, p. 452, July 1966.
2. W. T. Patton and J. D. Tillman, "An Analysis of the Terminal Properties of a Circular Antenna Array with a Synthesis Technique for Obtaining a Prescribed Radiation Pattern," Univ. of Tennessee, Scientific Report #2, June 1958.
3. C. E. Hickman, H. P. Neff and J. D. Tillman, "The Theory of Single-Ring Circular Antenna Arrays," Univ. of Tennessee, Scientific Report #4, July 1961.
4. J. D. Tillman, "The Theory and Design of Circular Antenna Arrays," Univ. of Tennessee, Report #6, January 1962.

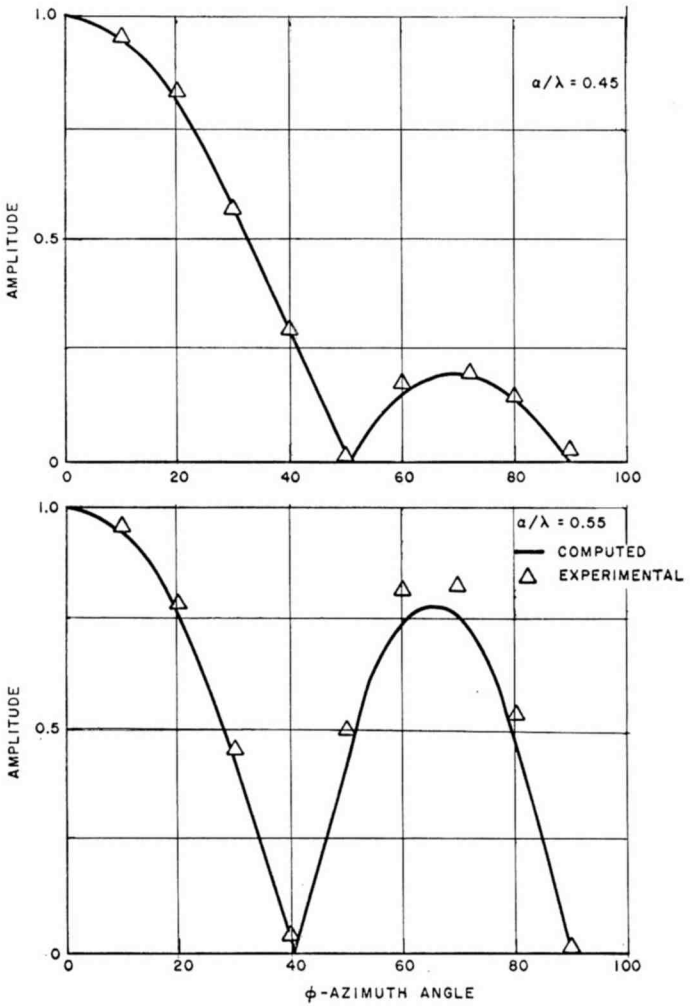

Fig. 39—Model B±1 subset azimuth sum pattern.

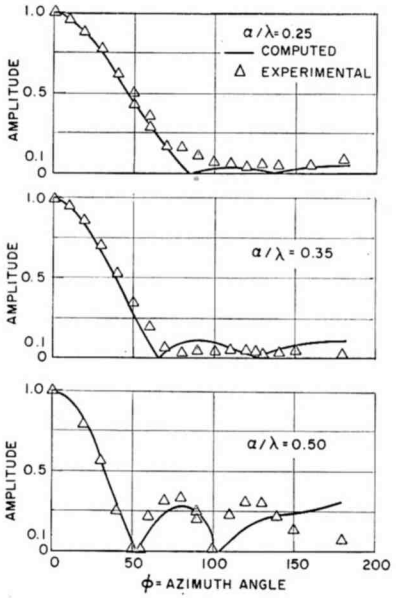

Fig. 40—Model B experimental azimuth sum pattern.

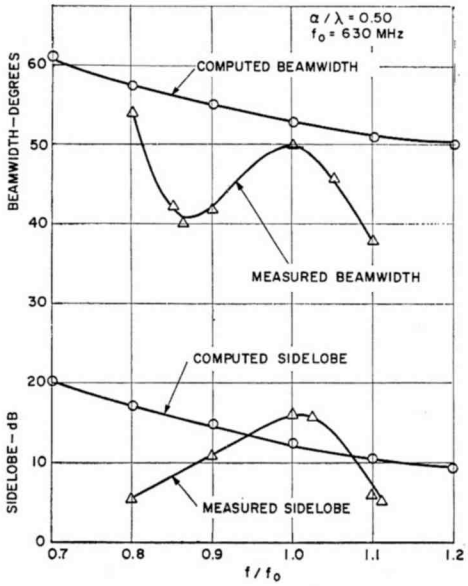

Fig. 41—Measured beamwidth and sidelobe versus f/f_0 of model B array.

ELECTRONIC BORESIGHT SHIFT IN SPACE-BORNE MONOPULSE SYSTEMS

By
H. Honda

RCA Aerospace Systems Division
Burlington, Mass.

Summary A simple method of analyzing the various contributions to the electronic boresight shift in a precision monopulse radar system is discussed. The various antenna and signal parameters that contribute to the shift are expressed in terms of equivalent branch and channel asymmetries. The effects of various error sources upon the overall boresight shift can then be determined easily by adding these asymmetries.

The error sources and their equivalent asymmetries are discussed and derived for a space-vehicle radar system that incorporates most of the possible errors in a monopulse system. Sample calculations of the contribution to electronic boresight shift by some of the error sources are made.

Introduction

ANGULAR ACCURACY and errors in monopulse systems have been discussed in the literature.[1-4] These articles treat errors from the overall systems viewpoint, considering the more general factors such as mechanical changes in antenna mount, receiver noise, and servo characteristics. In this paper, a comprehensive analysis is made of the electronic boresight shift in the monopulse receiving system, including that due to effects in the propagation path (multipath and polarization characteristics of the receive signal), the receiver radiation system, the microwave network, the r-f receiver

[1] D. K. Barton, "Instrumentation Radar AN/FPS-16 (XN-1)," RCA Moorestown, Final Report, Contract DA-36-034-ORD-151.

[2] D. K. Barton, "Accuracy of a Monopulse Radar," Conf. Proc., *3rd Nat. Conv. Mil. Elec.*, p. 179, June-July 1959.

[3] T. J. Vaughan, E. St. George, and R. H. Stanhope, "Error Analysis of Mobile Satellite Tracking Antenna System," *IEEE Trans. SET Rec.*, 1962 Nat. Symp. Space Elec. & Telemetry, paper No. 6.5.

[4] J. A. Develet, "Thermal-Noise Errors in Simultaneous-Lobing and Conical-Scan Angle-Tracking Systems," *IRE Trans*, Vol. SET-7, p. 42, Jan. 1961.

channels, and the phase detector. The paper is devoted to a method of evaluating the performance of the system as related to the error contributions within this portion of the system.

To obtain a simple approach for determining the electronic boresight shift, use is made of branch and channel asymmetry parameters defined by Redlien,[5] where the term "branch" denotes the transmission line between the radiator and the comparator and the term "channel" denotes the post-comparator line (i.e., the line through which the sum and difference signals are transmitted.) Various measurable component parameters of the system that contribute to the shift are interpreted in terms of these asymmetries, and their relationships are derived. This approach is convenient for analyzing the combined effects of many error sources, provided the overall boresight shift is not too large. The imperfections in the system may be expressed in terms of relative complex gain, $\exp(\alpha + j\beta)$ or $\exp(\epsilon + j\phi)$ for the branch and channel, respectively, where, α, β, ϵ, and ϕ are the branch gain, branch phase, channel gain, and channel phase asymmetries, respectively. Because of the exponential form, the α, β, ϵ, and ϕ contributions from the various error sources can be summed algebraically or statistically. The summed asymmetries can then be used in the expression for the boresight shift,[5]

$$\delta_o = \frac{E_s}{2S_d}\left[\beta \tan \phi - \alpha\right], \tag{1}$$

where E_s is the sum signal and S_d is the slope of the difference pattern. δ_o may also be expressed in terms of the measurable quantities null depth (N) and null shift in the antenna error pattern, δ_s,

$$\delta_o = \delta_s + N\frac{\tan \phi}{(S_d/E_s)}.$$

In the next section a description of a monopulse system is given. The error sources and the equivalent asymmetries of the error signals are derived and plotted in Section 3. Examples of the use of the curves are given in Section 4.

---

[5] The derivation of Equation (1) plus a much more sophisticated treatment of the subject is given by H. W. Redlien, Jr., "Theory of Monopulse Operation," Wheeler Laboratories, Inc., Rept. 434B; Jan. 6, 1953, Revised Aug. 17, 1960; AD#289128.

2. Description of the System

A receiver that has been used in a radar for space vehicles and that incorporates most of the possible error sources in a monopulse system is the polarization-duplexed cw system using phase modulation for ranging. It is basically an amplitude monopulse system using a Class I angle detector in Rhodes[6] notation. A detailed diagram of the receiver is shown in Figure 1. The multiplier chain is used both as the transmitter and the local oscillator. (The received signal is from a transponder, whose frequency is side-stepped to obtain the i-f.) The transmitted signal is phase modulated and distributed to four transducers, the output arm of each incorporating a polarizer. Thus, the linearly polarized wave in the transducer is converted to a circularly polarized radiated wave that propagates out through a Cassagrainian reflector system. The distribution network to the transducer is such that the radiated field is summed.

Part of the output from the multiplier chain is distributed to the three monopulse mixers in phase, i.e., in multiples of 2π. The received signal may be linearly polarized; in this case, half the power is converted to energy in the form of a linearly polarized wave of the same orientation as that transmitted (at the output of the transducer) and, hence, propagates down the transmit line; the other half is converted to energy in the form of a linearly polarized wave orthogonal to that transmitted and propagated down the receive line. The energy in the transmit line may be partially reflected from the transmitter and re-radiated.

The signals in the receive lines are heterodyned in separate mixers and amplified. An automatic gain control voltage is developed in the sum channel and used to control the gain of both the sum and difference channels. The outputs of these channels are fed into phase-sensitive detectors to obtain the error signal for the servo system.

The orientation of the linearly polarized wave impinging upon the antenna depends upon the relative orientation of the transponding vehicle and the radar, which may be a time varying function. Further, there may be multipath reflections from the surface upon which the vehicle rests.

3. Error Sources and Equivalent Asymmetries

Any residual signal that contributes to a differential change in branch amplitude and phase asymmetries (α, β), in channel phase

[6] D. R. Rhodes, "*Introduction to Monopulse*," McGraw-Hill Book Co., N. Y., 1959.

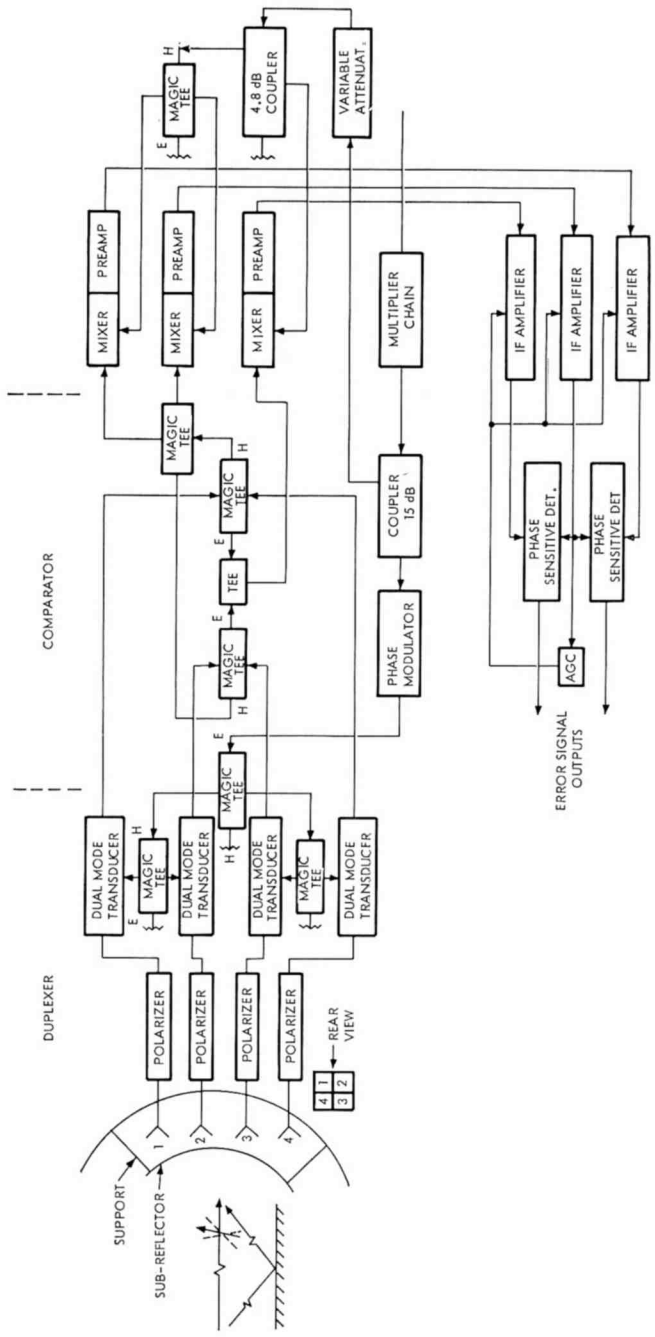

Fig. 1—Detailed diagram of polarization-duplexed system showing the essential features.

asymmetry (ϕ), and in the slope S_d/E_s (the error signal slope normalized to the sum-channel signal) is an error source. In addition to the more obvious sources of error, such as amplitude and phase differences in transmission lines and components, extraneous signals (such as internal and multipath reflections) are present in the precomparator lines and these can be treated as branch asymmetries, as shown in the Appendix.

The channel phase asymmetries are introduced not only by the differences in the components and lengths of transmission lines of the various channels, but by the changes in the apparent local oscillator injection. Thus leakages contribute to this asymmetry.

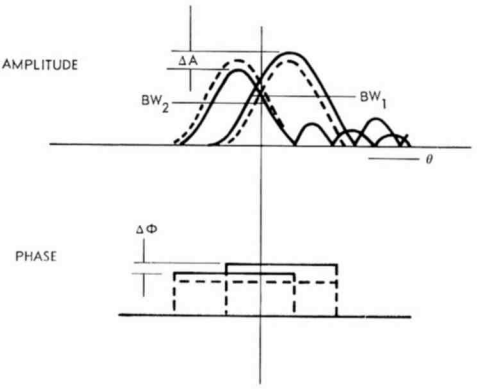

Fig. 2—Lobe-pattern differences causing boresight errors.

These possible sources of errors in the monopulse receiver, all of which contribute to the electronic boresight shift, are discussed in this section, and their equivalent asymmetries are derived in terms of measurable system and component parameters.

Antenna-Pattern Differences

Nonsymmetry in amplitude and/or phase in antenna-lobe patterns near the crossover will cause boresight shifts. The simplified lobe patterns shown in Figure 2 illustrate two possible sources of amplitude errors: differences in relative gain and differences in beam width. The possible causes for these changes include temperature differential across the aperture and vibration, both of which result in displacement of the feed and reflectors from the initially aligned position. Lateral displacement of the subreflector (in a Cassagrainian antenna) causes a gain change and a phase change, the former being dependent upon the beam-

deviation factor. Rotation of the subreflector about its mounting point also results in a gain change. Unequal heating of the feed may cause the feed to tilt and, hence, cause some changes equivalent to the lateral displacement of the subreflector. Minor effects may be caused by a change in feed horn aperture, which contributes to gain and beam width changes.

To determine the asymmetries from this error source, the pattern changes may be treated as a case of unequal input signal (see Appendix). The angle-dependent factors are separated out and treated as a slope change. For small changes in the pattern characteristics, the asymmetries can be derived in terms of the total differentials. Using the notations in the Appendix, (assuming a two-dimensional case for simplicity)

$$\frac{b_3}{b_4} = \frac{a_1 - a_2}{a_1 + a_2}$$

where, in the angular region of interest, a_1 and a_2 may be written as

$$a_1 = E_o g_{o1} \exp\left[- K \left(\frac{\theta - \theta_{o1}}{\theta_{B1}} \right)^2 \right] \exp\{j\psi_{o1}\}$$

$$a_2 = E_o g_{o2} \exp\left[- K \left(\frac{\theta - \theta_{o2}}{\theta_{B2}} \right)^2 \right] \exp\{j\psi_{o2}\}$$

where (for this Gaussian-shaped pattern) $K = 1.389$, E_o is the field from the target at the antenna terminals, g_{o1} and g_{o2} are the gains of the individual horns, θ is the angle from the axis of the antenna, θ_{o1} and θ_{o2} are the beam-offset angles, θ_{B1} and θ_{B2} are the half-power beam widths of the patterns, and ψ_{o1} and ψ_{o2} are the phases of the incoming signal measured at the radiator terminals. From the differential change of (b_3/b_4) from ideal condition near boresight, the equivalent branch gain and phase asymmetries are determined to be

$$\alpha_{eq} \cong \frac{dg_{o1} - dg_{o2}}{g_o} - 2K \frac{\theta_o}{\theta_B} \frac{d\theta_{o1} - d\theta_{o2}}{\theta_B} + 2K \left(\frac{\theta_o}{\theta_B} \right)^2 \frac{d\theta_{B1} - d\theta_{B2}}{\theta_B}$$

$$\beta_{eq} \cong d\psi_{o1} - d\psi_{o2} \,. \tag{2}$$

where g_o is the initial gain of the horns and θ_B is the initial beam width of the lobe patterns. For small changes from ideal conditions derived

above, there is no change in the slope. Where only the first differential is not sufficient, it may be shown that

$$\frac{S'_d}{E'_s} = \frac{1 + \dfrac{\Delta\theta}{\theta_o}}{\left(1 + \dfrac{\Delta\theta_B}{\theta_B}\right)^2} \frac{S_d}{E_s}, \tag{3}$$

where S_d is the slope of the difference pattern, E_s is the sum signal, and the primes indicate effective values.

Precomparator Transmission Line and Component Differences

The amplitude (in nepers) and phase (in radians) differences in the precomparator components, excluding the polarizer, contribute directly to the branch asymmetries and may be summed directly. The polarizers introduce more subtle changes, which are discussed later. In spacecraft applications, the component that perhaps contributes the most error with time is the feed-horn distortion due to unequal heating, as by the jets used to control the vehicle, causing differences in the electrical path length in the waveguide feed. A β-error is thus introduced.

Comparator Imbalance

Comparators may have inherent imbalances in any practical design. These imbalances are usually measured in terms of amplitude and phase, and thus may be added directly in the appropriate asymmetries. The imbalances contribute to α, β, and ϕ errors. The effects of mismatches are discussed later under isolation.

Other Transmission-Line Differences

In addition to the precomparator transmission line considered above, other transmission-line and component characteristics contribute to the boresight error. These lines and associated components include: (1) that between the comparator and the mixers, (2) local oscillator distribution network, and (3) i-f lines between the preamplifiers and the main amplifiers. These line differences contribute directly to the channel phase asymmetry, ϕ.

The rf line lengths between the comparator and the mixers are usually small and nearly equal, and, therefore, changes in the phase (and amplitude) difference are expected to be negligible. However, if

components such as filters are introduced in the line, appreciable phase changes may occur.

The rf line lengths in the local-oscillator (LO) distribution network may differ and be relatively long, depending on the physical layout. Also, components such as directional couplers, hybrid junctions, and tees are used in the distribution network. These will introduce phase differences in the various ports. Since the phase of the local oscillator signal is imparted to the i-f signal, this constitutes a channel phase asymmetry.

The rf line between the preamplifier and the main amplifier can be very long. Further, large amounts of flexure may be engendered in the line as a function of the antenna look angle. Nonuniformity of dielectric constant, distortion of the cable, etc., may lead to phase differences in the line for the three monopulse channels.

The asymmetries due to any of these sources can be directly calculated.

Microwave Transmit-Line Mismatches and Transit-to-Receive Isolation

The effect of mismatches in monopulse systems, such as that used in the example, manifests itself in a number of ways, including

(1) change in transmit-to-receive isolation in the duplexer at transmit frequency (this results in ϕ errors),

(2) change in transmit-to-receive isolation in the duplexer at receive frequency (resulting in α and β errors),

(3) change in sum-to-difference channel isolation at receive frequency (resulting in α, β, and ϕ errors),

(4) change in sum-to-difference channel isolation at transmit frequency (resulting in ϕ errors), and

(5) change in polarization characteristics (resulting in α and β errors).

The first of these effects is discussed here; the others are discussed in succeeding sections.

Lack of sufficient transmit–receive isolation in the duplexer at transmit frequency results in channel phase asymmetry, because the leakage signal entering the mixer and the signal entering the mixer by the proper local oscillator (LO) path will combine to give a phase shift to the resultant LO signal (the LO and transmitter frequencies are the same in the illustrative system being considered). If the leakage signal is sufficiently strong, it will unbalance the mixer so that cancellation of the leakage by the balanced mixers will be degraded. This problem

occurs if there is a change in phase difference between the leakages in the sum and difference channels; the problem is accentuated in the polarization-duplexed system, where symmetrical reflections such as those from the subreflector are directed into the receiver channel. Figure 3 shows the signal and leakage paths of interest.

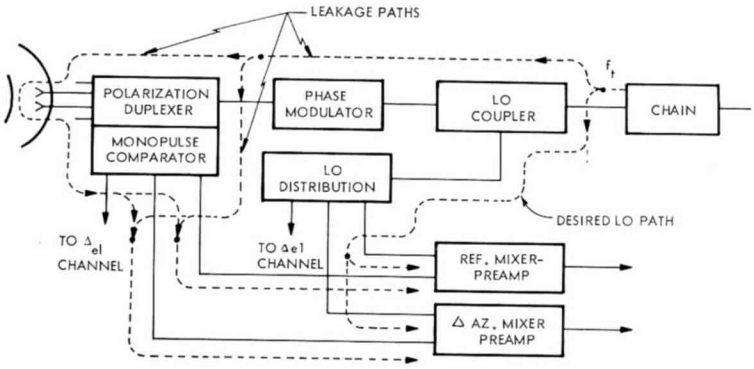

Fig. 3—Transmit–receive isolation problem at transmit frequency.

In the system considered here, ranging information is obtained from a phase-modulated signal, which is present during the angle tracking operation. In the derivation of the equivalent asymmetry, this modulation was assumed to be present. The use of balanced mixers is also assumed, which tends to cancel the leakage. There is, however, residual imbalance, and the level of the leakage may unbalance the mixer.

Let the LO signal be of the form $E_L = A_L \cos \omega_o(t - \tau_L)$ and the leakages in the sum and difference channels be of the form

$$e_\Sigma = A_\Sigma \cos \left[\omega_o(t - \tau_\Sigma) + \sum_{i=1}^{n} \Delta\theta_i \cos \rho_i(t - \tau_\Sigma)\right]$$

$$e_\Delta = A_\Delta \cos \left[\omega_o(t - \tau_\Delta) + \sum_{i=1}^{n} \Delta\theta_i \cos \rho_i(t - \tau_\Delta)\right]$$

and the received signal be of the form (neglecting doppler effects),

$$e_s = A_s \cos \left[\omega_s(t - \tau_s) + \sum_{i=1}^{n} \Delta\theta_j \cos \rho_j(t - \tau_s)\right]$$

where the τ's are delays referred to some reference time and may in-

clude equivalent of any phase shift introduced by the components in the lines. $\Delta\theta$'s and ρ's are the modulation indices and frequencies, respectively, A_s is the amplitude of the received signal, A_Σ and A_Δ are the magnitudes of the leakage currents in the sum and difference channels, and ω_o is the radian frequency of the LO signal.

By elementary mixer theory, the output current from the sum channel mixer is found to be

$$\Delta_i \propto \tfrac{1}{2} A_s \{(g_1+g_2)^2 A_L^2 + (g_1-g_2)^2 A_\Sigma^2 + \text{B}(g_1^2 - g_2^2) A_L A_\Sigma \cos(x-b)\}^{\frac{1}{2}}$$

$$\cos\left\{\omega_{i\text{-}f} t - \phi_s + \tan^{-1}\frac{(g_2-g_1)(A_\Sigma \sin x - (g_1+g_2)A_L \sin b}{(g_2-g_1)(A_\Sigma \cos x + (g_1+g_2)A_L \cos b}\right\}$$

where A_L is the magnitude of the LO signal, g_1 and g_2 are conversion gain for diode 1 and 2 of the balanced mixers, and

$$x = \omega_o \tau_\Sigma - \sum_{i=1}^{n} \lambda\theta_i \cos \rho_i (t - \tau_\Sigma) ,$$

$$b = \omega_o \tau_L ,$$

$$\phi_s = -\omega_s \tau_s + \sum_{i=1}^{n} \Delta\theta_j \cos \rho_j (t - \tau_s) .$$

A similar expression may be derived for the difference-channel mixer.

The channel asymmetry is obtained from the ratio $(\Delta i'/\Delta i)$, where $\Delta i'$ denotes the output current in the difference channel mixer. The expression for Δi shows that there is both amplitude and phase modulation upon the i-f output. If the phase modulation frequency is low, it appears at the final filter output before the phase detector; if the agc does not respond to this frequency, the modulation will appear at the phase detector output. Generally, the antenna servo system will not respond to this relatively high frequency, and no error is introduced by the phase modulation.

The phase term, i.e., the channel phase asymmetry associated with the ratio $\Delta i'/\Delta i$, becomes, after suitable manipulation,

$$\tan\phi \cong c_o d_o \sin\omega_o(\tau_\Delta - \tau_\Sigma) + J_o(\Delta\theta)\,[c_o^2 + d_o^2 - 2c_o d_o \cos\omega_o(\tau_\Delta - \tau_\Sigma)]^{\frac{1}{2}}$$

$$\sin\left[\omega_o(\tau_L - \tau_\Delta) - \tan^{-1}\frac{d_o \sin\omega_o(\tau_\Delta - \tau_\Sigma)}{-c_o - d_o \cos\omega_o(\tau_\Delta - \tau_\Sigma)}\right] \qquad (4)$$

where

$$c_o = \frac{1 - (g_2'/g_1')\ A_\Delta}{1 + (g_2'/g_1')\ A_L'} \frac{}{}, \quad d_o = \frac{1 - (g_2/g_1)\ A_\Sigma}{1 + (g_2/g_1)\ A_L} \frac{}{},$$

where $J_o(\Delta\theta)$ is the Bessel function of zero order. The primes are associated with the difference channel.

An example of how ϕ varies in a typical microwave network will now be considered. The ratio of the conversion loss of the diodes in a balanced mixer is a function of the leakage: A_Δ/A_L' or A_Σ/A_L, as the case may be. A typical variation in the conversion loss for worst-case

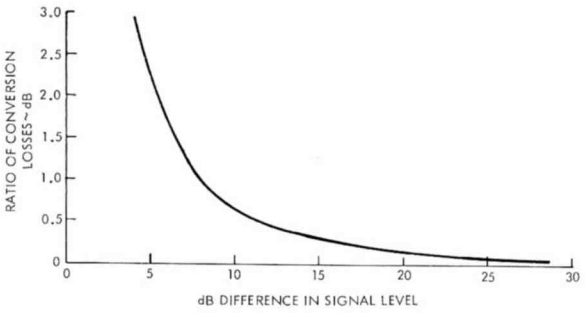

Fig. 4—Variation in conversion loss of mixers.

conditions is shown in Figure 4. Based upon this curve and assuming $A_\Delta/A_L = -10$ dB, and $\Delta\theta = 0.3$, the bounds for ϕ as a function of the ratio of the leakage to the LO level are as shown in Figure 5.

Mismatch in Transmit Line at Receive Frequency

The problem of duplexer isolation at receive frequencies is illustrated in Figure 6, where the linearly polarized received signal is divided equally into the transmit and receive arms in the precomparator circuit. With mismatches in the transmit and antenna lines, there would be coupling of signal into the receive line, and if the phase and amplitude of the coupled energy are unequal in the sum and difference channels, boresight shift will result. This cross-coupled signal is equivalent to having branch asymmetries. The problem is usually minor, and occurs only in polarization-duplexed system, as in the example considered here, and with received signal having opposite sense polarization components. The equivalent asymmetry is clearly a case of

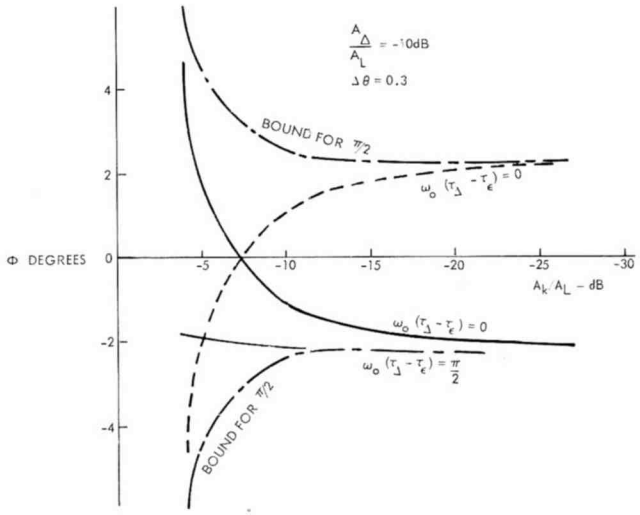

Fig. 5—Bounds for phase asymmetry due to transmitter leakage.

input signal imbalance, as discussed in the Appendix, and the functions to be determined are $\Delta a_1 \exp\{j\psi_1\}$ and $\Delta a_2 \exp\{j\psi_2\}$. Evidently,

$$\Delta a \exp\{j\psi\} = \sqrt{1/2}\, k_t \Gamma_t \Gamma_a a \exp\{-j(\phi_{\gamma t} + \phi_{\gamma a})\},$$

where k_t is reflected wave coupling factor due to the system polarization characteristics, Γ_t and Γ_a are the reflection coefficients in the transmit and antenna (common to receive and transmit signals) lines, respectively, and $\phi_{\gamma t}$ and $\phi_{\gamma a}$ are their respective phase shifts, including that due to the line-length differences.

The equivalent branch asymmetries may be obtained directly from

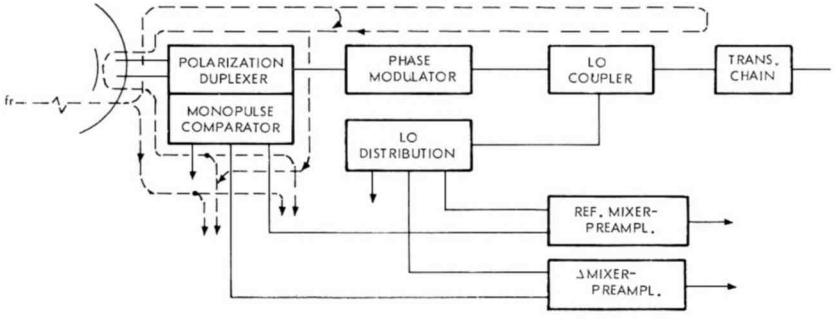

Fig. 6—Transmit–receive isolation problem at receive frequency.

the Appendix. Denoting the two branches of the comparator by subscripts 1 and 2,

$$\alpha_{eq} = M \cos (\phi_{\gamma t} + \phi_{\gamma})$$

$$\beta_{eq} = -M \sin (\phi_{\gamma t} + \phi_{\gamma}) \tag{5}$$

where

$$M = k_{t1}\Gamma_{a1}\Gamma_t \left[1 - \left(\frac{k_{t1}\Gamma_{a2}}{k_{t1}\Gamma_{a1}} \right) - 2 \left(\frac{k_{t2}\Gamma_{a2}}{k_{t1}\Gamma_{a1}} \right) \cos (\phi_{\gamma a1} - \phi_{\gamma a2}) \right]^{1/2}$$

$$\phi_{\gamma} = \tan^{-1} \frac{\sin \phi_{\gamma a1} - [k_{t2}\Gamma_{a2}/(k_{t1}\Gamma_{a1})] \sin \phi_{\gamma a2}}{\cos \phi_{\gamma a1} - [k_{t2}\Gamma_{a2}/(k_{t1}\Gamma_{a1})] \cos \phi_{\gamma a2}},$$

or, in terms of cross coupling (isolation) between the transmit and receive channels, k_c,

$$M = k_{c1}\Gamma_t \left[1 + (k_{c2}/k_{c1})^2 - 2(k_{c2}/k_{c1}) \cos (\phi_{\gamma a1} - \phi_{\gamma a2}) \right]^{\frac{1}{2}},$$

$$\phi_{\gamma} = \tan^{-1} \frac{\sin \phi_{\gamma a1} - (k_{c2}/k_{c1}) \sin \phi_{\gamma a2}}{\cos \phi_{\gamma a1} - (k_{c2}/k_{c1}) \cos \phi_{\gamma a2}}.$$

The above equations for α_{eq} and β_{eq} are parametric equations of a circle, with the phase of the transmit-line reflection as a parameter. If k_c, Γ_t, and $\phi_{\gamma a}$ are known, the branch asymmetries can readily be determined; if all the parameters are not known, the range of values for the asymmetries can be determined. From the plot of the above expression in Figure 7, for $k_{c2} = k_{c1}$ and $\phi_{\gamma a1} - \phi_{\gamma a2} = \pi$, the variation of the asymmetries as functions of the various parameters can be determined. (The above conditions for k_c and $\phi_{\gamma a}$ represent worst case).

Microwave Receive-Line Mismatches and Sum-to-Difference Channel Isolation

Precomparator mismatches tend to reduce the isolation between the sum and difference channels; if the post-comparator line presents a mismatch to the comparator, cross coupling of signal will occur between these channels. Coupling to the difference channel from the sum channel is of particular importance, since the signal level in the sum channel is at a much higher level. Figure 8 shows the sigal paths con-

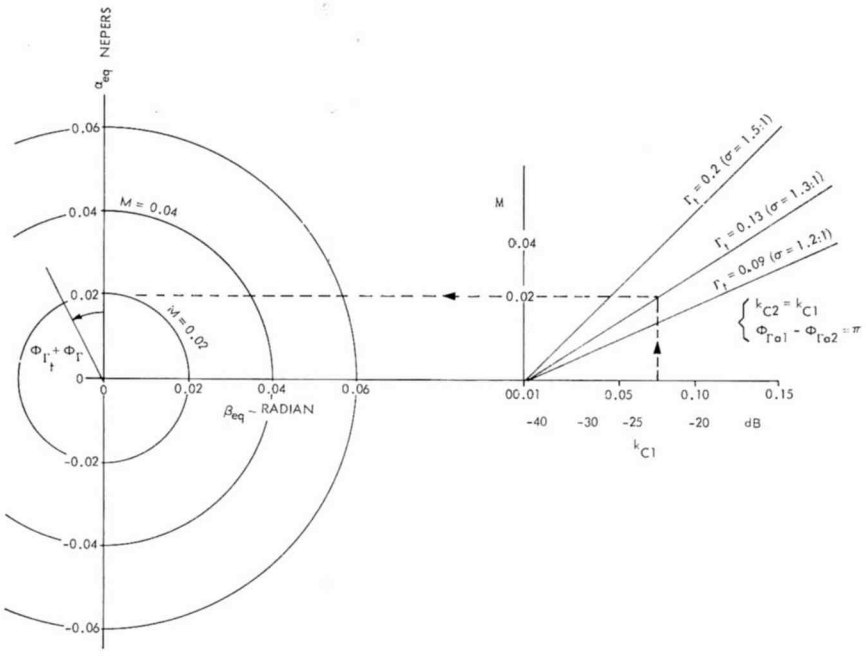

Fig. 7—Effect of transmit-line mismatch at receive frequency.

cerned in this problem. There is a corresponding reflected path to the other delta channel (not shown in Figure 8) and the reflected paths from the difference channels to the sum channel, which are of minor importance.

Time-invariant mismatches do not present serious problems, since the asymmetries introduced may be calibrated during the boresighting

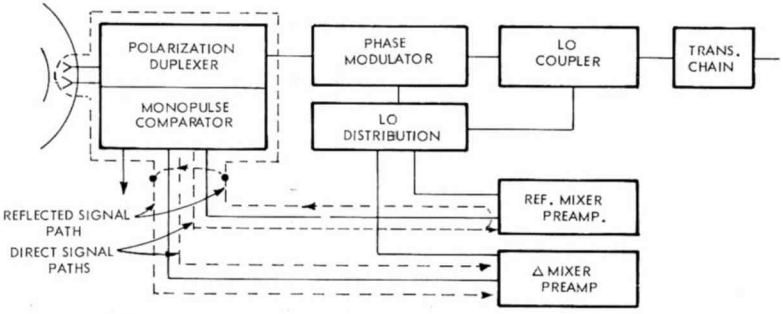

Fig. 8—Sum-to-difference channel-isolation problem.

procedure. However, the reflections from the mixer, and hence the isolation, can vary with time as a function of temperature. Also, the mixer impedance may vary with local-oscillator level, bias variation, signal level, and imbalance in mixers due to leakages and crystal degradation. The problem exists at both the transmit and receive frequencies, the former introducing ϕ errors and the latter, α, β, and ϕ errors.

We consider the receiver frequency case first. The asymmetries will be determined using scattering matrices of the mismatched elements and of the comparator, which will be assumed to be an ideal hybrid junction. Referring to Figure 9, if we assume the mismatched junc-

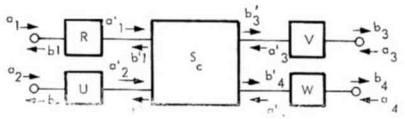

Fig. 9—Basic network for receive-line mismatch problem.

tions R, U, V, and W are lossless, their scattering matrices may be written in the form

$$[R] = \begin{bmatrix} r_{11} r_{12} \\ r_{12} r_{11} \end{bmatrix}$$

where r_{11} and r_{12} are in quadrature, and may be written

$$r_{11} = \Gamma_r$$

$$r_{12} = j\sqrt{1 - \Gamma_r^2}$$

Γ_r is the reflection coefficient of that junction.

By algebraic and matrix operations, the ratio of the outputs from the comparator, S_c, may readily be determined to be

$$\frac{b_4'}{b_3'} = \frac{A_1(v)}{A_1(w)} \frac{(\Delta'/\epsilon') - A_2(v)/A_1(v)}{1 - (\Delta'/\epsilon')A_2(w)/A_1(v)},$$

where

$$\begin{bmatrix} \epsilon' \\ \Delta' \end{bmatrix} = r_{12} a_1 \exp\{-j(\phi_{r1} + \phi_{r2})\} [\pm] u_{12} a_2 \exp\{-j(\phi_{u1} + \phi_{u2})\}$$

$$A_1(x) = \sqrt{2} - \frac{x_{11}}{\sqrt{2}} \exp\{-j2\phi_{x1}\}(r_{11} \exp\{-j2\phi_{r2}\} + u_{11} \exp\{-j2\phi_{u2}\})$$

$$A_2(x) = -\sqrt{1/2}\, x_{11} \exp\{-j2\phi_{x1}\}(r_{11} \exp\{-j2\phi_{r2}\} - u_{11} \exp\{-j2\phi_{u2}\})$$

and where the ϕ's are the phases associated with the line lengths between the mismatched junctions and the appropriate terminals of the hybrid junction or the input and output terminals.

In a practical design $\phi_{r1} + \phi_{r2} \cong \phi_{u1} + \phi_{u2}$, since this relationship governs the null depth of the difference pattern. For relatively small reflection coefficients, the outputs from the comparator becomes

$$\frac{b_4'}{b_3'} \cong \frac{\Delta'}{\epsilon'} - \frac{A_2(v)}{A_1(v)} .$$

Finally, the equivalent branch asymmetries, in terms of the sum-to-difference channel isolation, σ, and its phase ϕ_σ, becomes (assuming the cross coupling is caused primarily by the reflections)

$$\alpha_{eq} \cong -\tfrac{1}{2}(r_{11}^2 - u_{11}^2) + V_{11}\sigma \cos(2\phi_{v1} - \phi_\sigma) ,$$

$$\beta_{eq} \cong v_{11}\sigma \sin(2\phi_{v1} - \phi_\sigma) . \tag{6}$$

These expressions are again parametric equations for a circle in the α_{eq}-β_{eq} plane, with the center displaced $(r_{11}^2 - u_{11}^2)/2$ along the α_{eq} axis.

In terms of the scattering parameters r_{11} and u_{11} and their associated phases ϕ_r and ϕ_u,

$$\sigma = [r_{11}^2 + u_{11}^2 - 2u_{11}r_{11} \cos 2(\phi_{r2} - \phi_{u2})]^{1/2} ,$$

$$\phi_\sigma = \tan^{-1} \frac{r_{11} \sin 2\phi_{r2} - u_{11} \sin 2\phi_{u2}}{r_{11} \cos 2\phi_{r2} - u_{11} \cos 2\phi_{u2}} .$$

The channel phase asymmetry can readily be determined to be

$$\phi_{eq} = (\phi_{w1} - \phi_{w2}) - (\phi_{v1} - \phi_{v2}) . \tag{7}$$

Variation of α_{eq} and β_{eq} as a function of the component parameters v_{11} and σ is plotted in Figure 10, assuming $r_{11} = u_{11}$.

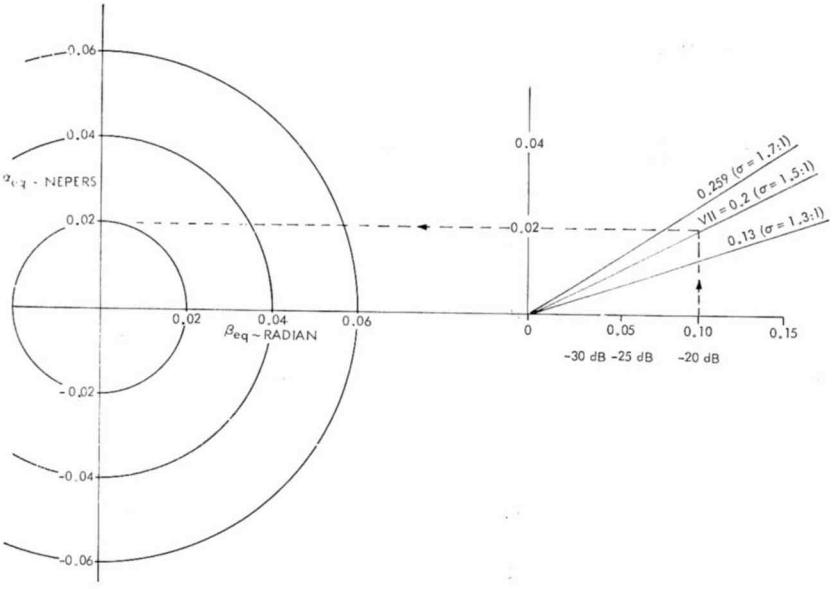

Fig. 10—Effect of receive-line mismatches.

Polarization Orientation and Polarizer Changes

In a system where individual horn outputs are circularly polarized, orientation of the incoming polarization may introduce boresight shifts because of dissimilarities in the polarizer. This nonuniformity causes the signal return in each of the comparator branches to differ both in amplitude and phase, thus introducing α and β errors. (To the first order, these errors are independent of the angular direction of the incident wave near the boresight axis.) A block diagram of the part of the system of interest is shown in Figure 11.

The combined effect of the differences in the polarizer, the mismatches in the feed, and the polarization response of the antenna pat-

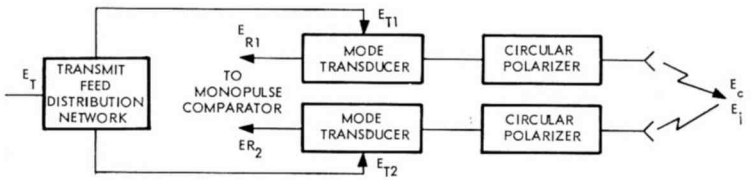

Fig. 11—Block diagram of antenna feed.

terns near the crossover can be lumped together into a single equivalent polarization system, which may take the form of a linear phase shifter that can be oriented with respect to the impinging wave components. This equivalent polarizer is characterized by its orientation, χ_p, and the differential phase shift β_p (between the parallel and perpendicular components of wave passing through the linear phase shifter). Figure 12 depicts the problem. The X-components are of interest; as shown, these components can differ in amplitude and in phase.

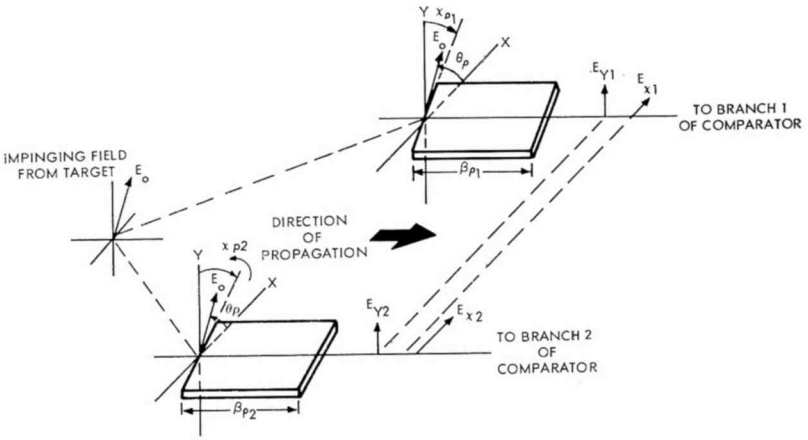

Fig. 12—Diagram showing polarization problem.

The temperature effect on the polarizer itself and upon the feed assembly as well as the orientation of the incoming wave polarization, is therefore a factor in this error. Mismatches in the system and unequal losses to the orthogonal linear components of the wave will also affect the polarization characteristics.

To analyze the errors introduced in the polarization system, consider the E-vector impinging upon the polarizer to be in the Y-direction upon transmission; the component of interest upon reception is that in the X-direction. To simplify the analysis, only tracking in two dimensions will be considered; thus only two polarizers are of concern, and these will be donated by subscripts 1 and 2.

This is a case of asymmetry in the branch "transfer" function, as discussed in the Appendix, and the quantity that is to be determined to obtain the equivalent asymmetries is $\exp\{\alpha_1 - \alpha_2\} \exp\{j(\beta_1 - \beta_2)\}$. If the impinging **E**-vector is at an angle θ_p to the X-axis of the equivalent polarizer, then

$$\vec{\mathbf{E}}_{op} = E_o(\hat{\imath}\cos\theta_p + \hat{j}\sin\theta_p)$$

using the standard vector notations. Upon passing through one of the polarizers, the X-component of the wave, which is the component of interest, is given by

$$E_x = E_o[\exp\{-j\beta_p\}\sin(\theta_p + \chi_p)\sin\chi_p + \cos(\theta_p + \chi_p)\cos\chi_p]$$

Since E_o is "a" in the notation used in the Appendix, equating the real and imaginary parts of the expansion of $\exp(\alpha + j\beta)$ to the corresponding parts of the expression in the brackets in the above equation, squaring, and rearranging terms, we obtain

$$\exp\{2\alpha\} = \cos^2\theta_p - \tfrac{1}{2}\sin 2(\theta_p + \chi_p)\sin 2\chi_p[1 - \cos\beta_p] .$$

The ratio of the imaginary part to the real part results in an expression from which is derived the phase asymmetry,

$$\tan\beta = \frac{-[\cos\theta_p - \cos(\theta_p + 2\chi_p)]\sin\beta_p}{[\cos\theta_p - \cos(\theta_p + 2\chi_p)]\cos\beta_p + [\cos\theta_p + \cos(\theta_p + 2\chi_p)]} .$$

In terms of the deviations from circularly polarized condition, i.e., $\chi_p = (\pi/4) + \lambda$ and $\beta_p = \pi/2 + \mu$, letting the polarizer parameters relating to polarizer 1 be λ and μ and those relating to polarizer 2 be $\lambda + \lambda_\Delta$ and $\mu + \mu_\Delta$, where λ_Δ and μ_Δ are small, the equivalent branch asymmetries become

$$\alpha_{eq} \cong \alpha_o \sin(2\theta_p + \chi_a) , \tag{8}$$

$$\beta_{eq} \cong \beta_c + \beta_o \sin(2\theta_p + \chi_\beta) ,$$

where

$$\alpha_o = \tfrac{1}{2}(D_1^2 + F_1^2)^{\frac{1}{2}} ,$$
$$\chi_a = \tan^{-1}(D_1/F_1) ,$$
$$\beta_c = c_o(1 - \tfrac{1}{2}a_3c_1 - \tfrac{1}{2}a_4c_2) ,$$
$$\beta_o = c_o[(c_1 - a_3)^2 + (c_2 - a_4)^2]^{\frac{1}{2}} ,$$
$$\chi_\beta = \tan^{-1}(c_1 - a_3)/(c_2 - a_4) ,$$
$$D_1 \cong \mu_\Delta[4(\lambda + \lambda_\Delta)^2 - 1] + 4(2\lambda\lambda_\Delta - \lambda_\Delta^2)(1 + \mu) ,$$
$$F_1 \cong -2[\lambda\mu_\Delta + \lambda_\Delta + \mu\lambda_\Delta + \lambda_\Delta\mu_\Delta] ,$$
$$c_o \cong \tfrac{1}{2}(1 + \mu + \mu_\Delta + 2\lambda_\Delta - \tfrac{1}{4}\mu^2 - 4\lambda^2 - \lambda_\Delta^2 + 2\lambda\mu_\Delta + \frac{3}{2}\mu_\Delta\lambda_\Delta - \tfrac{1}{2}\mu\mu_\Delta - 4\lambda\lambda_\Delta) ,$$
$$a_3 \cong -\tfrac{1}{2}(\mu_\Delta + 2\mu + \mu_\Delta\lambda_\Delta - 2\lambda_\Delta^2 - 8\lambda^2 - 8\lambda\lambda_\Delta) ,$$
$$a_4 \cong \lambda_\Delta + 2\lambda - \lambda^2 - \tfrac{1}{4}\mu_\Delta^2 + 2\mu\lambda - \mu_\Delta\lambda + \mu\lambda_\Delta + \tfrac{1}{2}\mu_\Delta\lambda_\Delta ,$$
$$c_1 \cong 2(\lambda_\Delta + \lambda\mu_\Delta - \tfrac{1}{2}\lambda_\Delta\mu_\Delta - \tfrac{1}{2}\mu\mu_\Delta - \mu\lambda_\Delta - \tfrac{1}{4}\mu_\Delta^2 - 2\lambda_\Delta^2) ,$$
$$c_2 \cong \mu_\Delta - \mu_\Delta\lambda_\Delta + 2\lambda\mu_\Delta - 4\lambda\lambda_\Delta - \mu\mu_\Delta - \mu_\Delta^2 .$$

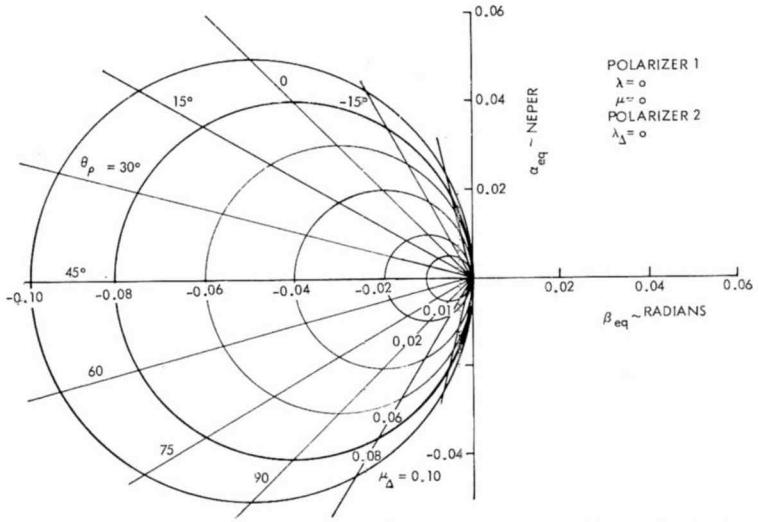

Fig. 13—Equivalent branch asymmetries due to polarization orientation for $\lambda_\Delta = 0$.

The above equations for the asymmetries are parametric equations in terms of the parameter, θ_p, of an ellipse with its origin displaced along the β_{eq} axis and oriented at a 45° angle to that axis. A set of curves for various values of λ_Δ is plotted on the $\alpha_{eq} - \beta_{eq}$ plane, with one of the polarizers assumed to be perfectly circular ($\lambda = \mu = 0$). Contours of constant μ_Δ and constant polarization angle θ are shown in Figures 13 through 16 for $\lambda_\Delta = 0$, 0.01, 0.02, and 0.04 radian, respectively.

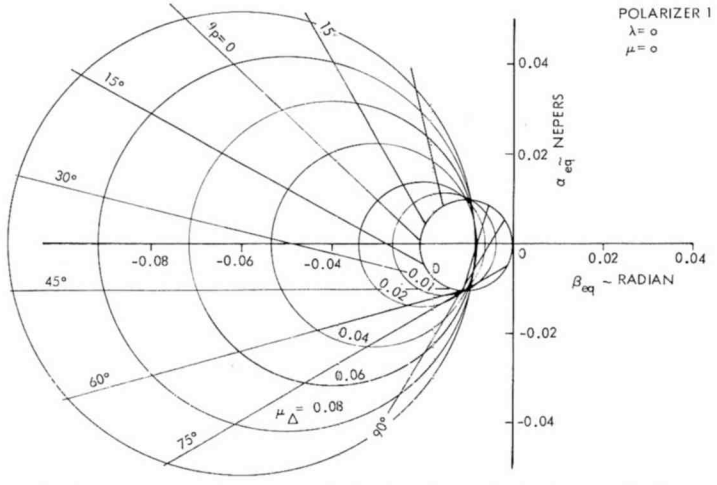

Fig. 14—Equivalent branch asymmetries due to polarization orientation for $\lambda_\Delta = 0.01$.

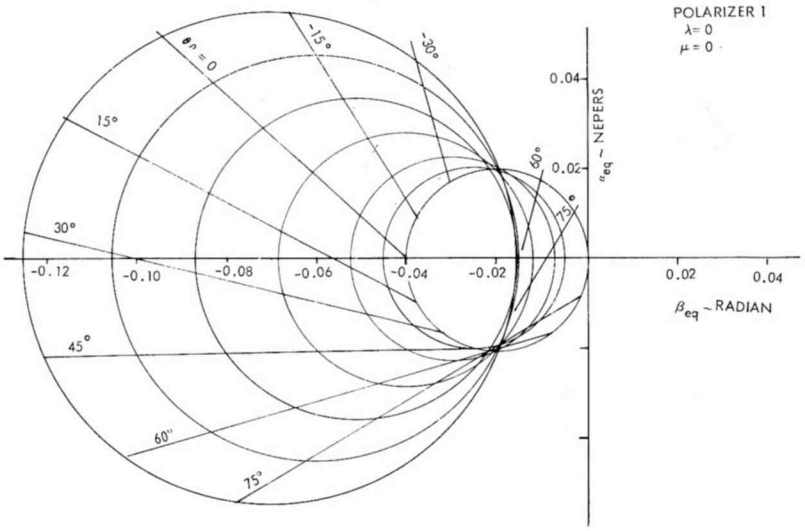

Fig. 15—Equivalent branch asymmetries due to polarization orientation for $\lambda_\Delta = 0.02$.

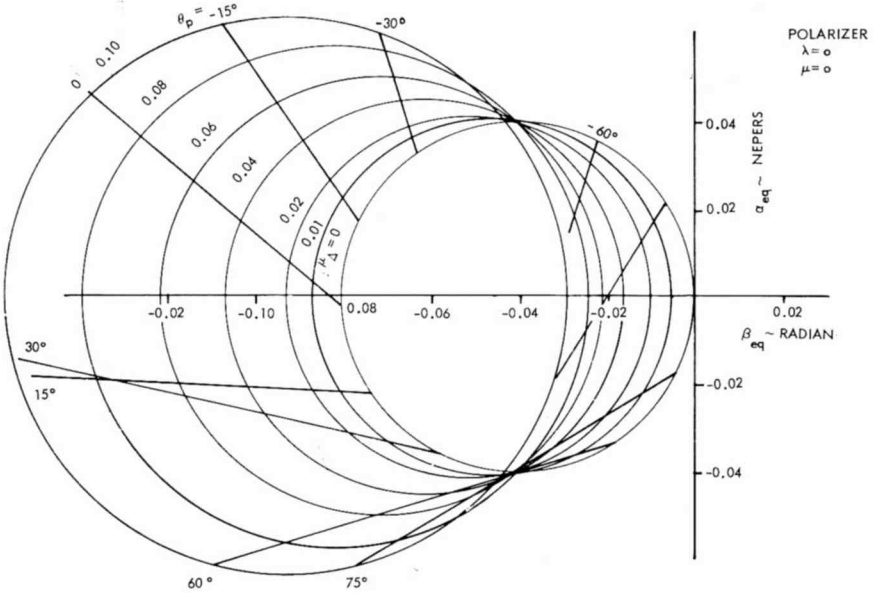

Fig. 16—Equivalent branch asymmetries due to polarization orientation for $\lambda_\Delta = 0.04$.

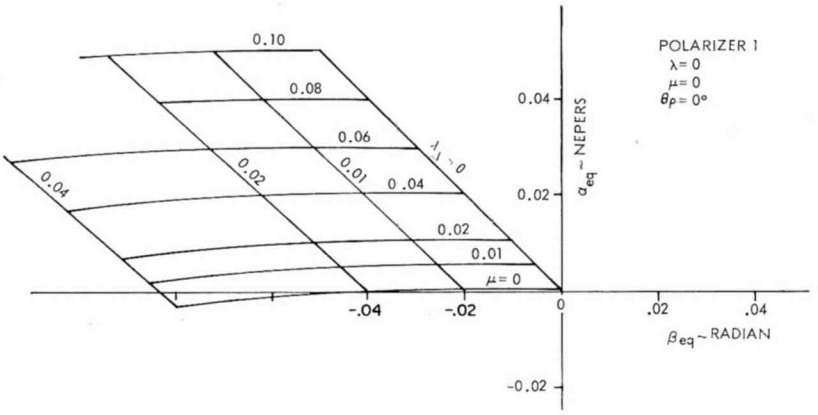

Fig. 17—Effect of change of polarizer parameters for 0° input-wave polarization orientation.

Another condition of interest is the variation in branch asymmetries with changes in the polarizer parameters for cases where the input wave polarization is constant. This may be obtained from the set of curves in the above figures for the condition of one polarizer being perfect. The values obtained from these curves are plotted in the $\alpha_{eq} - \beta_{eq}$ plane for polarization orientations of 0 and 45°, as shown in Figures 17 and 18, respectively.

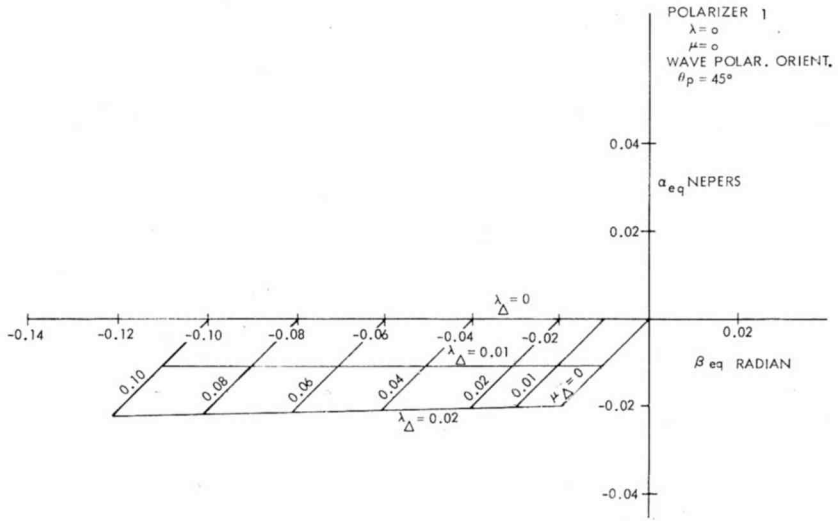

Fig. 18—Effect of polarizer parameter changes for 45° input-wave polarization orientation.

Cross-Coupling in Mixers and LO Distribution Network

Three basic problems are associated with cross coupling in the local-oscillator distribution network and in the mixers. These are: (1) coupling of LO signal from one mixer to the other through the distribution network, (2) coupling of LO signal from one mixer to another through the signal path in the comparator, and (3) coupling of received signal from one mixer to the other through the LO distribution network. (Coupling of received signal from one mixer to the other through the comparator was discussed previously.) These sources result in ϕ-errors. Figures 19, 20, and 21 show the signal paths for each of the above cases for one of the difference channels and for the sum channel.

In the first case, the resultant of the LO signal from the mixer and the cross-coupled LO signal resulting from the reflections from the various mixers gives rise to channel phase error between the reference (sum) channel and one of the difference channels, given approximately by

$$\phi_{eq} \cong k_{L12}[\Gamma_2 \sin (2\phi_1 + \phi_{\Gamma 2} - \Gamma_1 \sin (2\phi_1 + \phi_{\Gamma 1})] + \Gamma_3(k_{L13} - k_{L23}) \sin (2\phi_1 + \phi_{\Gamma 3}) , \quad (9)$$

and gain asymmetry of

$$\epsilon_{eq} \cong k_{L12}[\Gamma_2 \cos (2\phi_1 + \phi_2) - \Gamma_1 \cos (2\phi_1 + \phi_{\Gamma 1})] + \Gamma_3(k_{L13} - k_{L23}) \cos (2\phi_1 + \phi_{\Gamma 3}) , \quad (10)$$

where $\Gamma_i \exp \{j\phi_{\Gamma i}\}$ is the complex reflection coefficient of the mixers, with subscripts appropriate to each mixer; k_{Lij} is the coupling coefficient in the LO distribution network from the ith to the jth mixer, and ϕ_i is the phase shift introduced in the line between the distribution network and the mixers (assumed equal in the above approximation).

For the case of LO coupling through the mixer and the comparator, the balance of the mixers must be considered. If the coupling is sufficiently high, it may unbalance the mixers. Denoting the conversion gain of the balanced mixers as g_{mn} where m refers to the mixer and n to the diode in that mixer, and k_{mi} and k_{cij} as the coupling coefficients from the LO terminals of the mixer to its signal terminals and the comparator, respectively, the equivalent channel asymmetry between two of the channels is given by

$$\phi_{eq} \cong \phi_{s1} - \phi_{s2} + \chi_{11} \frac{1 - (g_{12}/g_{11})(M_{12}/M_{11})}{1 + (g_{12}/g_{11})(M_{12}/M_{11})} - \chi_{21} \frac{1 - (g_{22}/g_{21})(M_{22}/M_{21})}{1 + (g_{22}/g_{21})(M_{22}/M_{21})} , \quad (11)$$

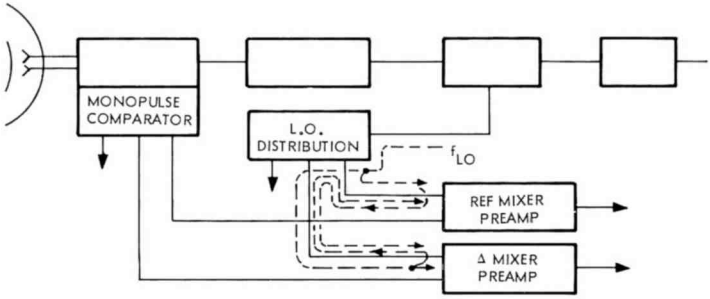

Fig. 19—Crosscoupling of LO signal through LO path.

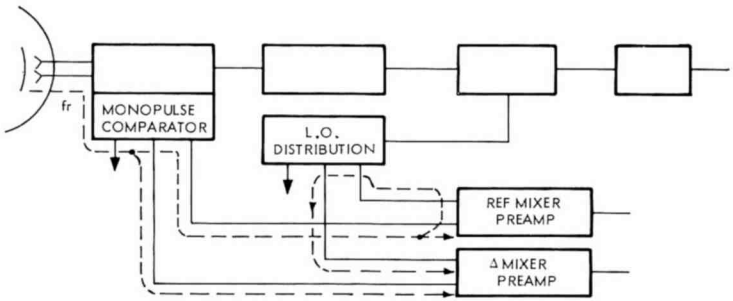

Fig. 20—Crosscoupling of received signal through LO path.

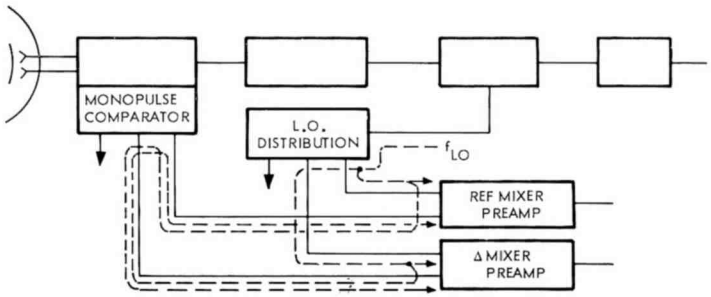

Fig. 21—Crosscoupling of LO signal through receive path.

where

$$\frac{M_{12}}{M_{11}} \cong 1 - 2[k_{m2}k_{c12}\cos(\phi_{L2}+\phi_1+\phi_2) + k_{m3}k_{c13}\cos(\phi_{L3}+\phi_1+\phi_3)],$$

$$\frac{M_{22}}{M_{21}} \cong 1 - 2[k_{m1}k_{c12}\cos(\phi_1+\phi_2-\phi_{L2}) + k_{m3}k_{c23}\cos(\phi_{L3}-\phi_{L2}+\phi_2+\phi_3)].$$

and ϕ_{s1} and ϕ_{s2} are the received signal phases.

The cross coupling of the received signal through the mixer and the LO distribution network is analogous to the above case, with the received signal in the place of the LO. Also, the coupling of interest is primarily from the sum channel to the difference channel, since the signal strength in the former is very much greater than that in the latter in the angular region of interest. The channel phase asymmetries are then given by

$$\phi_{eq} = \phi_{L2} - \phi_{s2} - \tan^{-1}\frac{g_{21}M_{21}\sin\chi'_{21} + g_{22}M_{22}\sin\chi'_{22}}{g_{21}M_{21}\cos\chi'_{21} + g_{22}M_{22}\cos\chi'_{22}} + \tan^{-1}\frac{g_{11}M_{11}\sin\chi_{11} + g_{12}M_{12}\sin\chi_{12}}{g_{11}M_{11}\cos\chi_{11} + g_{12}M_{12}\cos\chi_{12}}, \quad (12)$$

where

$$\begin{Bmatrix} M_{11} \\ M_{12} \end{Bmatrix} = \left\{1 \pm \left[\frac{E_{s2}}{E_{s1}}k_{m2}k_{L12}\cos(2\phi_1+\phi_{s2}) + \frac{E_{s3}}{E_{s1}}k_{m3}k_{L13}\cos(2\phi_1+\phi_{s3})\right]\right\}$$

$$\sin\begin{Bmatrix}\chi_{11}\\ \chi_{12}\end{Bmatrix} \cong \begin{Bmatrix}\chi_{11}\\ \chi_{12}\end{Bmatrix} \cong \pm\left[\frac{E_{s2}}{E_{s1}}k_{m2}k_{L12}\sin(2\phi_1+\phi_{s2}) + \frac{E_{s3}}{E_{s1}}k_{m3}k_{L13}\sin(2\phi_1-\phi_{s3})\right]$$

$$\begin{Bmatrix} M_{21} \\ M_{22} \end{Bmatrix} \cong \left\{\left(\frac{E_{s2}}{E_{s1}}\right)^2 + (k_{m1}k_{L12})^2 \pm 2\frac{E_{s2}}{E_{s1}}[k_{m1}k_{L12}\cos(2\phi_1-\phi_{s2})]\right\}^{\frac{1}{2}},$$

$$\begin{Bmatrix} \chi'_{21} \\ \chi'_{22} \end{Bmatrix} \cong \pm\tan^{-1} - \frac{k_{m1}k_{L12}\sin(2\phi_1-\phi_{s2})}{(E_{s2}/E_{s1}) \pm k_{m1}k_{L12}\cos(2\phi_1-\phi_{s2})}.$$

Typical curves for the effect of cross coupling for the three cases are given in Figures 22, 23 and 24.

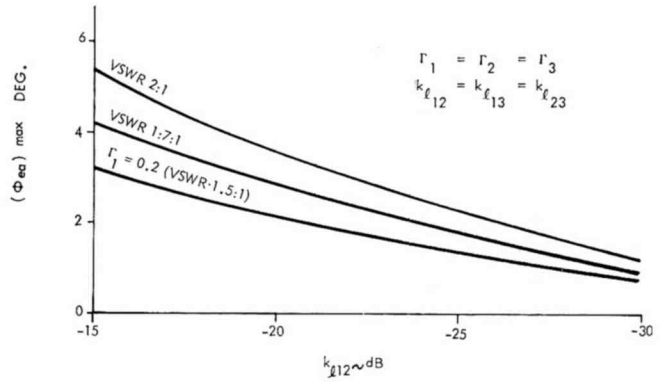

Fig.22—Effect of LO coupling through LO distribution network.

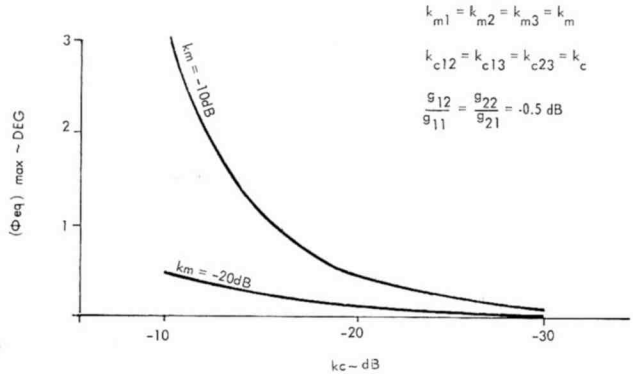

Feg. 23—Effect of LO coupling through mixer and comparator.

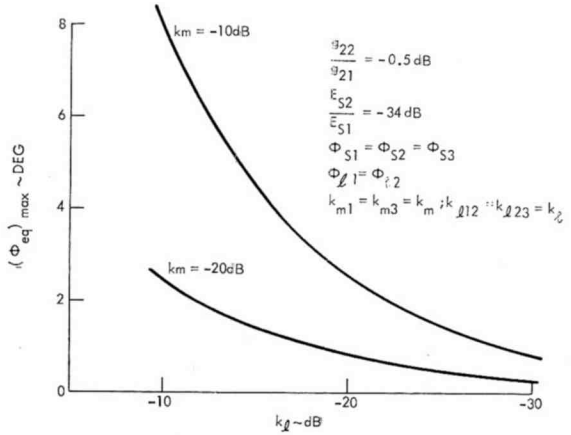

Fig. 24—Effect of signal coupling through mixer and LO distribution network.

Change in Receiver Phase and Gain

Some of the factors affecting the phase difference between the sum and difference channel are: (1) agc action with change in input signal level, (2) filter and other component phase change with temperature, and (3) LO phase differences to various mixers, similar to that discussed for the rf case, but of lesser importance. The lack of balance in the phase detector and other factors contribute to the phase detector errors. These phase differences enter directly into the boresight shift equation as channel phase asymmetry.

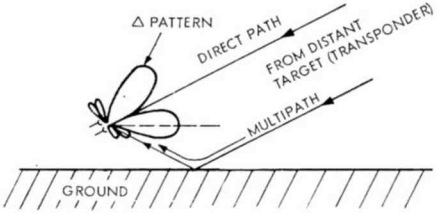

Fig. 25—Geometry of multipath condition.

Multipath

Energy received by a radar system located near the ground is a vector sum of the energy that arrives from the target over the direct path and that which is reflected or scattered from the terrain near the radar antenna. The geometry of the situation where this problem occurs is shown in Figure 25. If the multipath signal is relatively high, a boresight shift results.

The multipath energy may be considered to be an extraneous signal and hence to result in α and β error. It is a function of the ground-reflection coefficient, difference-pattern side-lobe level (the sum-pattern side-lobe level is of second-order importance), and the position of the target.

This approach is slightly different from that used by other investigators.[7] Strictly speaking, for the effect of "spurious" signals to qualify as branch asymmetries, the signal in the branch arm of the comparator in which the asymmetry is assumed must be independent of the angle of arrival of the signal. However, the multipath signal

[7] D. K. Barton, "*Radar System Analysis*," Prentice-Hall, Inc., N. Y., 1964.

received near the peak of the difference pattern is essentially constant for small changes in target position about the boresight axis. Further, we are mainly interested in the limiting value for side-lobe level, i.e., the locus of maximum values of the side-lobe level.

This situation corresponds to the case of input signal "imbalance" (see Appendix), and the functions required are $\Delta a_i \exp\{j\psi_1\}$ and $\Delta a_2 \exp\{j\psi_2\}$. The signals in each of the two radiators, in the elevation plane, consists of a direct path signal $a = E(\theta)$ and a multipath signal $e_m(\theta)$. These signals are related to the voltage pattern function of the individual radiators. Assuming the system is equally responsive to any orientation of impinging linear polarization,

$$a_1 = E_o g_1(\theta - \theta_o)$$

$$a_2 = E_o g_2(\theta - \theta_o)$$

$$e_{m1}(\theta) = \Delta a_1 \exp\{j\psi_1\} = E_o \rho g_1(\theta - 2\theta_E - \theta_o) \exp\{j\psi_m\},$$

$$e_{m2}(\theta) = \Delta a_2 \exp\{j\psi_2\} = E_o \rho g_2(\theta - 2\theta_E - \theta_o) \exp\{j\psi_m\},$$

where θ_E is the antenna pointing angle above the horizon, ρ is the ground-reflection coefficient, and ψ_m is the phase shift due to increased path length in multipath and to the reflectivity characteristics of the ground. By use of the expression in the Appendix, the following equivalent branch asymmetries are readily obtained:

$$\alpha_{eq} \cong \frac{2\Delta_s}{\Sigma} \cos\psi_m, \qquad (13)$$

$$\beta_{eq} \cong \frac{2\Delta_s}{\Sigma} \sin\psi_m,$$

where Δ_s/Σ is the difference pattern side-lobe level relative to the peak of the sum pattern. This is a parametric equation of a circle for constant ρ and (Δ_s/Σ). Figure 26 shows a procedure for determining the asymmetries.

The foregoing analysis may readily be extended to the case where the system has different responses to horizontal and vertical polarization, or, more specifically, where the H- and E-plane patterns of the radiators are different.

4. Sample Calculations

In the preceding section the equivalent asymmetries were derived in terms of system or subsystem parameters. Sample calculations of these asymmetries and their contribution to the boresight shift (for some error sources in certain type of antenna systems with time-varying parameters) are given in this section. (Time-invariant parameters

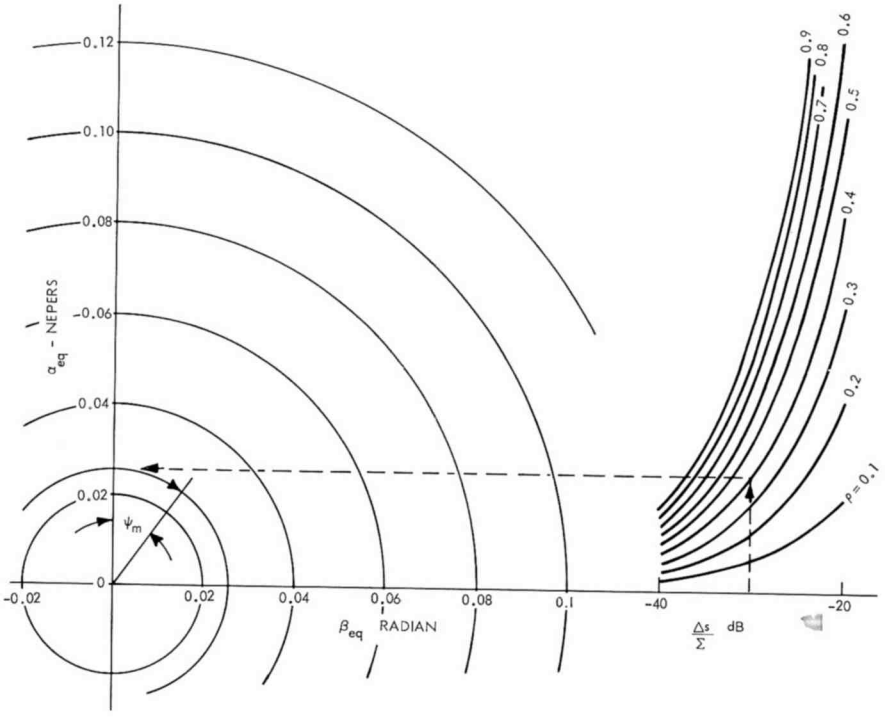

Fig. 26—Equivalent asymmetries due to multipath.

are generally not important, since they can be calibrated.) The less obvious error sources are considered, since the more obvious sources can be readily calculated.

The error contribution of the particular error source to the boresight shift should, strictly speaking, be determined in the presence of asymmetries due to the remaining error sources; that is, each of the asymmetries, α, β, and ϕ, should be summed, vectorially or statistically, before the boresight shift is determined by use of Equation (1). At the risk of misleading the reader, however, the contributions from the

various sources discussed in this section are computed assuming the following initial or mean values: $\phi = 30°$ and $(S_d/E_s) = 18\ \mathrm{VV}^{-1}$ radian^{-1}.

Antenna Radiation System Parameters

Changes in the radiator are rather difficult to assess analytically in terms of the lobe-pattern beam width and gain parameters. However, the changes in the beam offset angle, θ_o, can more readily be determined. In a Cassegrain system, for example, the physical parameters that may affect the pattern characteristics are

(1) feed-horn displacement and rotation,

(2) subreflector displacement and rotation,

(3) main-reflector orientation,

(4) subreflector distortion,

(5) main-reflector distortion.

Only the first two factors are considered here. The characteristics of the Cassegrain antenna can be analyzed by use of the equivalent parabola concept. The displacement of the feed and the subreflector can then be related to the off-focus displacement of the apparent feed source in this equivalent parabola.

For feed-horn displacement, an unequal increase in temperature (e.g., higher on the upper side than on the lower side) would result in a lengthening and bending of the feed and subsequent displacement of the phase centers of the monopulse feed horns. For small changes, referring to Figure 27, it may readily be shown that,

$$x_1 \cong \tfrac{1}{4}(3l_u + l_L - 4l_o)\,; \quad y_1 \cong \tfrac{1}{4}d\left[1 - \frac{d^{-2}}{2}(3l_u - l_L)(l_u - l_L)\right]$$

$$x_2 \cong \tfrac{1}{4}(l_u + 3l_L - 4l_o)\,; \quad y_2 \cong -\tfrac{1}{4}d\left[1 - \frac{d^{-2}}{2}(l_u + 3l_L)(l_u - l_L)\right]$$

where the lengths l_u and l_L are related to temperature by

$$l_u = l_o(1 + \alpha_T T_u)$$
$$l_L = l_o(1 + \alpha_T T_L)$$

and where l_o is the length at 0°C. α_T is the coefficient of linear expansion for the metal used, and T_u and T_L are the temperature changes (from 0°C) for the upper and lower side of the feed, respectively.

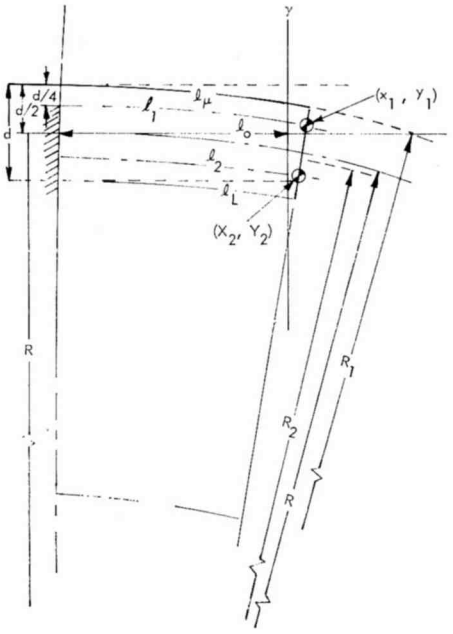

Fig. 27—Feed phase center displacement.

The lateral displacement, y, has the most effect upon the beam offset angle. The lateral displacement of the feed-horn aperture image behind the subreflector is

$$y' = y\,(F_v/F_R)$$

where F_v is the virtual focal distance and F_R is the real focal distance, as shown in Figure 28. The feed image offset angle is therefore

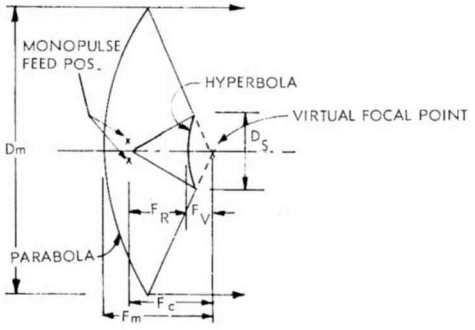

Fig. 28—Geometry of Cassegrain system.

$$\delta = (y'/F_m) = (y/F_m)\,(F_v/F_R)\ ,$$

where F_m is the distance from the parabola vertex to the virtual focus.

The shift in the beam is a function of the "beam deviation factor",[8] which in turn is a function of the focal-length-to-diameter ratio of the paraboloid reflector, $f(F_m/D_m)$. The beam shift is therefore

$$d\theta_o = \delta f(F_m/D_m)$$

For $(F_m/D_m) = 0.375$, the deviation factor is given by Y. T. Lo[8] as 0.86.

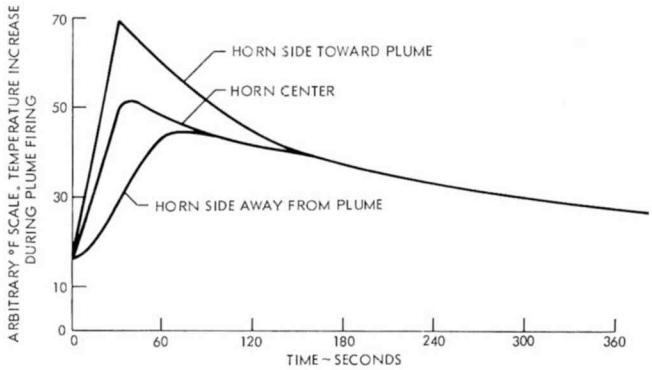

Fig. 29—Feed-horn temperature changes during worst-position firing of jets —single plume.

The equivalent asymmetry due to this source can now be calculated by use of Equation (2). A typical example of the bending of the feed horn is that due to jets heating the horn. Temperature changes during such firing as a function of time are shown in Figure 29.[9] The equivalent branch amplitude asymmetry was calculated assuming the following values for the parameters: $l_o = 4.75$ inches, $\alpha_T = 13.7 \times 10^{-6}/°\mathrm{F}$ (aluminum), $F_v = 1.38$ inch, $F_R = 3.08$ inches, $F_m = 9$ inches, and $d = 1.6$ inches. The resultant curve is shown in Figure 30. Under the conditions stated at the beginning of the section, and using Equation (1), the contribution to boresight shift by the bending of the feed horn at time equal to 30 seconds is 0.006 milliradian.

Another contributor to the antenna pattern change is the change

[8] Y. T. Lo, "On the Beam Deviation Factor of a Parabolic Reflector," *IRE Trans.*, Vol. AP-8, p. 347, May 1960.

[9] Private communication with Dr. F. Weiss, RCA Defense Electronic Products.

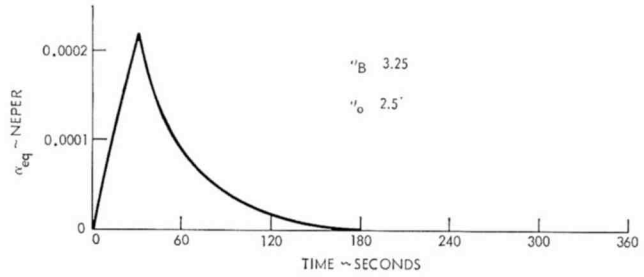

Fig. 30—Branch amplitude asymmetry due to feed-horn heating.

in the subreflector position relative to the primary reflector and its rotation with differences in temperature. Figure 31 is a diagram of a subreflector mounted on the reflector assembly by means of four struts. To simplify the analysis, it is assumed that (1) the point at which the struts are attached to the parabola remains stationary with temperature, (2) the struts are free to pivot about these fixed points, and (3) the struts are connected at the points of intersection of their centerlines. We also assume that the axis of the hyperbola maintains a constant angle with the center lines of the struts and that the struts are rigid. Then, the position of the vertex of the hyperbola, as a function of the change in lengths of the struts and hyperbola support tube and of the orientation of the axis of the hyperbola, is given by

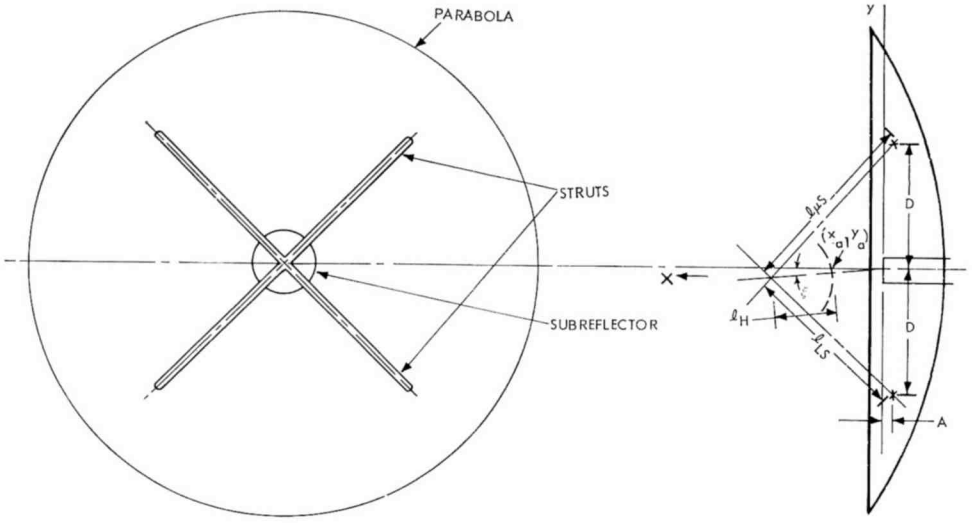

Fig. 31—Subreflector and its displacement.

$$x_a \cong A + l_{us}\{1 - (D/l_{us}) + (\Delta l_s/2D)^2\}^{\frac{1}{2}} - l_H$$

$$y_a \cong -\tfrac{1}{2}(l_{us}/D)\Delta l_s + \tfrac{1}{2}l_H(\Delta l_s)(D^{-2} - l_{us}^{-2})^{\frac{1}{2}}$$

$$\xi \cong \sqrt{\tfrac{1}{2}}\Delta l_s(D^{-2} - .l_{us}^{-2})^{\frac{1}{2}}$$

where D is the half distance between the strut attachment, A is its distance to the focal plane, l_{us} and l_{Ls} are the upper and lower strut lengths, respectively, l_H is the distance of the hyperbola vertex to the point of intersection of the struts, and

$$\Delta l_s = l_{us} - l_{Ls} .$$

The relationship of l_{us}, l_s, and l_H to temperature is given by

$$l_{us} = l_s(1 + \alpha_{Ts}T_{us}) \cos \chi_s ,$$

$$l_{Ls} = l_s(1 + \alpha_{Ts}T_{us}) \cos \chi_s ,$$

$$l_H = l_{Ho}(1 + \alpha_{TH}T_H) ,$$

where l_s and l_{Ho} are the lengths of the struts and hyperbola support tube at 0°C, respectively, α_{Ts} and α_{TH} are the appropriate coefficient of linear expansion, and T_{us}, T_{Ls}, and T_H are the temperature changes for the upper and lower struts and the hyperbola support tube.

The feed image-offset angle becomes, by simple geometry, approximately

$$\delta_1 = (F_v/F_R)(y_u \cos 2\xi + y_a + 2x_a \tan \xi \sin 2\xi) - y_a ,$$

$$\delta_2 = (F_v/F_R)[(y_L - y_a) \cos 2\xi + x_a \tan \xi(\sin \xi + \cos 2\xi)] + y_a .$$

Again, the beam shift is a function of the "beam deviation factor".

Figure 32 gives a representative plot of the variation in temperature difference between the struts as a function of time.[9] With the aid of this curve, the change in branch amplitude asymmetry with time is shown in Figure 33, assuming the following parameters: $A = 1.9$ inches, $D = 9.64$ inches, $F_m = 9$ inches, $l_s = 13.5$ inches, $F_v = 1.38$ inches, $F_R = 3.08$ inches, $\alpha_{Ts} = \alpha_{TH} = 4.8 \times 10^{-6}/°\text{F}$, $|y_u| = |y_L| = 0.4$ inch.

Precomparator Transmission Line and Component Differences

The transmission lines in the precomparator networks are generally designed to be very nearly equal, and since they are enclosed, temperature differentials between the branch lines are expected to be small. The feed horns are exposed, however, and may be subjected to greater thermal differences, as discussed previously. (The polarizers, located

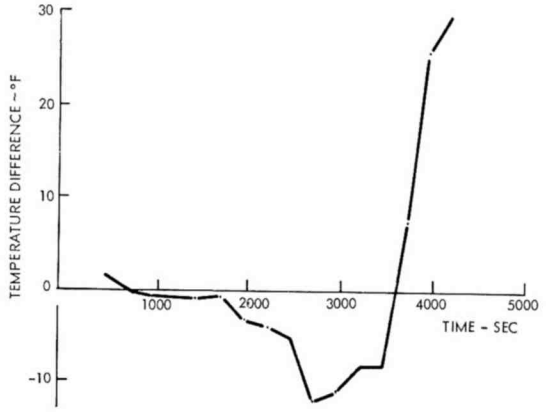

Fig. 32—Temperature difference between subreflector support spars.

close to the horn structure may also be subjected to greater temperature, as discussed later.) This introduces phase asymmetries. The following discussion is confined to the feed-horn distortion in the elevation plane.

Referring to Figure 27, the mean lengths of the upper and lower waveguides (feed horns) are, respectively,

$$l_1 = \tfrac{1}{4}(l_L + 3l_u) ,$$
$$l_2 = \tfrac{1}{4}(3l_L + l_u) .$$

Assuming that the guide wavelength, λ_g, in the two horns changes little with temperature, the phase difference becomes

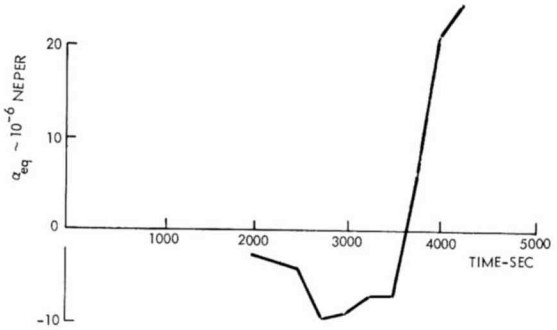

Fig. 33—Branch asymmetry due to subreflector support spar changes.

$$\beta = \pi l_o \alpha_T (T_u - T_L)/\lambda_g .$$

For the variation in temperature shown in Figure 29, the difference in phase shift, β, as a function of time is plotted in Figure 34. The maximum boresight shift contribution (time = 30 seconds) becomes 0.064 milliradian, a negligible amount generally.

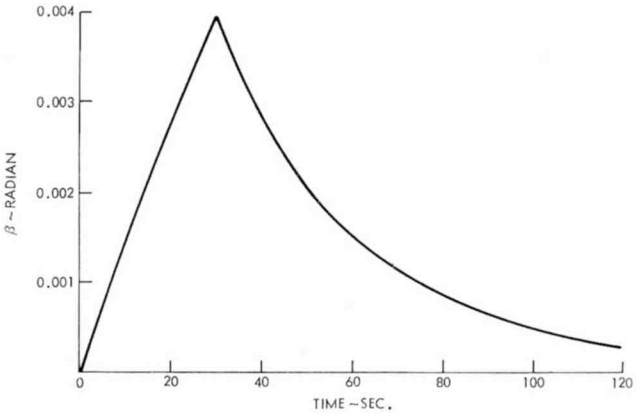

Fig. 34—Phase asymmetry due to heating of horns.

Mismatches in Microwave Transmit Line and Duplexer Isolation

In a Cassegrain system, a certain amount of the energy reflected from the subreflector impinges upon the feed horn; for a circularly polarized, polarization-duplexed system, this energy appears at the receive terminals of the comparator, thus degrading the transmit-to-receive isolation. This energy constitutes a leakage signal. There are several ways of cancelling this reflection, two of which will be examined. One is by use of matching windows in the feed horn; the other is by use of "vertex plate" matching at the vertex of the subreflector. Figures 35 and 36 show some typical values of the isolation (and hence leakage) as a function of the feed-horn-to-subreflector spacing for the two cases.[10] The horn–subreflector spacing may vary with time; in a lunar mission under descent condition, for example, the spacing may vary as shown in Figure 37.[9] On the basis of these figures and Figure

[10] Private communication with W. E. Powell, RCA Defense Electronic Products.

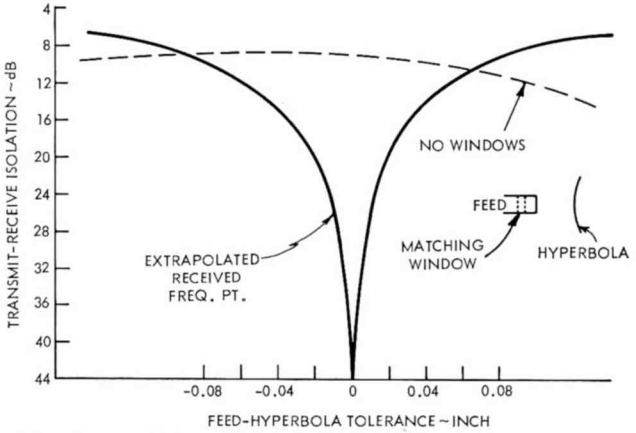

Fig. 35—Transmit-to-receive isolation with matching windows.

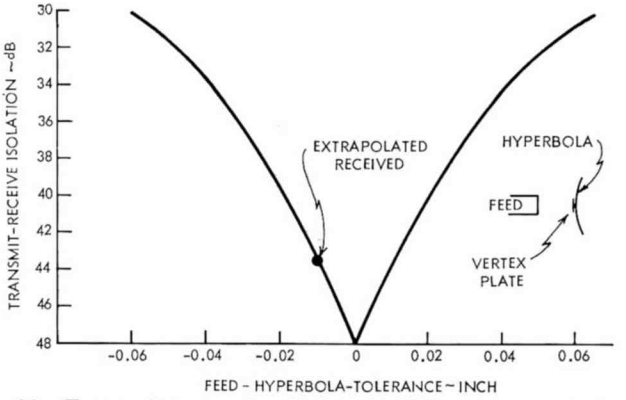

Fig. 36—Transmit-to-receive isolation with vertex matching.

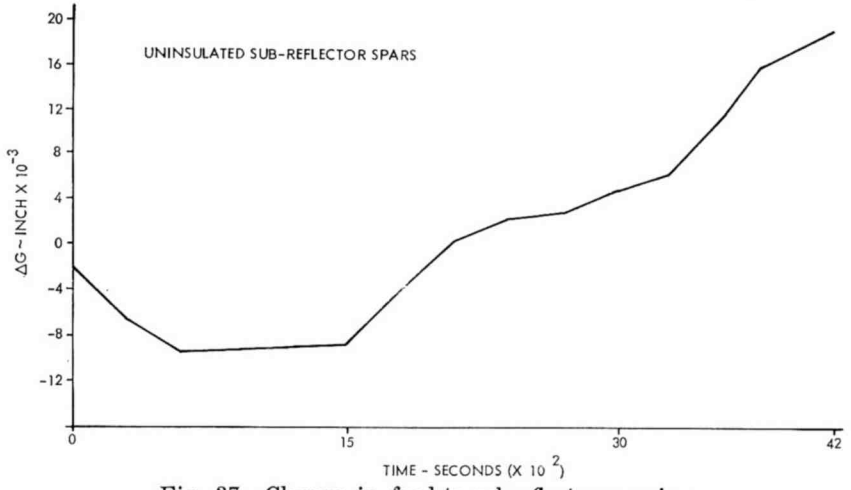

Fig. 37—Change in feed-to-subreflector spacing.

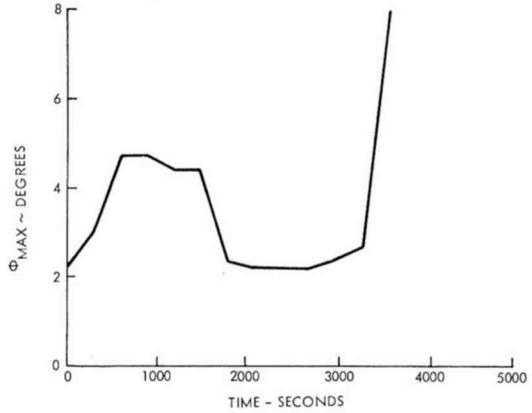

Fig. 38—Variation in channel phase asymmetry due to transmitter leakage (maximum values).

5, the worst-case values of ϕ are plotted in Figures 38 and 39. Since the exact values of $\omega_o(\tau_\Delta - \tau_\Sigma)$ and $\omega_o(\tau_L - \tau_\Delta)$ in Equation (4) are not known, only the bounds for ϕ are given.

Mismatches in Microwave Transmit Line at Receive Frequencies

In the illustrative system described in Section 2, some of the parameters of Equation (5) are time functions that vary cyclically at a frequency dependent upon the modulation of the phase modulator. Since the modulation frequency is relatively high, the variations introduced in the boresight angle may be expected to be filtered out in the antenna servo system. There are other variables, k_{c1}, for example, which are more slowly varying functions of time. (It is assumed that $k_{c2} \cong k_{c1}$ and $\phi_{\gamma a1} \cong \phi_{\gamma a2}$, and that the variation in k_{c1} is the same as that of

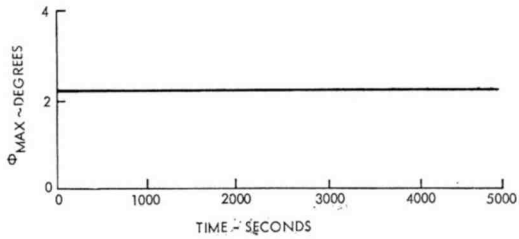

Fig. 39—Bound for channel phase asymmetry due to transmitter leakage (vertex match).

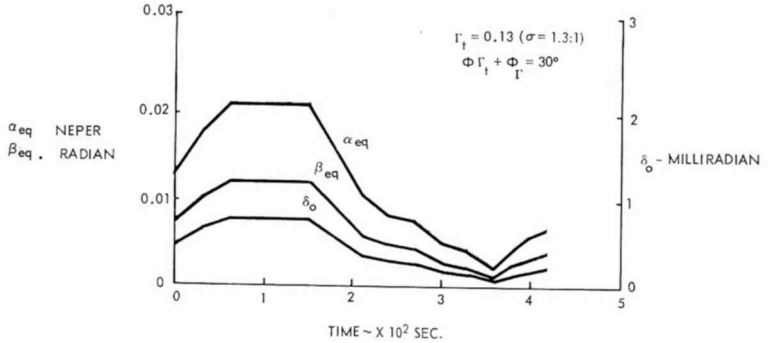

Fig. 40—Variation in branch asymmetry due to receive frequency T-R cross-coupling (with window matching).

the coupling at the output of the comparator.) The variation of the asymmetries is determined from Figures 35 and 36, by choosing the appropriate point on the curve, i.e., the point corresponding to the receive frequency. Using the variation in the horn-subreflector spacing with time shown in Figure 37, the variations in the branch asymmetries are as shown in Figures 40 and 41. The contribution to the boresight shift under conditions given at the beginning of this section are also shown in the figures.

Microwave Receive-Line Mismatches and Sum-to-Difference Channel Isolation

If the comparator outputs are terminated in the mixers, the variations in their reflection coefficients are of concern. These reflection coefficients are dependent upon the LO level and the signal level, as well as on temperature. In the system we have used as an example, the transmitter output and, hence, the LO level, may vary as much as 1.7:1 with temperature. Extrapolating from Carr's data,[11] the VSWR

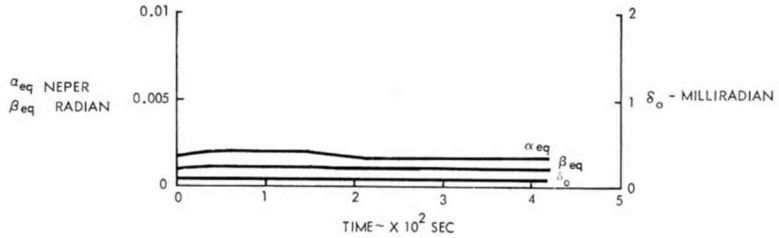

Fig. 41—Variation in branch asymmetry with vertex matching.

[11] J. W. Carr, "The Stabilization of Mixer Diode Performance Against Local Oscillator Power Changes with Optimum DC Bias," *IEEE Trans.*, Vol. MTT-11, p. 123, March 1963.

at signal level may vary from 1.5:1 to 1.7:1, and at LO level from 2.1:1 to 2.4:1. (The phase of the reflection coefficient is not known.) These values indicate relatively small changes in the reflection coefficient (about 0.06).

Assuming $r_{11} = u_{11}$ in Equation (6), the absolute values of α_{eq} or β_{eq} are

$$|\alpha_{eq}| = |\beta_{eq}| \cong 0.06\sigma .$$

As an example, a 20-dB isolation (σ) between the sum and difference channels will give

$$|\alpha_{eq}| \cong 0.006 .$$

The contribution to boresight shift is 0.26 milliradians, which is small but not insignificant.

Polarization Orientation and Polarizer Changes

The equivalent asymmetries for polarizer errors derived in Section 3 are in terms of the equivalent polarizer parameters, which contain both the polarization errors due to the radiation pattern and the physical polarizers. The characteristics usually measured in a polarization system are the far-field axial ratio and the orientation of the polarization ellipse. The relationship between these characteristics and the equivalent polarizer parameters can be determined from the wave polarization chart in rectangular coordinates, where contours of constant axial ratio and/or contours of polarizer parameters are plotted. The coordinates are those of the linear components of the transmitted wave. Mathematically, the relationship between the linear wave components, E_x, E_y, and δ (differential phase between these components) and the polarizer parameters, χ_p and β_p, are

$$E_x = E_{yi} \sin 2\chi_p \sin \tfrac{1}{2}\beta_p ,$$
$$E_y = E_{yi}(1 - \sin^2 2\chi_p \sin^2 \tfrac{1}{2}\beta_p)^{\frac{1}{2}} ,$$
$$\delta = \tfrac{1}{2}\pi + \tfrac{1}{2}\beta_p - \tan^{-1} (\sin \beta_p)/(\cos \beta_p + \tan^2\chi_p) ,$$

for the case of a linearly polarized wave (E_{yi}) impinging upon the polarizer in the plane containing the Y-axis.

The relationships between the axial ratio and orientation of the polarization ellipse and the linear wave components have been derived

in the literature.[12] When these relationships (polarizer and polarization ellipse) are plotted together, the bounds for the polarizer parameters are obtained. Care must be exercised in using the measured values of the system polarization ellipse, since the overall value is the composite of the polarization characteristics of the individual radiators. Figure 42 illustrates the variation of the equivalent polarizer parameter. Here the characteristics of the transmitted wave are

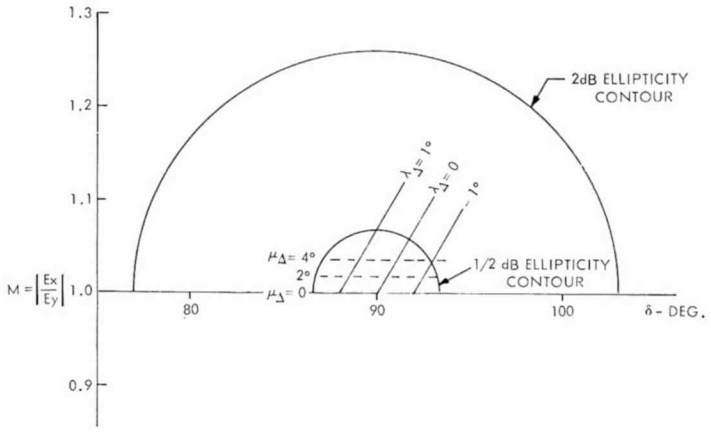

Fig. 42—Wave polarization chart showing effect of variations in polarizer parameters.

plotted assuming one of the polarizers to be perfectly circular and the other to have errors (to simplify the discussion, only one tracking plane is considered). It is assumed that the E-vectors feeding the polarizers are identical. It is possible to have wide variation in the parameters of the individual polarizers, while maintaining a relatively low overall axial ratio. For a 2-dB ratio, the equivalent polarizer phase, β_p, may vary as much as 29.5° and the orientation as much as 7.2° (not simultaneously). For an axial ratio of 0.5-dB and for $\lambda = 1°$ ($\cong 0.02$ radian), $\mu = 6°$ ($\cong 0.10$ radian). From Figure 15, it is seen that β_{eq} varies from -0.016 to -0.125 and α_{eq} from -0.054 to 0.054, depending upon the orientation of the impinging E-field. The maximum contribution to the boresight shift is therefore 2 milliradians.

Multipath

The asymmetries for this error source, and hence the boresight shift, are dependent upon the complex reflection coefficient, the normal-

[12] John D. Kraus, *Antennas*, McGraw-Hill Book Co., N. Y., 1950.

ized difference pattern side-lobe levels, and the difference in the path lengths of the direct signal and the multipath signal. For the sample calculation, the radar is assumed to be located on a vehicle on a smooth surface and to be tracking a flying vehicle. (In practice, the surface will not be smooth and the reflection will have a statistical character. However, the mean value may be approximated by that from a smooth surface.)

The normalized difference pattern for vertical polarization that is representative of that for a Cassegrain antenna is shown in Figure 43.

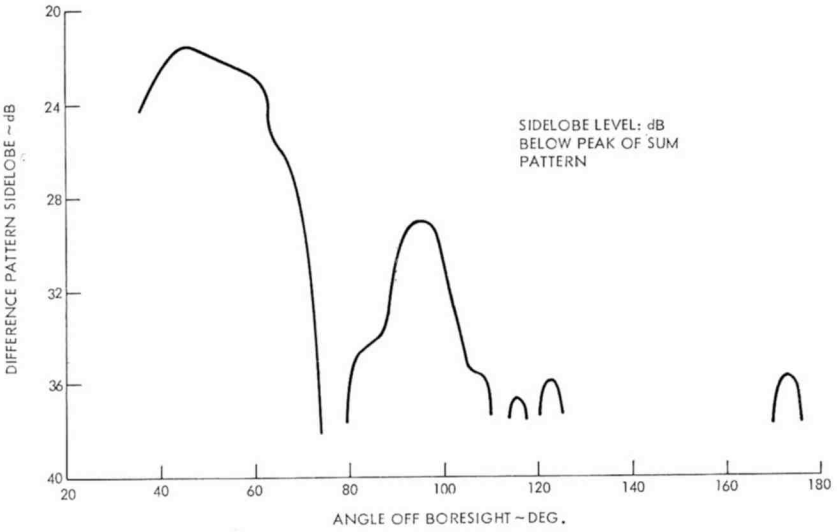

Fig. 43—Normalized difference pattern.

The ground reflection coefficient for vertical polarization is assumed to be

$$\rho_v = \frac{2.72 \sin \psi_g - (2.72 - \cos^2 \psi_g)^{\frac{1}{2}}}{2.72 \sin \psi_g + (2.72 - \cos^2 \psi_g)^{\frac{1}{2}}},$$

which is representative of a dry sandy soil. ψ_g is the grazing angle. The reflection coefficients for various orientations of the incident linear polarization are plotted in Figure 44. By use of Figure 26 and Figures 43 and 44, the maximum values for α_{eq} (or β_{eq}) may be determined; a plot of α_{eq} is shown in Figure 45 as a function of the elevation angle of the target. The contribution to boresight shift is also shown.

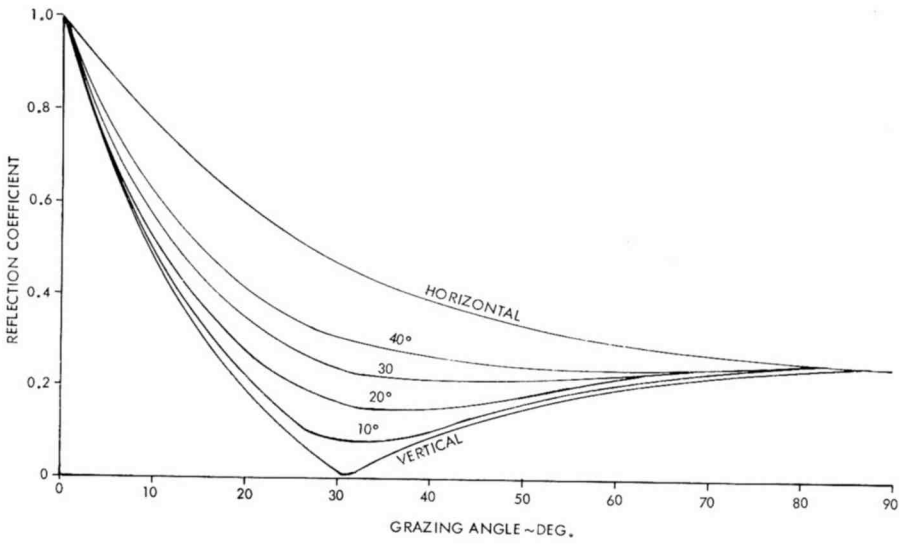

Fig. 44—Model of reflection coefficient used in study.

5. Conclusion

A method of analyzing the various contributions to the electronic boresight shift in a precision monopulse system has been described. The approach taken is to express the various antenna and signal

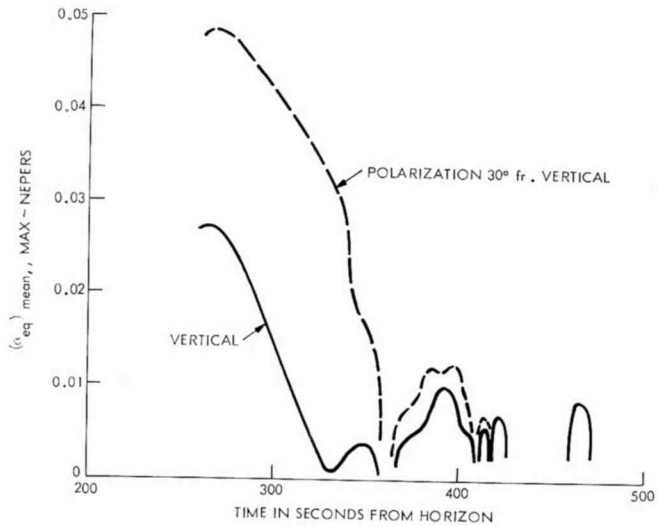

Fig. 45—Asymmetries due to multipath.

parameters that contribute to the electronic boresight shift in terms of equivalent branch and channel asymmetries. This permits the additions, vectorially or statistically, of the effects of various error sources, from which the boresight shift can be calculated. Whether or not a given error contributor is significant may readily be determined by finding its equivalent asymmetry. This approach permits ready determination as to whether the tolerances of a given antenna parameter may be relaxed, thus leading to a cost effective design.

From the example of the characteristics given, and with careful design, it is seen that most of the errors can be reduced to a negligible value. For a system that transmits circular polarization (and where individual polarizers are used in each of the monopulse horns) and that receives linear polarization, degradation of polarization characteristic is the major contributor to boresight shift. Multipath may also be a significant contributor if the radar is operated near ground (or other reflecting objects).

Acknowledgment

The author acknowledges with gratitude, the encouragement and advice of W. C. Curtis. The antenna performance data provided by the RCA Antenna Skill Center, Moorestown, N. J., is greatly appreciated.

Appendix—Approach to Determining Equivalent Branch Asymmetries

Let the comparator be a magic tee; its scattering matrix is

$$\overline{S} = \frac{j}{\sqrt{2}} \begin{bmatrix} 0 & 0 & 1 & 1 \\ 0 & 0 & -1 & 1 \\ 1 & -1 & 0 & 0 \\ 1 & 1 & 0 & 0 \end{bmatrix}$$

The form of the network is shown in Figure 46. With the incident waves a_3 and a_4 equal to zero,

$$b_1 = b_2 = 0$$

$$b_3 = \frac{j}{\sqrt{2}} (a_1 - a_2)$$

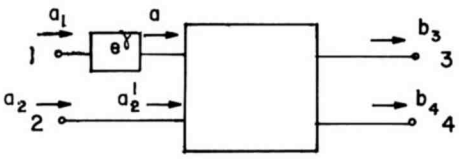

Fig. 46—Four-port network.

$$b_4 = \frac{j}{\sqrt{2}}(a_1 + a_2)$$

$$\frac{b_3}{b_4} = \frac{a_1 - a_2}{a_1 + a_2} = \frac{\Delta}{\Sigma} = -\frac{1 - A}{1 + A} \tag{14}$$

where $A = (a_1/a_2)$ and where Δ is the difference channel signal and Σ is the sum channel signal. We are interested in the ratios of the signals in the channel terminals (3 and 4) and in the ratios of the signal at the branch terminals (1 and 2) for determining the asymmetries. In an ampliture monopulse system, a_1 and a_2 are in phase.

Branch Asymmetries

Consider now the case with branch asymmetries as shown in Figure 47. In matrix notation,

$$\begin{bmatrix} b_1' \\ b_2' \\ b_3 \\ b_4 \end{bmatrix} = [S] \begin{bmatrix} a_1' \\ a_2' \\ a_3 \\ a_4 \end{bmatrix}$$

But

$$a_1' = a_1 e^{\gamma}$$

$$a_2' = a_2$$

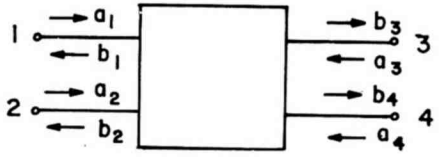

Fig. 47—Network with branch asymmetry.

where $\gamma = \alpha + j\beta$ and where a_1 and a_2 are in phase. Hence, for $a_3 = a_4 = 0$

$$b_3 = \frac{j}{\sqrt{2}}(a_1' + a_2') = \frac{j}{\sqrt{2}}(a_1 e^{\gamma} - a_2)$$

$$b_4 = \frac{j}{\sqrt{2}}(a_1' + a_2') = \frac{j}{\sqrt{2}}(a_1 e^{\gamma} + a_2)$$

$$\frac{b_3}{b_4} = \frac{|a_1| e^{\gamma} - |a_2|}{|a_1| e^{\gamma} + |a_2|} \tag{15}$$

Now, for γ small, $e^{\gamma} \approx 1 + \gamma$. Therefore

$$\frac{b_3}{b_4} \approx \frac{a_1 + a_1\gamma - a_2}{a_1 + a_1\gamma + a_2} = \frac{a_1 - a_2 + a_1\gamma}{a_1 + a_2 + a_1\gamma} = \frac{\dfrac{a_1 - a_2}{a_1 + a_2} + \dfrac{a_1}{a_1 + a_2}\gamma}{1 + \dfrac{a_1}{a_1 + a_2}\gamma} \tag{16}$$

where a_1 and a_2 are understood to be magnitudes. Since γ is assumed small and $a_1/(a_1 + a_2) < 1$, then

$$\left[1 + \frac{a_1}{a_1 + a_2}\gamma\right]^{-1} \cong 1 - \frac{a_1}{a_1 + a_2}\gamma + \left(\frac{a_1}{a_1 + a_2}\gamma\right)^2 \cdots$$

Equation (16) now becomes

$$\frac{b_3}{b_4} \cong \frac{a_1 - a_2}{a_1 + a_2} + \frac{2a_1a_2}{(a_1 + a_2)^2}\gamma + \frac{2a_1^2a_2}{(a_1 + a_2)^3}\gamma^2 + \cdots$$

$$\cong \frac{a_1 - a_2}{a_1 + a_2} + \frac{2a_1a_2}{(a_1 + a_2)^2}\gamma .$$

Near the boresight axis, $a_1 \approx a_2$ and since $\gamma = \alpha + j\beta$, there results

$$\frac{b_3}{b_4} \cong \frac{\Delta}{\Sigma} + \frac{\alpha}{2} + j\frac{\beta}{2} . \tag{17}$$

Difference in Branch Transfer Function

The case of differences in branch transfer function can readily be inferred from the foregoing discussion. In its simplest form, we may consider the incoming wave to be multiplied by e^{γ} in each of the branches. It can readily be seen that ratio of the outputs (corresponding to Equation (15), for example) will be

$$\frac{b_3}{b_4} = \frac{a_1 \exp\{\gamma_1 - \gamma_2\} - a_2}{a_1 \exp\{\gamma_1 - \gamma_2\} + a_2},$$

i.e., for small values of α and β, the branch asymmetries are

$$\alpha_{eq} = \alpha_1 - \alpha_2$$
$$\beta_{eq} = \beta_1 - \beta_2 .$$

Input Signal "Imbalance"

Suppose the system is perfect but additional signal is injected into the comparator branches, that is, let a_1 be $a_1 + \Delta a_1 \exp\{j\psi_1\}$ and a_2 be $a_2 + \Delta a_2 \exp\{j\psi_2\}$. The equation corresponding to equation (14) becomes (ψ_1 and ψ_2 are phase differences of the additional signal injected into the system with respect to a_1 and a_2, respectively, and a_1 and a_2 are in phase),

$$\frac{b_3}{b_4} = \frac{a_1 + \Delta a_1 \exp\{j\psi_1\} - a_2 - \Delta a_2 \exp\{j\psi_2\}}{a_1 + \Delta a_1 \exp\{j\psi_1\} + a_2 + \Delta a_2 \exp\{j\psi_2\}}$$
$$= \frac{\dfrac{a_1 - a_2}{a_1 + a_2} + \dfrac{\Delta a_1 \exp\{j\psi_1\} - \Delta a_2 \exp\{j\psi_2\}}{a_1 + a_2}}{1 + \dfrac{\Delta a_1 \exp\{j\psi_1\} + \Delta a_2 \exp\{j\psi_2\}}{a_1 + a_2}}.$$

Assuming that Δa_1 and Δa_2 are very small compared to a_1 and a_2, the above expression may be approximated by

$$\frac{b_3}{b_4} \cong \frac{a_1 - a_2}{a_1 + a_2} + \frac{\Delta a_1 \exp\{j\psi_1\} - \Delta a_2 \exp\{j\psi_2\}}{a_1 + a_2}$$
$$- \frac{\Delta}{\Sigma} \frac{\Delta a_1 \exp\{j\psi_1\} + \Delta a_2 \exp\{j\psi_2\}}{a_1 + a_2}$$
$$- \frac{(\Delta a_1)^2 \exp\{2j\psi_1\} - (\Delta a_2)^2 \exp\{2j\psi_2\}}{(a_1 + a_2)^2} + \ldots$$

$$\cong \frac{\Delta}{\Sigma} + \frac{1}{\Sigma}\left[\Delta a_1\left(1-\frac{\Delta}{\Sigma}\right)\cos\psi_1 - \Delta a_2\left(1+\frac{\Delta}{\Sigma}\right)\cos\psi_2\right]$$

$$+ j\frac{1}{\Sigma}\left[\Delta a_1\left(1-\frac{\Delta}{\Sigma}\right)\sin\psi_1 - \Delta a_2\left(1+\frac{\Delta}{\Sigma}\right)\sin\psi_2\right]. \tag{18}$$

If $\psi_1 = \psi_2 = \psi$,

$$\frac{b_3}{b_4} \cong \frac{\Delta}{\Sigma} + \frac{1}{\Sigma}\left[\Delta a_1 - \Delta a_2 - \frac{\Delta}{\Sigma}(\Delta a_1 + \Delta a_2)\right]\cos\psi$$

$$+ j\frac{1}{\Sigma}\left[\Delta a_1 - \Delta a_2 - \frac{\Delta}{\Sigma}(\Delta a_1 + \Delta a_2)\right]\sin\psi$$

Equivalent Branch Asymmetries

A comparison of Equations (17) and (18) shows that the equivalent branch asymmetries are

$$\alpha_{eq} \cong \frac{2}{\Sigma}\left\{\Delta a_1\left(1-\frac{\Delta}{\Sigma}\right)\cos\psi_1 - \Delta a_2\left(1+\frac{\Delta}{\Sigma}\right)\cos\psi_2\right\}$$

$$\beta_{eq} \cong \frac{2}{\Sigma}\left\{\Delta a_1\left(1-\frac{\Delta}{\Sigma}\right)\sin\psi_1 - \Delta a_2\left(1+\frac{\Delta}{\Sigma}\right)\sin\psi_2\right\}$$

For the case of $\psi_1 = \psi_2$,

$$\alpha_{eq} \cong \frac{2}{\Sigma}\left\{\Delta a_1 - \Delta a_2 - \frac{\Delta}{\Sigma}\left(\Delta a_1 + \Delta a_2\right)\right\}\cos\psi$$

$$\beta_{eq} \cong \frac{2}{\Sigma}\left\{\Delta a_1 - \Delta a_2 - \frac{\Delta}{\Sigma}\left(\Delta a_1 + \Delta a_2\right)\right\}\sin\psi\,.$$

RCA Technical Papers

Fourth Quarter, 1968

Any request for copies of papers listed herein should be addressed to the publication to which credited.

"Ambient-Sensitive Photoelectronic Behavior of CdS Sintered Layers," F. B. Micheletti and Coauthor, *Jour. Appl. Phys.* (October) .. 1968

"Character Impedance of Dielectric Supported Strip Transmission Line," M. A. Earle and P. Benedek, *Trans. IEEE GMTT* (Correspondence) (October) 1968

"Continuous UV Lasers," J. R. Fendley, Jr., *IEEE Jour. Quantum Electronics* (October) 1968

"Cryoelectric Hybrid System for Very Large Random Access Memory," R. A. Gange, *Proc. IEEE* (October) 1968

"Design of High-Performance FM Receivers Using High-Gain Integrated-Circuit IF Amplifiers," T. J. Robe and L. Kaplan, *Trans. IEEE GBTR* (October) 1968

"Development of the Perma-Chrome Color Picture Tube," R. H. Godfrey, T. M. Shrader, and R. C. Demmy, *Trans. IEEE GBTR* (October) 1968

"Comments on 'Distortion and Crosstalk of Linearly Filtered, Angle-Modulated Signals,'" T. T. N. Bucher, *Proc. IEEE* (Letters) (October) 1968

"Electroluminescence in $Al_xGa_{1-x}P$ Diodes Prepared by Liquid-Phase Epitaxy," H. Kressel and I. Ladany, *Jour. Appl. Phys.* (Communications) (October) 1968

"Electric Halftones," R. L. Hallows, Jr. and R. J. Klensch, *IEEE Spectrum* (October) 1968

"Linear Dichroism in Photochromic CaF_2," D. L. Staebler, W. Zernik, and Coauthor, *IEEE Jour. Quantum Electronics* (October) 1968

"M-ary Sequential Detection for Amplitude-Modulated Signals in One and Two Dimensions," M. Hecht and Coauthor, *Trans. IEEE GCOM* (October) 1968

Microwave Faraday Effect and Propagation in a Circular Solid-State Plasma Waveguide," H. J. Kuno and Coauthor, *Trans. IEEE GMTT* (Correspondence) (October) 1968

"Observations Concerning Radiative Efficiency and Deep-Level Luminescence in n-Type GaAs Prepared by Liquid-Phase Epitaxy," H. Kressel, F. Z. Hawrylo, M. S. Abrahams, and C. J. Buiocchi, *Jour. Appl. Phys.* (October) 1968

"On the Origin of Leakage Current in Ge(Li) Gamma-Ray Detectors," R. J. McIntyre, *Trans. IEEE GNS* (October) 1968

"A Technique for Trap Determinations in Low-Resistivity Semiconductors," L. R. Weisberg and H. Schade, *Jour. Appl. Phys.* (October) 1968

"Voltage Induction Method for Wicrowave Susceptibility Measurements," M. Toda, *Trans. IEEE GMTT* (October) 1968

"Blue-Green High-Powered Light Extends Underwater Visibility," E. Kornstein and H. Wetzstein, *Electronics* (October 14) ... 1968

"Current Fluctuations in the Acoustoelectric Steady State," L. Friedman, *Phys. Rev.* (15 October) 1968

"Ionic Surface States from a Band-Edge Method," J. D. Levine and Coauthor, *Phys. Rev.* (15 October) 1968

"No Need to Juggle Equations to Find Reflection—Just Draw Three Lines," R. S. Singleton, *Electronics* (October 28) 1968

"Photoinduced Reversible Charge-Transfer Processes in Transition-Metal-Doped Single-Crystal $SrTiO_3$ and TiO_2," B. W. Faughnan and Z. J. Kiss, *Phys. Rev. Letters* (28 October) 1968

"Cathodoluminescence of n-Type GaAs," J. I. Pankove, *Jour. Appl. Phys.* (November) 1968

"Comparison of Electrooptic Modulation Methods," W. J. Hannan and Coauthor, *Trans. IEEE GAES* (November) 1968

"Continuing Education for the Engineering Manager," J. M. Biedenbach, *IEEE Spectrum* (November) 1968

"Measurement of the Beam Profile of a CO_2 Laser," D. Meyerhofer, *IEEE Jour. Quantum Electronics* (Correspondence) (November) 1968

"Multiple-Target Monopulse Radar Processing Techniques," P. Z. Peebles, Jr. and Coauthor, *Trans. IEEE GAES* (November) 1968

"New Deep-Level Luminescence in GaAs:Sn," H. Kressel, H. Nelson, and F. Z. Hawrylo, *Jour. Appl. Phys.* (November) 1968

"The Performance Characteristics of Yttrium Oxysulfide—A New Red Phospor for Color Television," A. E. Hardy, *Trans. IEEE GED* (November) 1968

"Photo Erasable Dark Trace Cathode-Ray Storage Tube," W. Phillips and Z. J. Kiss, *Proc. IEEE* (November) (Letters) 1968

"*Q*-Switching of the CO_2 Laser," D. Meyerhofer, *IEEE Jour. Quantum Electronics* (November) 1968

"Reflective Liquid-Crystal Displays," A. Pinsky, *Electronics World* (November) 1968

"Studies of the Focal Region of a Spherical Reflector: Stationary Phase Evaluation," G. Hyde, *Trans. IEEE GAP* (November) 1968

"Use of General Purpose Simulation System (GPSS) Language," V. J. Bannan, *Trans. IEEE GSSC* (Technical Notes) (November) 1968

"Alignment-Inversion Walls in Nematic Liquid Crystals in the Presence of a Magnetic Field," W. Helfrich, *Phys. Rev. Letters* (25 November) 1968

"Additive Processing Techniques for Printed-Circuit Boards," R. J. Ryan, T. E. McCurdy, and N. E. Wolff, *RCA Review* (December) 1968

"All-Pass Network Synthesis," R. L. Crane, *Trans. IEEE GCT* (Correspondence) (December) 1968

"Apparatus for Chemical Vapor Deposition of Oxide and Glass Films," W. Kern, *RCA Review* (December) 1968

"Auger Recombination in GaAs," L. R. Weisberg, *Jour. Appl. Phys.* (December) 1968

"Calculation of the Electrical Parameters of Transistor Chips from Measurements Made on Packaged Units," A. I. Stoller, *RCA Review* (December) 1968

"The Choice: Innovation or Stagnation," E. W. Herold, *Trans. IEEE GEWS* (Guest Editorial) (December) 1968

"Controlled Oxidation of Silane," K. Strater, *RCA Review* (December) 1968

"DC Sputtering with RF-Induced Substrate Bias," J. L. Vossen and J. J. O'Neill, Jr., *RCA Review* (December) 1968

"Development of P-Channel Enhancement MOS Triodes," P. Delivorias, *RCA Review* (December) 1968

"Device Application Feasibility of Single-Crystal $CdCr_2Se_4$, a Ferromagnetic Semiconducting Spinel," C. P. Wen, B. Hershenov, H. Von Philipsborn, and H. L. Pinch, *Trans. IEEE GMAG* (December) 1968

"Diffusion Characteristics and Applications of Doped Silicon Dioxide Layers Deposited from Silane (SiH_4)," A. W. Fisher, J. A. Amick, H. Hyman, and J. H. Scott, Jr., *RCA Review* (December) 1968

"Diffusion Characteristics of Doped Silicon Dioxide Layers Deposited from Premixed Hydrides," A. W. Fisher and J. A. Amick, *RCA Review* (December) 1968

"Ham Radio: A Hobby for the Underprivileged," W. W. Watts, *Signal* (December) 1968

"Improvements to the ALBA Machine for Thinning Specimens for Electron Microscopy," M. S. Abrahams, C. J. Buiocchi, and M. D. Coutts, *Rev. Sci. Instr.* (Notes) (December) 1968

"Injection Electroluminescence in Alloyed ZnTe Junctions," D. P. Bortfeld and H. P. Kleinknecht, *Jour. Appl. Phys.* (Communications) (December) 1968

"Isolation Techniques for Fabricating Integrated Circuits. I. Laminate Substrates, J. A. Amick and A. W. Fisher. II. Dielectric Refill Techniques and Decal Air Isolation," A. I. Stoller and W. H. Schilp, Jr., *RCA Review* (December) 1968

"The Nucleus," A. G. Holmes-Siedle, *Trans. IEEE GNS* (December) 1968

"A Prediction and Selection System for Radiation Effects in Planar Transistors," W. Poch and A. G. Holmes-Siedle, *Trans. IEEE GNS* (December) 1968

"Recovery Rate and Capacitance Measurements on Irradiated Lithium-Containing Solar Cells," T. J. Faith, G. J. Brucker, A. G. Holmes-Siedle, and R. S. Neadle, *Trans. IEEE GNS* (December) 1968

"Reflective Liquid Crystal Television Display," J. A. Van Raalte, *Proc. IEEE* (December) 1968

"Relationship Between the Performance of a Linear Amplifier Microcircuit and the Isolation Technique Used in Its Construction," A. I. Stoller, *RCA Review* (December) 1968

"Simple Technique for Detection of Oxygen in Laboratory Furnaces," A. E. Widmer, *Rev. Sci. Instr.* (Notes) (December) 1968

"Symbols for Proofreading Your Own Copy or What to Do While Waiting for the Printer," C. W. Fields, *Trans. IEEE GEWS* (Correspondence) (December) 1968

"A Technique for Measuring Etch Rates of Dielectric Films," W. Kern, *RCA Review* (December) 1968

"Multiphoton Ionization of Atomic Hydrogen," W. Zernik, *Phys. Rev.* (Comments and Addenda) (5 December) 1968

"Study of Generation and Recombination of Free Carriers in $SrTiO_3$ by Two-Photon Excitation," J. J. Amodei and W. R. Roach, *Phys. Rev. Letters* (9 December) 1968

"High-Frequency Surface Impedance of Dirty Type-II Superconductors in the Surface-Sheath Regime," G. Fischer and Coauthor, *Phys. Rev.* (10 December) 1968

"Microwave Properties of Granular Superconductors," R. W. Cohen and J. I. Gittleman, *Phys. Rev.* (10 December) 1968

Patents Issued to RCA Inventors

Fourth Quarter 1968

October

3,404,073 Method of Forming Aligned Oxide Patterns on Opposite Surfaces of a Wafer of Semiconductor Material, J. H. Scott, Jr.
3,404,228 Deflection Yoke Mounting Structure, J. W. McLeod, Jr., and W. R. Abraham.
3,404,347 Gain Controlled Amplifier Using Multiple Gate Field-Effect Transistor as the Active Element Thereof, L. A. Kaplan and O. P. Hart.
3,404,373 System for Automatic Correction of Burst Errors, C. V. Srinivasan.
3,404,386 Fixed Read-Only Memory, D. H. Montgomery and S. T. Jolly.
3,404,387 Memory System Having Improved Electrical Termination of Conductors, H. Amemiya.
3,404,442 Method of Fabricating Directly Heated Cathode, S. E. Aungst and R. A. Lee.
3,405,044 Method of Making High Purity Metal Zeolite and Product Thereof, P. V. Goedertier.
3,405,264 Specimen Injector for Electron Microscopes with a Rotatable Specimen Holder, J. R. Fairbanks and B. F. Melchionni.
3,405,298 Photoconductive Device Having a Target Including a Selenium Blocking Layer, J. Dresner.
3,405,299 Vaporizable Medium Type Heat Exchanger for Electron Tubes, W. B. Hall and D. M. Ernst.
3,405,400 Nondestructive Readout Memory, H. V. Rangachar and L. Dillon, Jr.
3,405,403 Readback Circuits for Information Storage Systems, G. V. Jacoby and J. D. Gleitman.
3,406,068 Photographic Methods of Making Electron-Sensitive Mosaic Screens, H. B. Law.
3,406,343 PM/AM Multiplex Communication, S. J. Mehlman.
3,406,381 Print Hammer Energizing Arrangement, R. C. Peyton.
3,407,330 Protection Circuit for Cathode Ray Tube, P. C. Wilmarth.
3,408,510 Solid State Wave Amplitude Limiting Device, P. Mrozek.
3,408,535 Raster Correction Circuit, E. Lemke.
3,408,592 Transistor-Negative Resistance Diode Circuits Using D.C. Feedback, G. B. Herzog.
3,408,619 Superconductive Magnet Having Grease between Adjacent Winding Layers, E. R. Schrader.

November

3,409,339 Damping Device, R. J. Gehrung and L. J. Rhoda.
3,409,736 Phase and Frequency Correction System, R. N. Hurst and L. V. Hedlund.
3,409,878 Controlling Interchanges between a Computer and Many Communications Lines, J. L. Lindinger and Y. Rachovitsky.
3,409,893 Zigzag Radiator with Panel Reflector, M. S. O. Siukola.
3,410,203 Non-Inpact Printer Employing Laser Beam and Holographic Images, K. H. Fischbeck.
3,411,031 Transistor Deflection Circuit, J. A. Dean.
3,411,032 Transistor Television Deflection Circuits Having Protection Means, Chi-Sheng, Liu.
3,411,061 Fast Critically Damped Motor Drive System, D. J. Poitras.
3,411,149 Magnetic Memory Employing Stress Wave, R. Shahbender.
3,412,242 Method of Charging a Zinc Oxide Photoconductive Layer with a Positive Charge, E. C. Giaimo, Jr.

3,412,344 Semiconductor Plasma Laser, J. I. Pankove.
3,411,199 Semiconductor Device Fabrication, F. P. Heiman and K. H. Zaininger.
3,411,846 Electrophotography, S. Naroff.
3,412,265 High Speed Digital Transfer Circuits for Bistable Elements Including Negative Resistance Devices, E. C. Cornish.
3,413,063 Electrophotographic Apparatus, C. J. Young.
3,413,145 Method of Forming a Crystalline Semiconductor Layer on an Alumina Substrate, P. H. Robinson and D. J. Dumin.
3,413,417 Auxiliary Earphone Circuit for a High Voltage Transistor Amplifier, A. W. Cornell.
3,413,448 Information Handling Apparatus, M. Rosenblatt.
3,413,553 Method of Separating Conductors Extending from an Electrical Component for Testing Purposes, B. Genualdi and A. Checki, Jr.
3,413,597 Ground Speed and Time-To-Station Indicator for Use with DME, R. P. Crow.
3,413,612 Controlling Interchanges between a Computer and Many Communications Lines, F. E. Brooks, Y. Rachovitsky, J. L. Lindinger, M. F. Kaminsky, and R. A. Hammel.

December

3,414,669 Blanking Circuits for Television Receivers, D. H. Willis.
3,414,684 Video Recorder and/or Reproducer with Intermediate Tape Drive, A. Lichowsky.
3,414,820 Delayed AGC System Utilizing the Plateau Region of an Amplifier Transistor, K. Siwko and L. P. Thomas.
3,414,894 Magnetic Recording and Reproducing of Digital Information, G. V. Jacoby.
3,414,897 Display Device, J. C. Miller and C. M. Wine.
3,415,472 Shaft Mounting Device, H. Vodinh.
3,415,981 Electronic Computer with Program Debugging Facility, R. D. Smith and J. F. Callahan.
3,416,003 Non-Saturating Emitter-Coupled Multi-Level RTL-Circuit Logic Circuit, B. Walker.
3,416,063 Stabilized Sine Wave Inverter, W. B. Guggi.
3,416,086 Television Signal Converter Circuit, D. J. Carlson.
3,417,262 Phantom OR Circuit for Inverters Having Active Load Devices, Ying-Luh Yao.
3,417,282 Means for Stabilizing Television Deflection Circuits, C. J. Hall.
3,417,333 Error Corrector for Diphase Modulation Receiver, C. R. Atzenbeck.
3,417,339 Push-Pull Transistor Amplifiers with Transformer Coupled Driver, J. C. Sondermeyer.
3,418,161 Process for Preparing a Magnetic Recording Element, H. Bauer.
3,418,246 Rare Earth Activated Yttrium and Gadolinium Oxy-Chalcogenide Phosphors, M. R. Royce.
3,418,247 Rare Earth Activated Lanthanum and Lutetium Oxy-Chalcogenide Phosphors, P. N. Yocom.
3,419,712 Function Generation and Analog-To-Digital Conversion Using Superconducting Techniques, M. W. Green.
3,419,735 Monostable Multivibrator Control, H. G. Seer, Jr., and R. A. Dischert.
3,419,737 Hall Effect Inductive Element, M. Toda.
3,419,743 Electron Tube Having a Tensioned Cathode, D. B. Kaiser and R. Roth.
3,419,751 Protection for Horizontal Deflection Circuits, R. S. Hartz and W. S. Cranmer.
3,419,807 Circuit Protection for a Television Receiver, N. W. Hursh and J. Stark, Jr.
3,419,813 Wide-Band Transistor Power Amplifier Using a Short Impedance Matching Section, C. Kamnitsis.
3,419,851 Content Addressed Memories, J. R. Burns.

AUTHORS

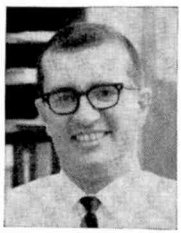

ROBERT L. BAILEY received a BSEE degree from Washington State University in 1958, and a Master's degree in Physics in 1968 from Franklin and Marshall College. He joined RCA Electronic Components, Lancaster, Pennsylvania in 1958, where he worked until 1963 on UHF circuit design for RCA's Cermolox tubes.

From 1963 to 1965, Mr. Bailey was responsible for the design and development of the L-Band, broadband amplifier module described in this journal. Since 1965, he has been working on circuit designs for high power rf transistors. He performed the major portion of the in pulsed RF service at L-band frequencies and, later, an design and development engineering work on a 1000 watt cw 400 MHz all transistor amplifier. He also designed several lower power transistor UHF amplifiers. During 1968, Mr. Bailey was engaged in designing circuits and systems to test and develop Electron Beam Injection Transistors (EBIT). At the present time, he is engaged in designing and developing high power, broadband (octave), UHF, all-transistor amplifiers for use in commercial and military systems.

Mr. Bailey is a member of Sigma Pi Sigma.

JOSEPH R. BURNS received the BSEE from Princeton University in 1959, and the MSEE from the same institution in 1962 while on the RCA Graduate Study Program. He received his Ph.D. degree in Electrical Engineering from Rutgers University, New Brunswick, N. J., in 1968. He joined RCA Laboratories in 1959 where he has engaged in research on micromagnetic memory elements and systems, high-speed transistor–tunnel-diode combinational and sequential logic circuits, and integrated semiconductor memory systems using large arrays of insulated-gate field-effect transistors. Dr. Burns is a member of the Institute of Electrical and Electronics Engineers.

KERN K. N. CHANG received his B.S. degree from National Central University, Chungking-Nanking, China, in 1940, his M.S. degree in electrical engineering from the University of Michigan in 1948, and his Ph.D. degree from the Polytechnic Institute of Brooklyn in 1954. From 1940 to 1945, he was associated with the Central Radio Manufacturing Works, Kumming, China, working on radio receivers; and from 1945 to 1947, he was a radio instructor in the Office of Strategic Services, U. S. Army, China Theatre. Since 1948, Dr. Chang has been a member of the technical staff at RCA Laboratories, Princeton, New Jersey. He has been engaged in research on magnetrons, traveling-wave tubes, beam-focusing devices, parametric amplifiers, tunnel-diode devices, solid-state bulk-effect devices, and IR devices. He is presently head and Fellow of the Solid-State Microwave Devices group at RCA Laboratories, Princeton, New Jersey; his current interests are in semiconductor amplifiers and oscillators. He was the 1964 achievement award winner of the Chinese Institute of Engineers, New York, Inc., for his outstanding contribution in the field of electron devices, and has been selected for listing in the "American Men of Science" published by the Jacques Cattell Press, Inc. He is the author of the book "Parametric and Tunnel Diodes" Prentice-Hall, Inc. He is a member of Sigma Xi.

I. P. CSORBA graduated from the Electrical Engineering Fundamentals at the Electrical Engineering Faculty of the Technical University of Budapest in 1952. In the same year he was admitted to the Communication Engineering Faculty, specializing in communication and electronics. In October, 1954, he received the Diplom Ingenieur Degree in Electrical and Communication Engineering. From 1955 to 1956 he worked as a research engineer at the War Technical Institute, Budapest. In December of 1956 he joined the research group of Rauland Corporation, Chicago, where he worked on electrostatic-type image converter tubes, television picture tubes, scan-converter tubes. From 1959 to 1961 he was with Motorola, Inc., Chicago, working primarily on electrostatic-type scan magnification. In November of 1961, he joined RCA as a member of the Photo and Image Tube Engineering Activity. Mr. Csorba has been active in the design and development of magnetic and electrostatic-type image tubes and photomultiplier tubes.

JESS EPSTEIN received the EE degree and MS degree in Physics from the University of Cincinnati in 1932 and 1934. In 1935, he joined the Research Division of RCA at Camden, New Jersey. Since joining RCA at Camden, New Jersey, he has also worked at RCA Laboratories, the Missile and Surface Radar Division, Corporate Staff, Research and Engineering, and Corporate Staff, Patents and Licensing. During his career, Mr. Epstein has specialized in electromagnetic propagation and radiating systems. Mr. Epstein is a Senior Member of the IEEE and a Member of Sigma Xi.

HAJIME HONDA received the BSEE degree from the University of Pennsylvania in 1944 and the MSEE degree from Drexel Institute of Technology in 1960. From 1946 to 1956 he was with the Philco Corporation in Philadelphia. In 1956 he joined RCA in Camden, N.J., and in 1963 he transferred to RCA Burlington, Mass. Mr. Honda's work has included design and development of microwave components for radar, design and performance analysis of radar antennas, and development of optical radar processing techniques and ICBM detection.

JOSEPH R. JASINSKI is an honors graduate of RCA Institutes, New York, New York. He joined RCA Electronic Components, Lancaster, Pennsylvania, in 1958 as an electronics technician working on the testing and evaluation of Cermalox power tetrodes to establish their capability in pulsed RF service at L-band frequencies and, later, an S-band coaxitron, an advanced tube-circuit component employing integrated double-tuned coaxial circuits. In 1964, Mr. Jasinski was assigned to the developmental L-band module program for the U.S. Electronics Command, Fort Monmouth, New Jersey, and has since been responsible for the prototype development and manufacture of all new module variants. His most recent efforts were the design of high-power, multi-tuned amplifiers for use in television transmitters and communications systems.

HENRY KRESSEL received the B.A. degree from Yeshiva College in 1955. He received the S.M. degree in Applied Physics from Harvard University in 1956, and the M.B.A. and Ph.D. degree from the University of Pennsylvania in 1959 and 1965, respectively. Dr. Kressel joined RCA Electronic Components and Devices, Somerville, N. J., in 1959. He has been instrumental in the research and development of high-frequency mesa, planar, and planar epitaxial silicon transistors. In 1961 Dr. Kressel became head of the microwave diode group, where he was responsible for research, development, and pilot-line engineering of gallium arsenide and silicon varactor diodes. From 1963 to 1965, he was on a leave of absence doing doctoral work in metallurgy. Upon his return to RCA in 1965, he became head of the Device Physics Group in the Technical Programs Laboratory (Somerville, N. J.). He joined RCA Laboratories, Princeton, in 1966. His current research interests are in the area is a member of the Institute of Electrical and Electronics Engineers and

ARNOLD R. MOORE received the BS degree in Chemistry from the Polytechnic Institute of Brooklyn in 1942 and the Ph.D. degree in Experimental Physics from Cornell University in 1949. In 1949 he joined the Technical Staff of RCA Laboratories. His work has involved transistor physics, optical absorption, magnetic susceptibility, and the acoustoelectric effect.

HERBERT NELSON received the B.S. degree from Hamline University in 1927 and the M.S. degree in physics from the University of Minnesota in 1929. From 1929 to 1930 he was an engineer with the Westinghouse Lamp Company in Bloomfield, New Jersey. In 1930, Mr. Nelson transferred to RCA Electronic Components in Harrison, New Jersey, where he engaged in electronic research and development. In 1953, he joined the semiconductor research group at the RCA Laboratories in Princeton, New Jersey.

Mr. Nelson's work has covered almost every important phase of vacuum tube and semiconductor device technology and research. His original contributions include novel space-charge amplifiers, vacuum gauges, and new types of transistor structures. His diffusion-lapping technique has led to silicon transistors with greatly improved characteristics and is especially useful for the fabrication of miniature integrated-type devices. Mr. Nelson is a member of Sigma Xi and of the American Physical Society.

JACQUES I. PANKOVE obtained his B.S. (1944) and M.S. (1948) degrees from the University of California. He received his doctorate from the University of Paris in 1960 for a study of infrared radiation in germanium. Since 1948, when he joined RCA Laboratories, he has made many contributions to the understanding, technology, and evolution of various semiconductor devices, including large-area photocells and transistors. He has worked in the field of superconductivity, studies of silicon carbide, and investigations of the optical properties of degenerate germanium and the electrical properties of tunnel diodes in germanium, as well as in superconductors and in thin oxide layers. Currently, he is concerned with the study of injection luminescence and laser action in gallium arsenide and other compounds.

ROBERT O. WINDER received an A.B. from the University of Chicago in 1954, a B.S. from the University of Michigan in 1956, an M.A. and Ph.D. from Princeton University (Mathematics Department) in 1958 and 1962. In 1957, Dr. Winder joined RCA at Camden where he worked on a small computer design and automatic programming. Since joining the RCA Laboratories in 1958, he has investigated a variety of subjects in computer systems, logic, and circuit design, with main emphasis in threshold logic—both theory and application. He has been visiting lecturer at the University of Pennsylvania, the University of California (Berkeley), Stevens Institute of Technology, Ohio State University, and LaSalle College. Dr. Winder is a member of the Association for Computing Machinery, the Institute of Electrical and Electronics Engineers, Phi Beta Kappa, and Phi Kappa Phi.

OAKLEY M. WOODWARD, JR. received the degree of Bachelor of Science in Electrical Engineering from the University of Oklahoma in 1938. He joined the Seismograph Service Corporation of Tulsa, Oklahoma, after graduation. During 1941, he was a research engineer at the RCA Manufacturing Company, Camden, N. J. In January 1942, he became a member of the technical staff at RCA Laboratories, Princeton, N. J. In 1961, he transferred to the RCA Antenna Skill Center, Missile & Surface Radar Division, Moorestown, N. J. Mr. Woodward is a Member of Sigma Xi, and a Senior Member of the Institute of Electrical and Electronics Engineers.

STATEMENT OF OWNERSHIP

Statement of Ownership, Management and Circulation (Act of October 23, 1962, Section 4369, Title 39, United States Code).

1. Date of filing: September 26, 1968. 2. Title of publication: RCA REVIEW. 3. Frequency of issue: Quarterly. 4. Location of known office of publication: RCA Laboratories, Princeton, New Jersey, 08540. 5. Location of the headquarters or general business offices of the publishers: RCA Laboratories, Princeton, New Jersey, 08540. 6. Names and addresses of Publisher, Editor, and Managing Editor: Publisher, RCA Laboratories, Princeton, New Jersey; Editor, C. C. Foster, RCA Laboratories, Princeton, New Jersey; Managing Editor, R. F. Ciafone, RCA Laboratories Princeton, New Jersey. 7. Owner: Radio Corporation of America, 30 Rockefeller Plaza, New York, New York, 10020. 8. Known Bondholders, Mortgagees, and other security holders owning or holding 1 percent or more of total amount of bonds, mortgages or other secuities: Metropolitan Life Ins. Co., 1 Madison Ave., New York, New York; New York Life Ins. Co., 51 Madison Ave., New York, New York.

I certify that the statements made by me above are correct and complete.

RALPH F. CIAFONE, *Managing Editor*